DESIGN AND DEVELOPMENT OF CO METHANATION CATALYSTS FOR A NOVEL COAL TO SNG PRODUCTION TECHNOLOGY

by

Burcu Acar

B.Sc. in Chemical Engineering, Boğaziçi University, 2012

M.Sc. In Chemical Engineering, Boğaziçi University, 2016

Submitted to the Institute for Graduate Studies in
Science and Engineering in partial fulfillment of
the requirements for the degree of
Doctor of Philosophy

Graduate Program in Chemical Engineering

Bogaziçi University

2024

to my family

ACKNOWLEDGEMENTS

Firstly, I would like to express my sincere gratitude to my thesis supervisor Prof. Ahmet Erhan Aksoylu for his guidance, immense knowledge, support, and trust in me. His guidance helped me in all the time of research and writing of this thesis. It was a privilege for me to work with him during my study.

My sincere thanks also go to Dr. Burcu Selen Çağlayan for her encouragement and guidance during my Ph.D. years. I would like to express my great appreciations for her for enlightening me by giving her practical advices whenever I needed throughout my work.

I would like to express my sincere appreciations for the members of my thesis committee, Prof. Ramazan Yıldırım, Prof. Alper Uzun, Prof. Birgül Tantekin Ersolmaz and Prof. Hasan Bedir, for devoting their valuable time to attend my thesis defense.

I am deeply grateful to two special people, Merve Eropak and Cihat Öztepe for guiding and helping me throughout my thesis. Besides their efforts in XPS and XRD analysis, they never hesitated to spend their time and effort for me.

I would like to thank to Elif Can, Elif Gençtürk, Beyza Yılmaz, Serhat Erşahin, Çağla Odabaşı, İpek Paksoy, Melek Selcen Başar, Ali Uzun, Onur Ordulu and all SNG&HydTec team members in the Chemical Engineering Department at Boğaziçi University for their friendship and making this period enjoyable.

I should also thank to Bilge Gedik Uluocak for her significant effort in SEM analyses conducted at Boğaziçi University Advanced Technologies Research and Development Center.

Very special thanks should be addressed to Serli Kiremitçiyan, Elif Tezel and Elif Tuğçe Çelik for their friendship, endless support and encouragement on any matter.

Finally, I wish to express my profound gratitude to my beloved family: my father, Mustafa Acar; my mother, Ayfer Acar; my sister, Kübra Acar; and my greatest joy, my niece, Nehir. Although my father passed away years ago, I continue to feel his trust and love. My amazing family, to whom this dissertation is dedicated, has always believed in me and given me love, strength, and courage to follow my dreams and desires.

Financial support provided by Presidency of Republic of Turkey Department of Strategy and Budget (Ministry of Development) through project 2016K12-2838 (2016K121160) is gratefully acknowledged.

ABSTRACT

DESIGN AND DEVELOPMENT OF CO METHANATION CATALYSTS FOR A NOVEL COAL TO SNG PRODUCTION TECHNOLOGY

The overall purpose of this research is to design and develop Ni-based methanation catalysts with high and efficient methane production activity, selectivity, and stability for realistic feed conditions with $H_2/CO<3$ by combining methanation and WGS reactions. Initially, preliminary tests were conducted on a conventional methanation catalyst, 15%Ni/γ-Al_2O_3, to evaluate the impact of experimental parameters on methanation performance. Secondly, various catalyst bed configurations using classical methanation and WGS catalysts were investigated. It was determined that using catalyst mixtures or sequential beds did not significantly enhance CH_4 yield compared to a pure methanation catalyst. The third section explored bifunctionality by integrating WGS and methanation reactions within a single catalyst. New Ni-based catalysts with different promoters, supports, and pretreatment conditions were synthesized and evaluated. At 400 °C and an H_2/CO ratio of 3, most catalysts exhibited high CO conversion values (93%-99%), with the highest conversion observed for 5%Ce-10%Ni/SBA-15-550. Reducing the H_2/CO ratio to 2 caused a drop in CO conversion for 1%Mg-10%Ni/γ-Al_2O_3 (from 92.9% to 84.2%) and 15%Ni/SBA-15-750 (from 92.7% to 72.6%), while other catalysts maintained stable conversion values. Temperature decrease significantly impacted performance. At 250 °C, only six out of sixteen catalysts exhibited CO conversion, with 5%Ce-10%Ni/γ-Al_2O_3 demonstrating the best performance (ca. 96%). Ce-Ni catalysts were characterized using XPS, XRD, HR-TEM, SEM, and RAMAN techniques. XPS analysis revealed enhanced electronic interactions with Ce addition, XRD indicated improved NiO reduction, RAMAN showed increased carbon deposition at lower temperatures, and SEM/TEM identified distinct Ce and Ni cluster formations influenced by the support material. Kinetic studies on the 5%Ce-10%Ni/γ-Al_2O_3 catalyst identified different kinetic regimes between 300-350 °C and 350-400 °C. Among the evaluated power-law type and Langmuir-Hinshelwood models, although Langmuir-Hinshelwood models had better predictive capabilities, all rate equations were inadequate for modeling the reaction.

ÖZET

YENİ BİR KÖMÜRDEN SENTETİK DOĞAL GAZ (SNG) ÜRETİM TEKNOLOJİSİ İÇİN CO METANASYON KATALİZÖRLERİNİN TASARIMI VE GELİŞTİRİLMESİ

Bu araştırmanın amacı, metanasyon ve WGS reaksiyonlarını birleştirerek H_2/CO oranının 3'ten düşük olduğu koşulları altında yüksek ve verimli metan üretim aktivitesine, seçicilik ve stabiliteye sahip Ni bazlı metanasyon katalizörleri tasarlamak ve geliştirmektir. İlk olarak, metanasyon performansı üzerinde deneysel parametrelerin etkisini değerlendirmek için geleneksel bir metanasyon katalizörü üzerinde ön testler gerçekleştirilmiştir. İkinci olarak, klasik metanasyon ve WGS katalizörleri kullanılarak çeşitli katalizör yatak konfigürasyonları üzerinde çalışılmıştır. Saf bir metanasyon katalizörü yerine katalizör karışımları veya ardışık yataklar kullanmanın CH_4 verimini önemli ölçüde artırmadığı belirlenmiştir. Üçüncü bölümde, WGS ve metanasyon reaksiyonlarını tek bir katalizör içinde birleştirerek bifonksiyonellik araştırılmıştır. Farklı promotörler, destekler ve ön işlem koşullarına sahip yeni Ni bazlı katalizörler sentezlenmiş ve test edilmiştir. 400°C'de, H_2/CO oranı 3 olduğunda, yüksek CO dönüşüm değerleri (%93-%99) elde edilmiş; en yüksek değer 5%Ce-10%Ni/SBA-15-550 için gözlemlenmiştir. H_2/CO oranının 2'ye düşürülmesi, 1%Mg-10%Ni/γ-Al_2O_3 (92.9%'dan 84.2%'ye) ve 15% Ni/SBA-15-750 (92.7%'den 72.6%'ya) katalizörlerinde CO dönüşümünde düşüşe neden olmuştur, ancak diğerleri stabil dönüşüm değerlerini korumuştur. Sıcaklık düşüşleri performansı önemli ölçüde etkilemiştir. 250°C'de, 16 katalizörden sadece 6'sı CO dönüşümü sergilemiş, 5%Ce-10%Ni/γ-Al_2O_3 en iyi performansı göstermiştir (%96). Ce-Ni katalizörleri, XPS, XRD, HR-TEM, SEM ve RAMAN teknikleri ile karakterize edilmiştir. XPS analizi Ce ilavesiyle artan elektronik etkileşimler, XRD daha iyi NiO indirgenmesi, RAMAN ise düşük sıcaklıklarda artan karbon birikimi göstermiştir. SEM ve TEM analizleri, destek malzemesinin etkisiyle belirgin Ce ve Ni küme oluşumlarını ortaya koymuştur. Kinetik çalışmalar, 5%Ce-10%Ni/γ-Al_2O_3 katalizörü üzerinde 300-350°C ve 350-400°C arasında farklı kinetik rejimler belirlemiştir. Langmuir-Hinshelwood modelleri daha iyi tahmin yeteneğine sahip olsa da, güç yasası ve LH modelleri reaksiyonu modellemede yetersiz kalmıştır.

TABLE OF CONTENTS

LIST OF FIGURES

LIST OF TABLES

LIST OF SYMBOLS

a	Order of K_{H_2} in Langmuir Hinshelwood type rate expression of CO methanation reaction
b	Rate order of CO in Langmuir Hinshelwood type rate expression of CO methanation reaction
c	Rate order of H_2 in Langmuir Hinshelwood type rate expression of CO methanation reaction
C	Concentration
e	Order of CO inhibition term in Langmuir Hinshelwood type rate expression of CO methanation reaction
f	Order of H_2O inhibition term in Langmuir Hinshelwood type rate expression of CO methanation reaction
g	Order of overall inhibition term in Langmuir Hinshelwood type rate expression of CO methanation reaction
E_A	Activation energy
F	Molar flow rate
$F_{CH_4,in}$	Molar flow rate of CH_4 in
$F_{CH_4,out}$	Molar flow rate of CH_4 out
$F_{CO,in}$	Molar flow rate of CO in
$F_{CO,out}$	Molar flow rate of CO out
$F_{CO_2,in}$	Molar flow rate of CO_2 in
$F_{CO_2,out}$	Molar flow rate of CO_2 out
k_0	Pre-exponential factor
k	Specific rate constant
K_{eq}	Equilibrium constant
n	Number of moles
P	Pressure
r	Reaction rate
R	Universal gas constant
t	Time
T	Temperature

x	Mole fraction
X	Conversion
V	Volume
W	Catalyst weight
wt	Weight
α	Rate order of H_2 in CO methanation reaction
β	Rate order of CO in CO methanation reaction
ΔH°_{298}	Standard enthalpy of reaction
δ	Rate order of CH_4 in CO methanation reaction
θ	Rate order of H_2O in CO methanation reaction
ε	Change in total number of moles for complete conversion/total moles fed
v_0	Volumetric flow rate in the feed stream
v	Volumetric flow rate in the product stream

LIST OF ACRONYMS/ABBREVIATIONS

AC	Activated Carbon
AGR	Acid Gas Removal
BSE	Back Scanning Electron
CCS	Carbon Capture and Sequestration
DI	Deionized
DRIFTS	Diffuse Reflectance Infrared Fourier Transform Spectroscopy
EDX	Energy Dispersive X-Ray
FTIR	Fourier Transform Infrared Spectroscopy
GC	Gas Chromatograph
GHSV	Gas Hourly Space Velocity
HPLC	High Performance Liquid Chromatography
LH	Langmuir Hinshelwood
MFC	Mass Flow Controller
MS	Mass Spectrometer
MSE	Mean Square Error
MW	Molecular Weight
RMSE	Root Mean Squared Error
RT	Room Temperature
SE	Secondary Electron
SEM	Scanning Electron Microscopy
SNG	Synthetic Natural Gas
TCD	Thermal Conductivity Detector
TEM	Transmission Electron Microscopy
TPR	Temperature Programmed Reduction
WGS	Water Gas Shift
XP	X-Ray Photoelectron
XPS	X-Ray Photoelectron Spectroscopy
XRD	X-Ray Diffraction

1. INTRODUCTION

Over the past centuries, daily requirements for chemical materials, electricity, transportation and heating fuels, have been largely produced from carbon-rich fossil sources (i.e. coal, oil and natural gas). Among them natural gas, which contains mainly CH_4, is accepted as the ideal fossil fuel due to its conversion efficiency, high energy density, and environmental friendliness owing to combustion with smoke- and slag-free composition (H. Wang et al., 2017).

Owing to uneven and limited distribution of the natural gas reserves, increasing demand for natural gas, and the concerns about the rising greenhouse gas emissions, industrial and academic studies have recently focused on the production of synthetic natural gas (SNG). The conventional process for synthetic natural gas production starts with the gasification of coal and/or biomass to synthetic gas (syngas). Following syngas cleaning and conditioning, which aims to remove impurities, the syngas -comprising H_2, CO, CO_2, CH_4, H_2O and heavy hydrocarbons- is subjected to methanation (Gao et al., 2012). This process involves the conversion of carbon oxides (CO and/or CO_2) and hydrogen in the syngas into methane and water through

$$CO + 3H_2 \leftrightarrow CH_4 + H_2O \qquad \Delta H = -206.1 \frac{\text{kj}}{\text{mol}}, \tag{1.1}$$

$$CO_2 + 4H_2 \leftrightarrow CH_4 + 2H_2O \qquad \Delta H = -165.0 \frac{kj}{mol}. \tag{1.2}$$

In conventional SNG production processes, final syngas cleaning prior to methanation is done in a Rectisol unit. The Rectisol process is a solvent-based acid gas removal (AGR) method commonly utilized to effectively eliminate almost all CO_2 and H_2S from syngas. It functions through a single absorption column with three distinct sections, where chilled methanol (-40 °C) acts as the solvent to selectively absorb CO_2 and H_2S. H_2S and COS are removed at the bottom section while CO_2 removal occurs at the top and middle sections of the tower. Heat of absorption is removed by the refrigeration coils in the middle section. After undergoing purification in the Rectisol unit, the syngas is directed to a methanation reactor where it undergoes conversion into synthetic natural gas (SNG) (Anderson et al., 1984).

Figure 1.1 shows the methanation unit of the industrial SNG process called TREMP (Topsoe Recycle Energy-efficient Methanation Process). This unit is designed by Haldor Topsoe. The process employs three adiabatic reactors, each operating at progressively lower temperatures. Due to the highly exothermic nature of methanation, lower temperatures are preferred to enhance methane formation and minimize carbon dioxide production via the water gas shift (WGS) reaction. A nearly stoichiometric mixture of hydrogen, carbon monoxide, and carbon dioxide is combined with recycled gas containing methane and fed into the initial reactor. The effluent from this stage undergoes cooling and division into a recycle stream and a feed stream for the subsequent reactor. The temperature increase in the initial reactor is effectively moderated by the recycle gas, which is employed to dilute the feed gas (Bell et al., 2011).

Haldor Topsøe asserted that MCR-2X, the catalyst for methanation, can be used at elevated temperatures, achieving high reaction rates and yielding a high-quality product. However, high temperatures may cause the coking and sintering of the catalyst (Gao et al., 2015). Furthermore, conventional process requires the utilization of a feed gas with $H_2/CO \approx 3$ (Bell et al., 2011). Over the last years, methanation catalysts and processes have been investigated intensively to synthesize a new catalyst which has high activity at low temperatures, enhanced stability at elevated temperatures, and ability to produce CH_4 at lower H_2/CO ratios, and to develop a novel process with enhanced energy efficiency. In order to achieve these purposes, different catalysts, particularly those incorporating group VIII metals have been produced and studied, among which $Ni/\alpha\text{-}Al_2O_3$ being the most studied methanation catalyst (H. Wang et al., 2017).

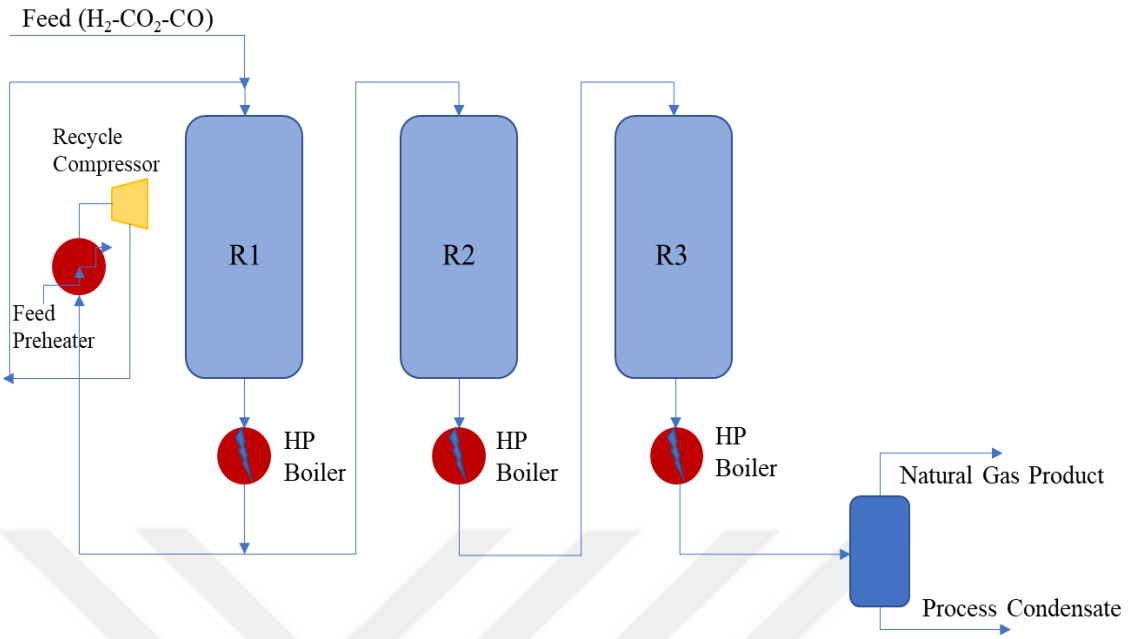

Figure 1.1. Haldor Topsoe TREMP for SNG production.

The current work is a comprehensive study involving the design and development of new catalysts for a novel, economically feasible, coal to SNG production technology. In the novel SNG technology, conventional technology is modified in many ways. The current work focuses on one of those novel modifications; the use of a novel catalyst(s) achieveing fuel-flexible methanation reactor as a replacement of conventionally used TREMP process and its catalysts. The aim of this study is to design and develop Ni-based methanation catalyst(s) having high and efficient methane production activity, selectivity and stability for realistic feed conditions with $H_2/CO<3$ through combining methanation and WGS reactions.

This extensive study is divided into five sections to systematically explore different aspects of catalyst development and evaluation. The first section of this study focused on preliminary tests to evaluate the impact of experimental parameters on methanation performance using a conventional catalyst. These initial tests provided valuable insights into the fundamental factors influencing catalyst efficiency. The second section investigated various catalyst bed configurations utilizing classical methanation and Water-Gas Shift (WGS) catalysts. The goal was to assess how different configurations affect methanation performance and to identify optimal setups for enhanced catalytic activity. In the third section, the study explored bifunctionality through the integration of WGS and methanation reactions within a single catalyst. New catalyst formulations were synthesized and evaluated,

varying in metals, metal precursors, metal loading combinations, preparation methods, and pretreatment conditions. This exploration aimed to develop catalysts with improved performance and stability. Ce-Ni catalysts, which yielded the highest and lowest performance results, were comprehensively characterized in the fourth section. Advanced characterization techniques such as X-ray Photoelectron Spectroscopy (XPS), X-ray Diffraction (XRD), High-Resolution Transmission Electron Microscopy (HR-TEM), Scanning Electron Microscopy (SEM), and Raman Spectroscopy were employed to understand the structural and chemical properties influencing catalyst performance. Finally, the fifth section focused on kinetic studies of the CO methanation reaction using the 5%Ce-10%Ni/γ-Al_2O_3 catalyst, which demonstrated the highest performance results. These studies provided a deeper understanding of the reaction mechanisms and kinetics, contributing to the optimization of catalyst design and operating conditions.

Chapter 2 offers an extensive literature review on the theoretical foundations of the gasification process and methane production. Chapter 3 details the experimental procedures and systems utilized for catalyst production in the current study. The results of performance tests, characterization, and kinetic analyses, along with corresponding discussions, are presented in Chapter 4. Lastly, Chapter 5 provides the conclusions drawn from this study and offers recommendations for future research.

2. LITERATURE SURVEY

Carbon-based fossil fuels, such as natural gas, coal, and crude oil, are pivotal energy sources integral to both industrial production and daily life. Notably, natural gas, primarily composed of methane, is acknowledged as an optimal fossil fuel due to its conversion efficiency, high energy density, and environmental friendliness, owing to its combustion producing smoke- and slag-free emissions. Recently, highly volatile natural gas prices and energy security concerns—stemming from the uneven and limited distribution of natural gas reserves—have driven increased interest in synthetic or substitute natural gas (SNG) production from syngas. Syngas, produced through the gasification of coal and/or biomass, has attracted growing attention (Wang et al., 2017). The main sequential steps of a typical SNG process are gasification, ash and sulfur removal, water-gas shift, CO_2 capture, and methanation.

2.1. Gasification

Gasification involves converting solid feedstocks such as coal, biomass, petroleum coke, or municipal wastes into synthesis or fuel gases (comprising H_2, CO, CO_2, and CH_4) using oxidizing agent gases like oxygen, air, steam, or CO_2. It is essentially the incomplete combustion of coal or other solid feedstocks, aimed at two main objectives: (i) transforming all non-ash components of the feedstock into gaseous form, and (ii) producing gases with maximum retention of the combustion heat value from the feedstock. A simplified gasification mechanism can be represented by the following series of reactions (Table 2.1) (Masnadi-Shirazi, 2014).

Table 2.1. Gasification Mechanism.

Reaction Type	**Reaction Formula**	
Pyrolysis	$Fuel + Heat \rightarrow Char,\ H_2,\ CO,\ CO_2,\ H_2O,\ CH_4,\ C_nH_m,\ Tar\ \ldots.$	(2.1)
Tar cracking	$Tar + Heat \rightarrow H_2 + CO + CO_2 + \cdots$	(2.2)
Combustion (oxidation)	$C + \frac{1}{2}O_2 \rightarrow CO + 110.6\frac{kJ}{mol}$	(2.3a)
	$C + O_2 \rightarrow CO_2 + 393.8\frac{kJ}{mol}$	(2.3b)
	$CO + \frac{1}{2}O_2 \rightarrow CO_2 + 283.2\frac{kJ}{mol}$	(2.3c)
Boudard reaction	$C + CO_2 \leftrightarrow 2CO - 172.6\ kJ/mol$	(2.4)
Steam-Carbon reactions	$C + H_2O \leftrightarrow H_2 + CO - 131.2\frac{kJ}{mol}$	(2.5a)
	$C + 2H_2O \leftrightarrow 2H_2 + CO - 89.8\frac{kJ}{mol}$	(2.5b)
Methanation	$C + 2H_2 \leftrightarrow CH_4 + 74.9\frac{kJ}{mol}$	(2.6)
WGS	$CO + H_2O \leftrightarrow CO_2 + H_2 + 41.4\frac{kJ}{mol}$	(2.7)
Steam-metahane reforming	$CH_4 + H_2O \leftrightarrow CO + 3H_2 - 206.1\frac{kJ}{mol}$	(2.8)

Gasifier units with technologies compatible with various existing or proposed SNG processes have been developed at lab and demo scales, as well as for industrial usage. Generally, gasifier units—which include fixed, fluidized, and transported bed reactors—operate at pressures ranging from 1 to 20 bars and at temperatures between approximately 700-1000 ºC (Masnadi-Shirazi, 2014). After the gasification process is completed, the inorganic fraction of the gasified feedstock turns into molten slag or solid ash, or, at relatively low temperatures, tar. Ash/slag and tar removal processes are integral parts of gasifier design. However, gasifiers operating at high temperatures do not produce significant amounts of tar. Syngas leaving the gasifier contains numerous impurities such as sulfur in

the form of H_2S, CO_2, and mercury. Sulfur removal from syngas is crucial to prevent SO_2 emissions and catalyst poisoning in subsequent reactors downstream. CO_2 can be eliminated either during impurity removal or following the WGS reaction unit. Carbon capture and sequestration (CCS) is one of the most important parts of coal gasification, as integrating CCS technology minimizes greenhouse gas emissions. Given its current high cost, around 40% of total power plant expenditures, there is a critical need to develop and scale cost-effective CCS options (Bell et al., 2011). The relationship between gasification and related technologies is shown in Figure 2.1.

A nearly pure hydrogen stream is required for some applications (e.g., fuel cells), whereas in others, such as methane production, a specific ratio of hydrogen to carbon monoxide is desired. However, gasifiers typically produce a lower ratio of hydrogen to carbon monoxide than desired. Studies conducted as part of the Tampa Electric Integrated Gasification Combined-cycle Project have shown statistically significant differences in average syngas composition between coal- and petcoke-derived processes. Coal gasified in the presence of O_2 with a volume based product composition of 44.06% CO, 14.73% CO_2, 37.95% H_2, 2.28% N_2, and 0.88% Ar, while petrocoke gasification produced a gas mixture of 48.29% CO, 13.61% CO_2, 34.02% H_2, 3.02% N_2, and 1% Ar (Tampa Electric Integrated Gasification Combined-cycle Project, 2014). Higher H_2 to CO ratios obtained in co-gasification studies, in which coal and biomass blends are gasified together. Kumabe et al., reported mole based product gas composition of 42.7% H_2, 3.6% CH_4, 22.9% CO, and 29.9% CO_2, when 50% coal-50% wood blend was gasified with steam and air (Kumabe et al., 2007). Although H_2 to CO ratio is slightly higher for some examples of co-gasification, this ratio still needs to be shifted towards a higher H_2 content; for example for methane production, H_2 to CO ratio should be at least 3. WGS is the traditional way to increase H_2 to CO ratio via reacting CO with H_2O to form H_2 and CO_2 (Bell et al., 2011).

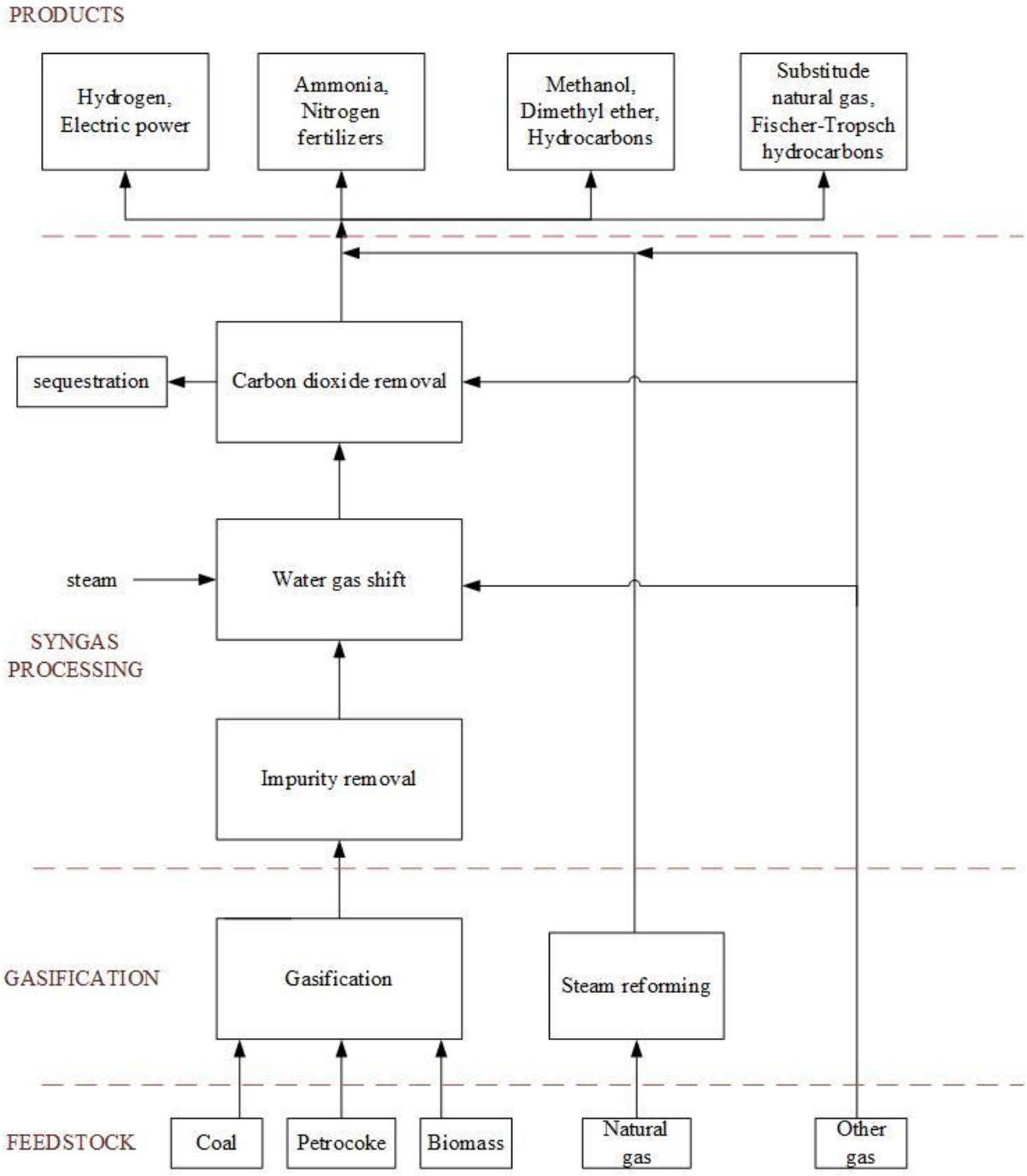

Figure 2.1. Gasification and related technologies.

Current attention towards coal gasification is driven by two important developments: (i) the recognition that the decline in traditional petroleum supplies alongside increasing demand for petroleum refinery products persists; and (ii) concerns about global warming stemming from greenhouse gas emissions. Gasification technologies provide relatively cost-efficient methods for utilizing coal to produce transportation and heating fuels while minimizing greenhouse gas emissions (Bell et al., 2011).

2.2. Methanation

The methanation reaction was was pioneered by Sabatier and Senderens at the outset of the 20th century. Their studies demonstrated that metals such as Ni, Ru, Rh, Pt, Fe, and Co catalyze the reaction between CO and H_2 to produce CH_4 and H_2O. However, it was not until the late 1970s that the methanation reaction began to attract industrial interest due to the growing demand for natural gas and the uneven and limited distribution of reserves (Razzaq et al., 2013).

The main reactions involved in the methanation process are listed in Table 2.1. The most important key reactions in the SNG production process are CO methanation (R1) and CO_2 methanation (R2). Both methanation reactions are highly exothermic, thermodynamically viable, and exhibit favorable kinetics at lower temperatures, while their reaction rates diminish at higher temperatures (H. Wang et al., 2017). Therefore, previous literature has primarily focused on methanation at relatively low temperatures (approximately 200–400 °C). However, this temperature range is suboptimal for energy recovery, as SNG production processes with high concentrations of CO and/or CO_2 can lead to significant temperature increases (600–700 °C). Although Haldor Topsøe documented that MCR-2X, the catalyst for methanation, could be used at elevated temperatures, achieving high reaction rates and yielding a high-quality products, these high temperatures can also lead to catalyst sintering and coking. In summary, methanation catalysts must exhibit stability at high temperatures while remaining active at low temperatures to initiate the reaction in the SNG production process. Another significant reaction affecting SNG production is the inverse methane CO_2 reforming (R3), where CO reacts with H_2 to produce CH_4 at a lower H_2/CO ratio compared to R1. The Boudouard reaction (R4) is also crucial, as carbon acts as a vital intermediate in the methanation process facilitated by the catalyst. Additionally, water plays a dual role: it participates in the WGS reaction (R5) and alters the composition and catalytic behavior of the catalysts (Gao et al., 2015). All these reactions are also favorable at low temperatures (≤ 400 °C) due to their exothermic characteristics. It can be concluded that, low temperature and high-pressure values are preferred for overall SNG production process. However, for low temperature CO and/or CO_2 methanation reactions, development of a sufficiently active catalyst remians a challenge.

Table 2.2. The main reactions involved in the methanation of carbon oxides (H. Wang et al., 2017).

No	Reaction Type	Reaction Formula	$\Delta H_{298K}\left(\frac{kj}{mol}\right)$
R1	CO methanation	$CO + 3H_2 \leftrightarrow CH_4 + H_2O$	-206.1
R2	CO_2 methanation	$CO_2 + 4H_2 \leftrightarrow CH_4 + 2H_2O$	-165.0
R3	Inversed methane CO_2 reforming	$2CO + 2H_2 \leftrightarrow CH_4 + CO_2$	-247.3
R4	Boudouard reaction	$2CO \leftrightarrow C + CO_2$	-172.4
R5	Water–gas shift	$CO + H_2O \leftrightarrow CO_2 + H_2$	-41.2
R6	Methane cracking	$CH_4 \leftrightarrow 2H_2 + C$	74.8
R7	Carbon monoxide reduction	$CO + H_2 \leftrightarrow C + H_2O$	-131.3
R8	Carbon dioxide reduction	$CO_2 + 2H_2 \leftrightarrow C + 2H_2O$	-90.1
R9	-	$nCO + (2n+1)H_2 \leftrightarrow C_nH_{2N+1} + nH_2O$	-
R10	-	$nCO + 2nH_2O \leftrightarrow C_nH_{2n} + nH_2O$	-

2.2.1. Methanation Catalysts

Over the past decade, there has been intensive investigation into methanation catalysts. Different catalysts, predominantly those incorporating Group VIII metals, have been synthesized and studied to achieve high activity at low temperatures and enhanced stability at elevated temperatures. This section of the literature research will discuss the roles of catalyst components in CO methanation in four parts: (i) metals, (ii) supports, (iii) promoters, and (iv) preparation methods.

Supported transition metal (Ni, Co, Fe, Ru, Rh, Pd, Os, Ir, and Pt) catalysts have received extensive research attention in CO methanation, with Ni and Ru emerging as the most thoroughly studied metals. Vannice quantified catalytic activity in terms of turnover numbers of surface metal atoms, ranking the methanation activities of Group VIII metals as

follows: Ru > Fe > Ni > Co > Rh > Pd > Pt > Ir (Vannice, 1975). Although catalysts based on Ru exhibited higher activity and stability compared to those based on Ni, the preference and extensive investigation of Ni as the active metal were driven by the high prices of Ru (Kopyscinski et al., 2010). Several studies focused on the relation of catalytic activity to the Ni particle size and loading: Zhao et al. observed maximum production on Ni particles having size around 41.8 nm for Ni–Al_2O_3 (Zhao et al., 2012), while Gao et al. stated that the catalyst with particle sizes ranging from 10 to 20 nm exhibited superior catalytic performance and minimal carbon deposition for Ni/α-Al_2O_3 (Gao et al., 2013). Hwang et al. demonstrated that CO conversion increased with Ni loading from 20 wt.% to 40 wt.%, plateauing thereafter for loadings exceeding 40 wt.% in Ni–Al_2O_3 xerogel catalysts (Hwang et al., 2011). Besides being used as active metal, Co can also be used as a promoter and/or combined with Ni or Pt to synthesize bimetallic catalysts for enhancing activity and stability: The addition of Co enhanced the catalytic performance of MoO_3/Al_2O_3 catalysts in sulfur-tolerant methanation (B. Wang et al., 2014a). In terms of particle size; nanosized (20 nm) Co_3O_4 catalysts exhibited higher CO adsorption capacities than that of larger (49 and 80 nm) particle size catalysts (Zhu et al., 2012). Fe-based catalysts exhibit low activity and susceptibility to carbon deposition in methanation. Consequently, Fe is typically employed as a secondary metal alongside Ni to create alloy or bimetallic catalysts. (H. Wang et al., 2012). Kustov et al. (Kustov et al., 2007) and Tian et al. (Tian et al., 2013) showed that the addition of Fe improved the activity of the catalyst.

γ-Al_2O_3 is widely preferred as a support in methanation catalysts because of its diverse crystal forms and its advantageous chemical and textural properties. However, it suffers from a few drawbacks: (i) phase transformation at high temperatures, leading to pore structure collapse and catalyst sintering; and (ii) surface acidity that can induce carbon deposition. To overcome these challenges, some studies have focused on synthesizing mesostructured γ-Al_2O_3 (Li et al., 2015). In other studies on Al_2O_3, the attention was on the use inert α-Al_2O_3 as the catalyst support, free of acids. On the other hand, the surface area of α-Al_2O_3 was insufficient to attain a high dispersion of the metal. (Gao et al., 2013). Zeolites are crystalline aluminosilicates with micropores that impose significant limitations on diffusion in many catalytic processes. Mesoporous zeolites have been preferred as support materials for methanation catalysts to overcome these limitations (Teh et al., 2015). SiO_2 provides a notable advantage over alternative support materials due to its flexibility in

adjusting and managing the average pore diameter, specific surface area, and pore volume. In CO methanation, CeO_2 is frequently employed not only as a support but also as structural and electronic enhancers. CeO_2 suppresses deposition through its reversible transformation between CeO_2 and Ce_2O_3 under oxidizing and reducing environments. Additionally, it improves heat resistance, promotes even distribution of metals, and alters the electronic properties of metals via strong interactions between the metal and the support material (H. Wang et al., 2017).

Various promoters have been added to catalysts to impart essential properties, such as high sulfur resistance, anti-sintering, and anti-coking. Using VO_x as a promoter has improved the activity and thermal stability of catalysts. Liu et al. employed VO_x in ternary ordered mesoporous Ni–V–Al catalysts and illustrated that VO_x heightened catalytic activity in CO methanation. During lifetime tests, the Ni–V–Al catalyst demonstrated substantial enhancements in both resistance to coking and prevention of sintering. These improvements were credited to decreased size of Ni particles, the controlling effect of the mesoporous channels, and the integration of VOx (Liu et al., 2015). In a study conducted by Si et al., it was found that the addition of La_2O_3 as a promoter to a Ni/ZrO_2 catalyst enhanced catalytic activity by restraining the growth of NiO particles and increasing Ni dispersion (Si et al., 2016). Hu et al. synthesized Ni/Al_2O_3 catalysts using MgO as promoter via the impregnation method and stated that the addition of MgO improved the stability of the catalyst (Hu et al., 2012).

In the literature, diverse techniques and methods have been utilized to synthesize methanation catalysts. The most frequently used methods are co-precipitation, impregnation, sol–gel, and mechanical mixing. To enhance the resistance to sintering in catalysts used for methanation, alternative approaches including deposition–precipitation, dual templating, hard-templating, hydrothermal synthesis, and solution combustion have also been utilized (H. Wang et al., 2017). Previous studies conducted by Kruissink and his group showed that co-precipitated $Ni–Al_2O_3$ catalysts exhibited higher stability during high-temperature methanation compared to those obtained through impregnation. This increased stability was attributed to the high dispersion of active metal and strong metal-support interaction in the co-precipitated $Ni–Al_2O_3$ catalysts (Alzamora et al., 1981; Kruissink et al., 1981). Zhang et al., synthesized Ni/SiO_2 catalysts using the plasma treatment method and showed that plasma

treatment significantly enhanced the dispersion of active components and increased the catalytical reactivity (Zhang et al., 2013). As the catalysts prepared by plasma decomposition demonstrated high activity and improved sulfur-resistance, Teh et al., mentioned plasma decomposition as an effective preparation method for Ni/SiO_2 catalysts (Teh et al., 2015).

Previous research has indicated that, beyond catalyst type and preparation methods, the methanation reactions of carbon oxides are influenced by multiple factors including temperature, pressure, and the composition of the syngas mixture.

2.2.2. Effect of Temperature & Pressure

Gao et al., investigated the effects of pressure, temperature, H_2/CO ratio, and the introduction of additional compounds (such as CH_4, H_2O, O_2, and C_2H_4) into the feed gas (syngas) on carbon monoxide conversion, methane yield, and carbon deposition. In their study, two commercial Ni-based CO methanation catalysts were used. They determined that increased pressure results in higher CO conversion rates, attributed to the volumetric reduction characteristic of CO methanation reactions. Moreover, under constant pressure, reducing the temperature results in increased CO conversion, owing to the exothermicity of the reaction. Their research indicated that high operation temperatures require high operation pressures to obtain appreciable CH_4 yields. Since high operating pressures and temperatures in the chemical industry are not economically preferable, their study suggested the development of new catalysts that are sufficiently active at low temperatures and stable at high temperatures as well (Gao et al., 2012).

2.2.3. Effect of H_2/CO Ratio

As mentioned in the gasification subsection, syngas from the gasifier exhibits variable composition, resulting in varying H_2/CO ratios. Based on the stoichiometric ratio of the CO methanation reaction (R1), a minimum H_2/CO ratio of 3 is necessary in the feed to methanation reactors to achieve high CO conversion rates. Typically, this ratio is adjusted through the water-gas shift (WGS) reaction (R5) (Bell et al., 2011). However, the H_2/CO ratio at the gasification outlet is generally around 1, making it challenging to precisely achieve a ratio of 3 without additional hydrogen feed. Therefore, understanding the impact

of this ratio on the methanation process is crucial. Gao et al. demonstrated that CO conversion did not significantly vary at various H_2/CO ratios (1, 3, and 5). However, at 30 atm pressure, a higher ratio was found to enhance CO conversion, while higher H_2/CO ratios led to increased CH_4 yield at both 1 atm and 30 atm, particularly at elevated reaction temperatures. Conversely, lowering the H_2/CO ratio to 1 dramatically decreased CH_4 yield at both pressures, indicating that at lower ratios, CO was predominantly converted into non-synthetic natural gas (SNG) products through side reactions (Table 2.1) (Gao et al., 2012).

2.2.4. Effects of the Addition of Other Compounds

Trace amounts of O_2 are inevitably present in syngas throughout the gasification process. According to Gao et al., the presence of O_2 in the gas mixture decreases CH_4 selectivity between 200 and 800 °C due to CO's partial oxidation. Consequently, increasing O_2 in the feed gas reduces CH_4 yield. However, introducing O_2 at 1 atm reduces deposited carbon by reacting with C* to form CO_2, particullarly with a H_2/CO/O_2 ratio of 3/1/0.5. (Gao et al., 2012).

Syngas contains a certain amount of CH_4, and it is common practice in industrial methanation processes to recycle the product gas, which contains H_2O and CH_4, in order to dilute the feed gas for controlling reaction temperatures. Therefore, understanding the effect of CH_4 on the methanation reaction is crucial. According to a study by Gao et al., adding CH_4 in varying ratios did not significantly alter conversion and yield values at both 1 and 30 atm pressures. However, the deposition of carbon sharply increased with an elevated CH_4 ratio above 400 °C at each pressures, primarily because of methane cracking reaction (R6) at elevated temperatures (Table 2.1). In conclusion, to achieve high CH_4 yield with low carbon deposition and optimize energy efficiency, CH_4 should be present in the feed gas but maintained at a low level (Gao et al., 2012).

Industrial experience has demonstrated that adding steam to the reactants can prevent carbon formation on methanation catalysts. In figure 2.4, the effect of steam addition to the feed gas was given at 1 and 30 atm. Steam addition led to a modest reduction in CO conversion particularly at high temperatures for both 1 atm and 30 atm pressures, as steam was generated as a product, thereby suppressing CO methanation (R1) in accordance with

Le Chatelier's principle. Similarly, the introduction of steam resulted in a small change in CH_4 yield. However, the addition of steam significantly reduces the accumulation of carbon at atmospheric pressure, particularly under elevated temperatures. When the steam ratio reached 0.5, carbon deposition was completely absent. The decrease in the carbon formation was attributed to inhabitation of reactions R7 and R8 due to water addition (Gao et al., 2012).

In a research by Abdel-Mageed et al., the influence of water content in the feed gas on the selectivity of CO methanation was investigated using a quartz tube microreactor under differential reaction conditions, employing a 5.0 wt. % Ru/Al_2O_3 catalyst. Initially, they studied the kinetics of CO and CO_2 methanation, alongside the CO methanation selectivity, using a dry feed gas at 190 °C. Subsequently, they tested a wet feed gas (containing 15% H_2O), and then returned to a dry feed gas. Their results indicated that adding water to the feed gas increased the CO methanation rate while decreasing the CO_2 methanation rate. Importantly, they found that once water addition to the feed gas ceased, reaction rates and selectivity values did not decrease. The higher reaction rate observed with the wet feed gas was attributed to a decrease in particle size distribution. TEM assessments of the particle size distribution of Ru on the catalyst validated this discovery, demonstrating a shift from an average particle size of 2.2 nm following reaction with dry reformate to diminished values (average particle size of 1.68 nm) after exposure to reformate containing 15% H_2O (Abdel-Mageed et al., 2015).

It is also a fact that the gaseous hydrocarbon compounds content of syngas, such as C_2H_6 and C_2H_4, significantly increases the likelihood of carbon formation (Kopyscinski et al., 2010). In studies examining the effect of C_2H_4 (as a typical example of a hydrocarbon compound) on CO methanation, researchers observed a significant reduction in CH_4 yield as C_2H_4 concentration increased in the feed stream. The authors suggested that this decrease occurred because C_2H_4 competed with CO for reaction with H_2, thereby facilitating the Boudouard reaction (R4). Furthermore, the pyrolysis of C_2H_4 at high temperatures increased carbon formation, which likely contributed to the decline in CH_4 yield (Gao et al., 2012).

2.2.5. Methanation with Different Syngas Compositions

As mentioned above, syngas from gasifiers has variable composition. However, in the related literature, studies have not extensively focused on the effect of different H_2/CO ratios. Only a few studies have investigated real feed gas compositions, such as those derived from the product gas composition at the gasifier outlet. In this subsection, we will explore studies that simulated and utilized the gasifier outlet stream composition as the feed gas composition for methanation.

S. Wang et al., studied the methanation of bio-syngas in a continuous-flow, fixed-bed reactor over a biochar supported catalyst, employing a feed gas mixture consisting of hydrogen, carbon monoxide, carbon dioxide, and methane in the proportions 35%, 40%, 20%, and 5%, respectively. They observed an increase in CO conversion as the temperature increased across Ru/ABC catalysts with varying Ru loadings, whereas CO_2 conversion declined with increasing temperature for the 1.0 Ru/ABC and 0.5 Ru/ABC catalysts. The decrease in CO_2 conversion was attributed to an accelerated water-gas shift (WGS) reaction rate at higher temperatures. At elevated temperatures, the WGS reaction rate escalated, causing the CO_2 production rate to exceed its consumption rate (Table 2.2) (S. Wang et al., 2014).

Ding et al. studied bio-syngas methanation over an Al_2O_3–CeO_2 composite-supported Ni. Methanation experiments were conducted in a continuous flow fixed-bed reactor with a feed gas mixture containing H_2, CO, CO_2, and N_2 (15.3%, 40.2%, 27.5%, and 17% respectively, at 100 ml/min), alongside a water stream (26 ml/min), over a temperature range of 300–500 °C. The findings demonstrated that Ni/Al_2O_3–CeO_2 achieved superior methanation performance at lower temperatures (at 350 °C, CO conversion of 91.6% and CH_4 selectivity of 92%) in contrast to Ni/ZrO_2, Ni/Al_2O_3, and Ni/Al_2O_3–SiO_2. Analysis indicated that the addition of CeO_2 to Al_2O_3 increased the surface Ni species and enhanced the dispersion of NiO on the Al_2O_3–CeO_2 surface (Ding et al., 2015).

Table 2.3. Catalytic efficiency of the bio-syngas methanation process.

Catalyst	Temperature (K)	X_{CO} (%)	X_{CO_2} (%)	S_{CH_4} (%)	Y_{CH_4} (%)
0.1 Ru/ABC	633	0.3	0	31.3	0.3
0.1 Ru/ABC	653	1.6	0	33.5	0.4
0.1 Ru/ABC	673	2.8	0	44.1	0.9
0.1 Ru/ABC	693	3.9	0	50.4	1.7
0.5 Ru/ABC	633	14	2.7	44.7	2.2
0.5 Ru/ABC	653	16.5	1.6	46.3	2.4
0.5 Ru/ABC	673	17.6	-1.4	54.1	3.5
0.5 Ru/ABC	693	24.7	-3.4	60.7	4.7
1.0 Ru/ABC	633	17.1	-1.3	60.9	2.5
1.0 Ru/ABC	653	22.3	-2.1	61.9	4.4
1.0 Ru/ABC	673	27.3	-16.2	69.9	9.4
1.0 Ru/ABC	693	36.3	-33	69.5	12.5

MoS_2-based catalysts show activity at modest H_2/CO ratios ($H_2/CO = 1.0$) and reduce the cost of methanation reactions from syngas by eliminating the necessity of the WGS reaction. Moreover, MoS_2-based catalysts are widely recognized for their sulfur resistance during methanation, while Ni-based catalysts are known to be highly sensitive to sulfur poisoning. B. Wang et al. systematically investigated how varying sulfidation temperatures affect the selectivity and activity of a $NiO–MoO_3/\gamma\text{-}Al_2O_3$ catalyst for CO methanation under sulfur-rich conditions. The prepared catalysts underwent characterization using N_2 physisorption, temperature-programmed sulfidation, XRD, Raman spectroscopy, XPS, and TEM. Characterization results showed that the $NiMoO_4$ on the $NiO–MoO_3/\gamma\text{-}Al_2O_3$ catalyst were sulfided when the sulfidation temperature reached or exceeded 300 °C. In assessing catalysts for sulfur-tolerant methanation from syngas, it was found that the sample sulfided at 400 °C was most likely to exhibit a predominant NiMoS type I structure. Catalytic performance was evaluated by using a continuous-flow fixed-bed reactor. Before the reaction, the catalyst underwent sulfidation in situ at 400 °C for approximately 4 hours using a 3 vol.% H_2S/H_2 flow at 1 atm. The catalytic activity was tested at 550 °C and 3.0 MPa using a syngas stream with an H_2/CO ratio of 1.0, which contained 0.12 vol.% H_2S and 20 vol.% N_2, at a gas hourly space velocity of 5000 h^{-1}. It was observed that when the sulfidation

temperature exceeded 400 °C, there was a noticeable decrease in catalytic activity. This decline was stemmed from the crystallization of MoS_2 and the progressive conversion of the NiMoS phase as the sulfidation temperature increased (B. Wang et al., 2014b).

Jurascik et al. conducted an exergy analysis on the units of a biomass-to-SNG (synthetic natural gas) process. Exergy analysis, rooted in the second law of thermodynamics, is a promising method for evaluating and enhancing chemical processes. Their study involved a comprehensive exergy analysis of an SNG production process based on woody biomass gasification. Key components of the process included the gasifier, gas cleaning units, synthetic gas compression, methanation reactors, and final SNG conditioning units. The process was simulated using the Aspen Plus flow-sheeting program, where optimal process conditions, particularly for the methanation reactors, were determined and applied in simulations. Internal exergy losses across various system units were assessed, revealing that the greatest losses occurred in the gasifier, the methanation unit, and CO_2 capture section. Operating the gasifier at 700 °C and 1 bar, the first methanation reactor at 580 °C, and the second methanation reactor at 405 °C achieved peak exergetic efficiency at 72.6%. Their findings demonstrated that increasing gasification pressure positively influenced the exergetic efficiency of SNG production, while decreasing the temperature of methanation reactors led to improved overall exergetic efficiency of the process (Jurascik et al., 2009).

Furthermore, studies on the thermodynamic calculations of hydrocarbon production reactions have identified methanation of CO_2 and CO as highly advantageous, given their significantly faster reaction rates compared to other reactions forming hydrocarbons or alcohols (De et al., 2016). However, achieving an efficient methanation process requires the use of effective catalysts. Over the years, numerous studies have focused on designing catalysts for both CO_2 and CO methanation. Since the pioneering work of Sabatier and Senderens in 1902, Ni-based CO methanation catalysts have consistently been recognized as the most effective catalysts for the methanation reaction (Aziz et al., 2015; Gao et al., 2015).

Most of the methanation studies, employing CO, CO_2, H_2 and CH_4 feed gas mixture, aimed to produce deep-cleaned hydrogen for fuel cells directly through selective CO

methanation. Since they mostly focus on cleaning the trace amount of CO (~ 1 vol.% CO) by selective reaction of H_2 with CO to produce CH_4 (Chen et al., 2014; Tada and Kikuchi, 2014), their studies do not fall into the scope of our work.

2.2.6. Common Problems Related to Methanation Reactions and Proposed Solutions

One can find the common problems related to methanation process and the proposed solutions in Table 2.3. below (Gao et al., 2015; Wang et al., 2017).

Table 2.4. The common problems and proposed solutions related to methanation reaction.

COMMON PROBLEMS	**PROPOSED SOLUTIONS**
Low H_2/CO ratio	WGS
Carbon deposition	Optimization of operating conditions Adding steam to the feed gas Increasing the H_2/CO ratio Adding promoters (CeO_2, MgO, etc.) Modification of catalysts with alloy formation
Sintering	Increasing the metal-support interaction (adopting improved preparation methods / CeO_2 support) Adding promoters
Increasing the sulfur resistance	Application of plasma decomposition Adding promoters Bi-metallic catalysts
Temperature elevation and localized hot zones resulting from the exothermic nature of the reaction	Recycling of products Dilution of process gas with inert or steam Installation of isothermal reactors CO_2 capture after methanation (Romano and Ruggeri, 2015)

2.2.7. Reaction Mechanism and Kinetics

More recent kinetic models for methanation use complex Langmuir-Hinshelwood (L-H) rate expressions, incorporating adsorption constants for adsorbed species such as H_2, CO, CH_4, and H_2O, while early kinetic models utilized a simple power-law to characterize the reaction kinetics without presuming a rate-determining step. Luyten and Jungers, who studied the formation of methane in a static system at 300 °C and H_2/CO ratios from 1 to 6 in the presence of nickel deposited on kieselguhr found the reaction rate expression as (Vlasenko et al., 1969)

$$r = kP_{H_2}^{0.9}P_{CO}^{-0.20}. \tag{2.9}$$

The E_A for this rate expression was found to be 27 kcal/mole.

Table 2.4 presents reactant orders for power law type rate expression which is expressed as

$$r = kP_{H_2}^{\alpha}P_{CO}^{\beta} \tag{2.10}$$

from numerous studies (Sughrue and Bartholomew, 1982).

Table 2.5. Reaction orders from different studies (Sughrue and Bartholomew, 1982).

T (K)	α	β
515	0.77	-0.31
537	0.65	-0.25
548	0.9	-0.20
550	0.91	-0.028

When the simple power-law approach often failed to account for the complex interactions and adsorption phenomena on the catalyst surface, the literature shifted from using power-law type rate equations to Langmuir-Hinshelwood (LH) type models for CO methanation. Comprehending the reaction mechanisms behind CO methanation is essential for advancing heterogeneous catalysts with improved activity, selectivity, and stability. The complex reaction mechanism of CO methanation continues to be a subject of ongoing debate in the literature. However, since methane production through CO hydrogenation can be regarded as the simplest example of the synthesis of hydrocarbons, it is possible to introduce

existing theories of the synthesis of hydrocarbons to explain the mechanism of formation of methane (Sarkari et al., 2012). Despite varying scholarly perspectives on the elementary processes underlying CO methanation on nickel surfaces, two principal mechanisms have been proposed in the literature: dissociative and associative CO methanation mechanisms. In the dissociative mechanism, the CO molecule dissociates on the catalyst surface before hydrogenation occurs. Conversely, in the associative mechanism, CO does not dissociate but instead reacts directly with H^* to form a COH_x complex (Miao *et al*., 2016) (Table 2.5).

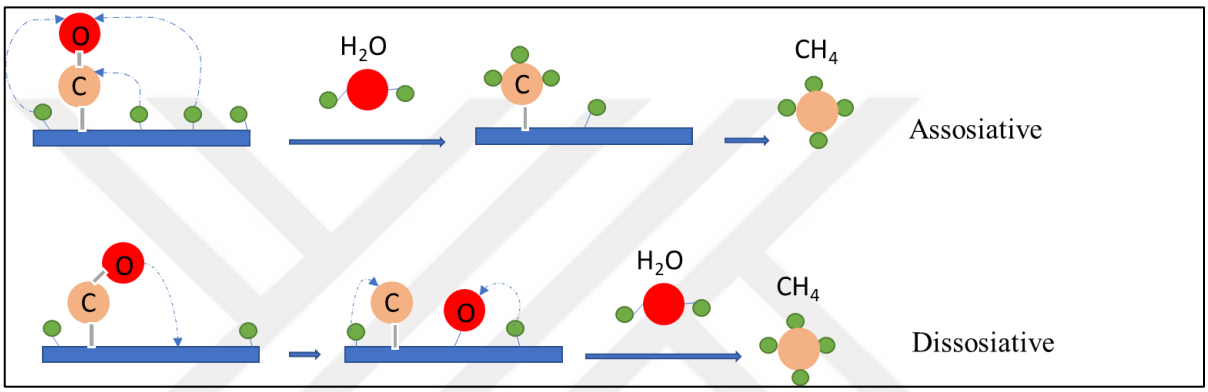

Figure 2.2. Associative and dissociative schemes for CO methanation.

H-assisted CO dissociation—where surface CO* reacts with surface H* to produce surface C*—was also discussed as a dissociative reaction path in the literature (Van Ho and Harriot, 1980; Escobar et al., 2015; Jimenez et al., 2019). For the associative mechanism, the formation of a formyl group (CHO) instead of a hydroxy carbonyl group (COH) was also proposed researchers (Sanchez-Escribano et al., 2007; Ye et al., 2020).

The Langmuir-Hinshelwood mechanism is a widely used model for describing the kinetics of surface-catalyzed reactions. It involves the following steps:

- Adsorption: Reactant molecules adsorb onto active sites of the catalyst surface.
- Surface Reaction: Adsorbed reactants interact on the surface to form products.
- Desorption: The product molecules desorb from the surface back into the gas phase (Atkins and De Paula, 2006).

Table 2.6. Two main reaction mechanisms for CO methanation reaction.

Dissociative Mechanism	Associative Mechanism	#
$H_2 + 2^* \leftrightarrow 2H^*$	$H_2 + 2^* \leftrightarrow 2H^*$	R1
$CO + * \leftrightarrow CO^*$	$CO + * \leftrightarrow CO^*$	R2
$CO^* + * \leftrightarrow C^* + O^*$		R3
	$CO^* + \alpha H^* \leftrightarrow COH^*_\alpha + \alpha^*$	R4
	$COH^* + * \leftrightarrow CH^* + O^* \; or \; C^* + OH^*$	R5
	$COH^*_v + \alpha H^* \leftrightarrow COH^*_w + \alpha^*$	R6
	$COH^*_x + \alpha H^* \leftrightarrow CH^*_Y + OH^*_z$	R7
$C^* + \alpha H^* \leftrightarrow CH^*_\alpha + \alpha^*$	$C^* + \alpha H^* \leftrightarrow CH^*_\alpha + \alpha^*$	R8
$CH^* + H^* \leftrightarrow CH^*_2 + *$	$CH^* + H^* \leftrightarrow CH^*_2 + *$	R9
$CH^*_2 + \alpha H^* \leftrightarrow CH^*_{2+\alpha} + \alpha^*$	$CH^*_2 + \alpha H^* \leftrightarrow CH^*_{2+\alpha} + \alpha^*$	R10
$CH^*_3 + H^* \leftrightarrow CH^*_4 + *$	$CH^*_3 + H^* \leftrightarrow CH^*_4 + *$	R11
$CH^*_4 \leftrightarrow CH_4 + *$	$CH^*_4 \leftrightarrow CH_4 + *$	R12
$CO^* + O^* \leftrightarrow CO^*_2 + *$	$CO^* + O^* \leftrightarrow CO^*_2 + *$	R13
$CO^*_2 \leftrightarrow CO_2 + *$	$CO^*_2 \leftrightarrow CO_2 + *$	R14
$O^* + H^* \leftrightarrow OH^* + *$	$O^* + H^* \leftrightarrow OH^* + *$	R15
$OH^* + H^* \leftrightarrow H_2O^* + *$	$OH^* + H^* \leftrightarrow H_2O^* + *$	R16
$H_2O^* \leftrightarrow H_2O + *$	$H_2O^* \leftrightarrow H_2O + *$	R17
$CO^* + OH^* \leftrightarrow CO^*_2 + H^*$	$CO^* + OH^* \leftrightarrow CO^*_2 + H^*$	R18
$CO^* + H_2O^* \leftrightarrow CO^*_2 + 2H^*$	$CO^* + H_2O^* \leftrightarrow CO^*_2 + 2H^*$	R19

The reaction rate is influenced by the surface coverages of the reactants and is typically expressed as

$$r = \frac{kK_AP_AK_BP_B}{(1+\mathrm{K_A}P_A+K_BP_B)^2} \tag{2.11}$$

where k is the rate constant, K_A and K_B are adsorption equilibrium constants.

Various simple Langmuir-Hinshelwood rate equations for CO methanation assuming each step is the rate-determining step can be written.

1. Assuming adsorption of CO or H_2 as the RDS can be written as

$$r = \frac{kK_{CO}P_{CO}}{1+K_{H_2}P_{H_2}+K_{CO}P_{CO}}, \quad (2.12a)$$

$$r = \frac{kK_{H_2}P_{H_2}}{1+K_{H_2}P_{H_2}+K_{CO}P_{CO}}. \quad (2.12b)$$

2. Assuming the surface reaction between adsorbed CO and H_2 as the RDS can be written as

$$r = \frac{kK_{H_2}P_{H_2}K_{CO}P_{CO}}{\left(1+K_{H_2}P_{H_2}+K_{CO}P_{CO}\right)^2}. \quad (2.13)$$

3. Assuming the desorption of CH_4 is the rate-determining step can be written as

$$r = \frac{kK_{CH_4}P_{CH_4}}{1+K_{CH_4}P_{CH_4}+K_{H_2}P_{H_2}+K_{CO}P_{CO}}. \quad (2.14)$$

Considering the H_2O inhibition effect and low H_2 pressures observed in our studies, a simplified Langmuir-Hinshelwood (LH) type model was developed as

$$r = \frac{kP_{H_2}P_{CO}}{\left(1+K_{H_2O}P_{H_2O}+K_{CO}P_{CO}\right)^2}. \quad (2.15)$$

Garbis et al. investigated the kinetics of CO methanation using a Ru catalyst in CO_2/H_2-rich gases in a fixed-bed reactor operating at 1 bar and temperatures ranging from 160 to 240 °C. Their study followed a surface-based Langmuir-Hinshelwood type approach to describe the kinetics of CO methanation (Garbis *et. al.,* 2019). In this approach, the reaction rate is determined by the adsorption and subsequent surface reaction of the reactants on the catalyst surface as

$$\mathrm{r}_{\mathrm{CH_4}} = \frac{kP_{H_2}P_{CO}}{\left(1+K_{H_2}P_{H_2}+K_{CO}P_{CO}\right)^2}. \quad (2.16)$$

A total of 16 possible rate determining steps proposed for two main CO methanation mechanisms can be found in Table 2.6 and Equations 2.17 and 2.18 (Kopyscinski et al., 2010).

If water is adsorbed as an H_2O molecule, the rate equation can be written as

$$r_{i,a} = \frac{k_1 K_{Cx} K_{H_2}^a P_{CO}^b P_{H_2}^c}{\left(1+\sqrt{K_{H_2} P_{H_2}}+K_{CO} P_{CO}+K_{H_2O} P_{H_2O}+K_{Cy} P_{CO}^e P_{H_2O}^f\right)^g}. \quad (2.17)$$

If water is adsorbed as a hydroxyl species (OH), the rate equation can be written as

$$r_{i,b} = \frac{k_1 K_{Cx} K_{H_2}^a P_{CO}^b P_{H_2}^c}{\left(1+\sqrt{K_{H_2} P_{H_2}}+K_{CO} P_{CO}+K_{OH} P_{H_2O} P_{H_2}^{-0.5}+K_{Cy} P_{CO}^e P_{H_2O}^f\right)^g} \quad (2.18)$$

The kinetic models 12b, 14b, and 6b provided good representations for the experimental data obtained from kinetic experiments conducted on a commercial Ni based catalyst at five different temperatures ranging from 280 to 360 °C, under a total pressure of 2 bar.

Van Ho and Harriot suggested an H-assisted CO dissociation mechanism on a Ni/SiO_2 catalyst. Consecutive reactions of this proposed mechanism can be written as

$$CO_{(g)} + * \leftrightarrow CO*\ , \quad (2.19)$$

$$H_{2(g)} + * \leftrightarrow 2H*\ , \quad (2.20)$$

$$CO* + 2H* \leftrightarrow C* + H_2O \quad RDS, \quad (2.21)$$

$$C* + 4H* \leftrightarrow CH_4. \quad (2.22)$$

Table 2.7. Rate determining steps for the main two proposed mechanisms.

Model	RDS	K_{Cx}	a	b	c	K_{Cy}	e	f	g
1	$CO + *$	-	0	1.0	0	-	-	-	1
2	$CO^* + *$	K_{CO}	0	1.0	0	-	-	-	2
3	$CO^* + H^*$	K_{CO}	0.5	1.0	0.5	-	-	-	2
4	$CO^* + 2H^*$	K_{CO}	1.0	1.0	1.0	-	-	-	3
5	$COH^* + *$	K_{COH}	0	1.0	0.5	K_{COH}	1.0	0.5	2
6	$COH^* + H^*$	K_{COH}	0.5	1.0	1.0	K_{COH}	1.0	0.5	2
7	$COH^* + 2H^*$	K_{COH}	1.0	1.0	1.5	K_{COH}	1.0	0.5	3
8	$COH_2^* + H^*$	K_{COH_2}	0.5	1.0	1.5	K_{COH_2}	1.0	1.0	2
9	$COH_2^* + 2H^*$	K_{COH_2}	1.0	1.0	2.0	K_{COH_2}	1.0	1.0	3
10	$COH_3^* + H^*$	K_{COH_3}	0.5	1.0	2.0	K_{COH_3}	1.0	1.5	2
11	$COH_3^* + 2H^*$	K_{COH_3}	1.0	1.0	2.5	K_{COH_3}	1.0	1.5	3
12	$C^* + H^*$	K_C	0.5	0.5	0.5	K_C	0.5	0	2
13	$C^* + 2H^*$	K_C	1.0	0.5	1.0	K_C	0.5	0	3
14	$CH^* + H^*$	K_{CH}	0.5	0.5	1.0	K_{CH}	0.5	0.5	2
15	$CH_2^* + H^*$	K_{CH_2}	0.5	0.5	1.5	K_{CH_2}	0.5	1.0	2
16	$CH_2^* + 2H^*$	K_{CH_2}	1.0	0.5	2.0	K_{CH_2}	0.5	1.0	3

If CO and H_2 in the gas phase are assumed to reach equilibrium with the adsorbed species on the surface, they contend for identical binding sites (Van Ho and Harriot, 1980). Identifying Equation 2.21 as the rate-determining step, the rate expression for a uniform surface is derived as

$$r_{CH_4} = \frac{kK_{CO}K_{H_2}P_{CO}P_{H_2}}{\left(1+K_{CO}P_{CO}+K_{H_2}P_{H_2}\right)^2}. \tag{2.23}$$

In 1984, a study investigated the kinetics of CO methanation using a Ni/Al_2O_3 catalyst within the temperature range of 453 K to 557 K. Nonlinear regression employed a modified Gauss-Newton method for parameter estimation. The model equations derived from this analysis underwent several statistical tests, including assessment of variance, standard

deviation of model parameters, and comparison of calculated and measured reaction rates to discriminate between models. The kinetics were explained by assuming equilibrium in the dissociative adsorption of CO and H_2 and described as

$$r_{CH_4} = \frac{kK_{CO}K_{H_2}^2 P_{CO}^{0.5} P_{H_2}}{\left(1+K_{CO}P_{CO}^{0.5}+K_{H_2}P_{H_2}^{0.5}\right)^3}. \quad (2.24)$$

The rate-limiting step involved the hydrogenation of surface C* to a CH_2-species, requiring two adsorbed hydrogen atoms (Klose and Baerns, 1984).

Choi et al. proposed a different rate expression which can be written as

$$r_{CH_4} = \frac{kK_{CO}K_{H_2}P_{H_2}^{0.5}P_{CO}}{\left(1+K_{CO}P_{CO}+K_H P_{H_2}+K_{CH_4}P_{CH_4}+K_{H_2O}P_{H_2O}P_{H_2}^{-1}\right)^2}. \quad (2.25)$$

This equation assumes associative mechanism with the formation of a formyl group as the rate determining step. While initially developed for methane steam reforming (Xu and Froment, 1989), the model's suitability for CO methanation using a Ni/ZrO_2 catalyst was successfully validated (Choi et al., 2021).

In 2015, a Langmuir-Hinshelwood type rate model, assuming H-assisted CO dissociation as the rate-determining step, was suggested by Escobar for a 1% $Ru/\gamma\text{-}Al_2O_3$ catalyst, within a temperature range of 200-300°C (Escobar et al., 2015). The suggested rate expression did not include an H_2O inhibition term and can be expressed as

$$r_{CH_4} = \frac{kK_{CO}K_{H_2}^{0.5}P_{H_2}^{0.5}P_{CO}}{(1+K_{CO}P_{CO})^2}. \quad (2.26)$$

Jimenez et al. demonstrated that H-assisted CO dissociation accurately describes the CO methanation reaction on Rh catalysts with varying mean cluster sizes under methanation conditions ($H_2/CO>3$, 250-300 °C). Their proposed Langmuir-Hinshelwood kinetic model focuses solely on the adsorbed CO as the predominant surface intermediate and can be written as

$$r_{CH_4} = \frac{kP_{H_2}P_{CO}}{(1+k_r\frac{P_{H_2O}}{P_{H_2}^{1.5}})(1+K_{CO}P_{CO})^2}. \quad (2.27)$$

In this expression, P_{H_2O} term was added to denominator to capture the inverse effect of H_2O on reaction rate. The parameter k′ denotes the ratio between the rates of carbon removal by H* and O* on Rh surfaces.

Sughrue and Bartholomew proposed a dual-step mechanism in 1982, where both steps were considered rate-controlling and in equilibrium with each other. The kinetic tests were conducted at 690 kPa using a Ni-based catalyst. CO partial pressures were varied from 5 to 12 kPa, while H2 partial pressures ranged from 12 to 30 kPa. Temperatures were adjusted between 473 K and 623 K. Throughout the experiments, the H_2/CO ratio was maintained near the stoichiometric value of 3 to ensure relevance for industrial applications. Steps of the proposed dual mechanism and rate expression are given through

$$H_2 + 2 * \leftrightarrow 2H *, \tag{2.28}$$

$$C * + H * \leftrightarrow CH * + *, \tag{2.29}$$

$$r_{CH_4} = \frac{k_1 k_2 P_{H_2}}{k_1\left(1+K_{H_2}^{0.5}P_{H_2}^{0.5}+K_{CO}P_{CO}\right)^2 + k_2(1+K_{CO}P_{CO})^2}. \tag{2.30}$$

In general, the experimentally obtained kinetic data indicate a complex Langmuir-Hinshelwood model where H_2 adsorption dictates the rate at low temperatures (<500 K), while at moderate temperatures (500-573 K), CO dissociation and/or carbon hydrogenation are co-determinants of the rate. At high temperatures (>573 K), the rate-determining step shifts to the hydrogenation of adsorbed carbon. CH_4 does not exhibit inhibitory effects on the rate of CO methanation, while H_2O acts as a potent inhibitor and irreversible poison, particularly under conditions of elevated temperatures and concentrations (Sughrue and Bartholomew, 1982).

3. EXPERIMENTAL WORK

3.1. Materials

3.1.1. Gases

All gases utilized in this study were provided by the Linde Group in Gebze, Turkey. The specifications and applications of these gases are detailed in Table 3.1.

Table 3.1. Specifications and applications of the gases used.

Gas	Formula	Specification	Application
Argon	Ar	99.998%	GC Carrier Gas, Inert
Carbon dioxide	CO_2	99.998%	GC calibration/Reactant
Carbon monoxide	CO	99.998%	GC calibration/Reactant
Dry Air	-	99.998%	Calcination/GC 6-way pneumatic valve
Hydrogen	H_2	99.998%	GC calibration/Reactant/Reducing agent
Methane	CH_4	99.998%	GC calibration/Reactant
Nitrogen	N_2	99.998%	Inert

3.1.2. Chemicals

All liquid and solid chemicals used in the catalyst preparation are presented in Table 3.2. Deionized water was used for all solution preparations.

Table 3.2. Chemicals used in catalyst preparations.

Chemical	**Formula**	**Specification**	**Source**	**MW (g/gmol)**
Aluminum oxide	γ-Al_2O_3	Catalyst support	Alfa Aesar	101.96
Cerium (III) nitrate hexahydrate	$Ce(NO_3)_3.6H_2O$	99.99%	Merck	434.22
Hydrochloric acid	HCl	37% aq. solution	Merck	36.46
Ethyl Alcohol	CH_3CH_2OH	99.95%		
Lanthanum (III) nitrate hexahydrate	$La(NO_3)_3.6H_2O$	99+%	Carlo Erba	433.01
Magnesium nitrate hexahydrate	$Mg\ (NO_3)_2.6H_2O$	99+%	Merck	256.41
Manganese (II) nitrate tetrahydrate	$Mn\ (NO_3)_2.4H_2O$	99+%	Merck	251.01
Nickel (II) nitrate hexahydrate	$Ni(NO_3)_2.6H_2O$	99+%	Merck	290.81
Pluronic P-123	$HO(CH_2CH_2O)_{20}(CH_2CH(CH_3)O)_{70}(CH_2CH_2O)_{20}H$			~5800
Tetraethoxysilane	$SiC_8H_{20}O_4$			208.33
Water	H_2O	Deionized	-	18.02
Zirconium oxide	ZrO_2	Catalyst support	Alfa Aesar	123.22

3.2. Experimental Systems

The experimental systems used for this research can be categorized into three distinct groups:

- Catalyst Preparation Systems: The set-ups used for support modification and incipient-to-wetness impregnation.

- Catalyst Characterization Systems: Analytical and spectroscopic techniques, along with specialized systems, are employed to characterize the physical and microstructural properties of the prepared catalyst samples and to examine changes during and/or after the reaction.

- Catalytic Reaction System: The continuous flow reactor system integrates precise control over liquid and gas flows, gas-liquid mixing capabilities, temperature-regulated transfer lines, a controlled reaction chamber, and provisions for sampling both input and output. The system serves as a platform for scientific evaluation of catalytic activity, selectivity, and stability.

3.2.1. Catalyst Preparation Systems

The catalyst preparation system comprises two distinct blocks, employed for the synthesis of one of the supporting materials, mesoporous silica sieve SBA-15, and for impregnation steps in catalyst preparation.

The system utilized for the synthesis of SBA-15 (Figure 3.1) comprises a 500 ml beaker, a Mettler Toledo pH-meter, a Heidolph impeller, and a Julabo water bath filled with distilled water. It is employed to initiate a reaction for synthesizing SBA-15 supporting materials. Subsequently, the produced SBA-15 materials undergo heat treatment in an autoclave reactor.

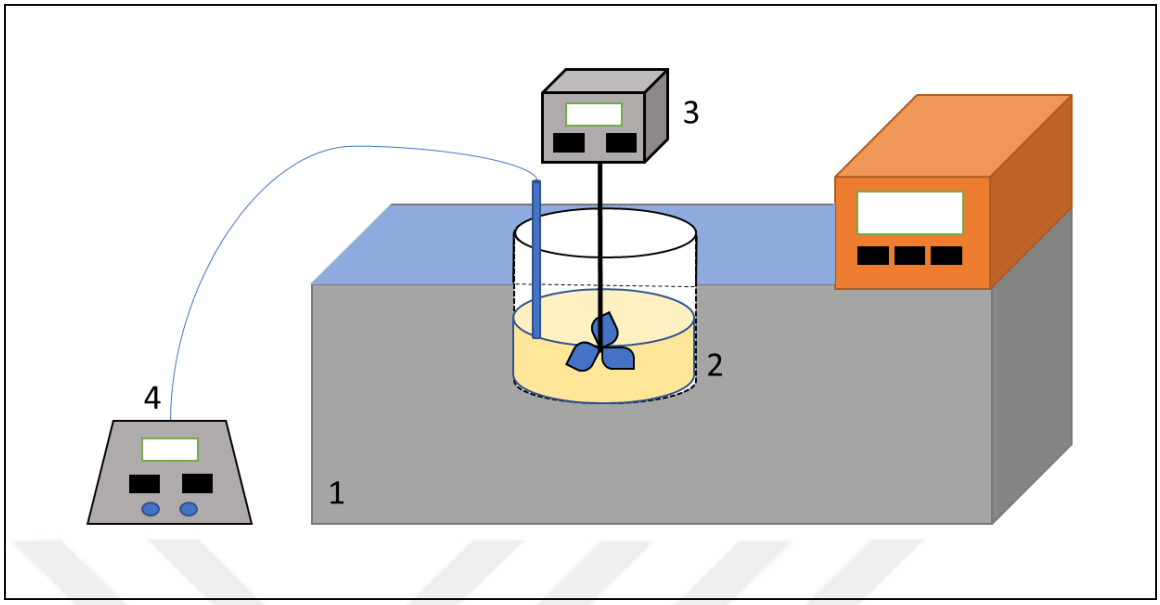

Figure 3.1. Schematic illustration of the SBA-15 preparation system (Ultrasonic mixer (1), Beaker (2), Stirrer (3), pH meter (4)).

The setup used for the incipient-to-wetness impregnation method (Figure 3.2) comprises a Büchner flask, a Retsch UR1 ultrasonic mixer for thorough mixing, a KNF Neuberger vacuum pump, and a Masterflex computerized-drive peristaltic pump. These components are employed to ensure uniform contact between the precursor solution and the support material. Additionally, the system includes a beaker containing silicone tubing and the precursor solution as essential elements.

In this method, a Büchner flask containing a predetermined amount of support material (2-5 g) underwent vacuum treatment both before and after adding the precursor solution. Vacuum evacuation was crucial to remove trapped air from the support material's pores, ensuring unimpeded penetration of the solutions and achieving a uniform dispersion of the active component. Before the impregnation, the support material underwent 30 minutes of ultrasonic mixing under vacuum. A peristaltic pump was employed to precisely deliver the precursor solution at a controlled rate of 0.4 ml/min through silicone tubing into the support material within the Büchner flask. Continuous ultrasonic mixing during impregnation ensured an even distribution of the precursor solution. After adding the precursor solution, the resulting thick slurry underwent an extra 90 minutes of ultrasonic mixing under vacuum. The resulting slurry was subsequently dried overnight in an oven at the specified temperature.

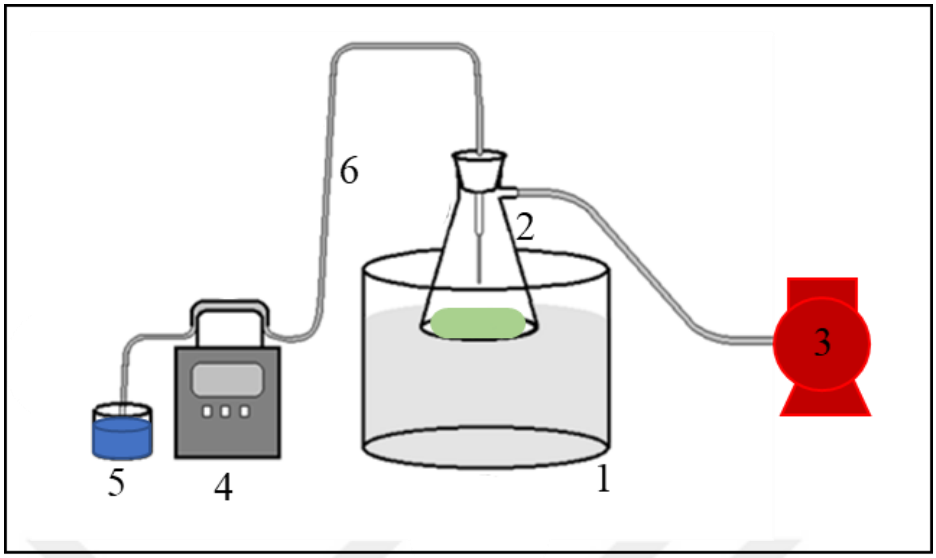

Figure 3.2. Schematic illustration of the impregnation system (Ultrasonic mixer (1), Büchner flask (2), Vacuum pump (3), Peristaltic pump (4), Beaker (5), Silicone tubing (6)).

Details regarding the methods and procedures specific to the catalyst are presented in Section 3.3.

3.2.2. Catalyst Characterization Systems

In this section of the current study, spectroscopic and analytical techniques, along with specialized systems, are utilized to characterize the microstructural and physical properties of the prepared catalyst samples. Moreover, these methods are applied to investigate changes occurring during and/or after the reaction of the freshly reduced catalyst samples.

3.2.2.1. X-Ray Photoelectron Spectroscopy

The investigation into the electronic interactions among metal components in freshly reduced samples, alongside the determination of oxidation states in metallic species on both fresh and spent samples, was conducted via the quantification of metallic phases utilizing X-ray photoelectron spectroscopy (XPS). Analyses were executed at the Synthetic Natural Gas and Hydrogen Production Technologies Laboratory (SNG&HydTec) employing a Phi 5000 VersaProbe III X-ray Photoelectron Spectrometer equipped with an Al source.

3.2.2.2. X-Ray Diffraction

Bruker D8 Discover X-ray diffraction system equipped with a Cu target X-ray generator operating at a scanning speed of 2°/min, is used to characterize the crystalline phases of the catalyst samples These analyses were conducted at the Synthetic Natural Gas and Hydrogen Production Technologies Laboratory (SNG&HydTec).

3.2.2.3. High-Resolution Transmission Electron Microscopy

Micrographs of the freshly reduced samples were captured using TEM to analyze their microstructure and morphology. This facilitated qualitative elemental analysis and provided insights into how metals were dispersed on the catalyst surface. The experiments were carried out at the N2Star Laboratory of KOÇ University, employing the Hitachi HF5000 200kV (S)TEM system.

3.2.2.4. Scanning Electron Microscopy

Micrographs of the freshly reduced catalyst samples were acquired using environmental scanning electron microscopy (ESEM) to examine their microstructure and morphology. Imaging was performed on a Philips XL 30 ESEM-FEG system, capable of achieving resolutions down to 2 nm. Both back-scattered electron (BSE) and secondary electron (SE) images were acquired at high magnification. These analyses were conducted at the Advanced Technologies Research and Development Center of Boğaziçi University.

3.2.2.5. Raman Spectroscopy

Raman spectroscopy was employed to investigate coke formations on spent catalyst samples. Using a Renishaw inVia Raman microscope, Raman spectra of both freshly reduced and spent catalyst samples were acquired. The system operated with a 514 nm, 20 mW Ar+ laser as the excitation source, delivering an intensity of approximately 10 mW. Each spectrum was acquired with a a total of 20 accumulations and 5-second acquisition time. These analyses took place at the Advanced Technologies Research and Development Center of Boğaziçi University.

3.2.2.6. Temperature Program Reduction

Temperature-programmed reduction (TPR) studies were conducted using a CATLAB-PCS system developed by Hiden Analytical Technologies. The Hiden CATLAB is a bench-top microreactor and combined mass spectrometer system designed for the rapid and reproducible characterization of catalysts and the study of chemical reactions. TPR studies were performed using a H_2-He mixture containing 5% H_2 on 75 mg catalyst samples, with the temperature increasing from room temperature to 900 °C at a ramp rate of 5 °C/min. The analyses were performed in the Synthetic Natural Gas and Hydrogen Production Technologies Laboratory (SNG&HydTec).

3.2.3. Catalytic Reaction System

The reaction system, illustrated in Figures 3.3 and 3.4, was designed, built, and evaluated in our laboratories. This system includes feed, reaction, and analysis sections.

The feed section consists of mass flow control systems, featuring 1/16", 1/8", and 1/4" stainless steel tubing. Additionally, it includes valves and fittings designed for gaseous species like CO, CO_2, CH_4, O_2, H_2, N_2, and equipments for handling liquids such as de-ionized water. Brooks model 5850E mass flow controllers (MFCs) were used to regulate the flow of inlet gases supplied by pressurized gas cylinders. The flow rates of CO, CO_2, H_2, and N_2 were set using the Brooks Instrument 0154 series control box, while the flow rates of O_2, CH_4, and dry air were regulated with the Brooks Instrument 0254 series control box. To prevent back-pressure fluctuations, on-off valves were strategically positioned before the MFCs. Each gas species had its independent line, providing the flexibility to finely adjust the desired feed compositions. Upstream of the reactor, a three-way valve was installed to divert dry feed components directly to the gas chromatograph, bypassing the reactor, for accurate feed analysis. The water feed utilizes the Agilent 1100 series HPLC pump. The stainless-steel tubing, responsible for conveying the feed, and the line leading to the reactor, which includes the reactant mixing zone, were both maintained at 140 ± 5 °C. This temperature was achieved using a 2m Cole-Parmer heating tape, coupled with a 16-gauge wire K-type sheathed thermocouple, and regulated by an Omron E5AN temperature controller. To prevent heat loss, ceramic wool insulation was applied to cover the heated

lines.

The reaction section is comprised of a furnace measuring 45 cm x 20 cm x 20 cm, equipped with a 2.4 cm inner diameter (ID) quartz down-flow microreactor. The furnace was controlled by a Eurotherm 3216P programmable temperature controller, alongside a K-type sheathed thermocouple for precise temperature monitoring. The 63 cm long quartz microreactor was attached to the system at both ends using stainless steel connectors welded to 1/4” stainless steel tubing. The central portion of the quartz microreactor was filled with quartz wool to securely hold the catalyst bed in a fixed position. To minimize heat loss, the top and bottom ends of the reactor furnace were insulated with ceramic glass wool. As a precautionary measure, cold traps were strategically positioned after the reactor. These traps efficiently removed steam generated and fed throughout the process, ensuring the protection of the gas chromatograph column from potential condensation issues.

Analysis of feed and product streams was conducted using an Agilent Technologies 6850 gas chromatograph (GC) equipped with a Thermal Conductivity Detector (TCD) and a HayeSep D column.

Figure 3.3. Photograph of the catalytic reaction system.

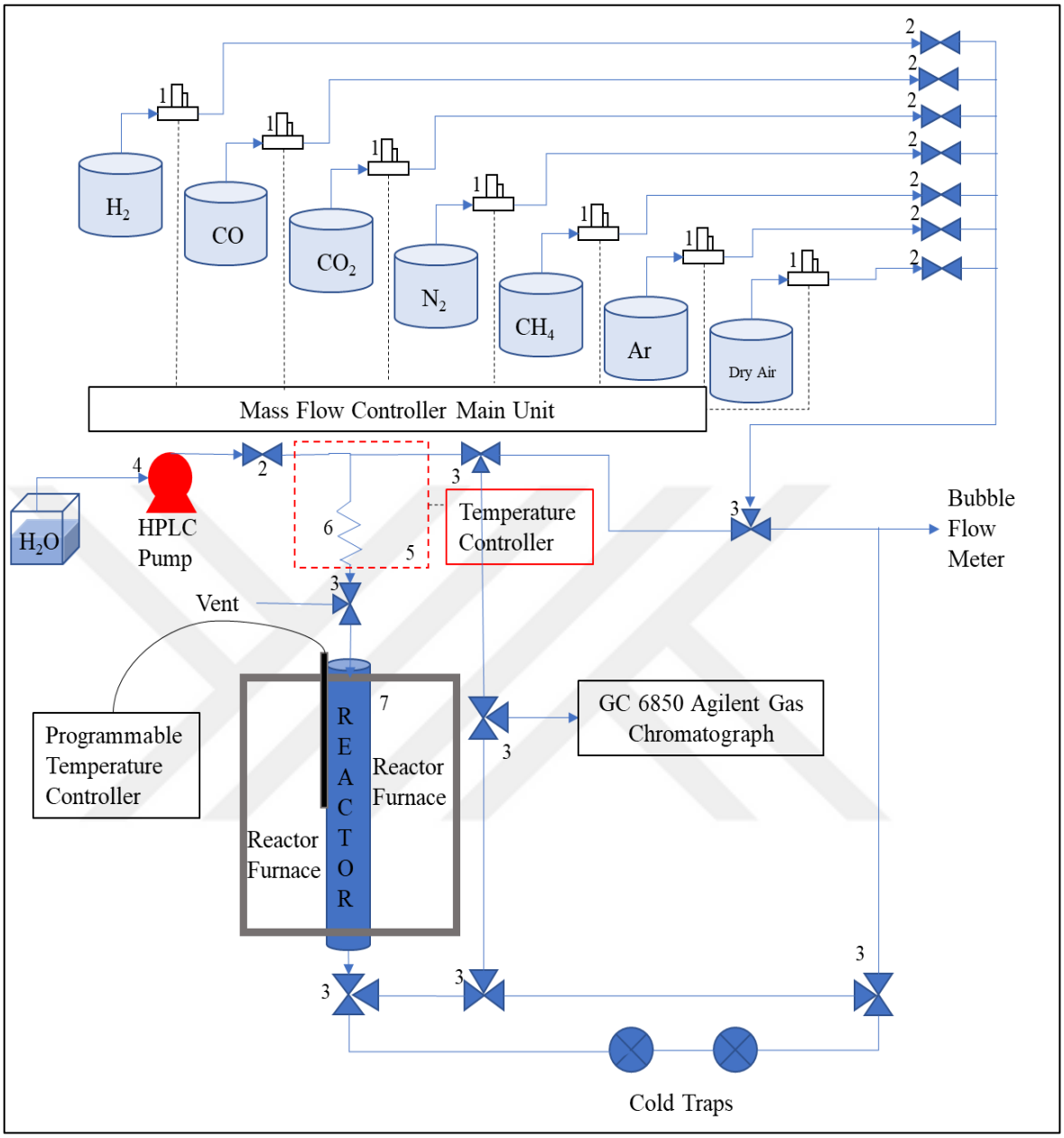

Figure 3.4. Schematic illustration of the catalytic reaction system (Mass flow controller (1), On-off valve (2), Three-way valve (3), HPLC Pump (4), Heating Zone (5), Mixing Zone (6) and Differential Reactor (7)).

3.3. Catalyst Preparation and Pretreatment

In this study, sixteen sets of catalysts were prepared using four different promoters: Cerium, Lanthanum, Magnesium, and Manganese, along with three different supports: γ-Al_2O_3, SBA-15, and ZrO_2. The catalysts were synthesized through the incipient to wetness method with sequential impregnation.

3.3.1. γ-Al_2O_3 Supported Methanation Catalysts

3.3.1.1. Preparation of γ-Al_2O_3 Support

The preparation of γ-Al_2O_3 involved the crushing and sieving of pellets to achieve particles within the size range of 354-250 μm (45-60 mesh). After sieving, the γ-Al_2O_3 particles were subjected to calcination at 600 °C for a duration of 2 hours in a muffle furnace under atmospheric conditions.

3.3.1.2. Synthesis of Metal-Impregnated γ-Al_2O_3 Supported Catalysts

Monometallic Ni/γ-Al_2O_3 catalysts were synthesized using the incipient-to-wetness impregnation method, employing an aqueous solution of $Ni(NO_3)_2.6H_2O$ (1.1 ml DI water/g support) as explained in Section 3.2.1. The resulting thick slurry, formed through ultrasonic mixing of the aqueous precursor salt solution and the support, underwent overnight drying at 110 °C Subsequently, the dried material was calcined at 600 °C for a duration of 2 hours, yielding the final Ni/γ-Al_2O_3 catalysts.

The bimetallic M-Ni/γ-Al_2O_3 catalysts (M= Ce, La, Mg, and Mn) were prepared by a sequential route in which an aqueous solution of $Ni(NO_3)_2.6H_2O$ was impregnated over initially prepared and calcined (at 600 °C for 2 hours) M/γ-Al_2O_3 catalyst, which was synthesized by the incipient-to-wetness impregnation method, employing the respective aqueous solutions of metal precursors (Table 3.2). The slurry containing two metals was dried overnight at 110 °C and then subjected to a final calcination at 600 °C for 2 hours.

To optimize catalytic activity, it is essential to perform a pretreatment where the active metals are reduced from their oxide state, which was formed during calcination, to their metallic state before initiating the reaction. This pretreatment is necessary, as catalysts in their oxide forms typically exhibit inactivity for the intended reactions.

TPR studies, as detailed in Section 3.2.2.6, were conducted at CATLAB. The TPR results indicated that a suitable reduction temperature for monometallic Ni/γ-Al_2O_3, and bimetallic Mg-Ni/γ-Al_2O_3 catalysts is 590 °C. On the other hand, for bimetallic Ce-Ni/γ-Al_2O_3, La-Ni/γ-Al_2O_3, and Mn-Ni/γ-Al_2O_3, reduction at 670 °C was found to be appropriate.

Table 3.3 presents a list of methanation catalysts prepared on a γ-Al_2O_3 support. The 3%La-10%Ni/γ-Al_2O_3(2) catalyst was prepared by altering the metal impregnation sequence. Additionally, the 3%La-10%Ni/γ-Al_2O_3(3.6 pH) catalyst was prepared using de-ionized water with a lower pH value.

Table 3.3. γ-Al_2O_3 Supported Methanation Catalysts.

#	**CATALYST**
1	10% Ni/γ-Al_2O_3
2	1%Mg-10%Ni/γ-Al_2O_3
3	1%La-10%Ni/γ-Al_2O_3
4	3%La-10%Ni/γ-Al_2O_3
5	3%La-10%Ni/γ-Al_2O_3(2)
6	3%La-10%Ni/γ-Al_2O_3(3.6 pH)
7	5%La-10%Ni/γ-Al_2O_3
8	5%Ce-10%Ni/γ-Al_2O_3
9	15% Ni/γ-Al_2O_3
10	1%La-15%Ni/γ-Al_2O_3
11	1.7%Mn-15%Ni/γ-Al_2O_3

Reduction procedure of the γ-Al_2O_3 supported catalysts began by placing the catalyst into the temperature-controlled zone of the quartz reactor. Initially, an inert N_2 flow of 50 ml/min was established for 10 minutes to purge O_2 from the system at room temperature (RT). Subsequently, the gas flow was switched from N_2 to H_2-N_2 mixture containing 50% H_2 and it was set to flow at 100 ml/min. The reduction process commenced by heating the catalyst from room temperature (RT) to the designated reduction temperature at a rate of 10 °C/min. The temperature was maintained at this predetermined reduction temperature for 2 hours during the reduction process. Following reduction, the gas flow was switched to nitrogen, flowing at 50 ml/min, to cool the microreactor down to the reaction temperature.

3.3.2. SBA-15 Supported Methanation Catalysts

3.3.2.1. Preparation of SBA-15 Support

In this study, all mesoporous SBA-15 materials were produced using the hydrothermal method (Zhao et al., 1998). The synthesis employed tetraethoxysilane (TEOS or SiC8H20O4) as the silica source and nonionic pluronic P123 as the structure-directing agent.

Steps of SBA-15 synthesis are listed below:

- 4 grams of P123 were dissolved in a mixture containing 120 ml of 2M hydrochloric acid (HCl) and 30 ml of deionized water. The dissolution process was carried out for 2 hours using an impeller operating at 500 rpm (Figure 3.1).
- The beaker containing the dissolved P123 solution was carefully positioned in a water bath set at 308 K. Gradually, 8.5 grams of TEOS was meticulously added drop by drop into the solution, accompanied by continuous stirring at 350 rpm (Figure 3.1).
- Subsequent to the complete addition of TEOS, the solution underwent stirring at 560rpm for an additional 22 hours (Figure 3.1).
- After the completion of the stirring period, the solution mixture was removed from the water bath and allowed to settle for nearly 20 minutes to facilitate color separation within the mixture.
- After color separation was observed, the mixture was transferred into a Teflon

autoclave supported externally by stainless steel. The autoclave was sealed using a Viton O-ring to prevent rusting and material loss.

- Subsequently, the sealed autoclave was placed in a furnace at 363 K for 2 days, initiating the second phase of the reaction between P123 and TEOS under elevated pressures.
- A filtration system, comprising a vacuum pump, filter paper, Buchner funnel, and Buchner flask, is employed to purify the SBA-15 particles. The solution obtained from the autoclave was precisely poured onto the filter paper and subjected to a systematic washing procedure. This involved sequential washing with deionized water and ethanol, repeated approximately 12 times each. The methodical repetition of this process ensured the complete removal of the green coloration from the solution.
- The filtered SBA-15 residue was subjected to a drying process in a furnace maintained at 353 K for 12 hours.
- Following the drying process, the residue was subjected to calcination in a muffle furnace under atmospheric conditions. The calcination temperatures, 823 K and 1023 K, were employed with a controlled ramping rate of 1 K/min, and the duration of the calcination was sustained for 6 hours.

The supports are named based on their respective calcination temperatures, SBA-15-550 and SBA-15-750.

3.3.2.2. Synthesis of Metal-Impregnated SBA-15 Supported Catalysts

Monometallic SBA-15 catalysts were synthesized using the incipient-to-wetness impregnation method, employing an aqueous solution of $Ni(NO_3)_2.6H_2O$ (ca. 9.3 ml DI water/g support) as explained in Section 3.2.1. The slurry obtained from ultrasonic mixing of the aqueous precursor salt solution and the support underwent overnight drying at 353 K. Subsequently, the dried material was calcined at 823 K with a controlled ramping rate of 2 K/min for a duration of 6 hours, yielding the final Ni/SBA-15-550 or Ni/SBA-15-750 catalysts.

Bimetallic 5%Ce-10%Ni/SBA-15-550 catalyst was produced by a sequential route in which an aqueous solution of $Ni(NO_3)_2.6H_2O$ was impregnated over initially prepared and calcined (at 823 K for 6 hours) 5% Ce/SBA-15-550 catalyst, which was prepared by the incipient-to-wetness impregnation method, employing the aqueous solution of $Ce(NO_3)_3.6H_2O$ (ca. 9.3 ml DI water/g support) as explained in Section 3.2.1. The final slurry containing two metals was dried overnight at 353 K and finally calcined at 823 K for 6 hours. Table 3.4 presents a list of methanation catalysts prepared on a SBA-15 support.

Table 3.4. SBA-15 Supported Methanation Catalysts.

#	**CATALYST**
1	5%Ce-10%Ni/SBA-15-550
2	10% Ni/SBA-15-550
3	15% Ni/SBA-15-550
4	15% Ni/SBA-15-750

The reduction process for the SBA-15 supported catalysts started with placing the catalyst into the temperature-controlled zone of the quartz reactor. Initially, an inert N_2 flow of 50 ml/min was introduced for 10 minutes to purge O_2 from the system at room temperature (RT). Subsequently, the gas flow was switched to a H_2-N_2 mixture containing 50% H_2, flowing at 100 ml/min. Reduction commenced by ramping the temperature of the catalyst from RT to 823 K at a rate of 10 K/min. The temperature was maintained at 823 K for 4 hours during the reduction process. Following reduction, the gas flow was switched back to N_2 at 50 ml/min to cool the quartz reactor down to the reaction temperature.

3.3.3. ZrO_2 Supported Methanation Catalyst

3.3.3.1. Preparation of ZrO_2 Support

The ZrO_2 support preparation involved crushing and sieving zirconia pellets to obtain particles within the size range of 354-250 μm (45-60 mesh). Subsequently, the prepared particles underwent calcination at 800 °C for 4 hours in a muffle furnace under atmospheric

conditions.

3.3.3.2. Synthesis of Metal-Impregnated ZrO_2 Supported Catalyst

Bimetallic 5%Ce-10%Ni/ZrO_2 catalyst was prepared by a sequential route in which an aqueous solution of $Ni(NO_3)_2.6H_2O$ was impregnated over initially prepared and calcined (at 600 °C for 2 hours) 5% Ce/SBA-15-550 catalyst, which was prepared by the incipient-to-wetness impregnation method, employing the aqueous solution of $Ce(NO_3)_3.6H_2O$ (ca. 0.6 ml DI water/g support) as explained in Section 3.2.1. The resulting slurry containing two metals was dried at 110 °C overnight and subsequently calcined at 600 °C for 2 hours.

During the TPR experiments conducted at CATLAB, it was determined that an optimal pretreatment procedure for the 5%Ce-10%Ni/ZrO_2 catalyst involves reduction using a 50% H_2 flow at 375 °C for a duration of 2 hours. The process started by placing the ZrO_2-supported catalyst into the temperature-controlled zone of a quartz reactor. Initially, an inert N_2 flow of 50 ml/min was introduced for 10 minutes to purge oxygen from the system at room temperature (RT). Subsequently, the gas flow was switched to a mixture of H_2-N_2 with 50% H_2 flowing at 100 ml/min. The catalyst was then heated gradually from RT to 375 °C at a rate of 10 °C/min to initiate the reduction process. The temperature was maintained at 375 °C for 2 hours during the reduction phase. Following reduction, the gas flow was switched back to N_2 at 50 ml/min to stabilize the reactor temperature to the desired reaction temperature.

3.4. Methanation Reactions

The methanation reactions conducted for this study can be categorized into three sections: performance tests, stability tests and kinetics tests.

3.4.1. Performance Experiments of Methanation Reaction

Methanation performance tests were conducted using two types of feeds: dry and moist feeds. Three distinct H_2/CO ratios and three different H_2O/CO ratios were employed for each feed type, as outlined in Table 3.5. The tests covered a range of temperatures,

including 200 °C, 250 °C, 300 °C, 350 °C, and 400 °C. Two different W/F (weight-to-flow) ratio levels, specifically 0.0125 and 0.0025 g*h/l, were utilized in these performance tests. Each performance evaluation involved testing 75 mg of freshly reduced catalyst samples for a duration of 6 hours.

Table 3.5. Reaction conditions for performance tests.

Reaction Set	T (ºC)	Feed Composition	W/F (g*h/l)	H_2/CO	H_2O/CO
P.1	400	45% H_2, 15% CO, 40% N_2 30% H_2, 15% CO, 55% N_2 15% H_2, 15% CO, 60% N_2	0.0125	3 2 1	0
P.2	200 250 300 350 400 450	45% H_2, 15% CO, 35% N_2, 5%H_2O 30% H_2, 15% CO, 50% N_2, 5%H_2O 15% H_2, 15% CO, 65% N_2, 5%H_2O	0.0125 0.0025	3 2 1	1/3
P.3	400	15% H_2, 15% CO, 65% N_2, 10%H_2O	0.0125	1	2/3

3.4.2. Stability Experiments of Methanation Reaction

Methanation performance stability tests were for two distinct H_2/CO ratios of 3, and 2. H_2O/CO ratio of 1/3 was employed for each feed type. The reactions were performed at two different temperatures, 250 °C, and 400 °C. W/F (weight-to-flow) ratio of 0.0125 g*h/l was utilized in these performance tests. Each stability evaluation involved testing 75 mg of freshly reduced catalyst samples for a duration of 72 hours.

Table 3.6. Reaction conditions for stability tests.

Reaction Set	T (ºC)	Feed Composition	W/F (g*h/l)	H_2/CO	H_2O/CO
S.1	400	45% H_2, 15% CO, 35% N_2, 5%H_2O 30% H_2, 15% CO, 50% N_2, 5%H_2O	0.0125	3 2	1/3
S.2	250	45% H_2, 15% CO, 35% N_2, 5%H_2O	0.0125	2	1/3

3.4.3. Kinetic Experiments of Methanation Reaction

Methanation kinetic reaction tests were conducted using two types of feed, namely dry and moist feeds. For each feed type, six different H_2/CO ratios and two H_2O/CO ratios were employed, as specified in Table 3.7.

Table 3.7. Reaction conditions for kinetics tests.

	T (˚C)	W/F (kg*s/l)			H_2 (bar)	CO (bar)	H_2O (bar)	CH_4 (bar)	CO_2 (bar)
		1	2	3					
1	350	0.009	0.006	0.004	0.4	0.1	0	0	0
2	350	0.009	0.006	0.004	0.3	0.1	0	0	0
3	350	0.009	0.006	0.004	0.2	0.1	0	0	0
4	350	0.009	0.006	0.004	0.15	0.1	0	0	0
5	350	0.009	0.006	0.004	0.15	0.125	0	0	0
6	350	0.009	0.006	0.004	0.15	0.075	0	0	0
7	350	0.009	0.006	0.004	0.15	0.05	0	0	0
8	350	0.009	0.006	0.004	0.4	0.1	0.041	0	0
9	350	0.009	0.006	0.004	0.3	0.1	0.041	0	0
10	350	0.009	0.006	0.004	0.2	0.1	0.041	0	0
11	350	0.009	0.006	0.004	0.15	0.1	0.041	0	0
12	350	0.009	0.006	0.004	0.15	0.125	0.041	0	0
13	350	0.009	0.006	0.004	0.15	0.075	0.041	0	0
14	350	0.009	0.006	0.004	0.15	0.05	0.041	0	0
15	350	0.009	0.006	0.004	0.3	0.1	0.041	0	0
16	350	0.009	0.006	0.004	0.3	0.1	0.082	0	0
17	350	0.009	0.006	0.004	0.3	0.1	0.123	0	0
18	350	0.009	0.006	0.004	0.3	0.1	0.041	0.05	0
19	350	0.009	0.006	0.004	0.3	0.1	0.041	0.10	0
20	350	0.009	0.006	0.004	0.3	0.1	0.041	0.15	0
21	350	0.009	0.006	0.004	0.3	0.1	0.041	0	0.05
22	350	0.009	0.006	0.004	0.3	0.1	0.041	0	0.10
23	350	0.009	0.006	0.004	0.3	0.1	0.041	0	0.15
24	300	0.009	0.006	0.004	0.3	0.1	0.041	0	0
25	400	0.009	0.006	0.004	0.3	0.1	0.041	0	0
26	325	0.009	0.006	0.004	0.3	0.1	0.041	0	0
27	375	0.009	0.006	0.004	0.3	0.1	0.041	0	0

The tests were carried out across a temperature range from 300 °C to 400 °C. Three distinct W/F (weight-to-flow) ratio levels —0.0025, 0.0017, and 0.0011 g*h/l—were utilized in these kinetic tests.

4. RESULTS AND DISCUSSION

The objective of this study is to design and develop Ni-based methanation catalysts that exhibit enhanced methane production activity, selectivity, and stability under realistic feed conditions with $H_2/CO<3$, achieved through the integration of CO methanation and water-gas shift (WGS) reactions. In this regard, the findings of this research will be presented and discussed across five primary sections:

- Preliminary tests evaluating the effect of experimental parameters on the catalyst performance.
- The investigation of various catalyst bed configurations on methanation performance utilizing classical methanation and WGS catalysts.
- Incorporating bifunctionality by combining WGS and methanation reactions in one catalyst. Preparing and testing new catalysts with different type(s) of metal(s) and metal precursor(s), metal loading/metal loading combination, preparation methods, and pretreatment conditions.
- Characterization of catalysts with Ce-Ni compositions via XPS, XRD, HR-TEM, SEM, and RAMAN.
- Kinetic studies of CO methanation reaction on 5%Ce-10%Ni/γ-Al_2O_3 catalyst.

4.1. Preliminary Tests

4.1.1. Determining the Reduction Temperatures

The temperature-programmed reduction (TPR) technique enables the characterization of metal–support interactions, the clarification of the role of additives as promoters in reduction, and the study of how different phases affect the reducibility of a specific compound in a multicomponent system. TPR tests were conducted on the prepared samples using a H_2-He mixture containing 5% H_2 on 75 mg catalyst samples, with the temperature increasing from room temperature to 900 °C at a ramp rate of 5 °C/min.

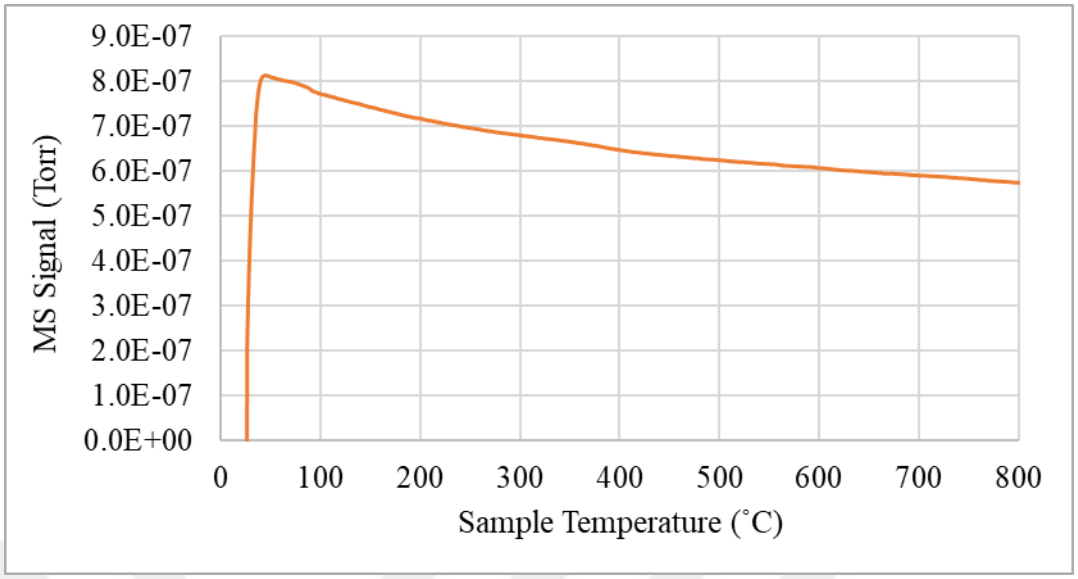

Figure 4.1. MS signals of H_2 molecules for 15% Ni/γ-Al_2O_3 in the exit stream of CATLAB Microreactor.

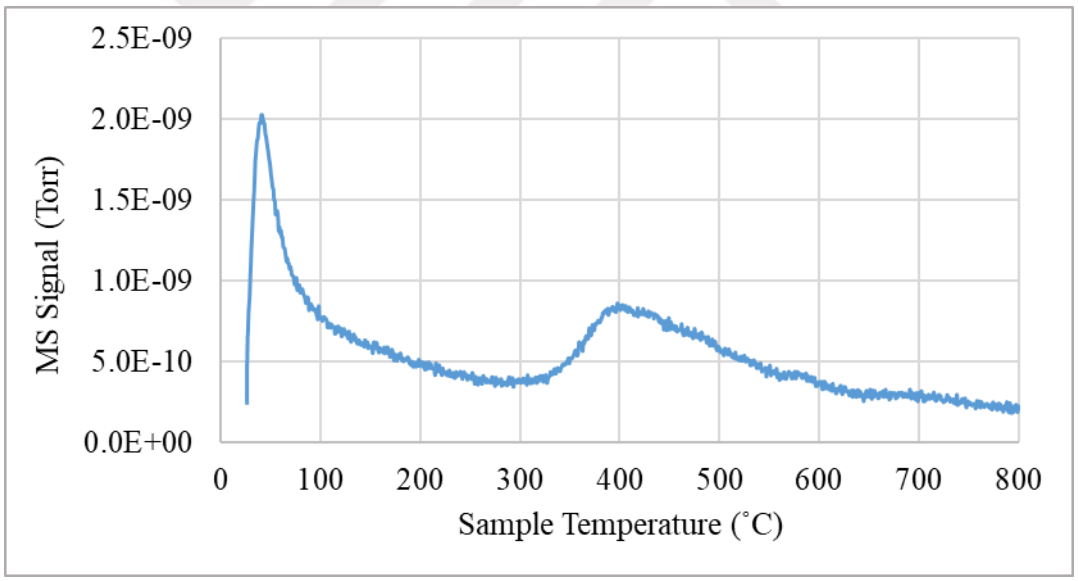

Figure 4.2. MS signals of H_2O molecules for 15% Ni/γ-Al_2O_3 in the exit stream of CATLAB Microreactor.

Figures 4.1 and 4.2 show the H_2-TPR profiles of the 15% Ni/γ-Al_2O_3 catalyst. A broad reduction peak in the range of 330-550 ˚C was observed, corresponding to the NiO species with moderate interactions with alumina. Based on their peak positions observed in TPR spectra, the reducible NiO species are divided into four types: α, β1, β2, and γ (Zhang et al., 2005; Hu et al., 2012).

Table 4.1. Classification of the reducible NiO species (Hu et al., 2012).

410 °C – 500 °C	α- type NiO	Free NiO species possessing a weak interaction with alumina support
580 °C – 740 °C	β- type NiO	
580 °C – 630 °C	β_1- type NiO	More reducible NiO in Ni-rich mixed oxide phase
690 °C -740 °C	β_2- type NiO	Less reducible NiO in Al-rich oxide phase
790 °C – 840 °C	γ- type NiO	Stable Nickel-Aluminate phase with spinel structure

According to classification given in Table 4.1, broad reduction peak in the range of 320 °C-520 °C was attributed to free NiO species possessing a weak interaction with γ-Al_2O_3 support, whereas small peak around 580 °C-590 °C was attributed to reducible NiO in Ni-rich mixed oxide phase which has a stronger interaction with alumina than the α-type NiO.

TPR profiles of γ-Al_2O_3-supported catalysts are given in Figure 4.3. After the addition of promoters, the H_2-TPR profiles of the Ni/γ-Al_2O_3 catalysts changed significantly. Peaks located in the range of 350-550 °C were still attributed to the reduction of NiO species with a low interaction with the alumina support. The peaks above 700 °C were attributed to the strong chemical interaction of Ni species with the alumina support ($NiAl_2O_4$), which is consistent with the XRD results.

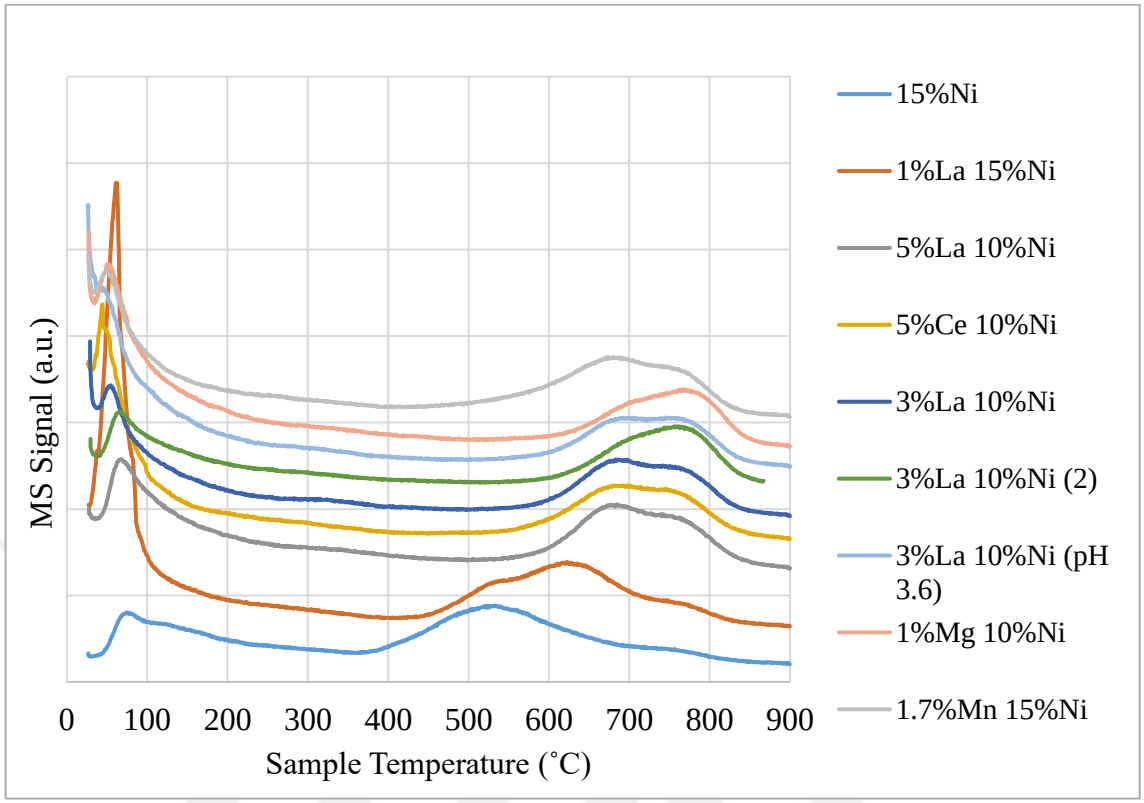

Figure 4.3. MS signals of H_2O molecules for γ-Al_2O_3 supported catalysts in the exit stream of CATLAB Microreactor.

Although TPR peaks exceed 700 °C, a maximum reduction temperature of 670 °C was selected to prevent any phase changes in Al_2O_3.

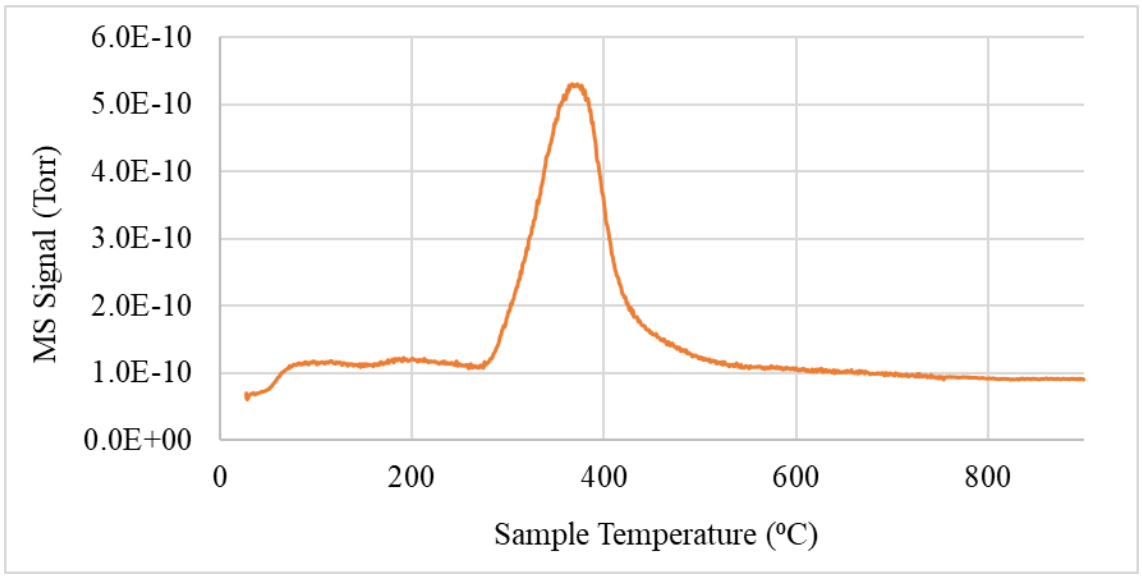

Figure 4.4. MS signals of H_2O molecules for 5%Ce-10% Ni/γ-Al_2O_3 in the exit stream of CATLAB Microreactor.

Figure 4.4 shows the TPR profile of the 5%Ce-10%Ni/ZrO_2 catalyst. A strong reduction peak at 375 °C was attributed to o bulk NiO with weak interaction with support (Dong et al., 2002).

The list of catalysts, along with their corresponding reduction temperatures and durations, can be found in Table 4.2**.**

Table 4.2. Reduction temperatures of the catalysts.

#	Catalyst	Reduction Temperature (°C)	Time (min)
1	10% Ni/ɣ-Al_2O_3	590	120
2	1%Mg-10%Ni/ɣ-Al_2O_3	670	120
3	1%La-10%Ni/ɣ-Al_2O_3	670	120
4	3%La-10%Ni/ɣ-Al_2O_3	670	120
5	3%La-10%Ni/ɣ-Al_2O_3 (2)	670	120
6	3%La-10%Ni/ɣ-Al_2O_3 (3.6 pH)	670	120
7	5%La-10%Ni/ɣ-Al_2O_3	670	120
8	5%Ce-10%Ni/ɣ-Al_2O_3	670	120
9	5%Ce-10%Ni/SBA-15	670	240
10	5%Ce-10%Ni/ZrO_2	375	120
11	15% Ni/ɣ-Al_2O_3	590	120
12	1%La-15%Ni/ɣ-Al_2O_3	670	120
13	1.7%Mn-15%Ni/ɣ-Al_2O_3	670	120
14	10% Ni/SBA-15-550	550	240
15	15% Ni/SBA-15-550	550	240
16	15% Ni/SBA-15-750	750	240

4.1.2. Catalyst Weight/Volumetric Flow Rate (W/F) Tests

To determine the W/F ratio would be used during our performance tests, various combinations of catalyst weight and volumetric flow rate were examined (Figure 4.5). The specific catalyst weight and volumetric flow rate combination (W/F=0.0125 g*h/L) that

yielded the optimal results (ca. 94%) in CO conversion tests was subsequently subjected to further testing to investigate mass transfer limitations. Reactions were conducted on 15% Ni/γ-Al_2O_3 catalyst at 400 °C under a feed gas flow with an H_2/CO ratio of 2 and an H_2O/CO ratio of 1/3.

Calculation procedures for CO conversion, CH_4 yield and CO_2 yield are given as

$$CO\ Conversion\ \% = \frac{F_{CO,in} - F_{CO,out}}{F_{CO,in}} x100, \quad (4.1)$$

$$CH_4\ Yield\ \% = \frac{F_{CH_4,out}}{F_{CO,in}} x100, \quad (4.2)$$

$$CO_2\ Yield\ \% = \frac{F_{CO_2,out}}{F_{CO,in}} x100. \quad (4.3)$$

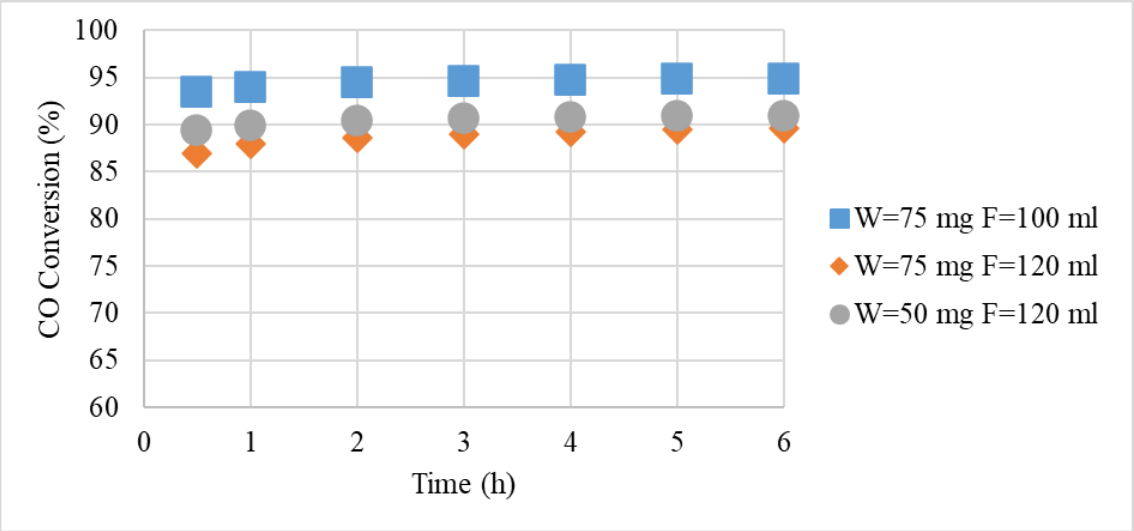

Figure 4.5. Effects of different W/F ratios on CO conversion.

At a constant W/F ratio of 0.0125 g*h/L, the effects of different catalyst weights and volumetric flow rates on CO conversion and CH_4 yield were examined. Regardless of the catalyst weight, both CO conversion (ca. 94%) and CH_4 yield (ca. 72%) remained consistent for a constant W/F ratio of 0.0125 g*h/L, indicating the absence of mass transfer limitations (Figure 4.6).

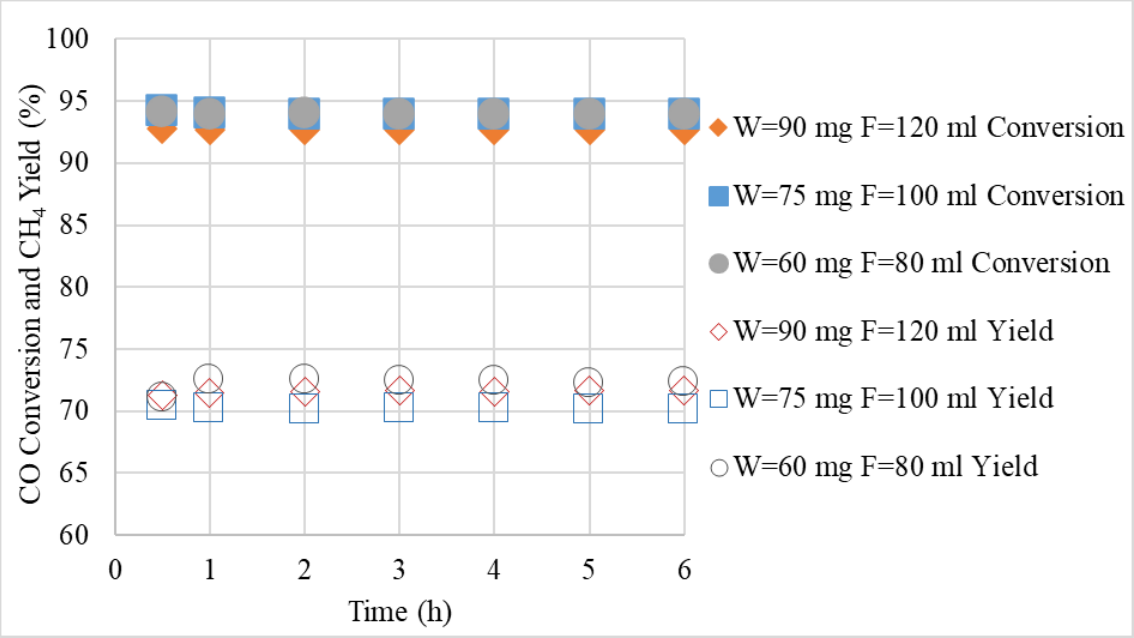

Figure 4.6. Effects of different catalyst weight and volumetric flow rate combinations on CO conversion and CH_4 yield for a constant W/F ratio of 0.0125 g*h/L.

4.1.3. Determining The Thermodynamic Limits

Thermodynamic limitations of the CO methanation reactions for different feed compositions were checked using the HSC Chemistry Application for thermodynamic calculations. In Figure 4.7, experimentally determined CO conversion values are presented alongside their corresponding thermodynamic limits calculated by the HSC application. Figure 4.8 shows the CH_4 yields obtained experimentally in comparison with their thermodynamic limits. Experimental data were collected through 6-hour performance tests conducted on 15% Ni/γ-Al_2O_3 catalyst at 350, 400 and 450 °C, under a feed gas flow with an H_2/CO ratio of 3 and an H_2O/CO ratio of 1/3.

All experimental values for CO conversion and CH_4 yields were found to be lower than the corresponding thermodynamic limits.

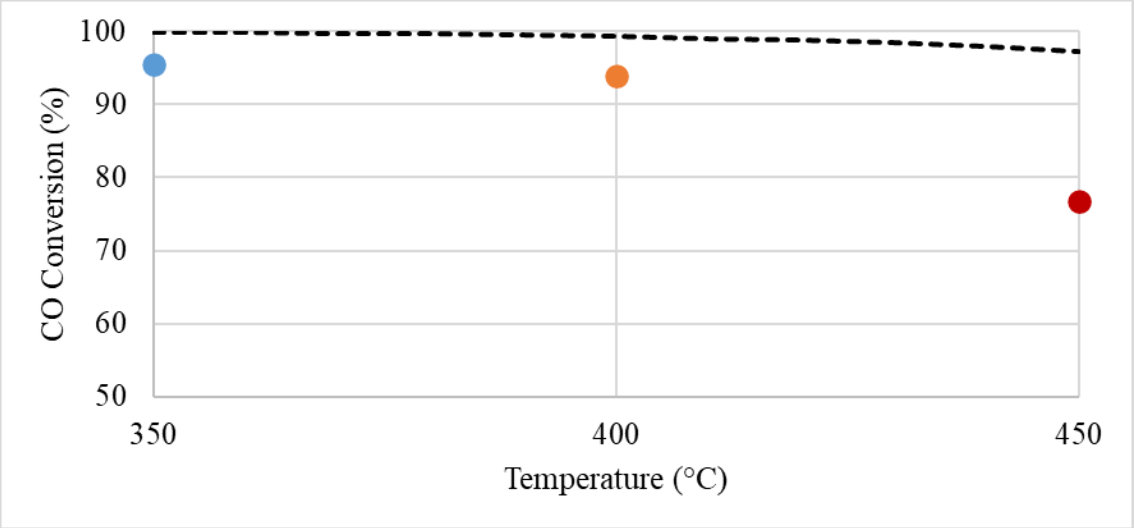

Figure 4.7. Average CO conversion values for H_2/CO=3 of a 6-hour performance test on the 15% Ni/γ-Al_2O_3 catalyst (●) alongside thermodynamic limits calculated by HSC (-).

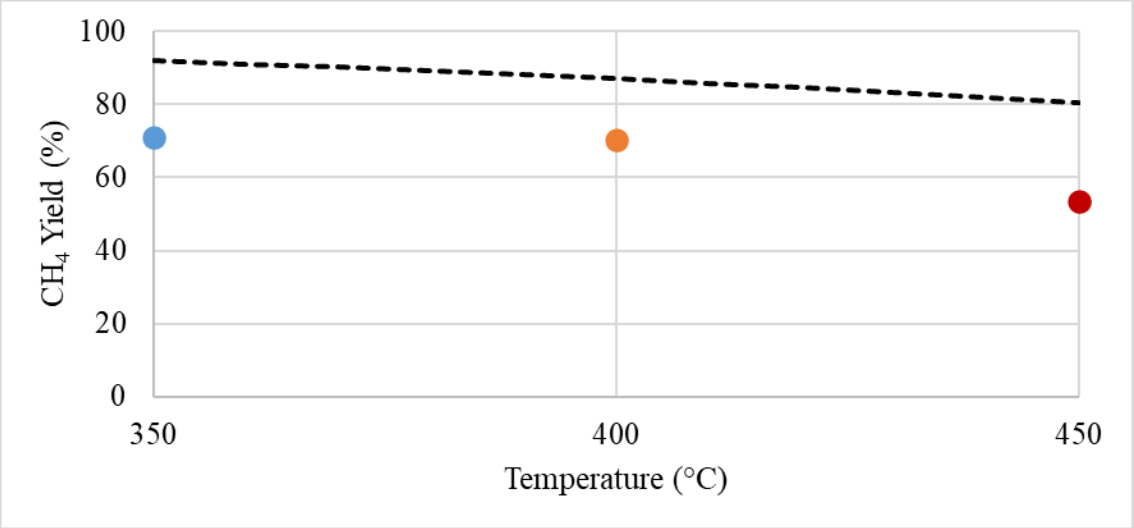

Figure 4.8. Average CH_4 yield values for H_2/CO=3 of a 6-hour performance test on the 15% Ni/γ-Al_2O_3 catalyst (●) alongside thermodynamic limits calculated by HSC (-).

In Figure 4.9, the CO conversions are presented alongside their corresponding thermodynamic limits, while Figure 4.10 demonstrates the CH_4 yields with respect to their thermodynamic limits for an H_2/CO feed ratio of 2. Once again, all experimental values for CO conversion and CH_4 yield were found to be lower than their corresponding thermodynamic limits, as expected.

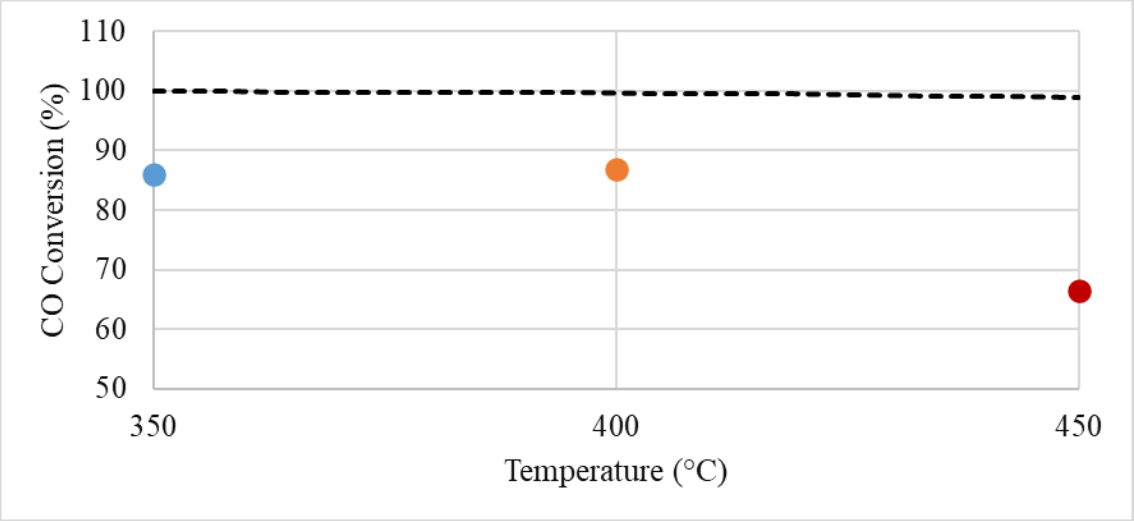

Figure 4.9. Average CO conversion values for H_2/CO=2 of a 6-hour performance test on the 15% Ni/γ-Al_2O_3 catalyst (●) alongside thermodynamic limits calculated by HSC (-).

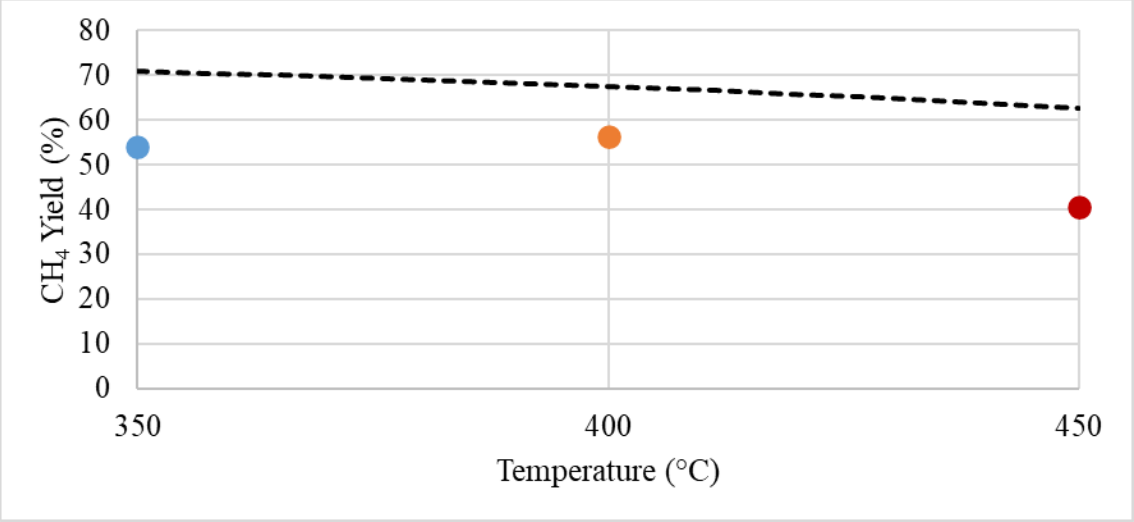

Figure 4.10. Average CH_4 yield values for H_2/CO=2 of a 6-hour performance test on the 15% Ni/γ-Al_2O_3 catalyst (●) alongside thermodynamic limits calculated by HSC (-).

4.2. The Investigation of Various Bed Configurations on Methanation Performance

The key reactions in SNG production are the CO methanation and CO_2 methanation reactions. However, the SNG production process also involves several other side reactions, both desired and undesired, which were detailed in Section 2.2. Especially for H_2/CO ratios lower than 3, CO is predominantly converted into non-SNG products through these side reactions.

In this section of the study, to minimize undesired side reactions and increase the probability of desired side reactions, various catalyst bed configurations containing CO methanation catalysts, CO_2 methanation catalysts, and WGS catalysts were utilized for methanation reactions. These bed configurations can be categorized into two parts.

- Physical mixture of WGS and methanation catalysts: WGS and methanation catalysts were mixed in varying weight ratios and examined under different feed conditions to evaluate their performance.

- Sequential beds of methanation reaction catalysts: Different methanation catalysts, prepared for CO and CO_2 methanation reactions, were utilized sequentially within the same reactor to enhance the methane production. Schematic representation of the bed configurations along with a photograph of a three-bed sequential configuration can be found in Figures 4.11 and 4.12.

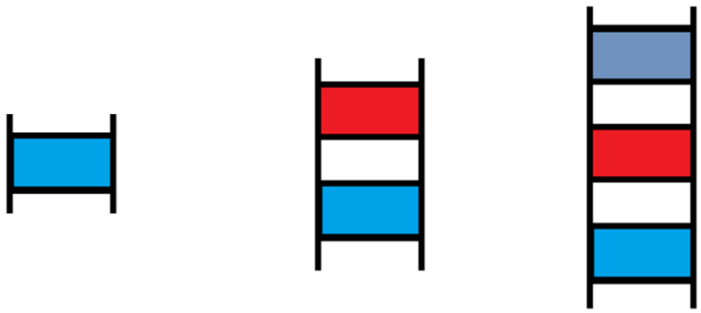

Figure 4.11. Schematic diagrams of one-bed, two-bed and three-bed configurations.

Figure 4.12. Photograph of a three-bed configuration.

4.2.1. Physical Mixture of WGS and Methanation Reaction Catalysts

Three WGS catalysts, 0.5%Pt-1%Re-0.5%V/CeO_2, 1%Pt-0.5%Re-0.5%V/CeO_2, and 0.5%Pt-1%Re-1%V/CeO_2, selected based on the results of a previous study conducted by our group, were used to prepare physical WGS-methanation catalyst mixtures. Temperature dependent CO conversion and net H_2 production rate values for the selected WGS catalysts can be found in Figures 4.13 and 4.14, respectively. These reactions were performed with an H_2O/CO ratio of 6.7 with following compositions: 32.7% H_2O, 30.0% H_2, 22.0% Ar, 10.4% CO_2, 4.9% CO (Kesim, 2017).

Table 4.3. WGS catalysts from a previous study conducted by Bahar Kesim in 2017.

WGS Catalyst
0.5%Pt-1%Re-0.5%V/CeO_2
1%Pt-0.5%Re-0.5%V/CeO_2
0.5%Pt-1%Re-1%V/CeO_2

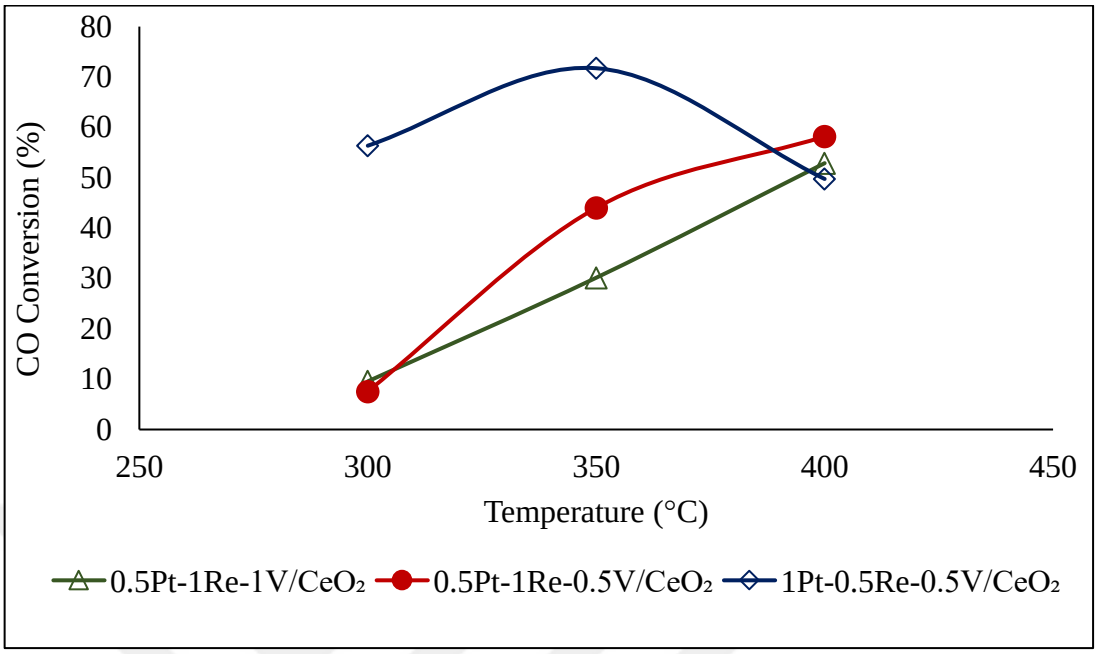

Figure 4.13. Temperature dependence of catalytic activity for WGS catalysts.

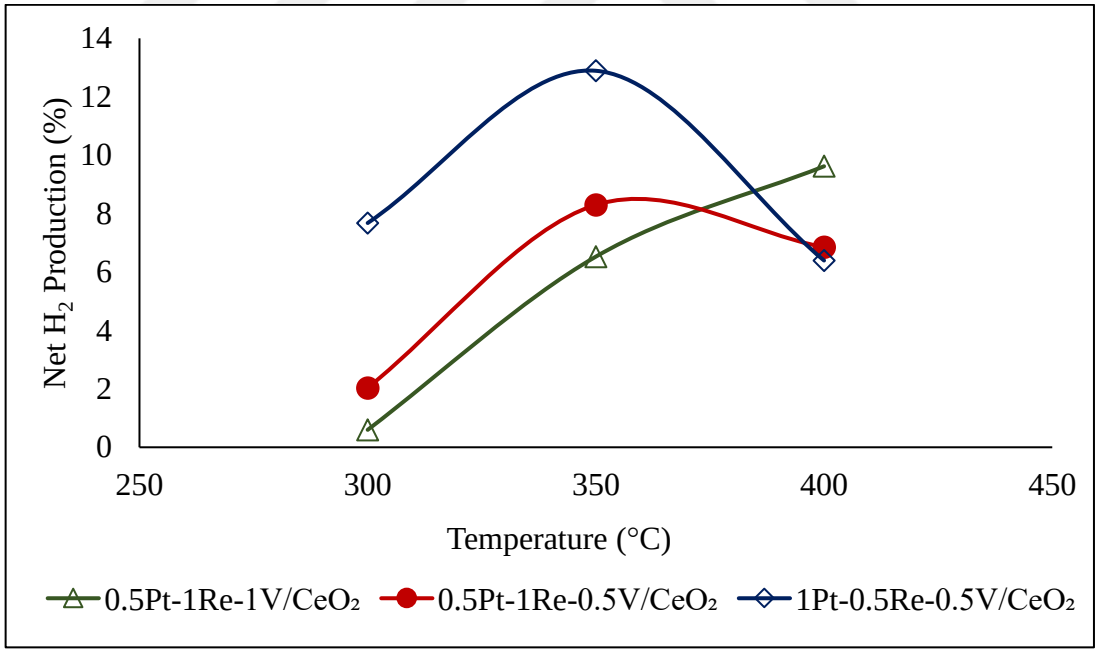

Figure 4.14. Temperature dependence of net H_2 production for WGS catalysts.

The three WGS catalysts from Bahar Kesim's study were mixed with a conventional methanation catalyst, 15% Ni/γ-Al_2O_3, and tested under feed conditions with an H_2/CO ratio of 2, and an H_2O/CO ratio of 1/3, in separate experiments. These experiments were conducted for a catalyst weight ratio of $W_{WGS}/W_{Methanation}$ = 0.25 at 400 °C (Table 4.4).

Table 4.4. Physical mixtures of selected WGS catalysts with a conventional methanation catalyst.

#	**Methanation Catalyst**	**WGS Catalyst**
1	60 mg 15% Ni/ɣ-Al_2O_3	15 mg 0.5%Pt-1%Re-0.5%V/CeO_2
2	60 mg 15% Ni/ɣ-Al_2O_3	15 mg 1%Pt-0.5%Re-0.5%V/CeO_2
3	60 mg 15% Ni/ɣ-Al_2O_3	15 mg 0.5%Pt-1%Re-1%V/CeO_2

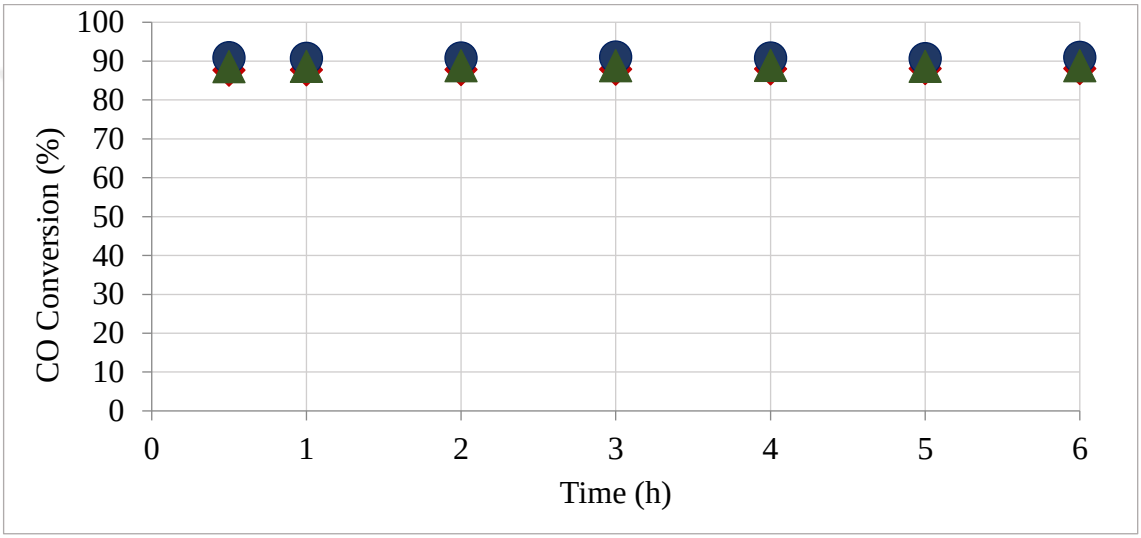

Figure 4.15. CO conversion values for performance tests conducted on physical mixtures of WGS-Methanation catalysts: 60 mg 15% Ni/ɣ-Al_2O_3 and 15 mg 0.5%Pt-1%Re-0.5%V/CeO_2 (♦), 60 mg 15% Ni/ɣ-Al_2O_3 and 15 mg 1%Pt-0.5%Re-0.5%V/CeO_2 (●), and 60 mg 15% Ni/ɣ-Al_2O_3 and 15 mg 0.5%Pt-1%Re-1%V/CeO_2 (▲).

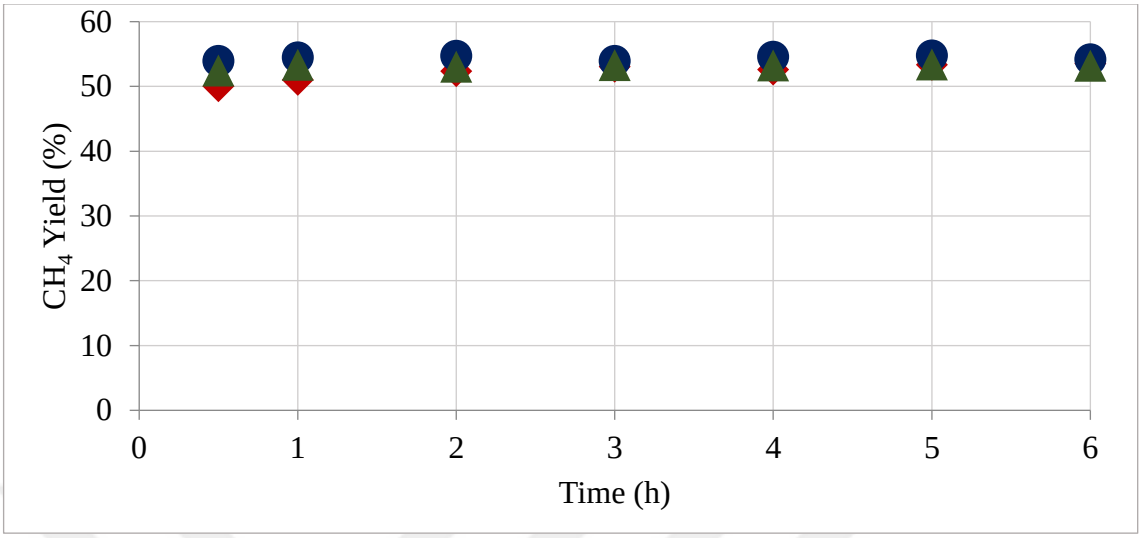

Figure 4.16. CH_4 yield values for performance tests conducted on physical mixtures of WGS-Methanation catalysts: 60 mg 15% Ni/ɣ-Al_2O_3 and 15 mg 0.5%Pt-1%Re-0.5%V/CeO_2 (♦), 60 mg 15% Ni/ɣ-Al_2O_3 and 15 mg 1%Pt-0.5%Re-0.5%V/CeO_2 (●), and 60 mg 15% Ni/ɣ-Al_2O_3 and 15 mg 0.5%Pt-1%Re-1%V/CeO_2 (▲).

The catalyst mixture that yielded the highest conversion value (ca. 91%) was found to be 60 mg 15% Ni/ɣ-Al_2O_3 and 15 mg 1%Pt-0.5%Re-0.5%V/CeO_2 catalyst mixture (Figures 4.15 and 4.16). Subsequently, the performance of the catalyst combination underwent further testing with varying weight ratios in order to determine the optimal mixing ratios. However, increasing the weight ratio of WGS catalyst to methanation catalyst from 0 to 1, under feed conditions with an H_2/CO ratio of 3, and an H_2O/CO ratio of 0, resulted in a decrease in CO conversions (from ca. 94% to ca. 75%) and CH_4 yields (from ca. 72% to ca. 53%) (Figures 4.17 and 4.18, respectively).

Table 4.5. Weight ratios for physical catalyst mixtures containing both methanation and WGS catalysts.

15% Ni/γ-Al_2O_3 & 1%Pt-0.5%Re-0.5%V/CeO_2					
#	**Rxn T**	**H_2/CO**	**Meth cat (mg)**	**WGS cat (mg)**	**W_{wgs}/W_{meth}**
1	400	3.00	75.00	-	0.00
2	400	3.00	60.00	15.00	0.25
3	400	3.00	50.00	25.00	0.50
4	400	3.00	37.50	37.50	1.00

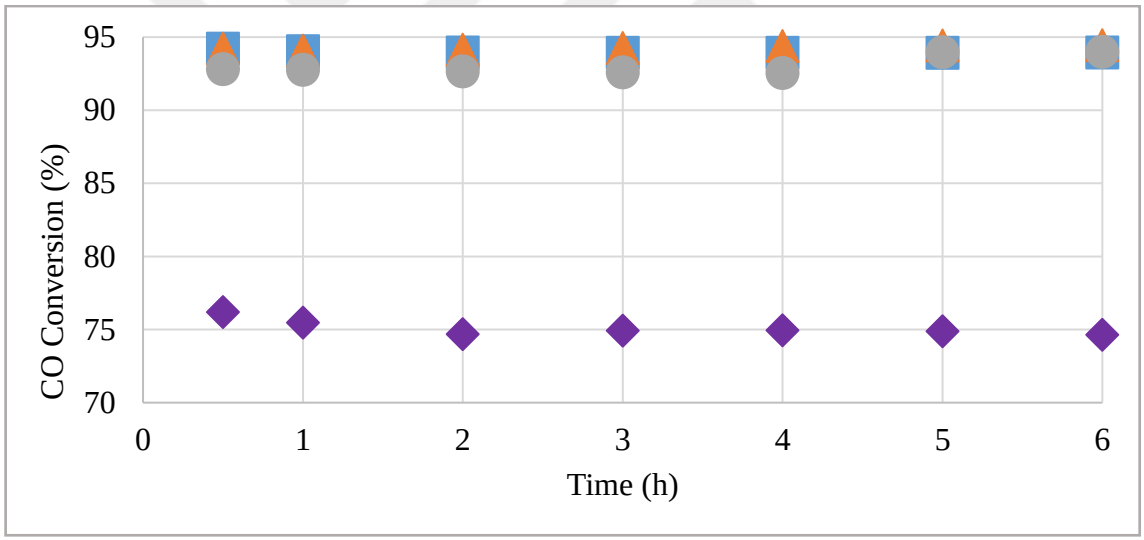

Figure 4.17. CO conversion values for performance tests conducted on physical mixtures of 15% Ni/γ-Al_2O_3 and 1%Pt-0.5%Re-0.5%V/CeO_2 catalysts with varying mixing ratios: $W_{WGS}/W_{methanation}$=0 (■), $W_{WGS}/W_{methanation}$=0.25 (▲), $W_{WGS}/W_{methanation}$=0.50 (●), $W_{WGS}/W_{methanation}$=1 (♦).

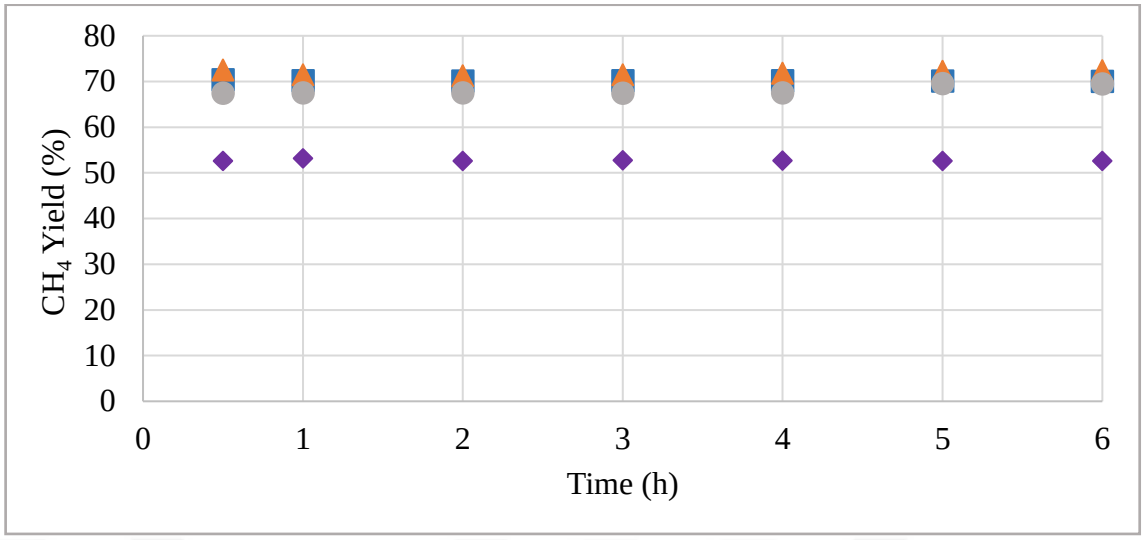

Figure 4.18. CH_4 yield values for performance tests conducted on physical mixtures of 15% Ni/ɣ-Al_2O_3 and 1%Pt-0.5%Re-0.5%V/CeO_2 catalysts with varying mixing ratios: $W_{WGS}/W_{methanation}$=0 (■), $W_{WGS}/W_{methanation}$=0.25 (▲), $W_{WGS}/W_{methanation}$=0.50 (●), $W_{WGS}/W_{methanation}$=1 (♦).

Both pure methanation catalyst, 15% Ni/ɣ-Al_2O_3, and physical catalyst mixture, containing 60 mg 15% Ni/ɣ-Al_2O_3 and 15 mg 1%Pt-0.5%Re-0.5%V/CeO_2 catalysts, were further tested for steam addition to the feed gas stream for three different H_2/CO ratios of 1, 2, and 3. The reactions were conducted at 400 °C. Steam was added to the feed gas stream with an H_2O/CO ratio of 1/3. Introducing steam into the feed gas stream led to increased CO conversion values, especially for H_2/CO ratio of 1 for both the pure methanation catalyst (from 57.3% to 80.7%) and the physical mixture of WGS and methanation catalysts (from 44.7% to 76.7%). However, the use of a catalyst mixture, as opposed to a pure methanation catalyst, did not result in a positive effect on the CO conversion and CH_4 yield values (Figures 4.19 and 4.20, respectively).

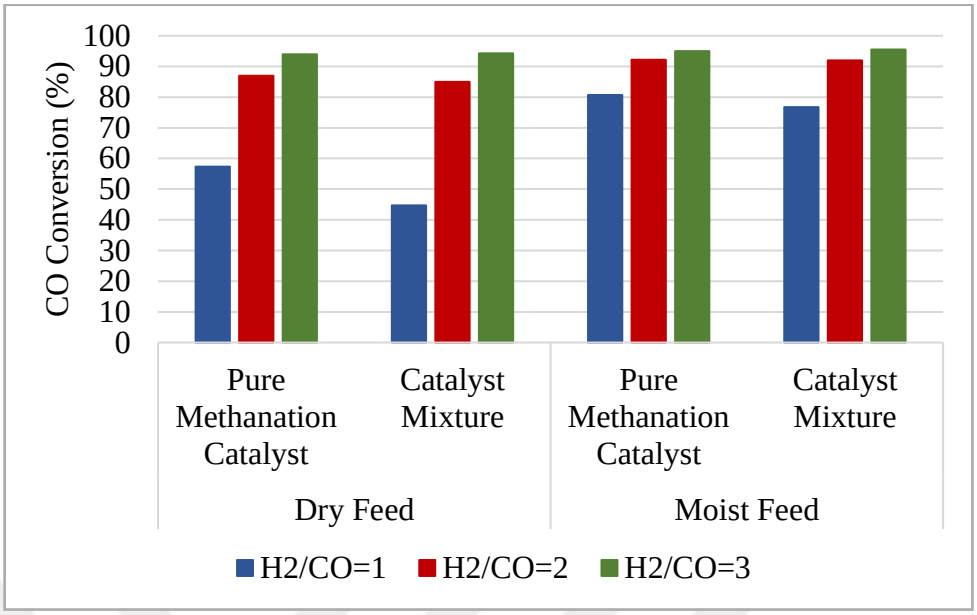

Figure 4.19. Average CO conversion values for 6-hour performance tests conducted on pure methanation catalyst, 15% Ni/ɣ-Al_2O_3, and physical mixtures of 15% Ni/ɣ-Al_2O_3 and 1%Pt-0.5%Re-0.5%V/CeO_2 catalysts under different feed conditions.

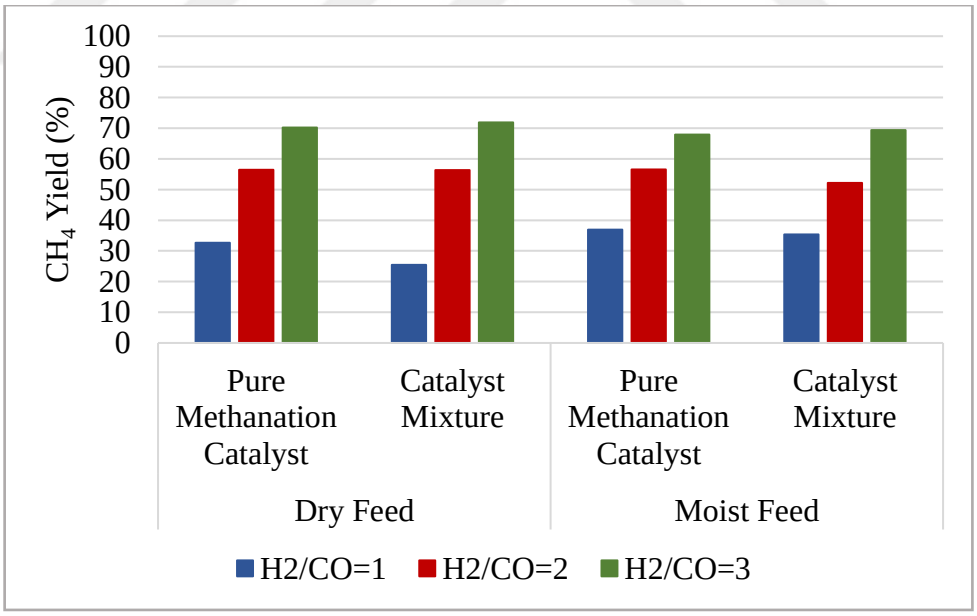

Figure 4.20. Average CH_4 Yield values for 6-hour performance tests conducted on pure methanation catalyst, 15% Ni/ɣ-Al_2O_3, and physical mixtures of 15% Ni/ɣ-Al_2O_3 and 1%Pt-0.5%Re-0.5%V/CeO_2 catalysts under different feed conditions.

4.2.2. Sequential Beds of Methanation Reaction Catalysts

Since utilizing a WGS catalyst did not result in a positive effect on the CO conversion and CH_4 yield values, and GC analysis showed the presence of excess CO, CO_2 and H_2 in the product stream, different methanation catalysts prepared for CO and CO_2 methanation reactions were utilized sequentially within the same reactor to enhance the methane production.

Investigations in literature and industry focus on nickel-based catalysts for both CO methanation and CO_2 methanation reactions. In this study, 15% Ni/γ-Al_2O_3, 1.7%Mn-15%Ni/γ-Al_2O_3, 3%La-10%Ni/γ-Al_2O_3, and 5%Ce-10%Ni/ZrO_2 catalysts were prepared for CO_2 methanation reaction. To identify the most effective CO_2 methanation catalyst to be incorporated into our catalyst bed configurations, the prepared catalysts were tested for CO_2 methanation performances at 400 °C under a feed gas stream with an H_2/CO_2 ratio of 4. All catalysts exhibited similar CO_2 conversion rates, ranging from 67% to 72% (Figures 4.21 and 4.22). 1.7%Mn-15%Ni/γ-Al_2O_3 and 5%Ce-10%Ni/ZrO_2 catalysts which demonstrated the slightly higher CO_2 methanation performances were used as the CO_2 methanation catalyst in our two-bed and three-bed catalyst configurations.

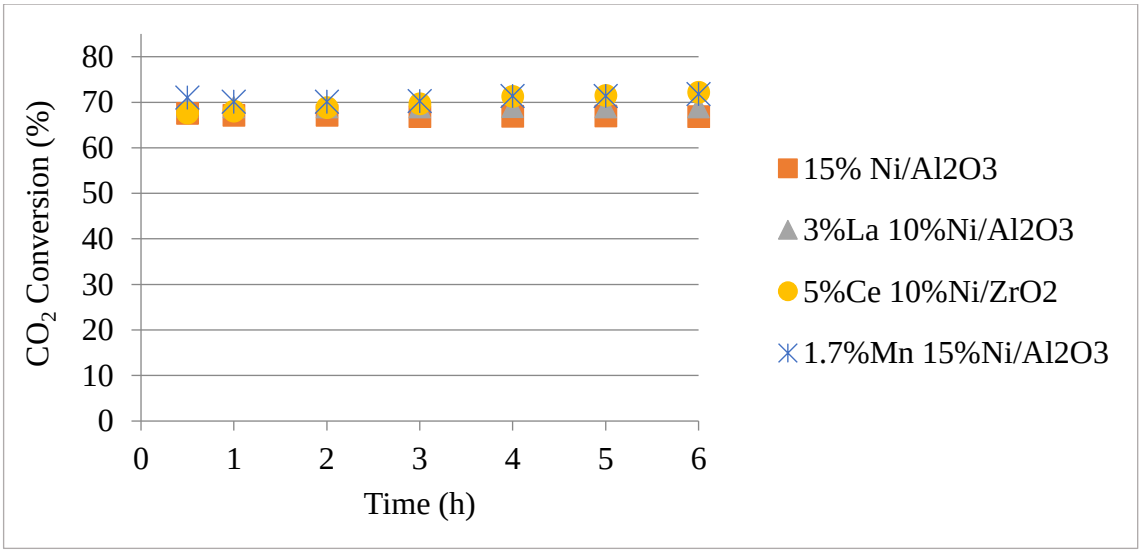

Figure 4.21. Conversion values for CO_2 methanation tests conducted on 15% Ni/γ-Al_2O_3, 1.7%Mn-15%Ni/γ-Al_2O_3, 3%La-10%Ni/γ-Al_2O_3, and 5%Ce-10%Ni/ZrO_2 for H_2/CO_2=4.

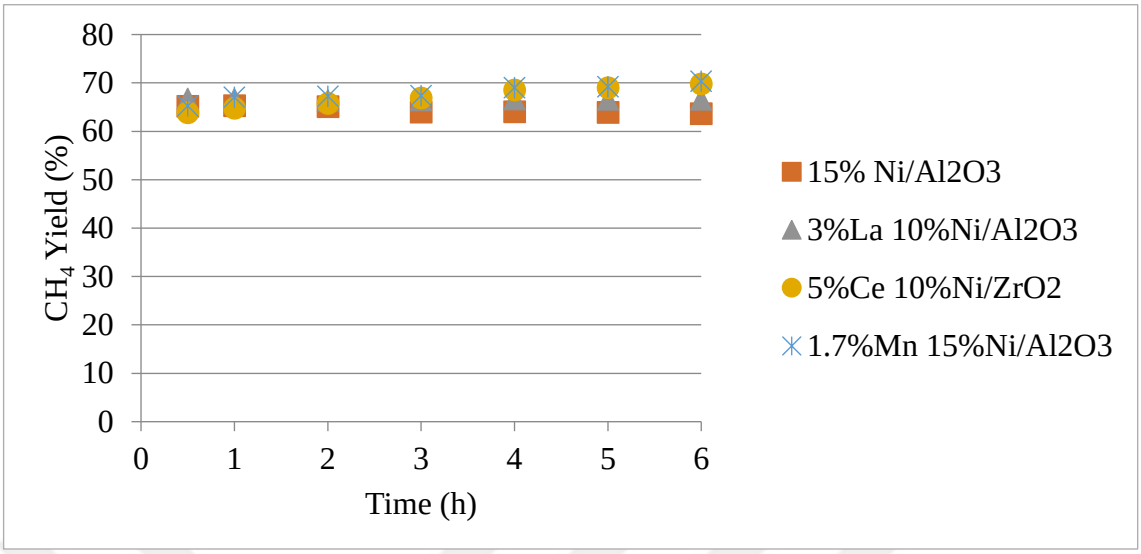

Figure 4.22. CH_4 yield values for CO_2 methanation tests conducted on 15% Ni/γ-Al_2O_3, 1.7%Mn-15%Ni/γ-Al_2O_3, 3%La-10%Ni/γ-Al_2O_3, and 5%Ce-10%Ni/ZrO_2 for H_2/CO_2=4.

The two-bed configuration, consisting of a CO methanation catalyst followed by a CO_2 methanation catalyst, was utilized with a 75 mg 5%La-10%Ni/γ-Al_2O_3 catalyst bed followed by a 75 mg 5%Ce-10%Ni/ZrO_2 catalyst bed. This bed configuration was tested at 400 ºC with two different feed gas streams: one containing an H_2/CO ratio of 3 and an H_2O/CO ratio of 1/3, and the other containing an H_2/CO ratio of 2 and an H_2O/CO ratio of 1/3. Utilizing a two-bed configuration with the specified catalysts increased the CO conversion and CH_4 yield results for both H_2/CO ratios (Figures 4.23-26). However, when the 5%La-10%Ni/γ-Al_2O_3 catalyst was tested in a one-bed configuration with its weight doubled (i.e., 150 mg), the same CO conversion and CH_4 yield results were obtained (Figure 4.27 and 4.28). This finding implies that the increase in CO conversion and CH_4 yield was a result of the higher W/F ratio.

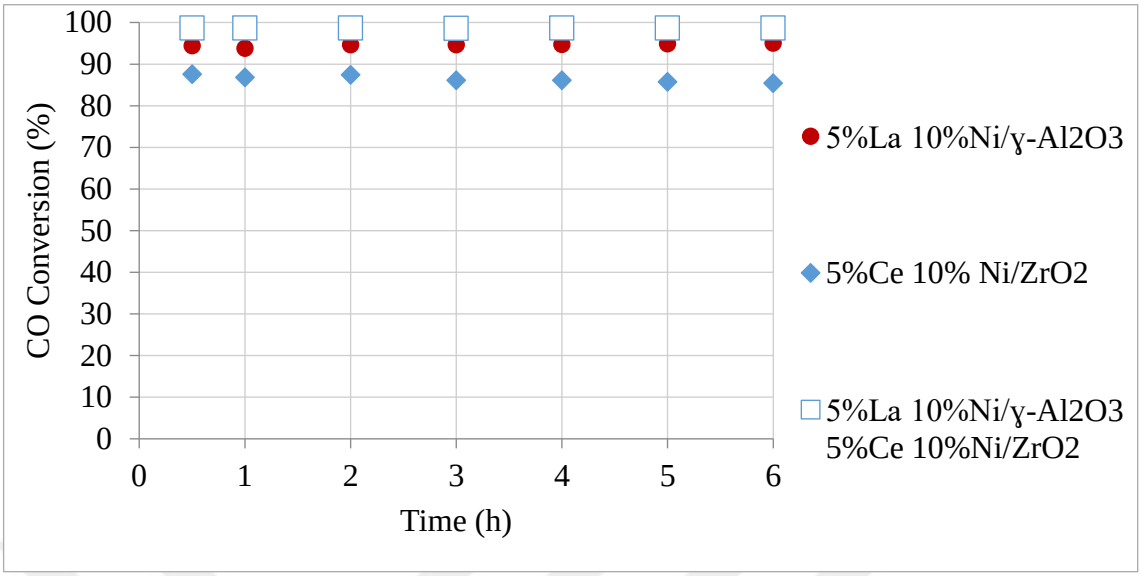

Figure 4.23. CO conversion values for performance tests conducted with $H_2/CO=3$ on one-bed 75 mg 5%La-10%Ni/γ-Al_2O_3, one-bed 75 mg 5%Ce-10%Ni/ZrO_2, and two-bed 75 mg 5%La-10%Ni/γ-Al_2O_3 catalyst followed by 75 mg 5%Ce-10%Ni/ZrO_2 configurations.

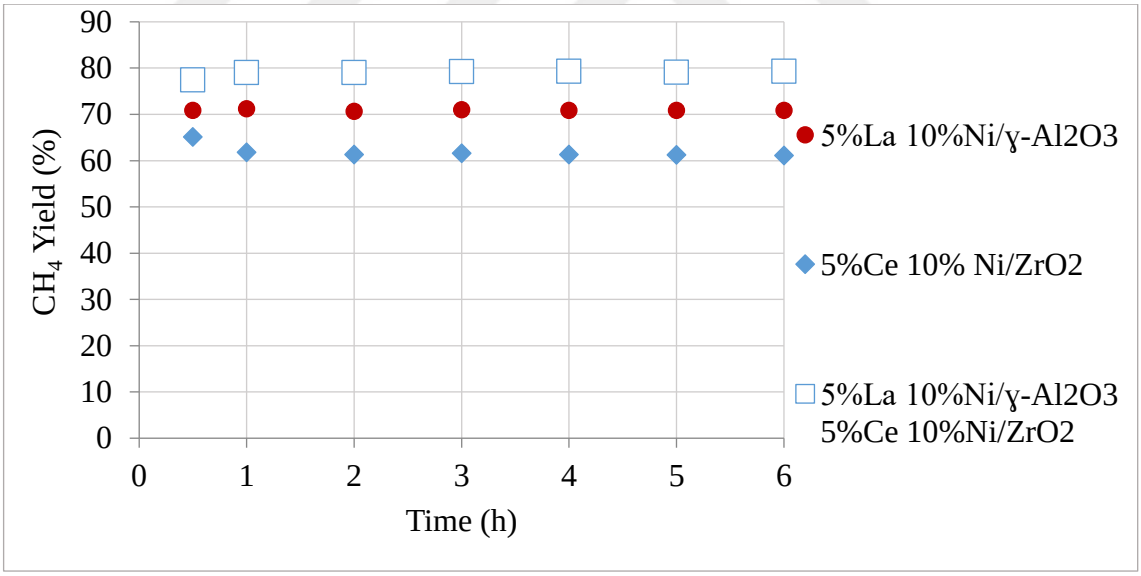

Figure 4.24. CH_4 yield values for performance tests conducted with $H_2/CO=3$ on one-bed 75 mg 5%La-10%Ni/γ-Al_2O_3, one-bed 75 mg 5%Ce-10%Ni/ZrO_2, and two-bed 75 mg 5%La-10%Ni/γ-Al_2O_3 catalyst followed by 75 mg 5%Ce-10%Ni/ZrO_2 configurations.

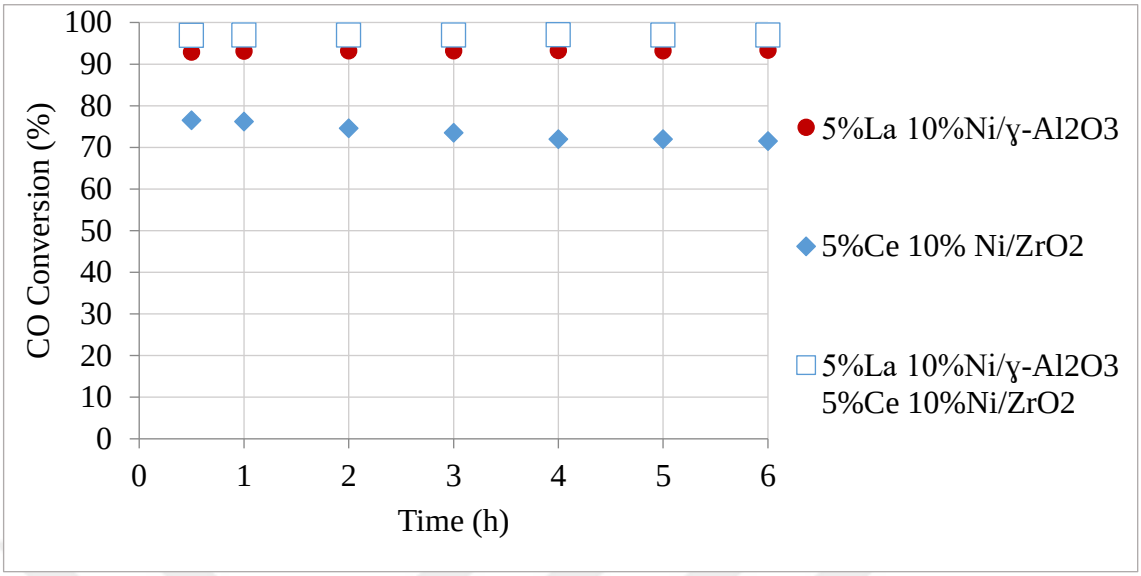

Figure 4.25. CO conversion values for performance tests conducted with $H_2/CO=2$ on one-bed 75 mg 5%La-10%Ni/γ-Al_2O_3, one-bed 75 mg 5%Ce-10%Ni/ZrO_2, and two-bed 75 mg 5%La-10%Ni/γ-Al_2O_3 catalyst followed by 5%Ce-10%Ni/ZrO_2 configurations.

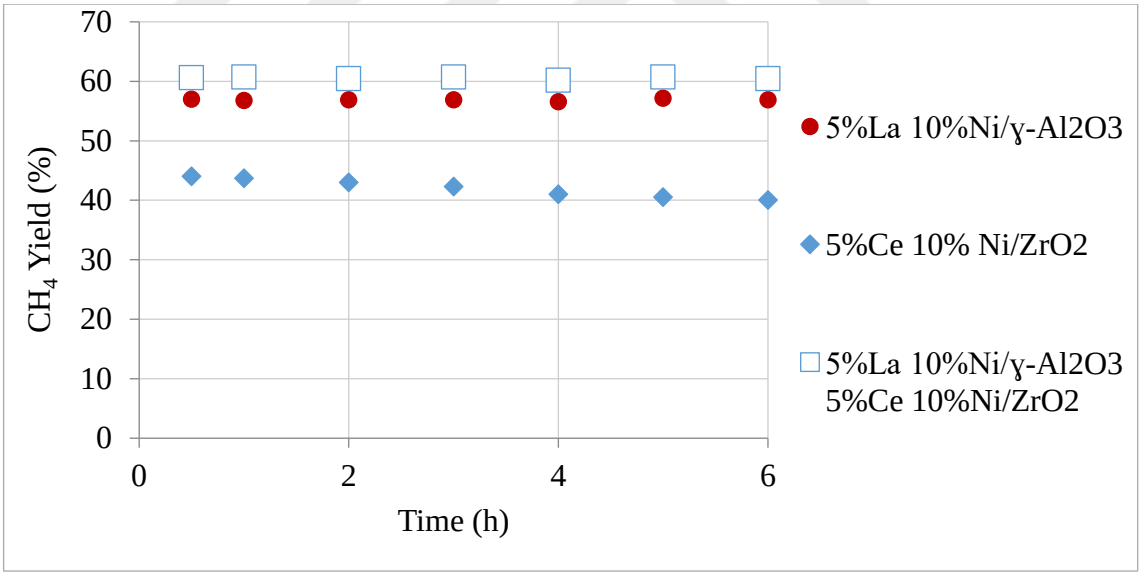

Figure 4.26. CH_4 yield values for performance tests conducted with $H_2/CO=2$ on one-bed 75 mg 5%La-10%Ni/γ-Al_2O_3, one-bed 75 mg 5% Ce 10% Ni/ZrO_2, and two-bed 75 mg 5%La-10%Ni/γ-Al_2O_3 catalyst followed by 5%Ce-10%Ni/ZrO_2 configurations.

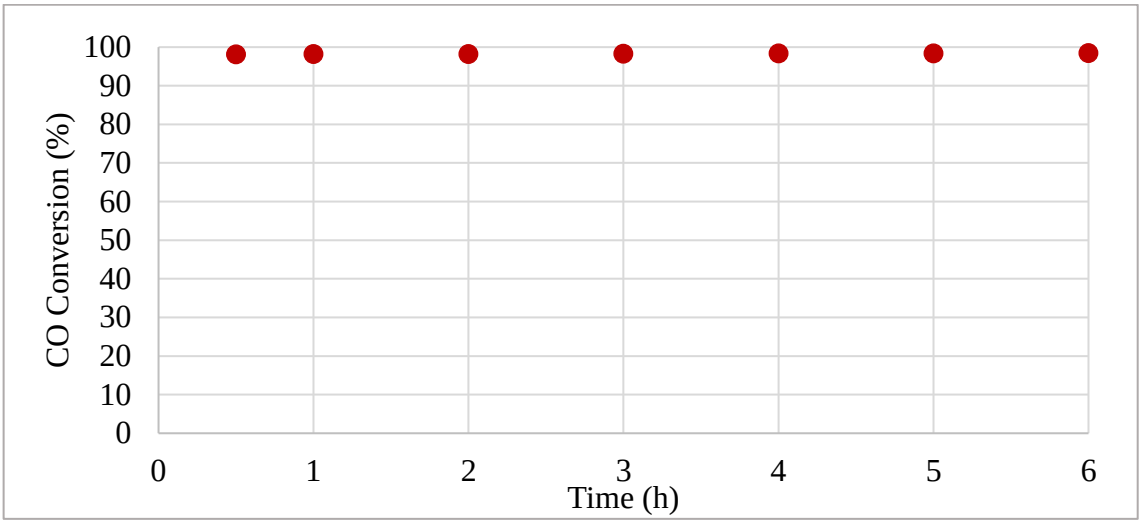

Figure 4.27. CO conversion values for performance tests conducted with $H_2/CO=2$ on one-bed 150 mg 5%La-10%Ni/γ-Al_2O_3 configuration.

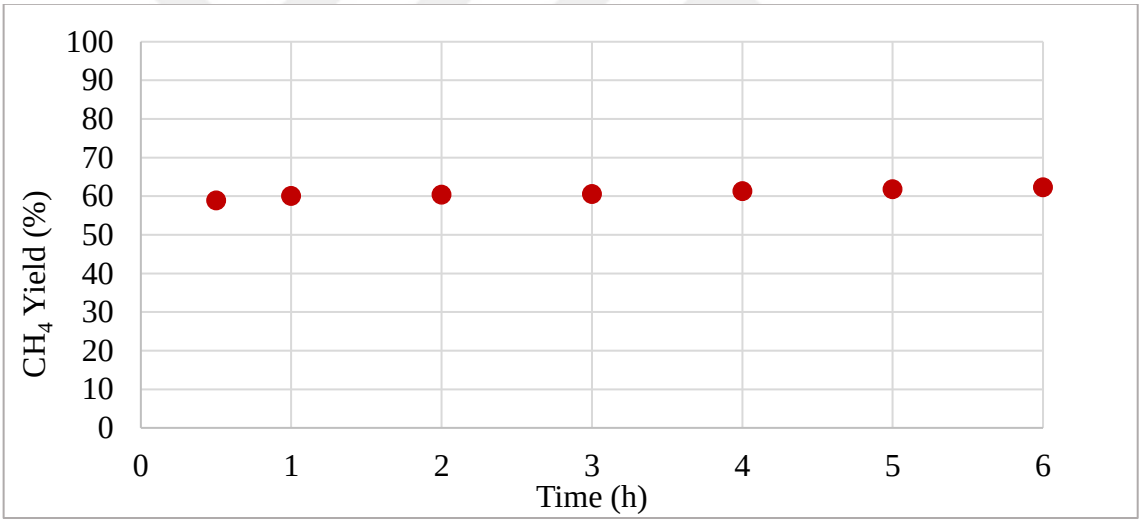

Figure 4.28. CH_4 yield values for performance tests conducted with $H_2/CO=2$ on one-bed 150 mg 5%La-10%Ni/γ-Al_2O_3 configuration.

A three-bed configuration was utilized with a CO_2 methanation catalyst bed positioned between two CO methanation catalyst beds. The configuration included a 50 mg 5%La-10%Ni/γ-Al_2O_3, followed by a 50 mg 1.7%Mn-15%Ni/γ-Al_2O_3, and another 50 mg 5%La-10%Ni/γ-Al_2O_3 catalyst beds. This three-bed configuration was tested at 350 ºC, 400 ºC, and 450 ºC under a feed gas flow with an H_2/CO ratio of 2 and an H_2O/CO ratio of 1/3. Additionally, one-bed configurations of 150 mg 5%La-10%Ni/γ-Al_2O_3, 150 mg 1.7%Mn-15%Ni/γ-Al_2O_3, and 150 mg 15% Ni/γ-Al_2O_3 catalysts were tested separately for the identical conditions to enable comparative analysis with the three-bed configuration. Figures

4.29 and 4.30 illustrate that the three-bed configuration did not demonstrate any superior performance in terms of CO conversion and CH_4 yield. Best CO conversion performance was exhibited by one-bed 150 mg 1.7%Mn-15%Ni/γ- Al_2O_3 configuration at 350 ºC (ca. 99%).

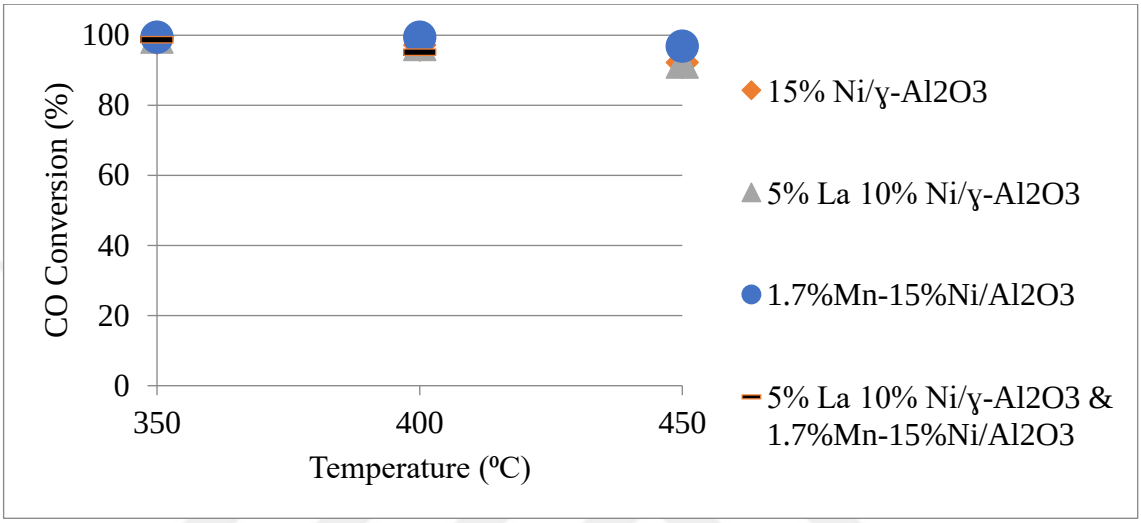

Figure 4.29. Average CO conversion values for 6-hour performance tests conducted with $H_2/CO=2$ on one-bed 150 mg 15% Ni/γ-Al_2O_3, one-bed 150 mg 5%La-10%Ni/γ-Al_2O_3, one-bed 150 mg 1.7%Mn-15%Ni/γ-Al_2O_3, and three-bed 50 mg 5%La-10%Ni/γ-Al_2O_3 & 50 mg 1.7%Mn-15%Ni/γ-Al_2O_3 & 50 mg 5%La-10%Ni/γ-Al_2O_3 configurations.

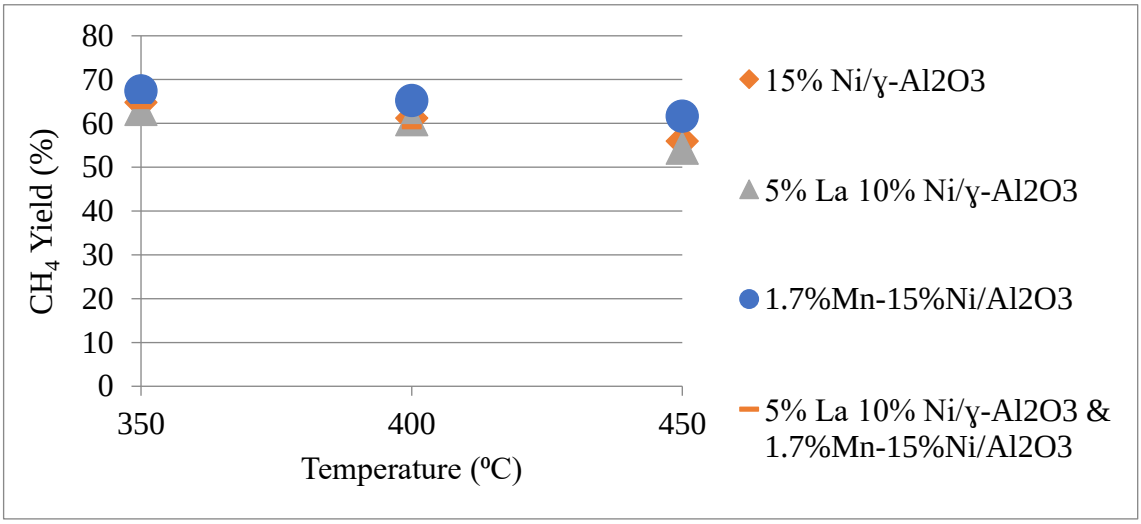

Figure 4.30. Average CH_4 yield values for 6-hour performance tests conducted with $H_2/CO=2$ on one-bed 150 mg 15% Ni/γ-Al_2O_3, one-bed 150 mg 5%La-10%Ni/γ-Al_2O_3, one-bed 150 mg 1.7%Mn-15%Ni/γ-Al_2O_3, and three-bed 50 mg 5%La-10%Ni/γ-Al_2O_3 & 50 mg 1.7%Mn-15%Ni/γ-Al_2O_3 & 50 mg 5%La-10%Ni/γ-Al_2O_3 configurations.

4.3. Incorporating Bifunctionality by Combining WGS and Methanation Reactions in One Catalyst

Due to the lack of improvement in CH_4 production performance by using physical WGS and methanation catalyst mixtures or sequential methanation catalyst beds, the WGS and methanation reactions were integrated into a single bifunctional catalyst. The prepared bimetallic catalysts were tested for three different H_2/CO ratios at five different temperatures. The reactions in this section of the study were conducted on 75 mg catalysts.

4.3.1. Effect of H_2/CO Ratio

CO methanation reactions were conducted on all catalysts at 400 °C for three H_2/CO ratios of 3, 2, and 1, while the H_2O/CO ratio was maintained at 1/3. Average conversion values for 6-hour experiments with error bars indicating the maximum and minimum values are presented in Figure 4.31. Corresponding yield values are given in Figure 4.32.

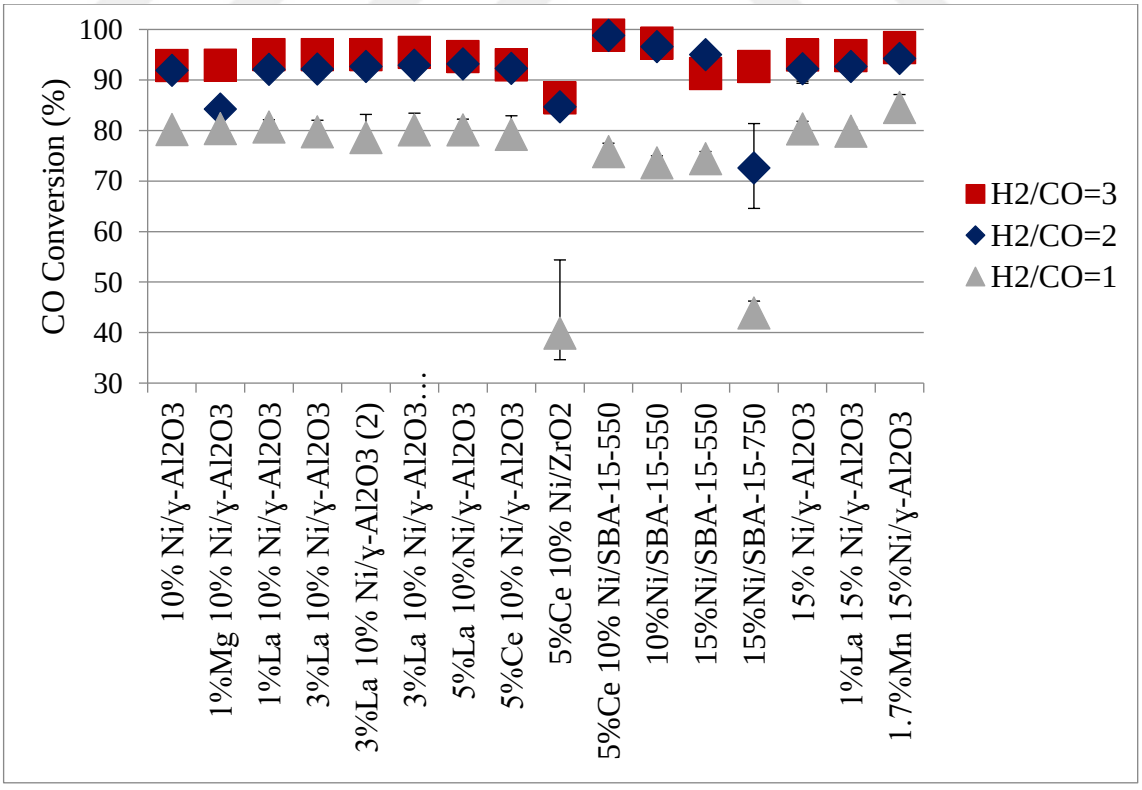

Figure 4.31. Average CO conversion values for 6-hour experiments conducted at 400 ºC for three H_2/CO ratios of 3, 2, and 1, with error bars indicating the maximum and minimum values.

At 400 °C, for H_2/CO=3, all catalysts, except 5%Ce-10%Ni/ZrO_2, exhibited similar CO conversion performances (ca. 93 to ca. 99%). The highest conversion performance was observed for 5%Ce-10%Ni/SBA-15-550 (98.8%), while the lowest CO methanation value was recorded for 5%Ce-10%Ni/ZrO_2 (86.5%) (Figure 4.31). Similarly, the highest CH_4 yield was achieved with 5%Ce-10%Ni/SBA-15-550 (74.6%), whereas the lowest yield was observed with 5%Ce-10%Ni/ZrO_2 (61.3%) (Figure 4.32).

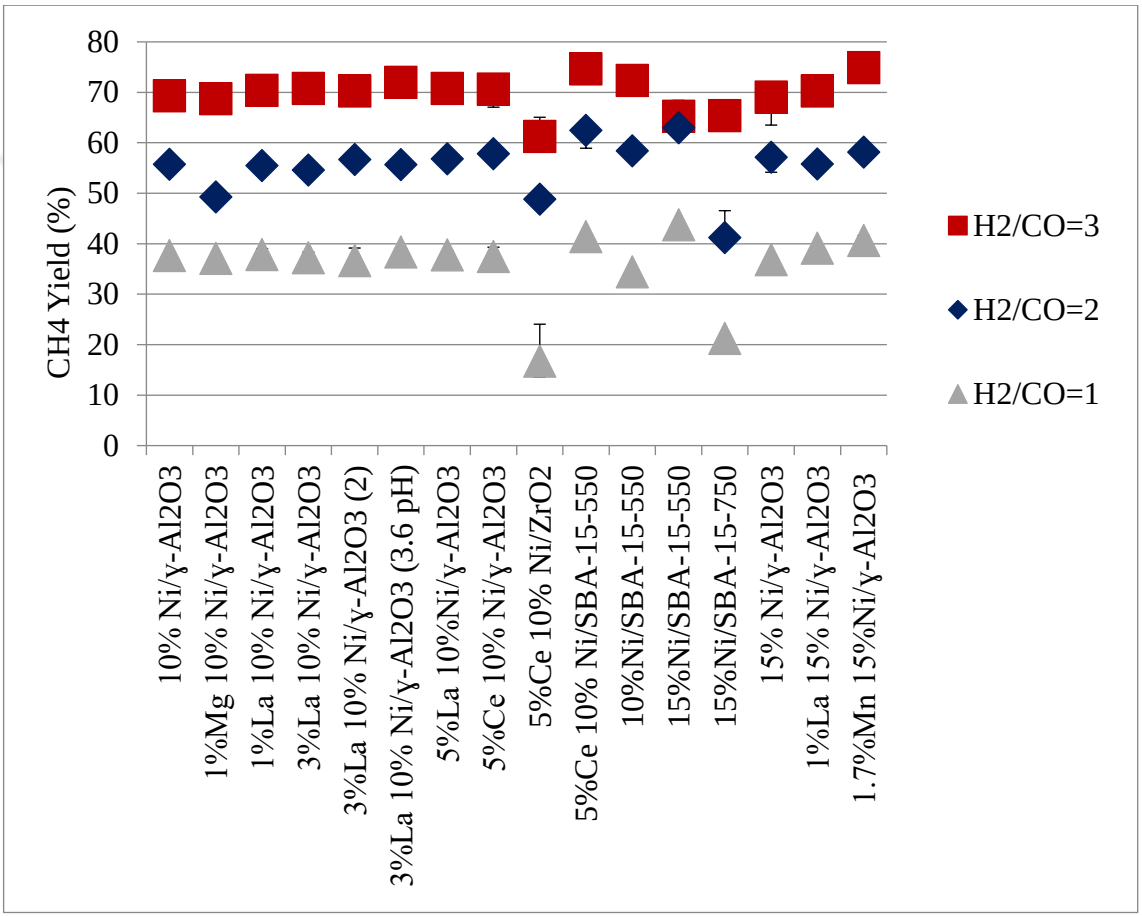

Figure 4.32. Average CH_4 yield values for 6-hour experiments conducted at 400 ºC for three H_2/CO ratios of 3, 2, and 1, with error bars indicating the maximum and minimum values.

When H_2/CO ratio was reduced to 2, CO conversion of 1%Mg-10%Ni/γ-Al_2O_3 decreased from %92.9 to 84.2%, while for 15% Ni/SBA-15-750 conversion value dropped from %92.7 to %72.6. However, the CO conversion values for the other catalysts did not exhibit significant changes when the H_2/CO ratio was decreased from 3 to 2. At this ratio, the highest conversion performance was observed for 5%Ce-10%Ni/SBA-15-550 (98.8%),

while the lowest CO methanation value was recorded for 15% Ni/SBA-15-750 (72.6%) (Figure 4.31). However, when the H_2/CO ratio was lowered to 1, both CO conversion and CH_4 yield values decreased for all catalysts (Figure 4.32).

For H_2/CO of 1, 1.7%Mn-15%Ni/γ-Al_2O_3 exhibited the highest conversion performance (84.6%), while the lowest CO methanation value was recorded for 5%Ce-10%Ni/ZrO_2 (39.9%) (Figure 4.31). Furthermore, the maximum CH_4 yield was obtained with 15% Ni/SBA-15-550 (43.8%), whereas the lowest yield was observed with 5%Ce-10%Ni/ZrO_2 (16.8%) (Figure 4.32).

4.3.2. Effect of H_2O/CO Ratio

In order to examine the effect of H_2O/CO ratio, performance tests were conducted for three different H_2O/CO ratios while maintaining a constant H_2/CO ratio of 1 on 15% Ni/ɣ-Al_2O_3 at 400 °C (Figure 4.20).

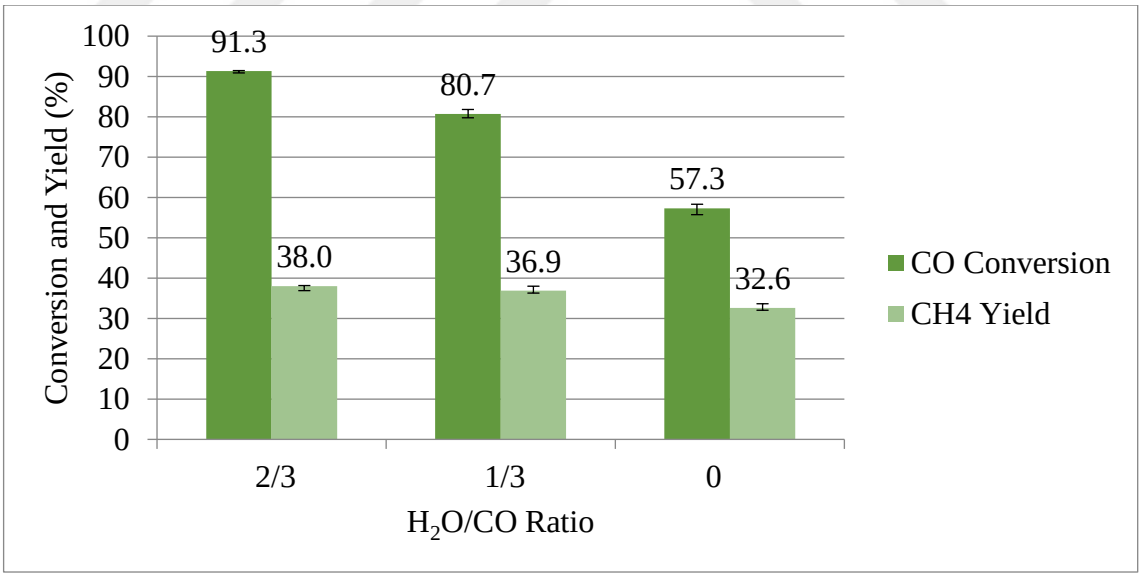

Figure 4.33. Average CO conversion and CH_4 yield values for 6-hour experiments conducted at 400 ºC for three H_2O/CO ratios of 2/3, 1/3, and 0, with error bars indicating the maximum and minimum values.

When H_2O/CO=0, CO conversion and CH_4 yield values were recorded as 57.3% and 32.6%, respectively. For H_2O/CO ratios of 1/3 and 2/3, CO conversion increased to 80.7%

and 91.3%, respectively. However, increase in the CH_4 yield amounts were very small compared to CO conversion values (Figure 4.20). The findings suggest that increasing the steam amount in the feed stream enhances the CO conversion. However, the additional CO reacted did not convert into CH_4 but into other side products such as CO_2 (Figure 4.33).

4.3.3. Effect of Temperature

In order to see the effect of temperature, 6 hour performance tests were conducted with H_2/CO ratio of 3 at 5 different temperatures: 200 °C , 250 °C, 300 °C, 350 °C, and 400 °C. H_2O/CO ratio of 1/3 was chosen for these experiments. CO conversion and CH_4 yield values at 400 °C were presented and discussed in a detailed fashion in Section 4.3.1. When the reaction temperature was reduced to 350 °C, the CO conversion and CH_4 yield of the 15% Ni/SBA-15-750 catalyst decreased from 92.7% to 45.2% (Figure 4.32), and from 65.6% to 25% (Figure 4.33), respectively. While these changes occurred in the performance of the 15% Ni/SBA-15-750 catalyst, the performance of the other catalysts remained consistent, with their CO conversion and CH_4 yield values similar to those observed at 400°C. At a reduced reaction temperature of 300 °C, both the 10% Ni/SBA-15 and 15% Ni/SBA-15-750 catalysts demonstrated the worst conversion and yield values while the performance of the other catalysts remained relatively stable. At this temperature, conversion for 15% Ni/SBA-15-750 was found to be 36.6%, whereas 10% Ni/SBA-15 exhibited 7% conversion (Figure 4.34). However, upon further decreasing the temperature to 250 °C, only six out of the remaining fourteen catalysts exhibited CO conversion performances (Figures 4.34). The list of these catalysts can be found in Table 4.6.

Table 4.6. Catalysts selected for further testing at 250 °C.

CATALYSTS
3%La-10%Ni/ɣ-Al_2O_3
5%La-10%Ni/ɣ-Al_2O_3
5%Ce-10%Ni/ɣ-Al_2O_3
5%Ce-10%Ni/ZrO_2
5%Ce-10%Ni/SBA-15-550
1.7%Mn-15%Ni/ɣ-Al_2O_3

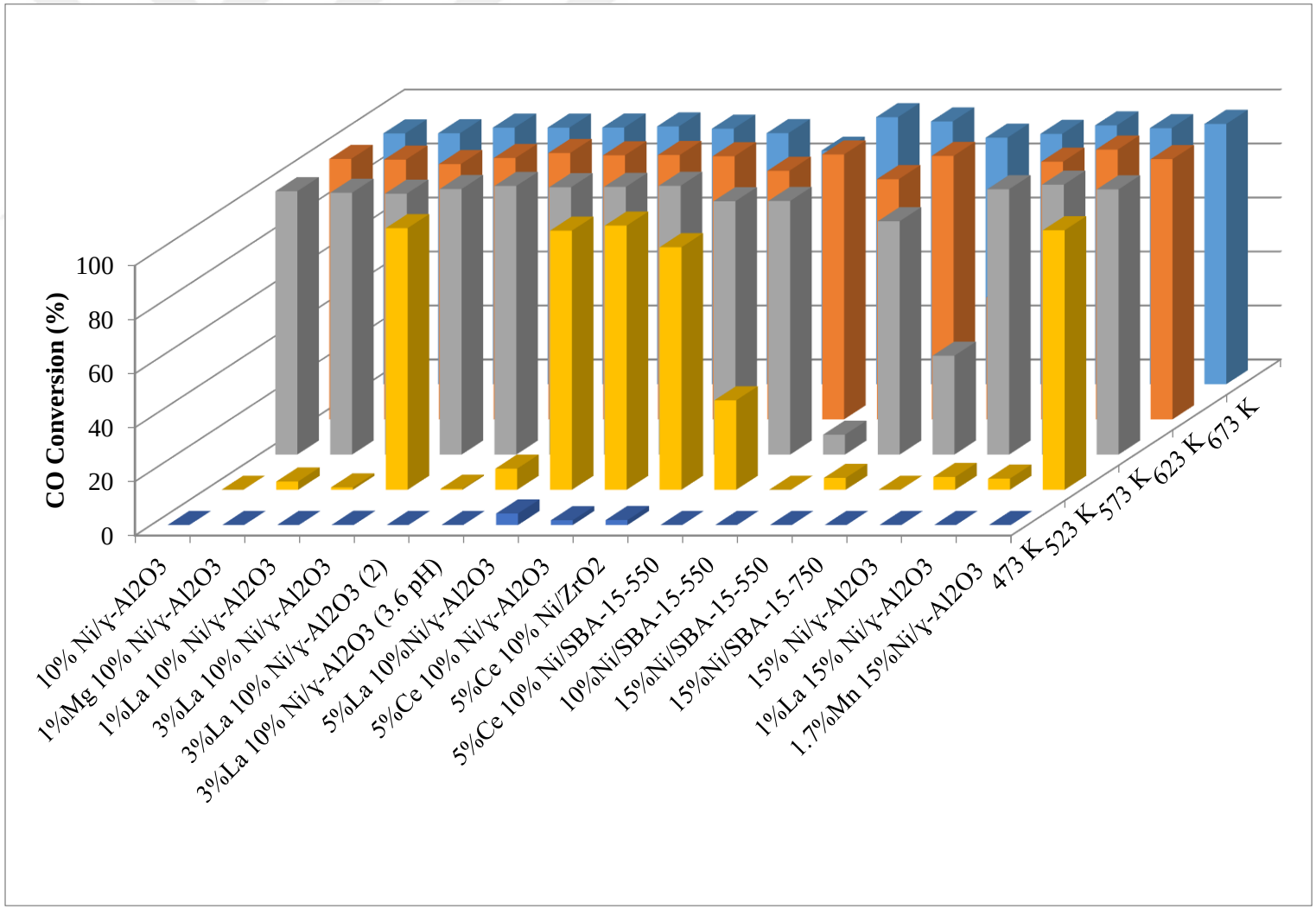

Figure 4.34. Average CO conversion values for 6-hour performance tests conducted with $H_2/CO=3$ at 5 different temperatures for all catalysts.

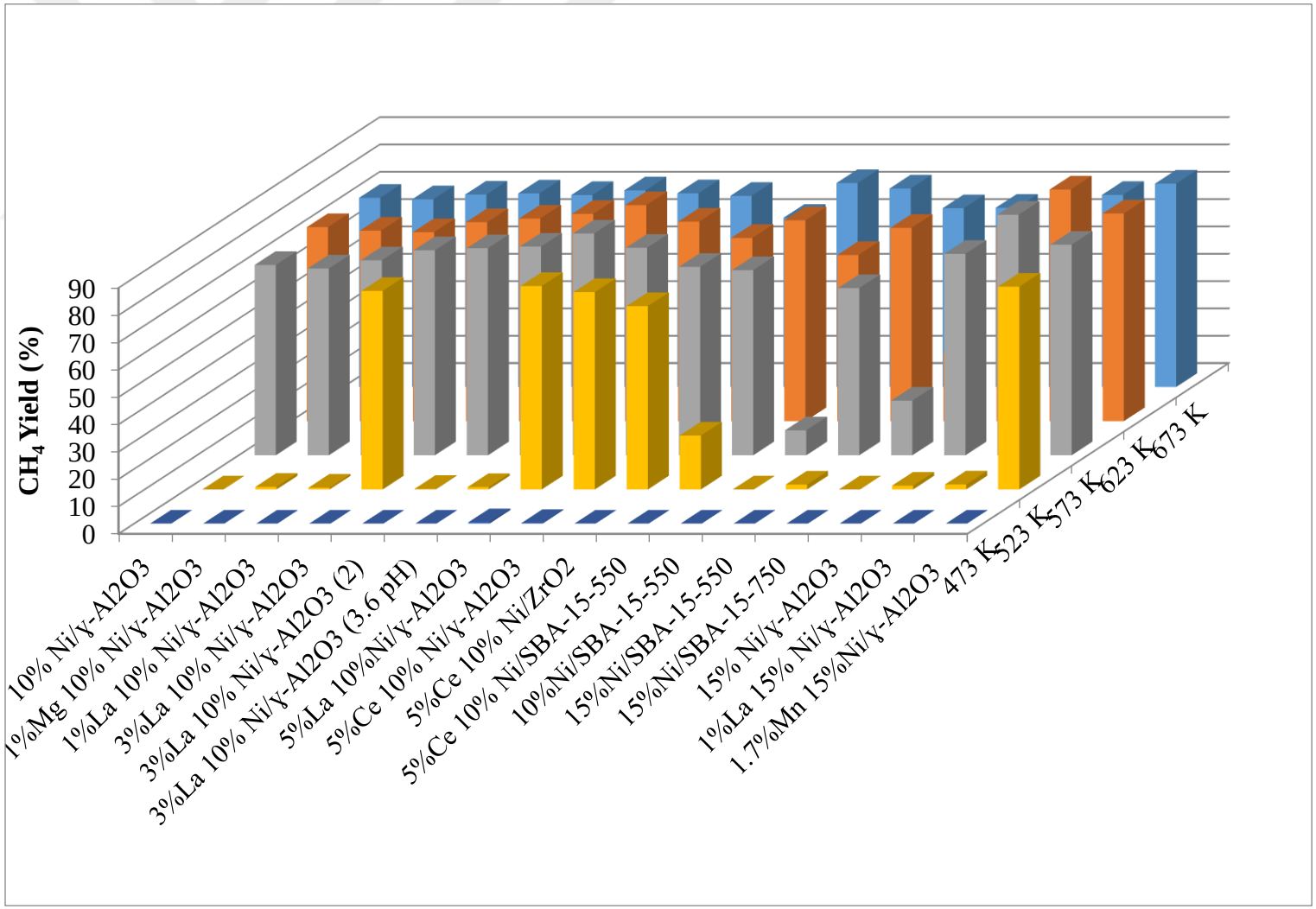

Figure 4.35. Average CH_4 yield values for 6-hour performance tests conducted with $H_2/CO=3$ at 5 different temperatures for all catalysts.

These six catalysts (Table 4.6) were further tested at 250 °C with an H_2/CO feed ratio of 2, and H_2O/CO ratio of 1/3. 5%Ce-10%Ni/γ-Al_2O_3 was found to be the only catalyst active at this temperature, exhibiting good catalytical activity and stability (Figure 4.36).

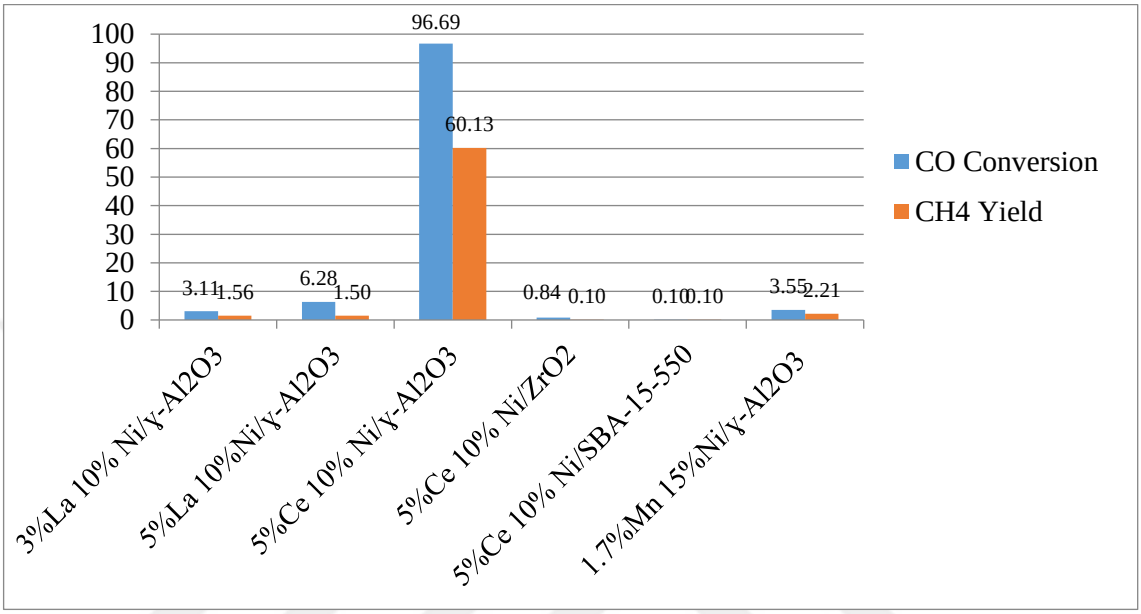

Figure 4.36. Average CO conversion and CH_4 yield values for 6-hour performance tests conducted with H_2/CO=2 at 250 ºC for 3%La-10%Ni/ɣ-Al_2O_3, 5%La-10%Ni/ɣ-Al_2O_3, 5%Ce-10%Ni/ɣ-Al_2O_3, 5%Ce-10%Ni/ZrO_2, 5%Ce-10%Ni/SBA-15-550, and, 1.7%Mn-10%Ni/ɣ-Al_2O_3.

In order to observe the performance difference between the catalysts at 250 °C, the amount of catalyst used in the experiments was reduced, and all sixteen sets of catalysts were tested for an H_2/CO feed ratio of 2.

4.3.4. Effect of Catalyst Weight at 250 ºC

To observe the performance differences between the catalysts at 250 °C, the catalyst amount used in the experiments was decreased to 15 mg and mixed with quartz particles to maintain the catalyst bed volume and eliminate hot spots. Decreasing the catalyst amount decreased the W/F ratio to 0.0025 g*h/L. Methanation reactions were performed with a H_2/CO feed ratio of 2 and a H_2O/CO ratio of 1/3. This time it was easier to see the performance difference between the catalysts. Specifically, the best conversion (89.6%) and yield (52.8%) results were obtained over 5%Ce-10%Ni/γ-Al_2O_3. The conversion and yield

values for experiments conducted with W/F=0.0025 g*h/L can be found in Figures 4.37 and 4.38, respectively.

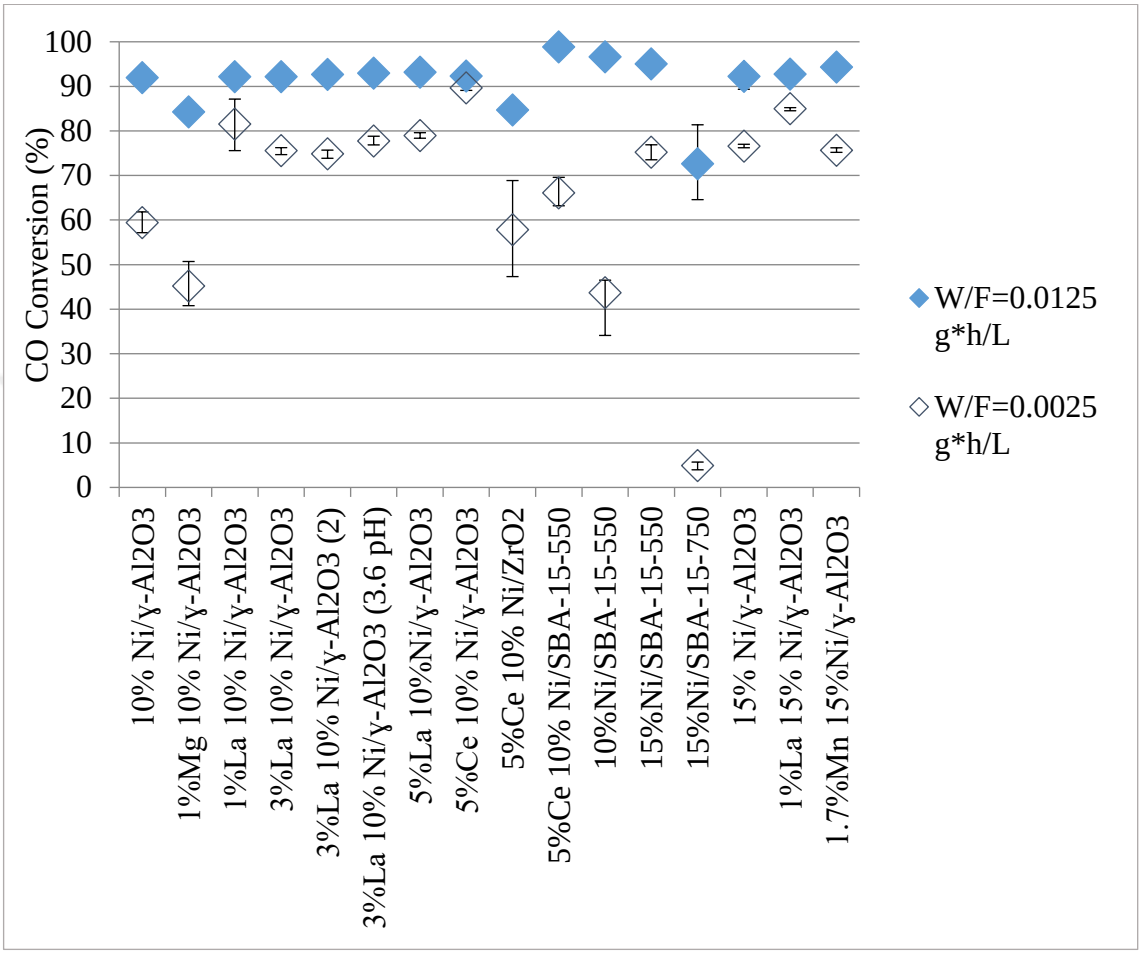

Figure 4.37. Average CO conversion values for 6-hour performance tests conducted with H_2/CO=2 at 250 ºC on all catalysts at two different W/F ratios: 0.0125 g*h/L and 0.0025 g*h/L.

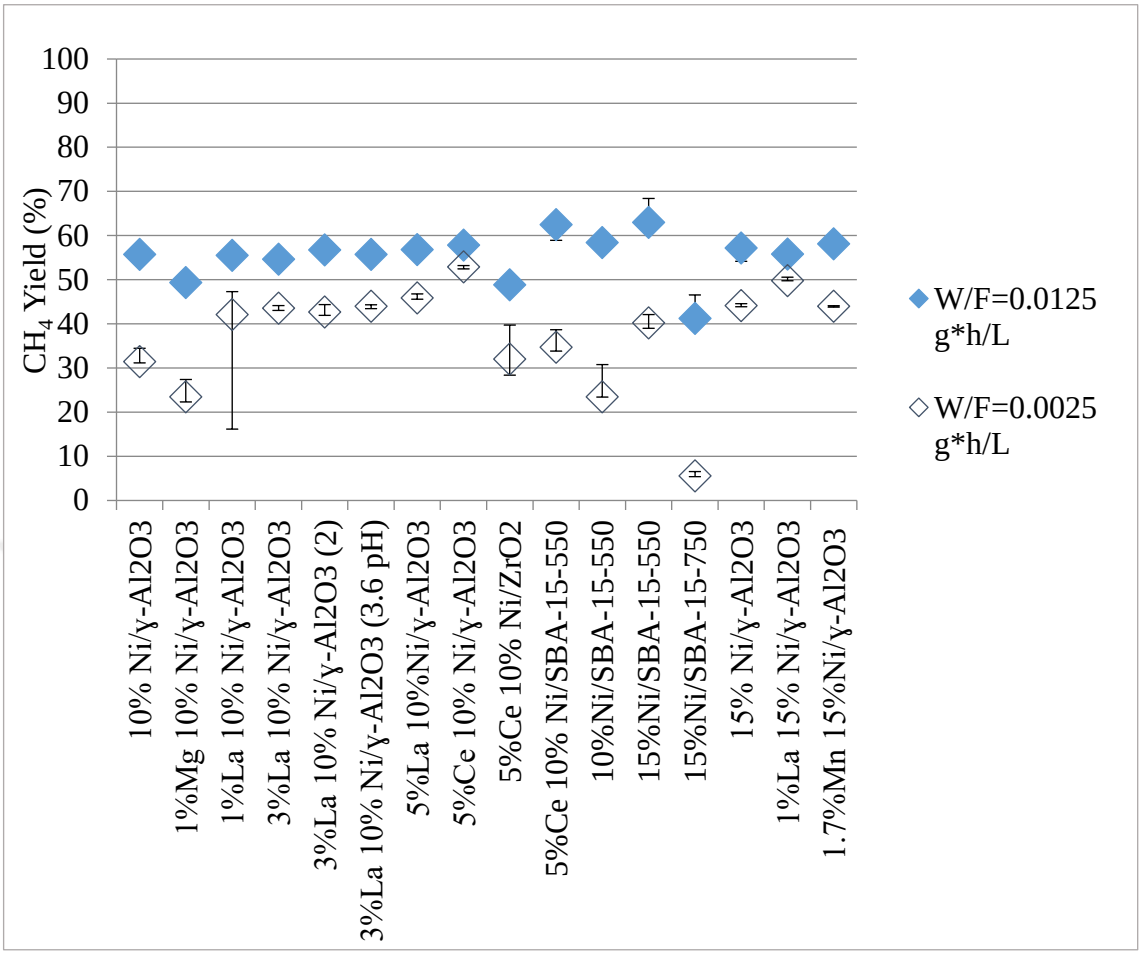

Figure 4.38. Average CH_4 yield values for 6-hour performance tests conducted with $H_2/CO=2$ at 250 ºC on all catalysts at two different W/F ratios: 0.0125 g*h/L and 0.0025 g*h/L.

4.3.5. Stability Tests on 5%Ce-10%Ni/γ-Al_2O_3

After confirming the superiority of 5%Ce-10%Ni/γ-Al_2O_3 catalyst at low temperatures with low H_2/CO ratios, the stability of the catalyst was tested. In all stability tests, H_2O/CO ratios were kept at 1/3. First stability test on the catalyst was performed at 400 °C with an H_2/CO ratio of 3 for 72 hours. Catalyst remained stable throughout the 72 hours with a CO conversion of ca. 94% (Figure 4.39), and CH_4 yield of ca. 70% (Figure 4.40).

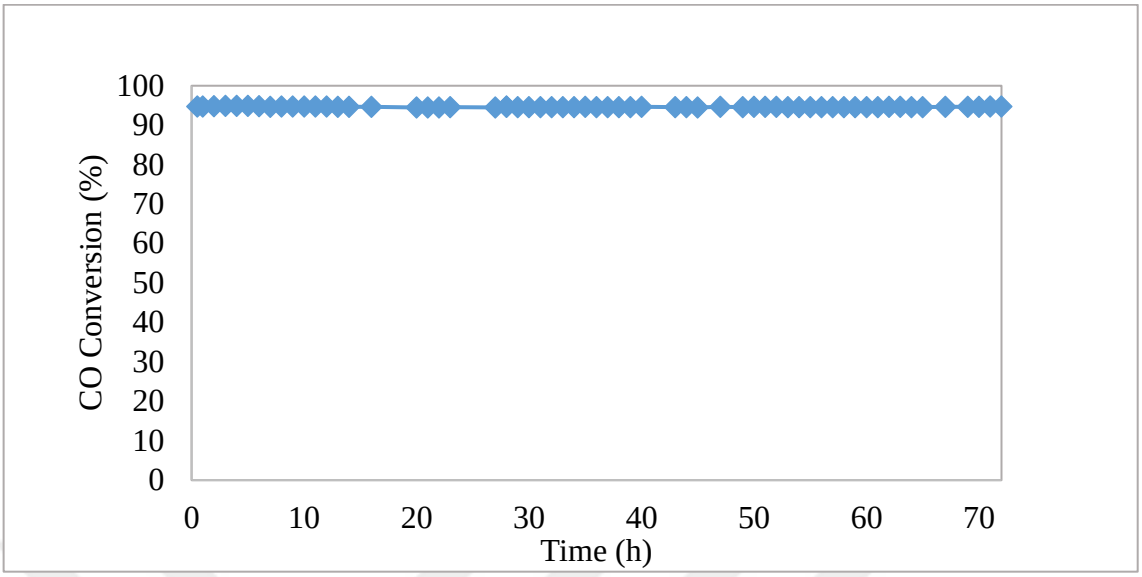

Figure 4.39. Conversion results of the stability test conducted on 5%Ce-10%Ni/γ-Al_2O_3 at 400 °C with an H_2/CO ratio of 3.

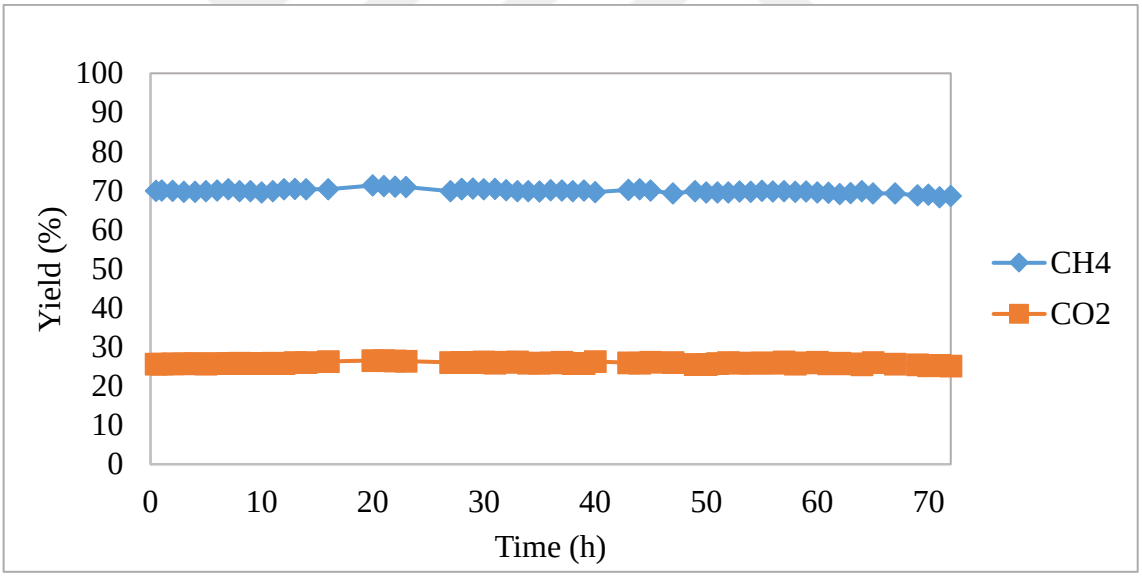

Figure 4.40. Yield results of the stability test conducted on 5%Ce-10%Ni/γ-Al_2O_3 at 400 °C with an H_2/CO ratio of 3.

A second stability test was conducted at the same temperature with a lower H_2/CO ratio of 2 for 72 hours, and once again, the catalyst demonstrated perfect stability. With this H_2/CO ratio, CO conversion was ca. 90% (Figure 4.41) while CH_4 yield was recorded as ca. 53% (Figure 4.42).

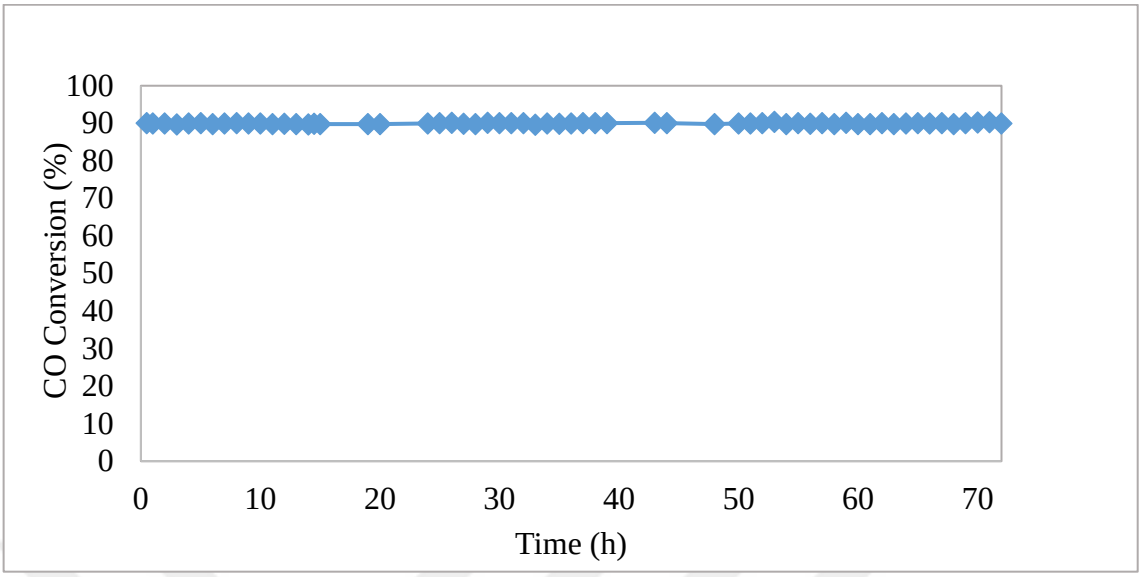

Figure 4.41. Conversion results of the stability test conducted on 5%Ce-10%Ni/γ-Al_2O_3 at 400 °C with an H_2/CO ratio of 2.

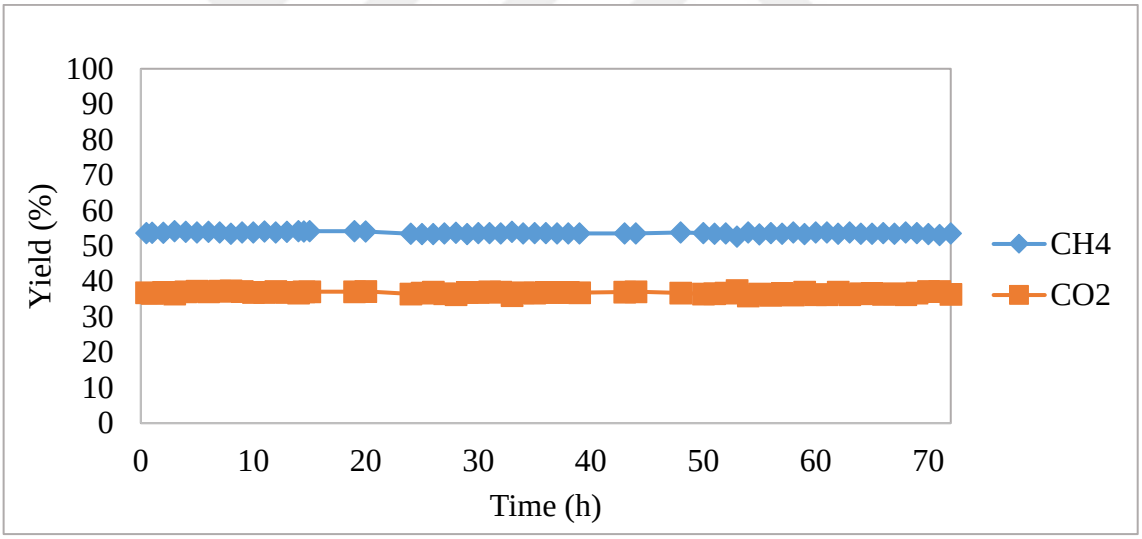

Figure 4.42. Yield results of the stability test conducted on 5%Ce-10%Ni/γ-Al_2O_3 at 400 °C with an H_2/CO ratio of 2.

The final stability experiment was conducted at 250 °C with an H_2/CO ratio of 2 for 72 hours. The reaction concluded with a 17% (from ca. 95% to ca. 79%) activity loss at the end of the experiment (Figure 4.43). Corresponding yield values can be found in Figure 4.44.

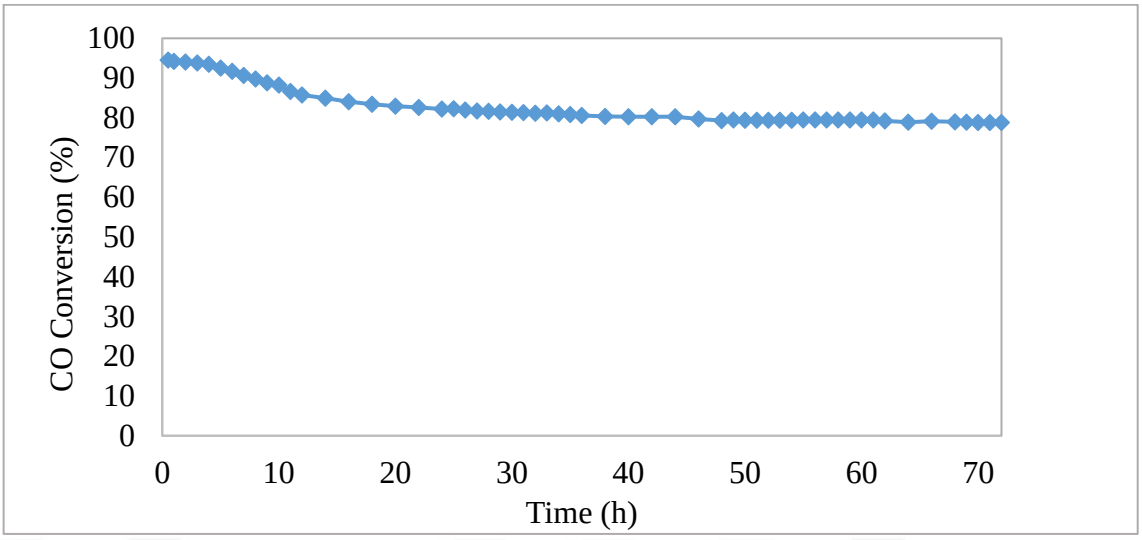

Figure 4.43. Conversion results of the stability test conducted on 5%Ce-10%Ni/γ-Al_2O_3 at 250 °C with an H_2/CO ratio of 2.

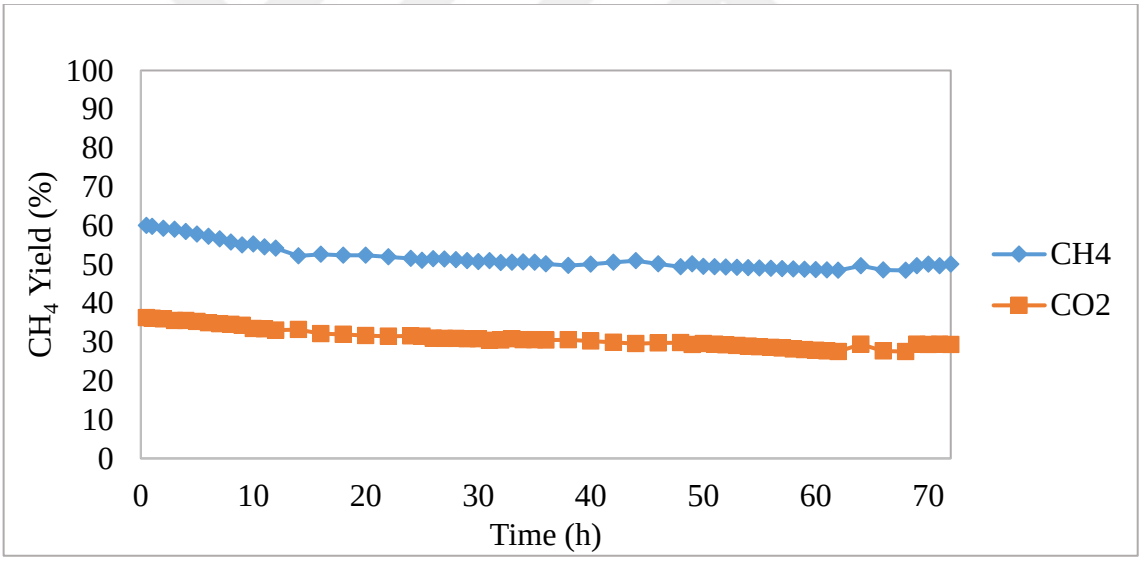

Figure 4.44. Yield results of the stability test conducted on 5%Ce-10%Ni/γ-Al_2O_3 at 250 °C with an H_2/CO ratio of 2.

4.4. Characterization of Ce-Ni Catalysts

4.4.1. XPS Analysis

The oxidation states of the metallic species present and the elemental composition of the catalyst surface were analyzed using XPS. Owing to the redox steps involved in the WGS and methanation reaction mechanisms, which significantly affect the oxidation states of

metal oxides, XPS is a crucial tool for evaluating the changes in these states throughout the reactions. This is achieved by analyzing the variances in the metallic species on the spent catalysts in contrast to those on freshly reduced samples. There, characteristic oxidation states of Ni were observed in the XPS spectra of the samples are comparatively analyzed.

General XPS spectra of all catalysts are presented in Figure 4.45. Absorption peaks were identified for Ni, O and C (Zhou and Shen, 2014). Figure 4.46 shows the Ni 2p3/2 spectra of freshly reduced and spent samples of 5%Ce-10%Ni/γ-Al_2O_3. The spent catalysts were tested at 400°C under a feed gas flow with an H_2/CO ratio of 2. The spectra revealed several distinct peaks indicative of different Ni species. The peak at 851.8 eV confirmed the presence of metallic Ni, while the peak around 853.4 eV corresponded to NiO. Additionally, a peak around 856 eV was associated with Ni^{2+} in octahedral coordination, typical of $NiAl_2O_4$ spinel-like species or possibly $Ni(OH)_2$ (Wang et al., 2011; Liu et al., 2018; Mebrahtu et al., 2019; Kim et al., 2020). Furthermore, a broad satellite peak at 862 eV was attributed to the rapid oxidation of small and active Ni particles when exposed to air (Wang et al., 2011).

All peaks observed on freshly reduced 5%Ce-10%Ni/γ-Al_2O_3 sample, although at slightly lower binding energies, were also observed for the freshly reduced 10% Ni/γ-Al_2O_3 catalyst (Figure 4.47). The introduction of Ce shifted the peaks to higher binding energy levels, indicating that more electronic cloud gathers around Ni atoms due to the redox process of Ce^{4+}/Ce^{3+} (Liu et al., 2018). The binding energy levels of the freshly reduced samples of both 5%Ce-10%Ni/γ-Al_2O_3 and 10% Ni/γ-Al_2O_3 catalyst can be found in Table 4.7.

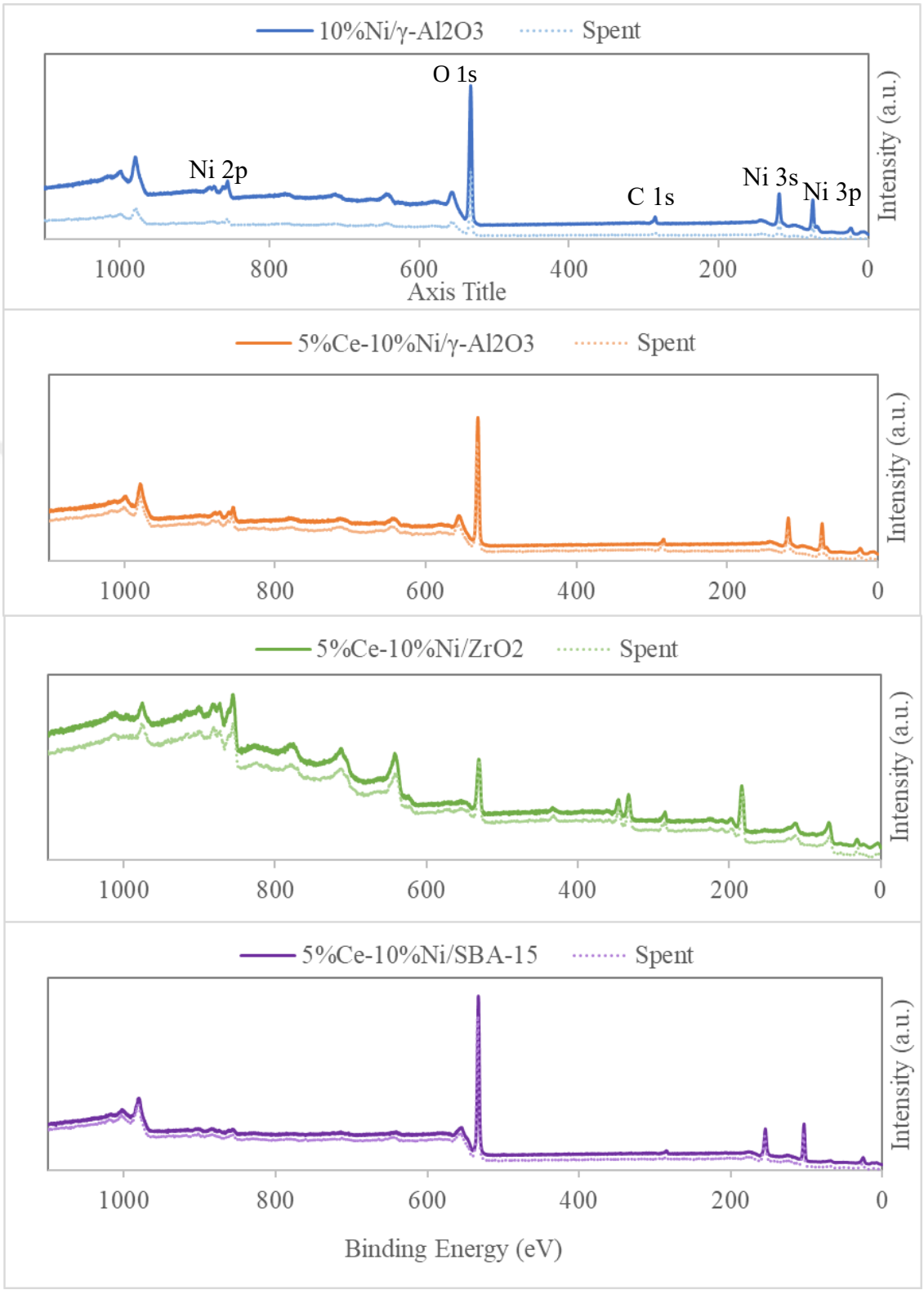

Figure 4.45. General XP Spectra of all freshly reduced and spent catalyst samples.

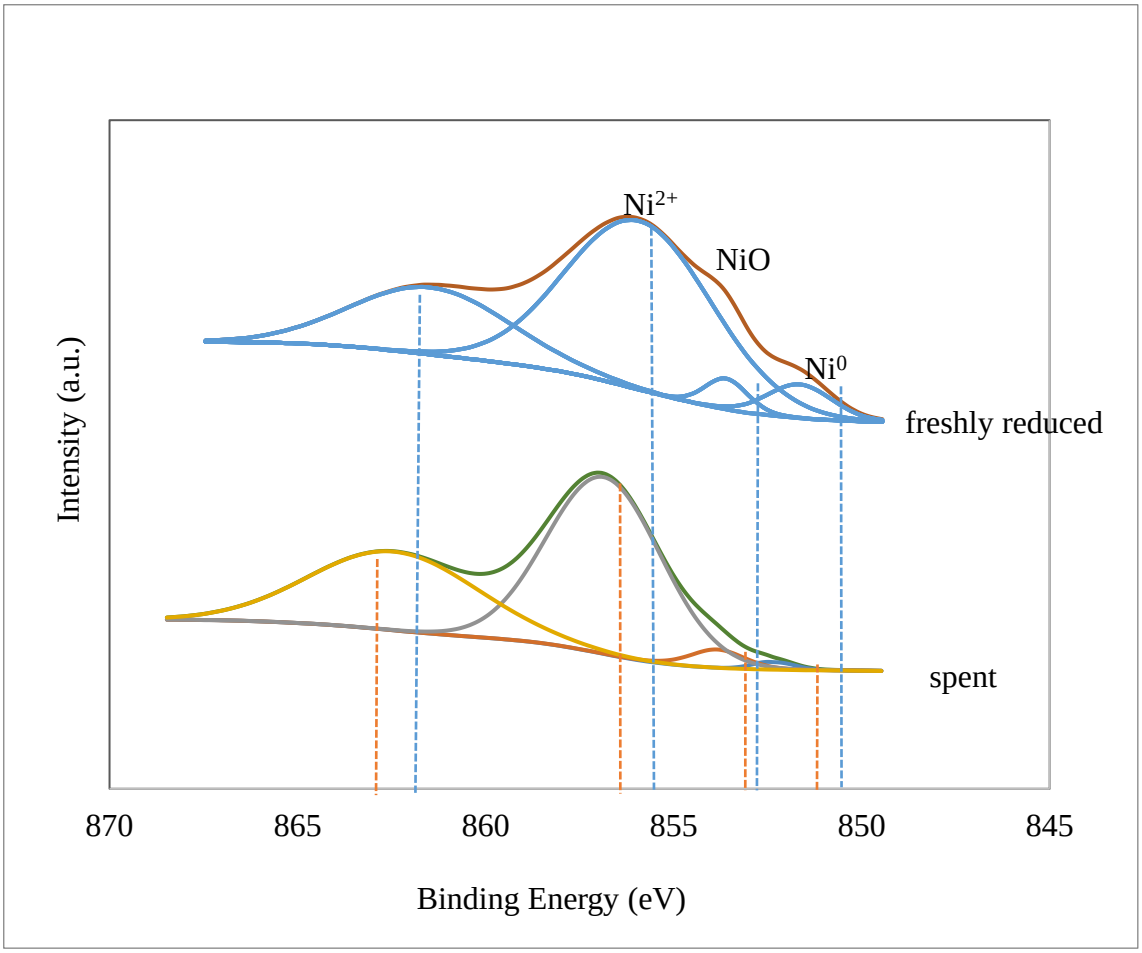

Figure 4.46. XP Spectra showing the Ni 2p3/2 region of freshly reduced and spent 5%Ce-10%Ni/γ-Al_2O_3 catalyst samples.

Table 4.7. Binding energy levels of Ni peaks on 10% Ni/γ-Al_2O_3 and 5%Ce-10%Ni/γ-Al_2O_3 catalyst sample.

Peak		**Binding Energy (eV)**	
		10% Ni/γ-Al_2O_3	**5%Ce-10%Ni/γ-Al_2O_3**
1	Ni^0	851.4	851.8
2	NiO	852.7	853.6
3	Ni^{2+}	855.7	855.9
4	Satellite	861.4	861.5

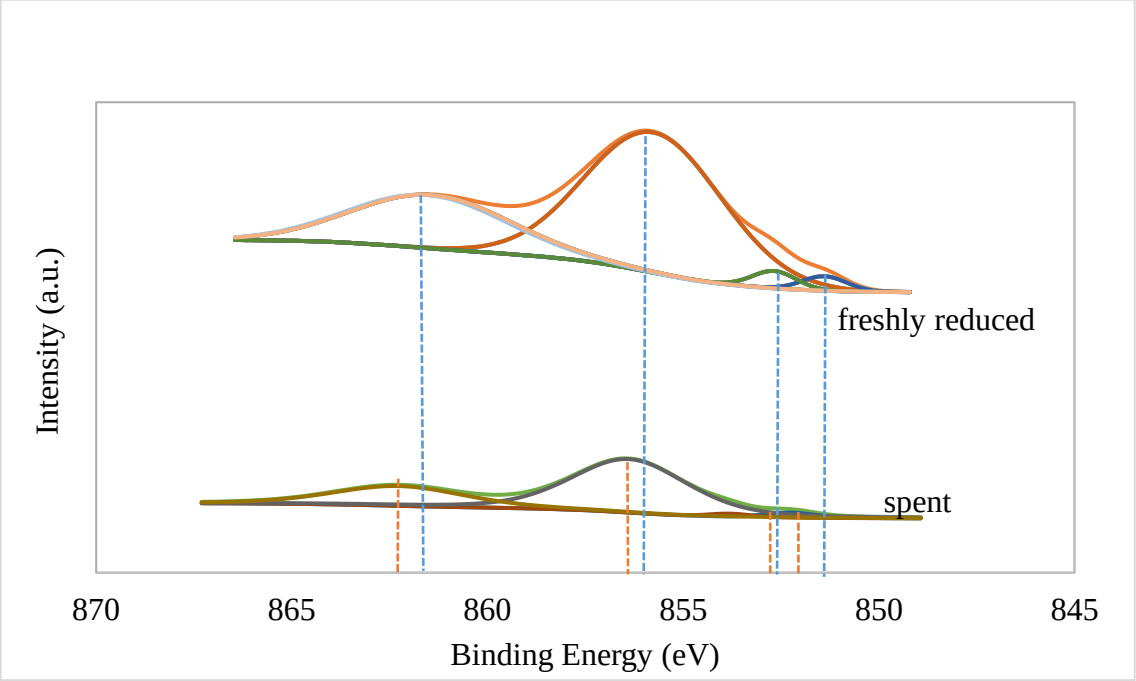

Figure 4.47. XP Spectra showing the Ni 2p3/2 region of freshly reduced and spent 10% Ni/γ-Al_2O_3 catalyst samples.

Similar Ni peaks observed on 5%Ce-10%Ni/ZrO_2 and 5%Ce-10%Ni/SBA-15-550 catalysts are presented in Figures 4.48 and 4.49. Binding energy levels of these peaks can be found in Table 4.8.

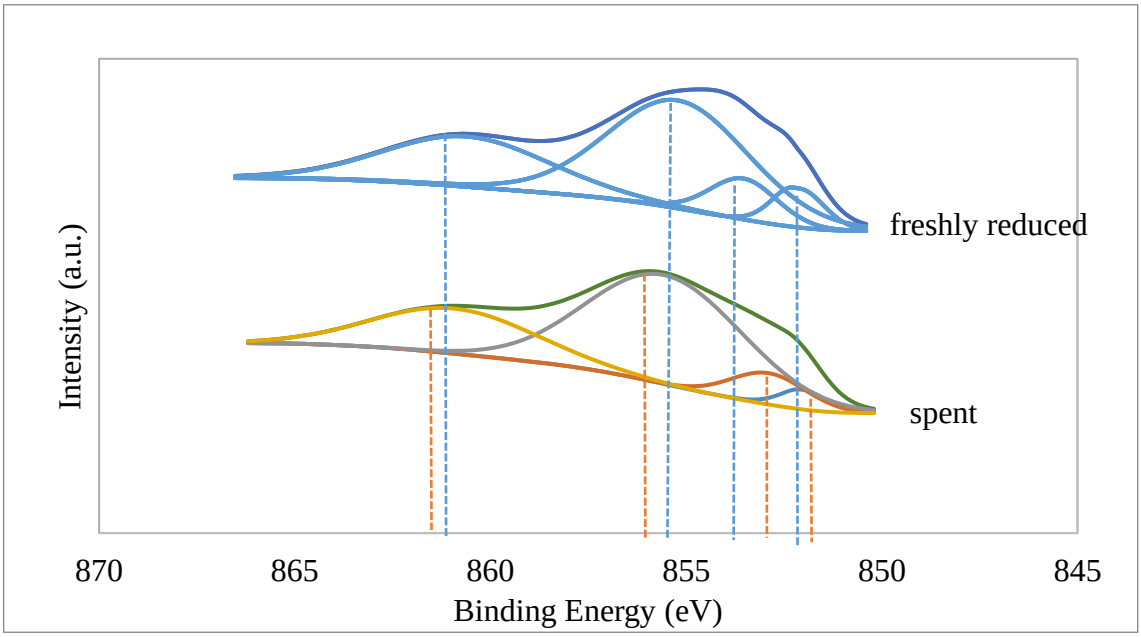

Figure 4.48. XP Spectra showing the Ni 2p3/2 region of freshly reduced and spent 5%Ce10%Ni/ZrO_2 catalyst samples.

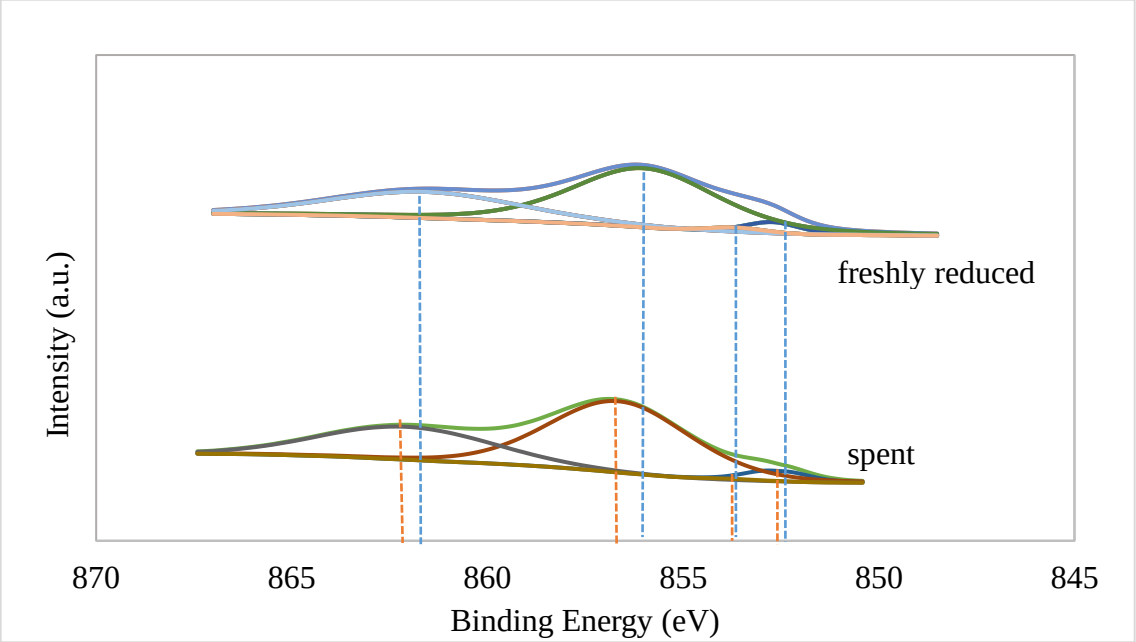

Figure 4.49. XP Spectra showing the Ni 2p3/2 region of freshly reduced and spent 5%Ce-10%Ni/SBA-15 catalyst samples.

Table 4.8. Binding energy levels of Ni peaks on 10% Ni/γ-Al_2O_3 and 5%Ce-10%Ni/γ-Al_2O_3 catalyst sample.

Peak		**Binding Energy (eV)**	
		5%Ce-10%Ni/ZrO_2	**5%Ce-10%Ni/SBA-15**
1	Ni^0	852.1	852.6
2	NiO	853.53	853.83
3	Ni^{2+}	855.2	856.56
4	Satellite	860.62	861.89

Comparing the Ni 2p3/2 spectra of freshly reduced and spent catalyst samples reveals a reduction in both metallic Ni and NiO percentages during the reaction across all catalysts (Table 4.9). However, this trend does not hold for Ni^{2+} content. The Ni^{2+} content decreases only for the 5%Ce-10%Ni/γ-Al_2O_3 catalyst, while it increases for all the other catalysts during the reaction. The decrease in Ni^{2+} content in the 5%Ce-10%Ni/γ-Al_2O_3 catalyst, as

opposed to the increase in other catalysts, can be attributed to several factors. These include the redox properties of Ce, surface hydroxylation effects, interactions with the support material, and electronic effects. The presence of Ce on the catalyst surface can significantly influence the amount and distribution of Ni^{2+} species, as well as the formation of different hydroxyl groups on the catalyst surface. Ce can dissociate water more effectively, which might reduce the formation of $Ni(OH)_2$ (Mebrahtu et al., 2019). This effect might vary with different supports. For instance, ZrO_2 and SBA-15 might interact differently with Ce and Ni, affecting the $Ni(OH)_2$ content.

Table 4.9. Ni^0, NiO and Ni^{2+} contents (%) of freshly reduced and spent catalysts.

Catalyst	Ni^0 (%)		NiO (%)		Ni^{2+} (%)	
	Freshly Reduced	Spent	Freshly Reduced	Spent	Freshly Reduced	Spent
5%Ce-10%Ni/γ-Al_2O_3	5.87	0.93	3.53	3.10	63.40	58.17
10% Ni/γ-Al_2O_3	2.23	2.43	2.62	1.19	66.02	67.82
5%Ce-10%Ni/ZrO_2	7.23	3.61	9.84	8.54	53.73	61.39
5%Ce-10%Ni/SBA-15	8.48	3.13	3.12	0.85	57.38	61.15

4.4.2. XRD Analysis

X-ray diffraction (XRD) patterns of the catalyst samples were acquired by using an X-ray generator with Cu target and scan speed of 2°/min. XRD spectra of freshly reduced 10% Ni/γ-Al_2O_3, 5%Ce-10%Ni/γ-Al_2O_3, 5%Ce-10%Ni/ZrO_2, and 5%Ce-10%Ni/SBA-15 samples are presented in Figure 4.50.

For the reduced 10% Ni/γ-Al_2O_3 and 5%Ce-10%Ni/γ-Al_2O_3 catalyst samples, both $NiAl_2O_4$ (PDF 01-1299) and NiO (PDF 75-0921) were observed on the XRD patterns. However, these two phases were not definitively distinguished by their diffraction features due to overlapping diffraction lines of γ-Al_2O_3 (PDF 75-0921). The XRD patterns of the reduced catalysts clearly showed the presence of metallic nickel, Ni^0 (PDF 70-1849). The decrease in the NiO diffraction peak with the addition of Ce suggested several possibilities: Ni^0 might have been more dispersed on the Ce-promoted catalysts, forming smaller particles;

Ce might have facilitated the reduction of NiO to Ni^0; or the synthesis and reduction conditions might have favored the transformation of NiO into another phase such as $NiAl_2O_4$. Additionally, the slightly sharper and more defined Niº peak on the Ce-promoted catalyst indicated better crystallization or larger crystallite sizes of Ni. Therefore, it seemed likely that some of the NiO had been reduced to Ni^0, contributing to the sharper Ni^0 peaks observed. For the 5%Ce-10%Ni/γ-Al_2O_3 catalyst sample, fluorite cubic phase CeO_2 (PDF 34-0394) peaks were visible on the XRD patterns (Figure 4.51) (Zhang et al., 2022).

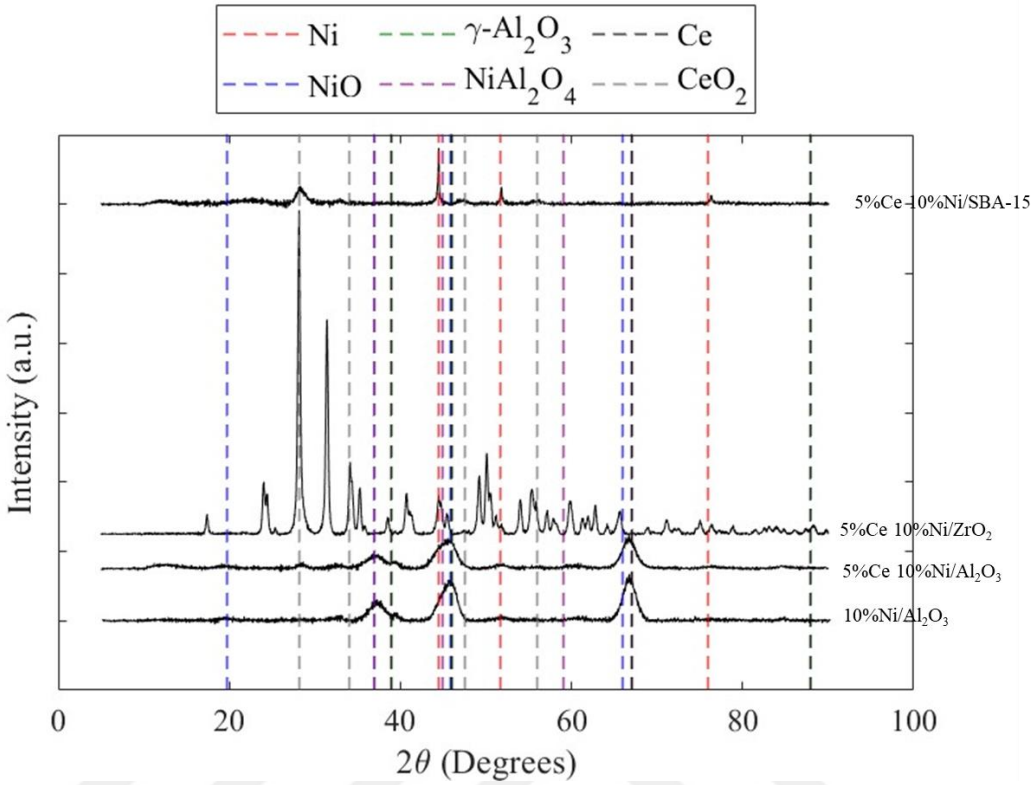

Figure 4.50. XRD profiles of freshly reduced 10%Ni/γ-Al_2O_3, 5%Ce-10%Ni/γ-Al_2O_3, 5%Ce-10%Ni/ZrO_2, and 5%Ce-10%Ni/SBA-15 samples.

The ZrO_2-supported 5%Ce-10%Ni/ZrO_2 catalyst, prepared according to the method described in the Experimental section, exhibited typical characteristics of ZrO_2 (PDF 65-1022) material. Metallic Ni (PDF 70-1849) peaks were observed in the powder XRD spectra of the 5%Ce-10%Ni/ZrO_2 and 5%Ce-10%Ni/SBA-15 catalysts. However, CeO_2 (PDF 34-0394) peaks were not observable in the ZrO_2-supported catalysts due to their overlapping with ZrO_2 peaks (Figure 4.52).

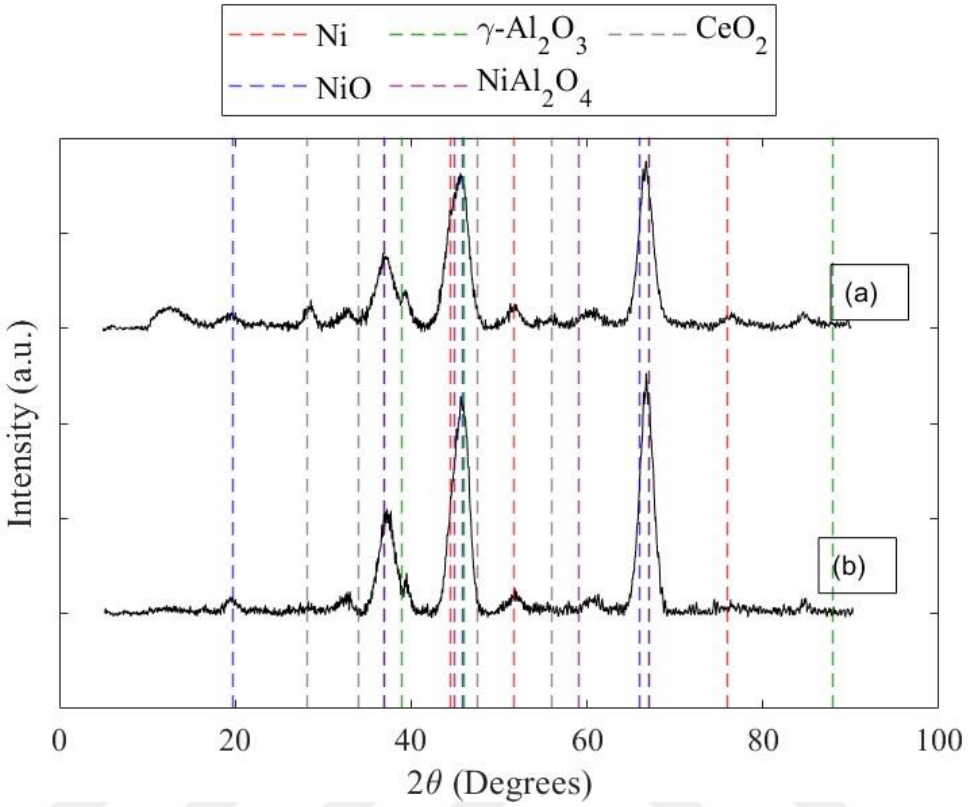

Figure 4.51. XRD profiles of freshly reduced 5%Ce-10%Ni/γ-Al_2O_3 (a), and 10% Ni/γ-Al_2O_3 (b).

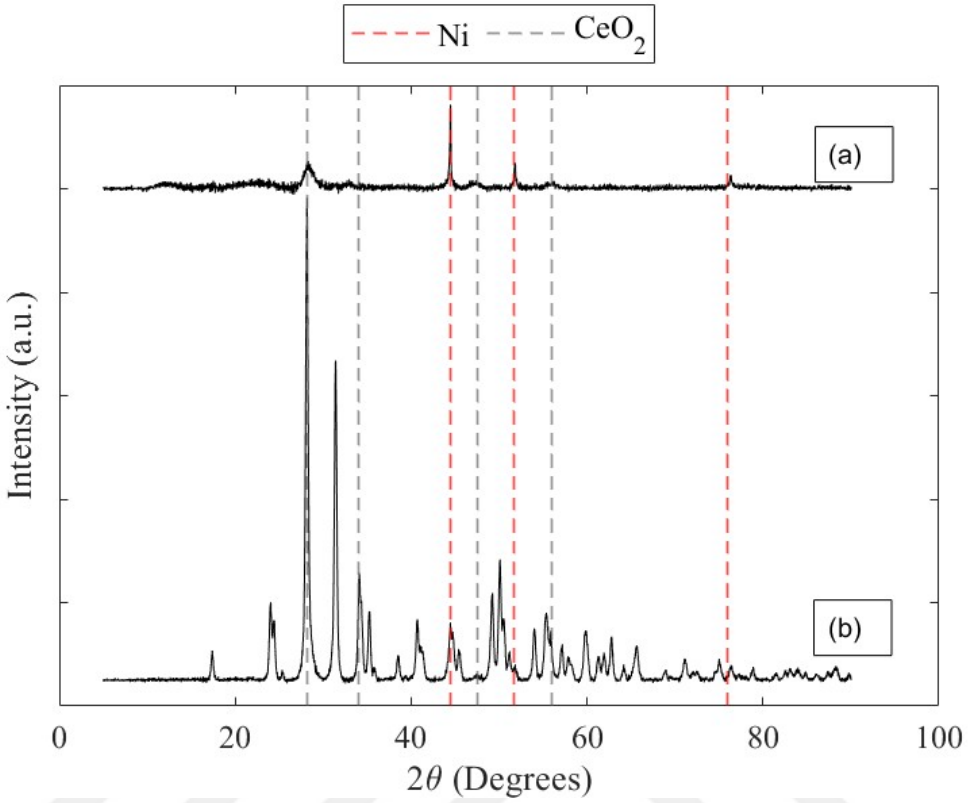

Figure 4.52. XRD profiles of freshly reduced 5%Ce-10%Ni/SBA-15 (a), and 5%Ce-10%Ni/ZrO_2 (b) samples.

Figure 4.53 presents the XRD spectra of three spent 5%Ce-10%Ni/γ-Al_2O_3 samples tested under different conditions: feed containing an H_2/CO ratio of 2 at 250 °C for 72 hours, feed containing an H_2/CO ratio of 2 at 400 °C for 6 hours, and feed containing an H_2/CO ratio of 3 at 400 °C for 72 hours. However, no significant differences were observed between those three spectra. The only noticeable difference was that the $NiAl_2O_4$ peaks were slightly more pronounced in the samples exposed to 72-hour stability tests. The increased prominence of $NiAl_2O_4$ peaks in the samples exposed to 72-hour stability test suggests that prolonged exposure, even at 250°C, facilitates the gradual formation of $NiAl_2O_4$ from NiO and Al_2O_3.

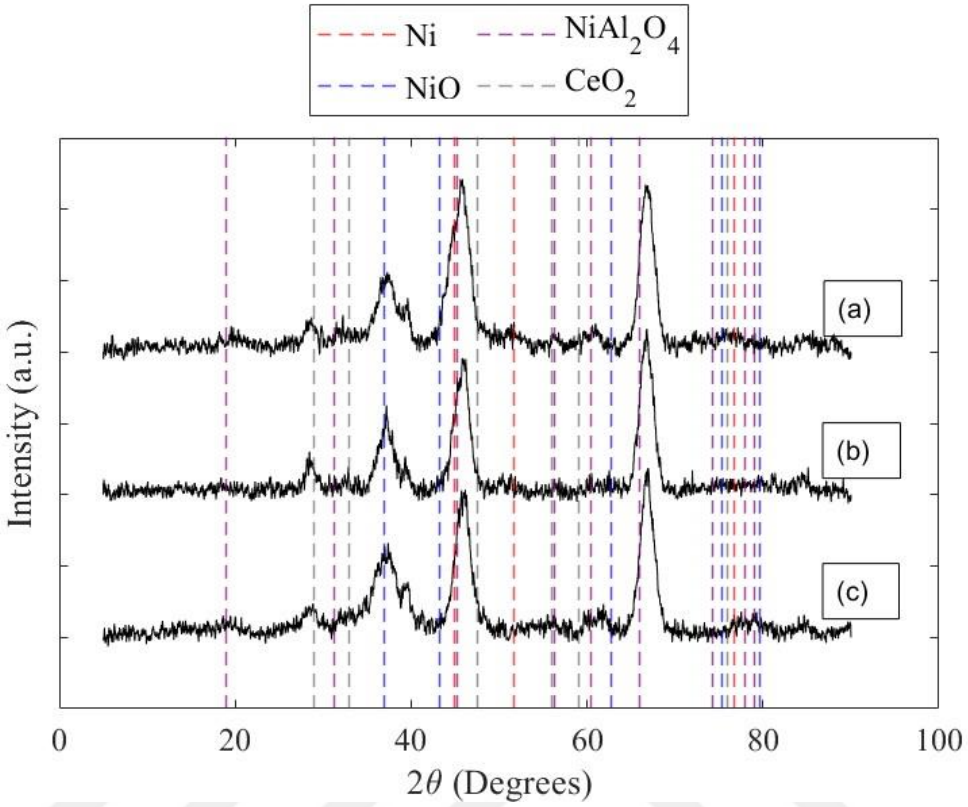

Figure 4.53. XRD profiles of spent forms of 5%Ce-10%Ni/γ-Al_2O_3 samples subjected to different temperatures and feed conditions: H_2/CO=2 at 250 ºC for 72 hours (a), H_2/CO=2 at 400 ºC for 6 hours (b), and H_2/CO=3 at 400 ºC for 72 hours (c).

4.4.3. Raman Spectropy Analysis

Raman spectroscopy is a technique used to determine vibrational modes of molecules and is commonly employed for identifying molecular structures. This method is particularly effective for detecting and characterizing carbon species on catalysts. By analyzing characteristic D and G bands in the Raman spectrum, it provides detailed information about different types of carbon, such as graphite and amorphous carbon. This enables the assessment of carbon deposition, quality, and structural changes on catalyst surfaces, offering insights into the nature of carbon species and their interactions with the catalyst (Hess, 2021).

Figure 4.54 presents the Raman spectra of spent forms of 5%Ce-10%Ni/γ-Al_2O_3 samples subjected to 72-hour stability tests with a feed containing an H_2/CO ratio of 2 at 400 ºC (a) and at 250 ºC (b). The peak at 448 cm^{-1} was identified as the fluorite-like phase of CeO_2, the presence of which was also confirmed by XRD spectra of the reduced samples (Kim et al., 2020). However, this peak was only visible in the spent catalyst sample tested at 400°C. The peak around 1340 cm^{-1} was attributed to D-band: associated with amorphous carbon species, whereas the peak around 1570-1590 cm^{-1} was related to the G band attributed to vibrations due to C-C stretching in graphitic carbon (Maziviero et al., 2024).

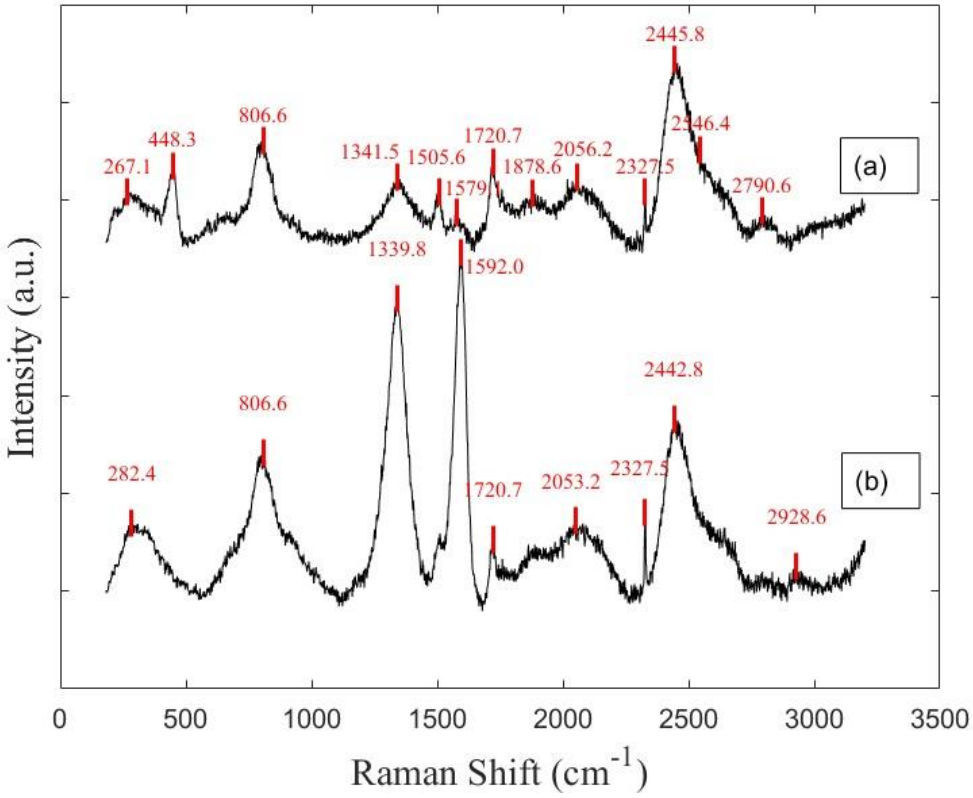

Figure 4.54. Raman spectra of spent forms of 5%Ce-10%Ni/γ-Al_2O_3 samples subjected to 72 hours stability tests at 400 ºC (a) and at 250 ºC (b).

During the methanation process, which occured in a carbon-rich environment, catalyst deactivation due to carbon deposition was expected. However, it was intriguing that deactivation occurred at 250 °C during a 72-hour stability test, whereas it did not occur under the same conditions at 400 °C (Figures 4.41 and 4.43). This suggests that the lower temperature might have created conditions that favored carbon deposition on the catalyst

surface, leading to its deactivation, while higher temperatures may have helped in preventing or reducing such deposition. Consequently, while Raman analysis of 5%Ce-10%Ni/γ-Al_2O_3 samples revealed that carbon deposition occurred in both samples, which were subjected to 72-hour stability tests at different temperatures, where the sample tested at 250 °C showed significantly more carbon deposition compared to the sample tested at 400 °C (Figure 4.54). It is noteworthy that Ni-based catalysts were reported to be prone to carbon formation at low temperatures via CO disproportionation (Audier et al., 1979; Miguel et al., 2015). The absence of the CeO_2 peak on the spent catalyst sample tested at 250 °C could be due to carbon deposition covering the catalyst surface and masking the CeO_2 signal.

4.4.4. SEM and HR STEM Analysis

Figures 4.55-4.57 show SEM images of freshly reduced 10% Ni/γ-Al_2O_3, 5%Ce-10%Ni/γ-Al_2O_3, 5%Ce-10%Ni/ZrO_2, and 5%Ce-10%Ni/SBA-15 catalyst samples, which were obtained using a MIX detector type. The combination of SEM and BSE properties enabled the brightening of Ce particles. The differentiation between the support and the particles was primarily associated with the atomic masses or atomic numbers of the respective elements.

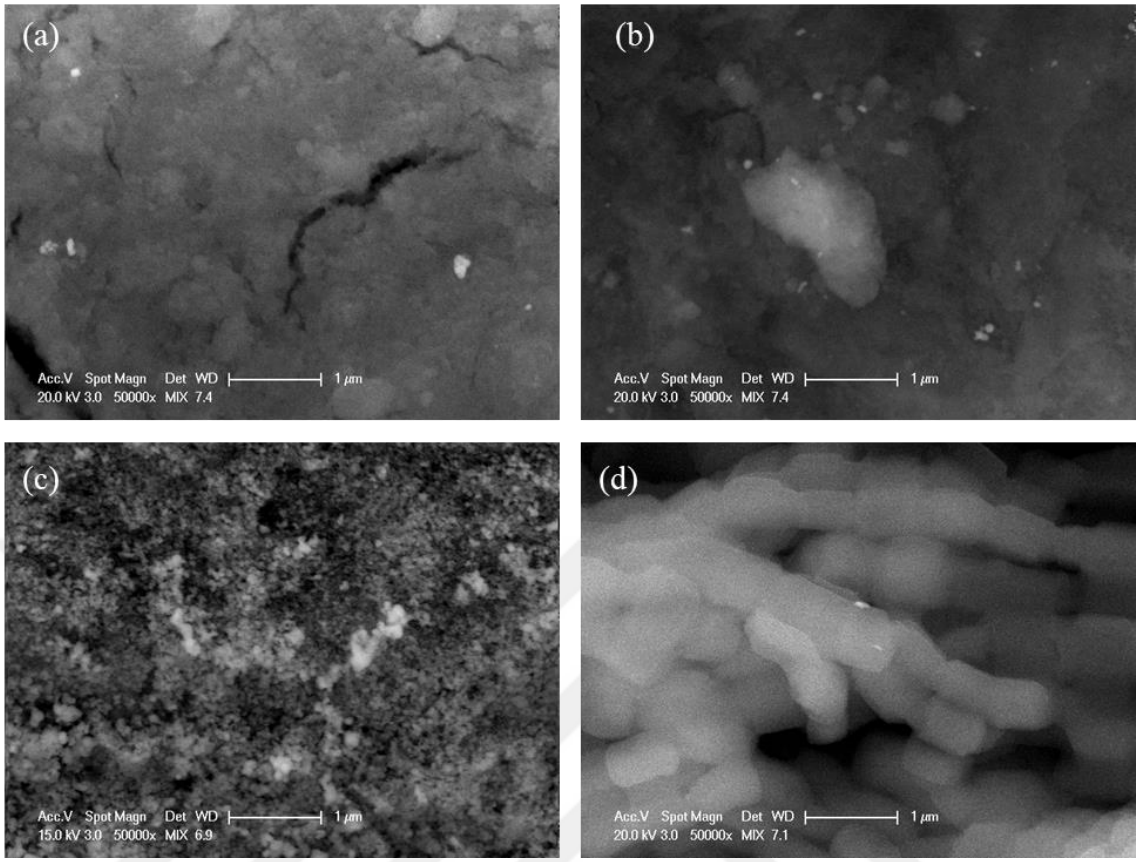

Figure 4.55. SEM images of freshly reduced 10% Ni/γ-Al_2O_3 (a), 5%Ce-10%Ni/γ-Al_2O_3 (b), 5%Ce-10%Ni/ZrO_2 (c), and 5%Ce-10%Ni/SBA-15 (d) (x50000).

SEM micrographs of freshly reduced 10% Ni/γ-Al_2O_3 sample revealed the presence of Ni clusters on the surface of γ-Al_2O_3. These Ni clusters, although present across the catalyst surface, were not uniformly distributed, indicating areas of higher and lower cluster concentration. Additionally, the SEM images also highlighted the presence of cracks on the catalyst surface of 10% Ni/γ-Al_2O_3 and 5%Ce-10%Ni/γ-Al_2O_3 samples. These cracks could potentially impact the structural integrity of the catalyst, but they might also provide beneficial pathways for reactant diffusion, enhancing the accessibility of active sites and influencing the distribution and stability of the Ni clusters (Figure 4.55(a)).

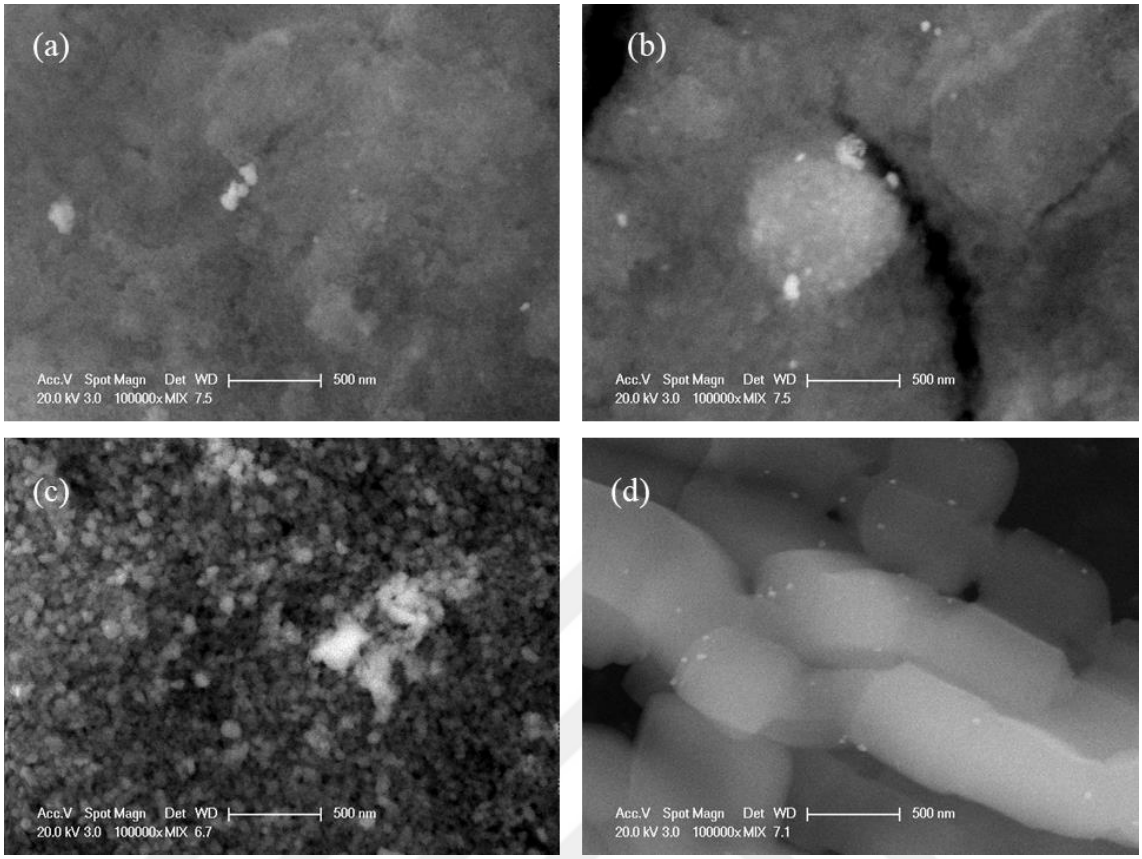

Figure 4.56. SEM images of freshly reduced 10% Ni/γ-Al_2O_3 (a), 5%Ce-10%Ni/γ-Al_2O_3 (b), 5%Ce-10%Ni/ZrO_2 (c), and 5%Ce-10%Ni/SBA-15 (d) (x100000).

Since the atomic mass of Ce is greater than that of Ni, its metallic form should be brighter in SEM micrographs. Figure 4.55(b), at a magnification of 50000x, presents the SEM image of the 5%Ce-10%Ni/γ-Al_2O_3 catalyst, synthesized via sequential impregnation (first Ce, then Ni), revealing distinct structural features on the surface. Highly bright clusters, indicative of Ce presence, were observed across the catalyst surface, confirming the successful deposition and formation of Ce-rich regions. Additionally, less bright aggregates were noted, likely corresponding to Ni-rich areas. Figure 4.56(b), at a magnification of 100000x, further clarifies these observations, showing that in certain regions, the highly bright Ce clusters appeared as discrete formations on top of the less bright Ni aggregates. This suggests that the initially deposited Ce formed clusters, while the subsequently added Ni aggregated around these Ce clusters. The variation in brightness and distribution of these clusters and agglomerations highlights the heterogeneous nature of the catalyst surface, which could significantly influence its catalytic performance by providing diverse active sites and affecting the overall reactivity.

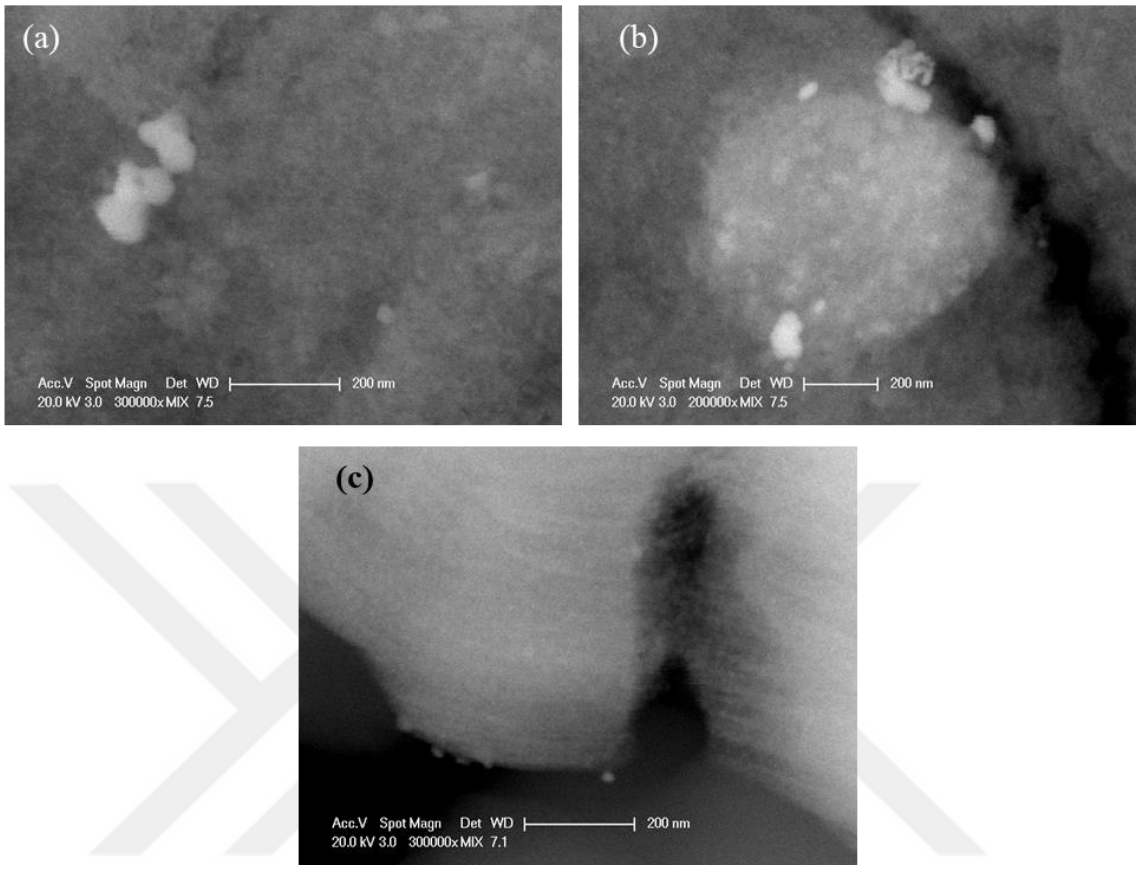

Figure 4.57. SEM images of freshly reduced 10% Ni/γ-Al_2O_3 (a), 5%Ce-10%Ni/γ-Al_2O_3 (b), and 5%Ce-10%Ni/SBA-15 (c) (x300000).

Figure 4.55(d) illustrates that mesoporous SBA-15 primarily consists of bundles of prismatic, tube-shaped silica chains. These chains are interconnected through strong interactions, forming a highly ordered and interconnected structure. The SEM images reveal that these prismatic tubes are arranged in parallel, creating a uniform and stable mesoporous network, which is essential for its applications in catalysis and adsorption. However, the specific arrangement where Ce clusters appeared as discrete formations on top of the Ni aggregates was not observed on the 5%Ce-10%Ni/ZrO_2 and 5%Ce-10%Ni/SBA-15 catalysts. This suggests that the interaction and distribution of Ce and Ni particles can vary significantly depending on the support material used.

Due to the malfunctioning of the EDX device, it was not possible to validate these results with EDX. However, STEM imaging and EDS mapping of the samples were also conducted using the HF5000 200kV (S)TEM, providing further insights into the elemental

distribution and confirming the presence and distribution of Ce and Ni on the catalyst surfaces.

High resolution (S)TEM images and corresponding EDS mappings of freshly reduced 10% Ni/γ-Al_2O_3, 5%Ce-10%Ni/γ-Al_2O_3, 5%Ce-10%Ni/ZrO_2, and 5%Ce-10%Ni/SBA-15 catalyst samples are given in Figures 4.58-4.61. The specific arrangement, where Ce clusters appeared as discrete formations on top of the Ni aggregates, was observed in the SEM imaging of the 5%Ce-10%Ni/γ-Al_2O_3 catalyst but was not present in the 5%Ce-10%Ni/ZrO_2 and 5%Ce-10%Ni/SBA-15 catalysts. This phenomenon was confirmed by EDS mapping, which revealed that the unique interaction and spatial arrangement of Ce and Ni clusters were significantly influenced by the support material.

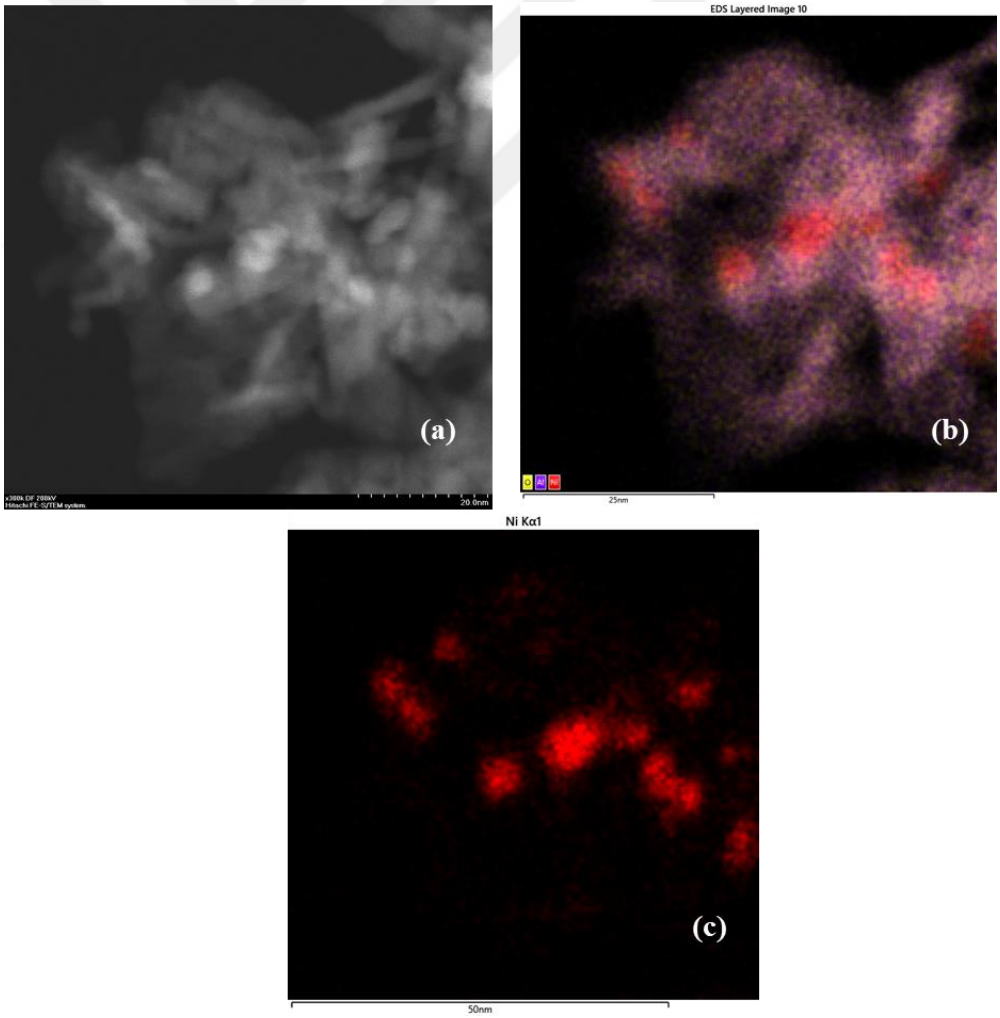

Figure 4.58. (a) STEM image of the 10% Ni/γ-Al_2O_3 catalyst; (b) Layered EDS mapping showing the overall elemental distribution; (c) EDS mapping of Ni distribution.

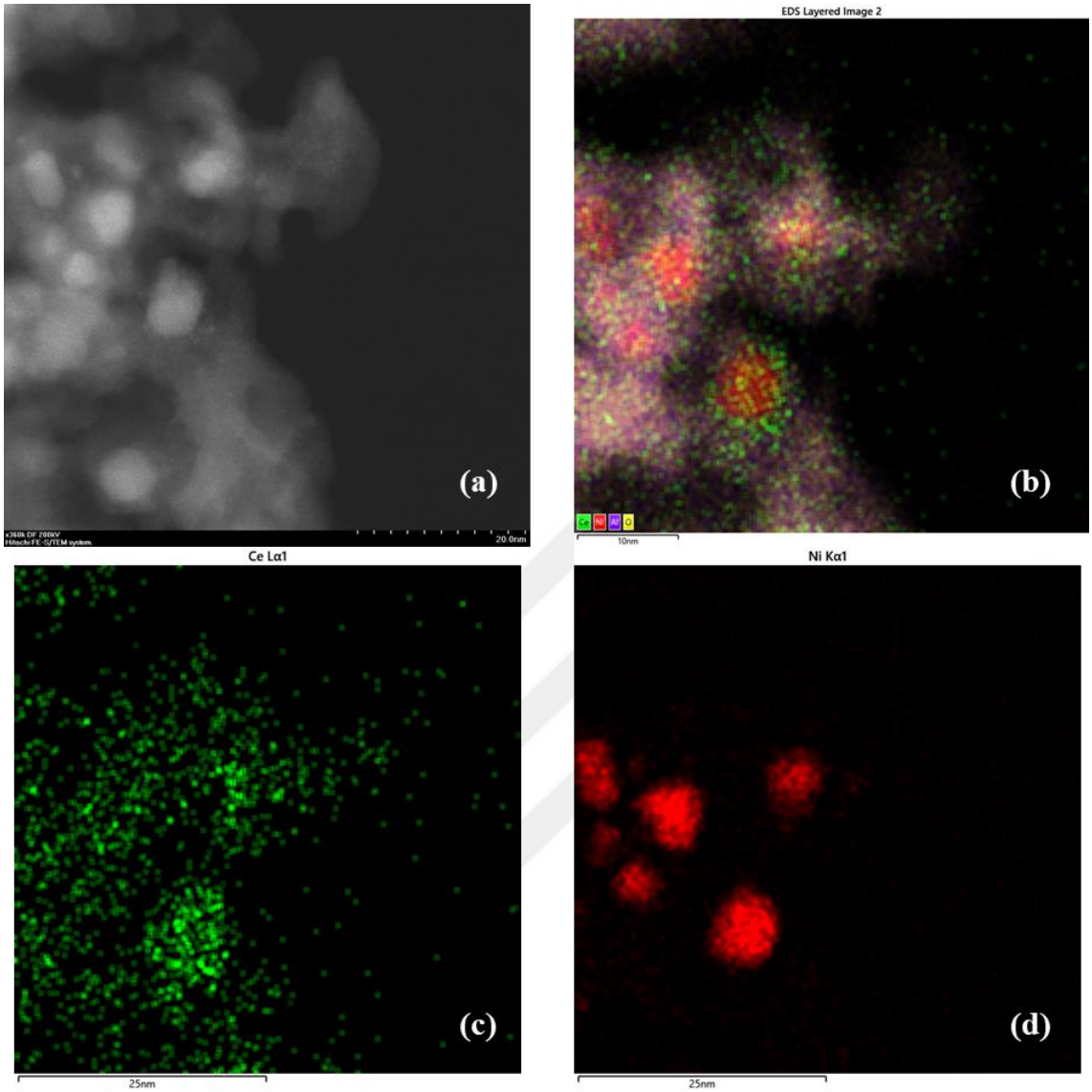

Figure 4.59. (a) STEM image of the 5%Ce-10%Ni/γ-Al_2O_3 catalyst; (b) Layered EDS mapping showing the overall elemental distribution; (c) EDS mapping of Ce distribution; (d) EDS mapping of Ni distribution.

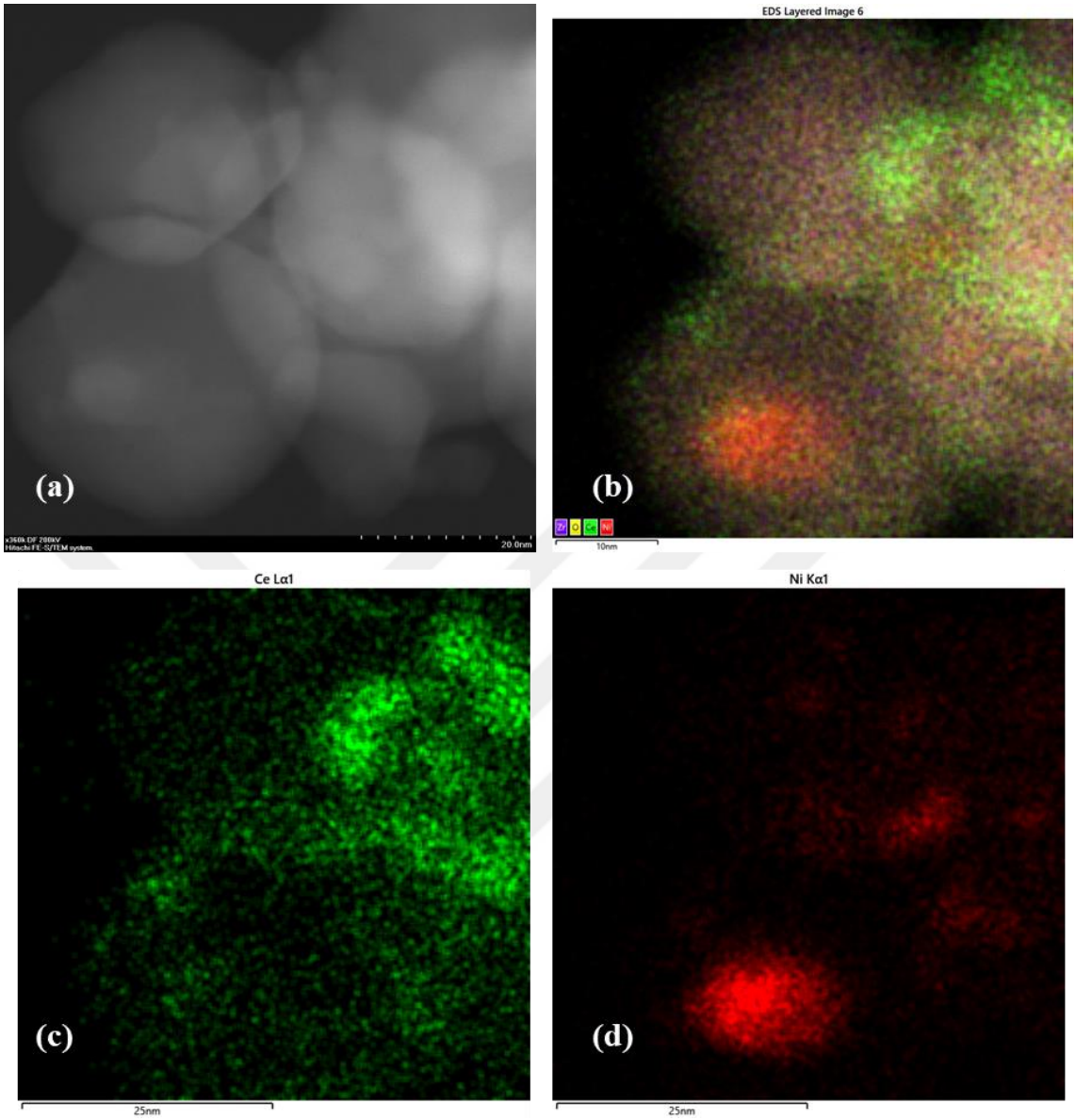

Figure 4.60. (a) STEM image of the 5%Ce-10%Ni/ZrO_2 catalyst; (b) Layered EDS mapping showing the overall elemental distribution; (c) EDS mapping of Ce distribution; (d) EDS mapping of Ni distribution.

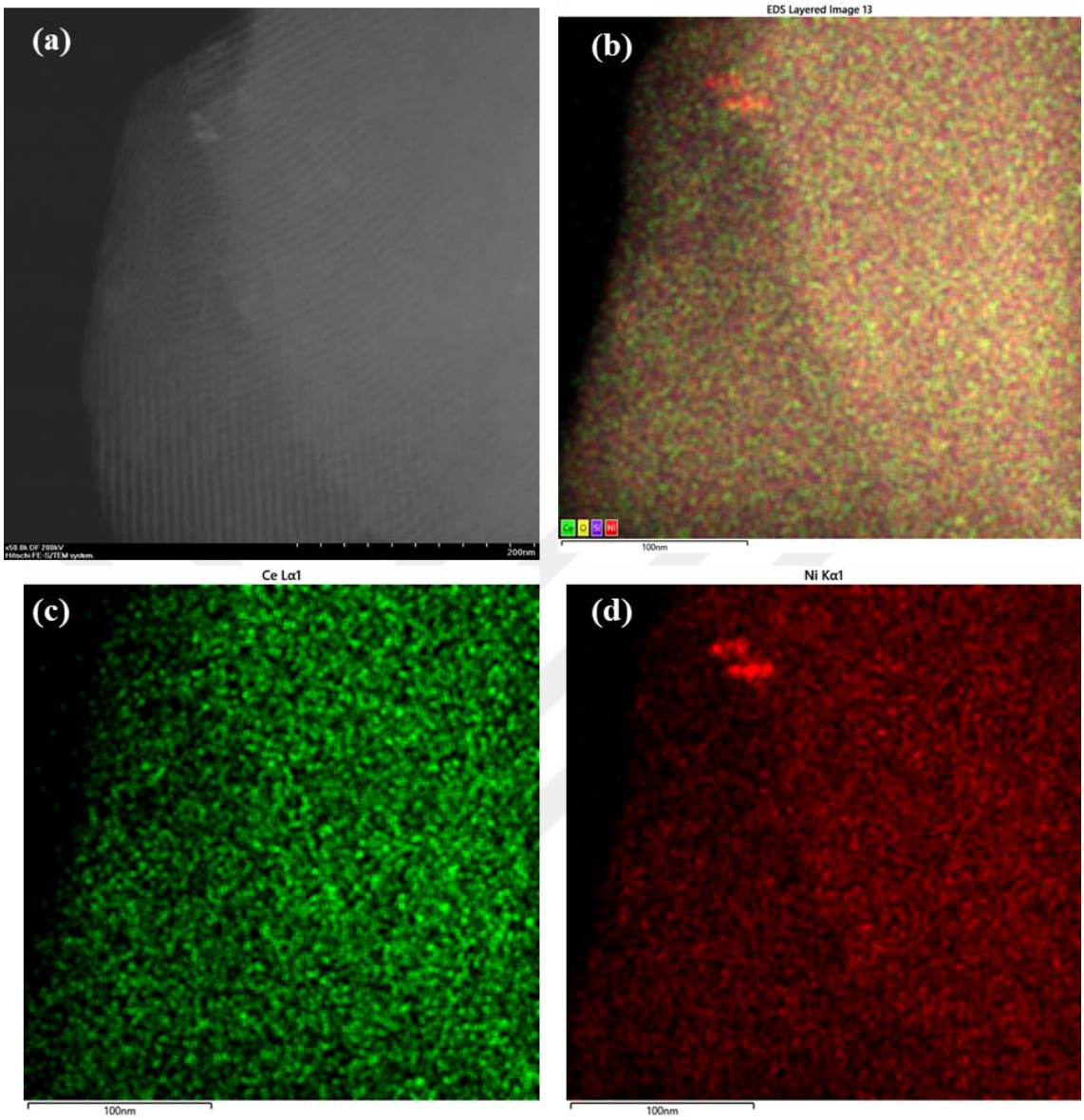

Figure 4.61. (a) STEM image of the 5%Ce-10%Ni/SBA-15 catalyst; (b) Layered EDS mapping showing the overall elemental distribution; (c) EDS mapping of Ce distribution; (d) EDS mapping of Ni distribution.

4.5. Kinetic Studies on 5%Ce-10%Ni/γ-Al_2O_3

The aim of this section is to estimate the rate-determining step and, if possible, to obtain a reliable rate equation for the CO methanation reaction over 5%Ce-10%Ni/γ-Al_2O_3, which can be used in reactor design. Kinetic experiments were conducted under differential conditions at atmospheric pressure with total feed flow rates of 100 ml/min and 120 ml/min. The reaction temperature was maintained at a constant 350 °C unless otherwise specified. The catalyst weight was varied between 8 and 15 mg to achieve significantly lower conversion levels, far from the corresponding thermodynamic equilibrium under these reaction conditions, ensuring that the reaction was controlled solely by kinetics.

The reaction rates based on catalyst mass in the kinetic measurements, (r_{CH_4}), were calculated from CO converted into CH_4 versus residence time (W/F_{CO}) data as

$$r_{CH_4} = \frac{dX_{CO}}{d\left(\frac{W}{F_{CO}}\right)}. \tag{4.4}$$

where X_{CO} is CO converted into CH_4, F_{CO} is carbon monoxide flow rate in the feed in ml/min converted to mmol/s, W is catalyst weight in mg and r_{CH_4} is the reaction rate in mmol/g*s.

CH_4 production rates were derived from intrinsic kinetic data in the initial rate region using the differential method of analysis. This well-established technique is commonly used to determine reaction orders and reaction rate expressions. By varying the W/F ratio, a wide range of conversions can be achieved with this method. During the kinetic tests, a series of experiments were conducted at different initial reactant concentrations. The initial rates were derived by differentiating the dataset and extrapolating it to zero W/F (Figure 4.62). The reaction rate values, determined from the slopes of the conversion versus residence time data, are presented in Table 4.10, with the corresponding plots available in Appendix A.

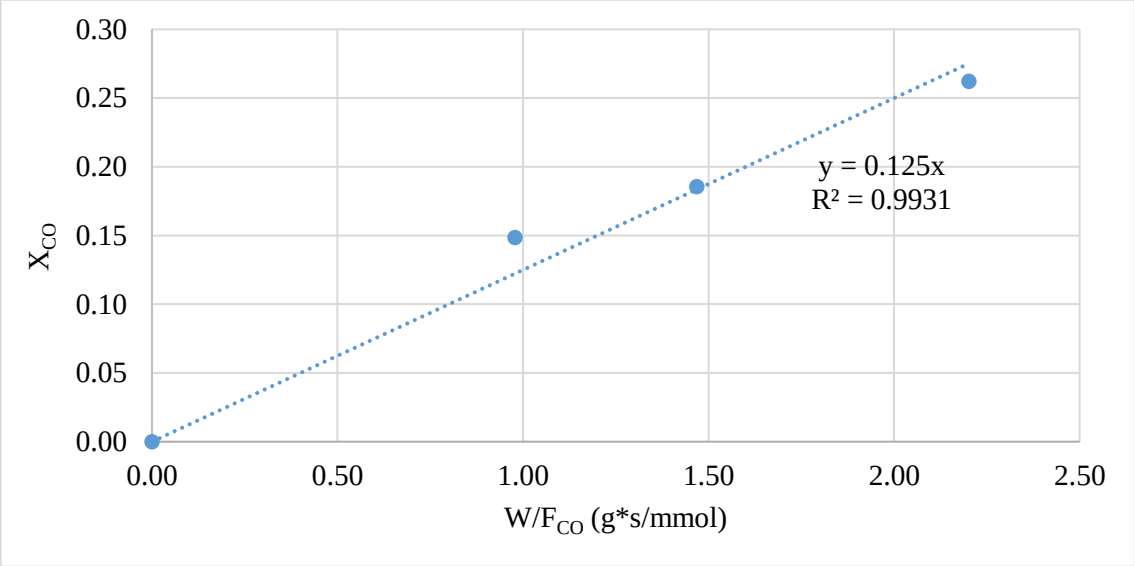

Figure 4.62. Fractional CO conversion versus residence time graph for Experiment 9.

The influence of partial pressure on methane production was examined at 350 °C by altering the pressure of one reactant while maintaining a constant pressure of the other reactant, as outlined in Table 3.7. The total flow rate was kept constant via using balance N_2.

Experiments 1-4 (Figure 4.63) demonstrate that increasing the partial pressure of H_2, while maintaining a constant partial pressure of CO, resulted in an increased production rate of CH_4. However, this increase was not linear and was not particularly significant between 0.2 and 0.3 bar. When the partial pressure dependency was examined for CO gas (Figure 4.64 and Experiments 4-7), for low partial pressures of CO (0.05-0.075 bar), increasing the partial pressure increased the CH_4 production rate. However, further increases in the partial pressures resulted in the decrease of the CH_4 production rate.

Table 4.10. Initial rates of CO methanation over the 5%Ce-10%Ni/γ-Al_2O_3 catalyst under conditions defined in Table 3.7.

#	T (˚C)	W/F (kg*s/l)			CH_4 Production Rate (mmol*g/s)	R^2
		1	2	3		
1	350	0.009	0.006	0.004	0.139	0.989
2	350	0.009	0.006	0.004	0.107	0.991
3	350	0.009	0.006	0.004	0.102	0.999
4	350	0.009	0.006	0.004	0.061	0.996
5	350	0.009	0.006	0.004	0.048	0.998
6	350	0.009	0.006	0.004	0.079	0.996
7	350	0.009	0.006	0.004	0.060	0.997
8	350	0.009	0.006	0.004	0.154	0.997
9	350	0.009	0.006	0.004	0.125	0.993
10	350	0.009	0.006	0.004	0.108	0.993
11	350	0.009	0.006	0.004	0.069	0.997
12	350	0.009	0.006	0.004	0.086	0.988
13	350	0.009	0.006	0.004	0.080	0.995
14	350	0.009	0.006	0.004	0.057	0.995
15	350	0.009	0.006	0.004	0.125	0.993
16	350	0.009	0.006	0.004	0.116	0.992
17	350	0.009	0.006	0.004	0.093	1.000
18	350	0.009	0.006	0.004	0.143	0.994
19	350	0.009	0.006	0.004	0.117	0.992
20	350	0.009	0.006	0.004	0.127	0.993
21	350	0.009	0.006	0.004	0.064	0.990
22	350	0.009	0.006	0.004	0.048	0.990
23	350	0.009	0.006	0.004	0.055	0.994
24	300	0.009	0.006	0.004	0.070	0.984
25	400	0.009	0.006	0.004	0.131	0.999
26	325	0.009	0.006	0.004	0.098	0.994
27	375	0.009	0.006	0.004	0.130	0.998

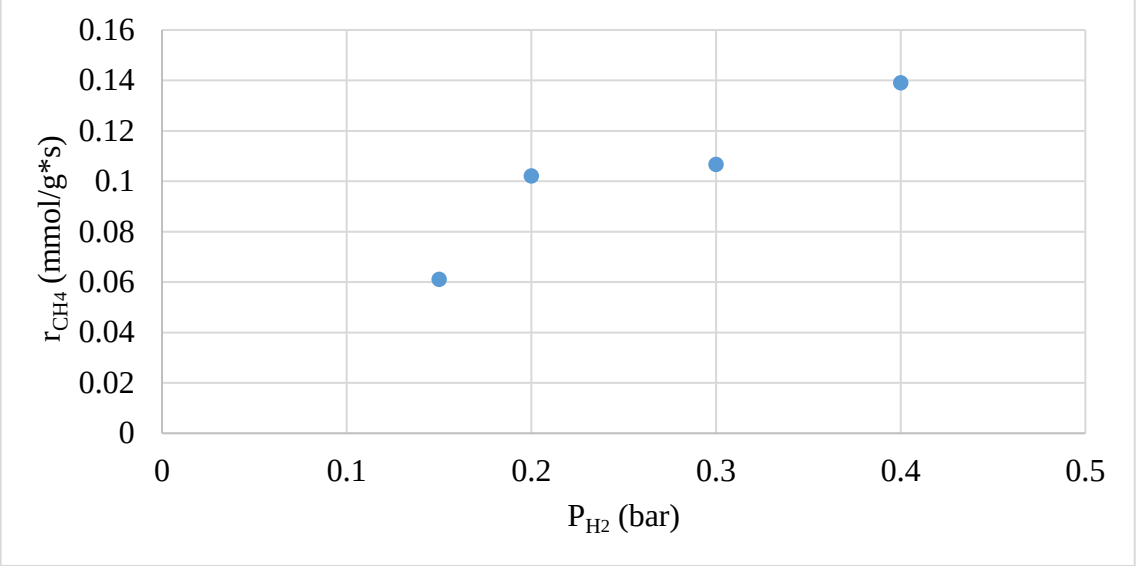

Figure 4.63. Effect of H_2 partial pressure on CH_4 production rate at 350 °C.

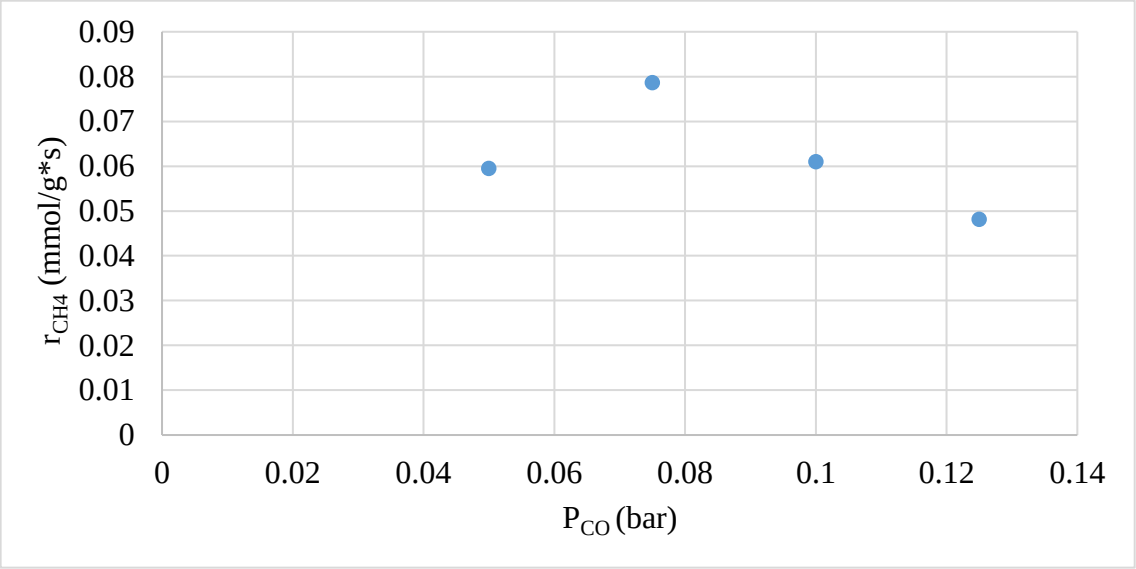

Figure 4.64. Effect of CO partial pressure on CH_4 production rate at 350 °C.

In order to gain a deeper understanding of the reaction dynamics, the effect of product gas addition to the feed gas stream was examined for CH_4 (Experiments 9, 18-20) and H_2O (Experiments 2, 15-17). For low partial pressures of both product gases (0-0.05 bar), increasing the partial pressures of the respective gases increased the CH_4 production rate. However, further increases in the partial pressure of CH_4 did not yield any meaningful relationship to the reaction rate, while further increases in the partial pressure of H_2O

decreased the reaction rate. Additionally, the effect of CO_2 addition to the feed gas stream was investigated (Experiments 9, 21-23). In those tests, increasing CO_2 partial pressure in the feed gas stream from 0 to 0.1 bar led to a decrease in reaction rate. However, when the partial pressure of CO_2 was further increased to 0.15 bar, no significant change in the reaction rate was observed (Figure 4.65).

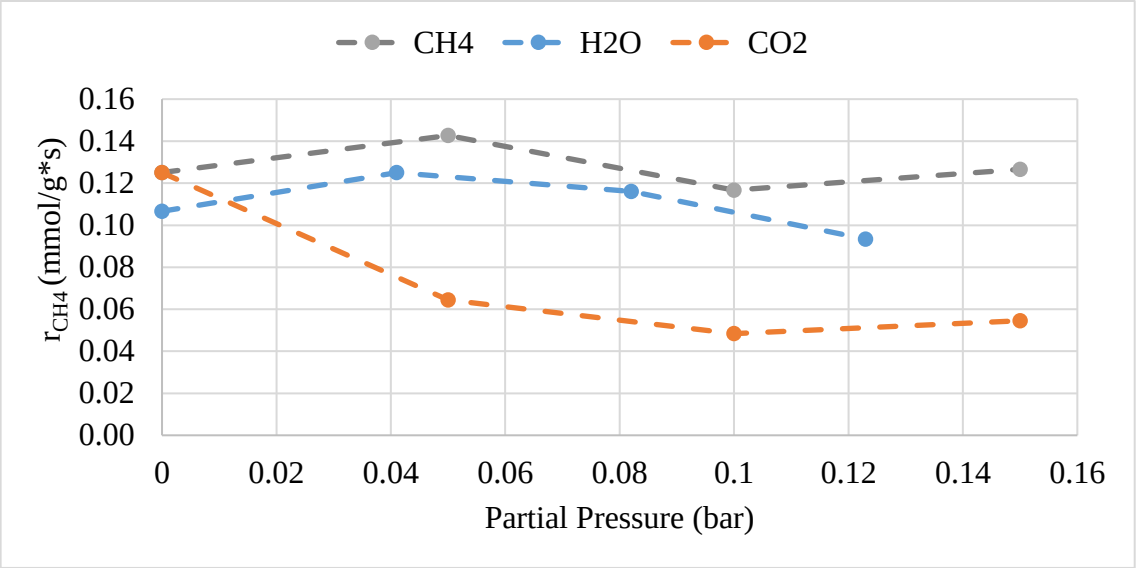

Figure 4.65. Effect of CH_4, H_2O, and CO_2 partial pressures on CH_4 production rate at 350 °C.

4.5.1. Power Law Type Kinetic Expression

Given the large quantity of possible side reactions in the process (Section 2.2) and the sensitivity of each reaction to reactant composition and changes in temperature, it was initially preferred to find a simple power-law type rate equation for design practicality, instead of deriving a complex mechanistic scheme. An empirical power-law type rate expression, which contains only the reactant terms, was initially applied to the CO methanation reaction, as

$$r\left(\frac{mmol}{g*s}\right) = kP_{H_2}^{\alpha}P_{CO}^{\beta}\,, \tag{4.4}$$

$$r\left(\frac{mmol}{g*s}\right) = k_0 e^{-\frac{E_A}{RT}}P_{H_2}^{\alpha}P_{CO}^{\beta}\,. \tag{4.5}$$

The rate values obtained from Experiments 1-7 (as detailed in Tables 3.7 and 4.9) were utilized to determine the reaction orders concerning the reactants. Reaction orders in Equation 4.4 were calculated by multivariable nonlinear regression using the Levenberg-Marquardt algorithm implemented in the lsqcurvefit function of MATLAB™ environment (Table 4.11).

Table 4.11. Reaction orders for power-law type rate expressions.

Experiments	α	β	δ	θ
1-7	0.777	-0.073	-	-
1-20	0.777	-0.073	-0.026	-0.028

At 350 °C, parameters for the power law type rate expression were written as

$$r\left(\frac{mmol}{g*s}\right) = 0.24\frac{mmol}{g*s*bar^{0.71}}P_{H_2}^{0.78}P_{CO}^{-0.07} \quad . \tag{4.6}$$

Predicted rate values versus the experimental rate values are given in Figure 4.66 for the power-law type rate expression. It was observed that this model did not explain the reaction data well, with R^2 and MSE values calculated as 0.85 and $1x10^{-4}$, respectively.

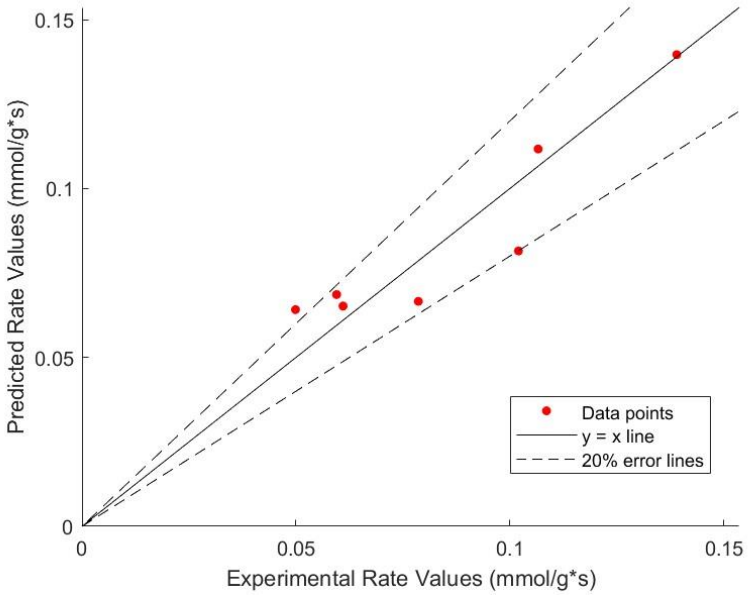

Figure 4.66. Predicted versus the experimental CH_4 production rates for power-law type rate expression.

In order to test the effect of products on the reaction rate, terms for product gases were incorporated into the power-law type rate expression as

$$r\left(\frac{mmol}{g*s}\right) = kP_{H_2}^{\alpha}P_{CO}^{\beta}P_{CH_4}^{\delta}P_{H_2O}^{\theta}. \quad (4.7)$$

The rate values obtained from Experiments 1-20 (in Tables 3.7 and 4.10) were used to calculate reaction orders with respect to reactants.

Reaction orders in Equation 4.7 were estimated by multivariable nonlinear regression as

$$r\left(\frac{mmol}{g*s}\right) = 0.24\frac{mmol}{g*s*bar^{1.65}}P_{H_2}^{0.78}P_{CO}^{-0.07}P_{CH_4}^{-0.03}P_{H_2O}^{-0.03} \quad (4.8)$$

using the Levenberg-Marquardt algorithm implemented in the lsqcurvefit function of MATLAB™ environment (Table 4.10). The parameters were calculated with a similar prediction efficiency (Figure 4.64). R^2 and MSE values calculated as 0.85 and $1x10^{-4}$, respectively.

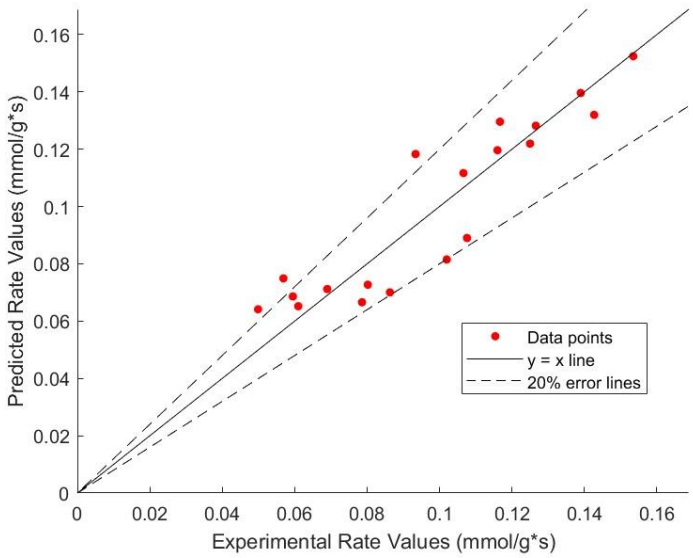

Figure 4.67. Predicted versus the experimental CH_4 production rates for power-law type rate expression with product effect.

To estimate the pre-exponential factor (k0) and the apparent activation energy (EA) as described in Equation 4.5, Experiment 9 was conducted at temperatures of 300, 325, 350, 375, and 400 °C. The resulting data are plotted in Figure 4.68, and the estimated parameter

values are presented in Table 4.12.

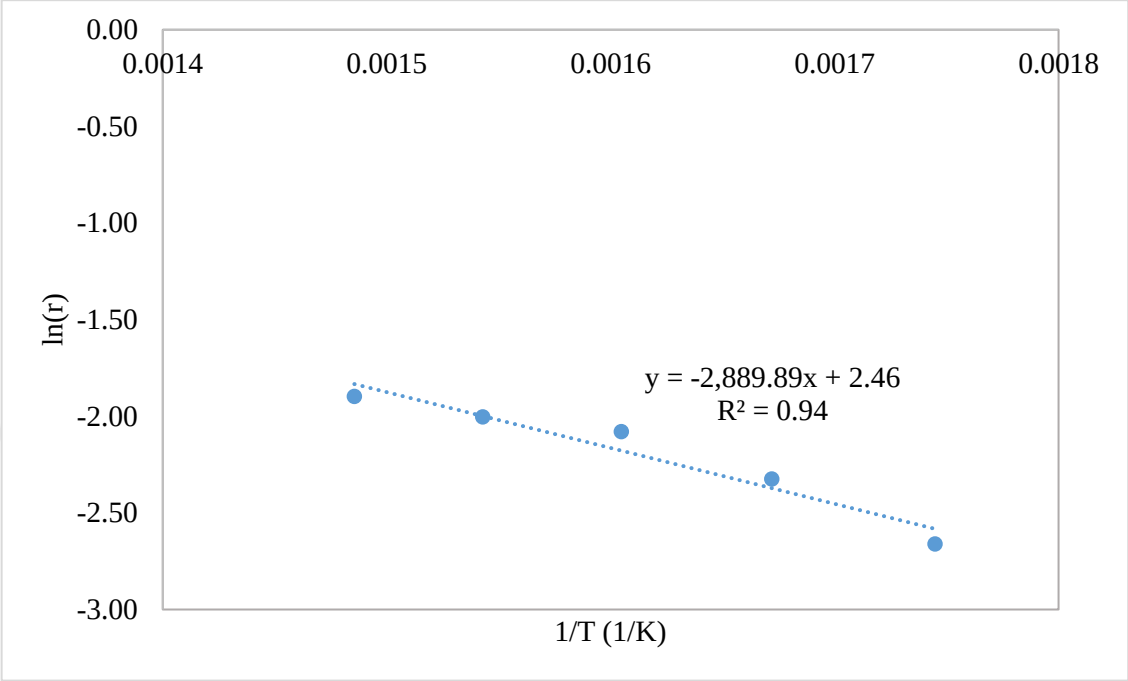

Figure 4.68. Arrhenius plot for CO methanation on 5%Ce-10%Ni/γ-Al_2O_3.

The increase in temperature significantly enhanced the reaction rate. However, a detailed analysis of the Arrhenius plot revealed that the rate data exhibited two distinct trends corresponding to two separate temperature zones: one between 300 and 350 °C, and the other between 350 and 400 °C. This indicates that the reaction kinetics differ significantly across these temperature ranges, potentially due to varying reaction mechanisms or different activation energies in these regions. To investigate further, the data were divided according to the temperature zones, and separate trendlines were added for each region (Figure 4.69). The activation energy and pre-exponential factors for these temperature zones are presented in Table 4.12. The decrease in activation energy with increasing temperature is consistent with findings in the literature. The change in activation energy in the higher temperature range suggests an alteration in the mechanism or the rate-determining step (Sughrue and Bartholomew, 1982).

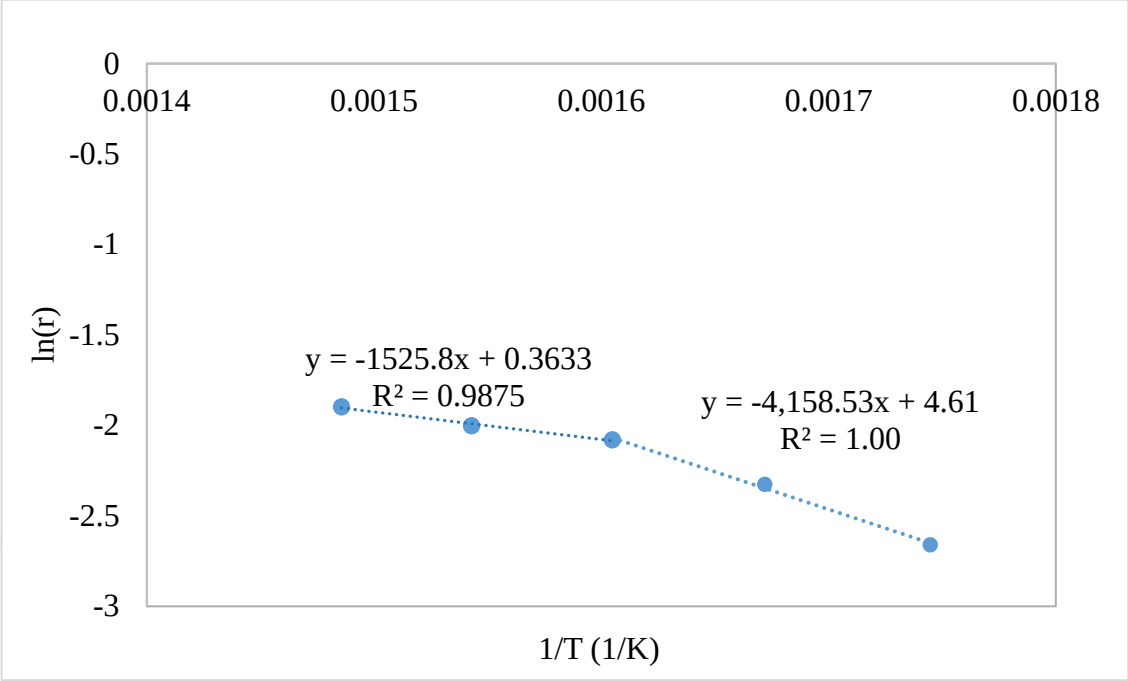

Figure 4.69. Arrhenius plots for CO methanation on 5%Ce-10%Ni/γ-Al_2O_3 in two temperature zones.

Table 4.12. Kinetic parameters for CO methanation.

Parameter	Units	Estimated for 300 °C - 400 °C	Estimated for 300 °C - 350 °C	Estimated for 350 °C - 400 °C
k_0	$\frac{mmol}{g * s * bar^{0.8}}$	35.4	303.7	0.73
E_A	$\frac{kj}{mol}$	24.0	34.6	12.7

The studies on power-law type rate expressions for methanation are explained in Section 2.2.7. Comparing kinetic parameters with those reported in the literature is complicated due to the fact that most studies were carried out under different conditions. In this study, the reaction orders of CO and H_2 were determined to be -0.07 and 0.78, respectively. These findings are consistent with the literature, where the order of CO has been reported to be ranging from 0 to -0.60, and the order of H_2 has been observed to be positive, often close to 1 (Vlasenko et al., 1969; Sughrue and Bartholomew, 1982). Additionally, it is mostly accepted in the literature that H_2O exhibits an inhibitory effect, while it has generally been reported that CH_4 does not exhibit inhibition (Sughrue and

Bartholomew, 1982). However, slightly negative reaction orders for both H_2O and CH_4 were found in this study. This indicates that while the inhibition by H_2O aligns with previous reports, the observed slight CH_4 inhibition warrants further investigation. Although the findings in this research agree with the corresponding literature to some degree, it is crucial to understand the mechanistic aspects of the methanation reaction. In the related literature, researchers have proposed Langmuir–Hinshelwood type reaction models for the CO methanation reaction. These models suggest that the reaction mechanism involves adsorption of both CO and H_2 on the catalyst surface, followed by surface reactions leading to the formation of methane. Therefore, a deeper investigation of these mechanistic pathways, including the role of inhibitory effects observed for H_2O and CH_4, is essential for a comprehensive understanding of the reaction kinetics.

4.5.2. Surface Reactions

Reaction mechanisms and the proposed Langmuir–Hinshelwood type reaction models of methanation reactions were explained in Section 2.2.7. In this part of the study, twelve kinetic models based on various mechanisms and RDS reactions were chosen for multivariable nonlinear regression analysis (Table 4.13). The Leave-One-Out (LOO) cross-validation methodology was employed for model discrimination, ensuring that considerations of physical meaningfulness were addressed.

Among the various data partitioning strategies used for model validation, LOO cross-validation is particularly noteworthy. It is a variant of the k-fold cross-validation method, where k is the number of data points. Each data point is used as the test set once, while the remaining data forms the training set. This method provides an almost unbiased estimate of the true prediction error but has high variance due to the minimal difference between training sets. Other common strategies include the single hold-out method, where a portion of the data, typically 10% to 30%, is randomly selected as the test set, and the remaining data forms the training set. In k-fold cross-validation, this process is repeated k times with the data partitioned into k disjoint subsets, each serving as the test set once, while the remaining subsets form the training set (Berrar, 2019).

The values of Mean Squared Error (MSE), Root Mean Squared Error (RMSE), R^2, and kinetic expression parameters obtained during the LOO cross-validation process for all models, where data points are systematically left out one at a time and predicted using the model trained on the remaining data, are provided in Appendix B. Based on LOO cross-validation results, none of the models performed exceptionally well overall (Figure 4.70). However, Model 7 emerged as the best in terms of RMSE, with an average RMSE of 1.16×10^{-2}, whereas Model 1 excelled in terms of MSE, with an average MSE of 2.11×10^{-4} (Table 4.14).

Table 4.13. The kinetic models and their corresponding RDS reactions selected for multivariable nonlinear regression analysis.

#	RDS	Rate
1	*Surface reaction*	$r_{CH_4} = \frac{kP_{H_2}P_{CO}}{\left(1 + K_{H_2}P_{H_2} + K_{CO}P_{CO}\right)^2}$
2	*Surface reaction*	$r_{CH_4} = \frac{kP_{H_2}P_{CO}}{\left(1 + K_{H_2O}P_{H_2O} + K_{CO}P_{CO}\right)^2}$
3	*H_2 Adsorption*	$r_{CH_4} = \frac{kK_{H_2}P_{H_2}}{1 + K_{H_2}P_{H_2} + K_{CO}P_{CO}}$
4	$C* + 2H*$	$r_{CH_4} = \frac{kK_{CO}K_{H_2}^2P_{CO}^{0.5}P_{H_2}}{\left(1 + K_{CO}P_{CO}^{0.5} + K_{H_2}P_{H_2}^{0.5}\right)^3}$
5	$C* + H*$	$r_{CH_4} = \frac{kK_CP_{CO}^{0.5}P_{H_2}^{0.5}}{\left(1 + \mathrm{K_C P_{CO}} + \mathrm{K_{OH} P_{H_2O} P_{H_2}^{-0.5}}\right)^2}$
6	$CH* + H*$	$r_{CH_4} = \frac{kK_{CH}P_{CO}^{0.5}P_{H_2}}{\left(1 + K_{OH}P_{H_2O}P_{H_2}^{-0.5} + K_{CH}P_{CO}^{0.5}P_{H_2}^{0.5}\right)^2}$
7	$COH* + H*$	$r_{CH_4} = \frac{kK_{COH}P_{CO}P_{H_2}}{\left(1 + K_{OH}P_{H_2O}P_{H_2}^{-0.5} + K_{COH}P_{CO}P_{H_2}^{0.5}\right)^2}$
8	$CO* + H*$	$r_{CH_4} = \frac{kK_{CO}K_{H_2}P_{H_2}^{0.5}P_{CO}}{\left(1 + K_{CO}P_{CO} + K_{H_2}P_{H_2} + K_{CH_4}P_{CH_4} + K_{H_2O}P_{H_2O}P_{H_2}^{-1}\right)^2}$
9	$CO* + H*$	$r_{CH_4} = \frac{kK_{CO}P_{H_2}^{0.5}P_{CO}}{\left(1 + K_{CO}P_{CO} + K_{H_2O}P_{H_2O}P_{H_2}^{-1}\right)^2}$
10	$CO* + H*$	$r_{CH_4} = \frac{kK_{CO}K_{H_2}^{0.5}P_{H_2}^{0.5}P_{CO}}{(1 + K_{CO}P_{CO})^2}$
11	$HCO* + H*$	$\mathrm{r_{CH_4}} = \frac{kP_{H_2}P_{CO}}{(1 + k'\frac{P_{H_2O}}{P_{H_2}^{1.5}})(1 + K_{CO}P_{CO})^2}$
12	$H_2 + 2*$ $C* + H*$	$r_{CH_4} = \frac{k_1k_2P_{H_2}}{k_1\left(1 + K_{H_2}^{0.5}P_{H_2}^{0.5} + K_{CO}P_{CO}\right)^2 + k_2(1 + K_{CO}P_{CO})^2}$

Model 1 was a simple Langmuir-Hinshelwood model based on the surface C* hydrogenation, which was the rate-determining step. This model was relevant to both

dissociative and associative mechanisms (Figure 4.68) and notably lacked an H_2O inhibition term but included a surface coverage term for H_2. In contrast, Model 7, developed on the basis of an associative mechanism and assuming COH* hydrogenation as the RDS, incorporated a term for H_2O inhibition, considering OH* as the adsorbed species (Figure 4.69).

All rate expressions and LOO cross-validation graphs for the 12 models were re-evaluated, considering the information from power-law type rate expression calculations and experimental observations, which consistently indicate that while H_2 has a positive reaction order lower than 1, there is H_2O inhibition effect on the reaction rates. Models 2 and 11, although poor at predicting reaction rate values overall, demonstrated slightly superior performances in predicting low reaction rate values. Model 2, a simple Langmuir-Hinshelwood (LH) model, took the surface C* hydrogenation as the rate-determining step (RDS) and included an H_2O inhibition term but lacked an H_2 coverage term. In contrast, Model 11, developed based on an associative mechanism and assuming CHO* hydrogenation as the RDS, also incorporated an H_2O inhibition term.

In light of this information, the observed H_2O inhibition effect in our experimental data indicated that Model 1, which lacked this term, should be excluded from further consideration. However, literature identifies C* hydrogenation as the most probable RDS at temperatures above 300 °C, warranting further discussion of Model 1.

Despite Models 2 and 11 demonstrating slightly better performance at low reaction rates, they were not deemed optimal for overall predictions. Therefore, based on the LOO cross-validation results, Model 7 emerged as the best candidate, though with some reservations.

Table 4.14. Average RMSE and MSE Values of Kinetic Models from LOO Cross-Validation Calculations

#	RDS	Rate	Average RMSE	Average MSE
1	*Surface reaction*	$r_{CH_4} = \frac{kP_{H_2}P_{CO}}{\left(1 + K_{H_2}P_{H_2} + K_{CO}P_{CO}\right)^2}$	1.23E-02	2.11E-04
2	*Surface reaction*	$r_{CH_4} = \frac{kP_{H_2}P_{CO}}{\left(1 + K_{H_2O}P_{H_2O} + K_{CO}P_{CO}\right)^2}$	1.45E-02	3.27E-04
3	*H_2 Adsorption*	$r_{CH_4} = \frac{kK_{H_2}P_{H_2}}{1 + K_{H_2}P_{H_2} + K_{CO}P_{CO}}$	1.26E-02	2.12E-04
4	$C* + 2H*$	$r_{CH_4} = \frac{kK_{CO}K_{H_2}^2P_{CO}^{0.5}P_{H_2}}{\left(1 + K_{CO}P_{CO}^{0.5} + K_{H_2}P_{H_2}^{0.5}\right)^3}$	1.27E-02	2.24E-04
5	$C* + H*$	$r_{CH_4} = \frac{kK_CP_{CO}^{0.5}P_{H_2}^{0.5}}{\left(1 + K_CP_{CO} + K_{OH}P_{H_2O}P_{H_2}^{-0.5}\right)^2}$	1.29E-02	2.88E-04
6	$CH* + H*$	$r_{CH_4} = \frac{kK_{CH}P_{CO}^{0.5}P_{H_2}}{\left(1 + K_{OH}P_{H_2O}P_{H_2}^{-0.5} + K_{CH}P_{CO}^{0.5}P_{H_2}^{0.5}\right)^2}$	1.21E-02	2.14E-04
7	$COH* + H*$	$r_{CH_4} = \frac{kK_{COH}P_{CO}P_{H_2}}{\left(1 + K_{OH}P_{H_2O}P_{H_2}^{-0.5} + K_{COH}P_{CO}P_{H_2}^{0.5}\right)^2}$	1.16E-02	2.26E-04
8	$CO* + H*$	$r_{CH_4} = \frac{kK_{CO}K_{H_2}P_{H_2}^{0.5}P_{CO}}{\left(1 + K_{CO}P_{CO} + K_{H_2}P_{H_2} + K_{CH_4}P_{CH_4} + K_{H_2O}P_{H_2O}P_{H_2}^{-1}\right)^2}$	1.40E-02	2.89E-04
9	$CO* + H*$	$r_{CH_4} = \frac{kK_{CO}P_{H_2}^{0.5}P_{CO}}{\left(1 + K_{CO}P_{CO} + K_{H_2O}P_{H_2O}P_{H_2}^{-1}\right)^2}$	1.25E-02	2.72E-04
10	$CO* + H*$	$r_{CH_4} = \frac{kK_{CO}K_{H_2}^{0.5}P_{H_2}^{0.5}P_{CO}}{(1 + K_{CO}P_{CO})^2}$	1.21E-02	2.50E-04
11	$HCO* + H*$	$\mathrm{r_{CH_4}} = \frac{kP_{H_2}P_{CO}}{(1 + k'\frac{P_{H_2O}}{P_{H_2}^{1.5}})(1 + K_{CO}P_{CO})^2}$	1.37E-02	2.83E-04
12	$H_2 + 2*$ $C* + H*$	$r_{CH_4} = \frac{k_1k_2P_{H_2}}{k_1\left(1 + K_{H_2}^{0.5}P_{H_2}^{0.5} + K_{CO}P_{CO}\right)^2 + k_2(1 + K_{CO}P_{CO})^2}$	1.31E+04	1.31E+04

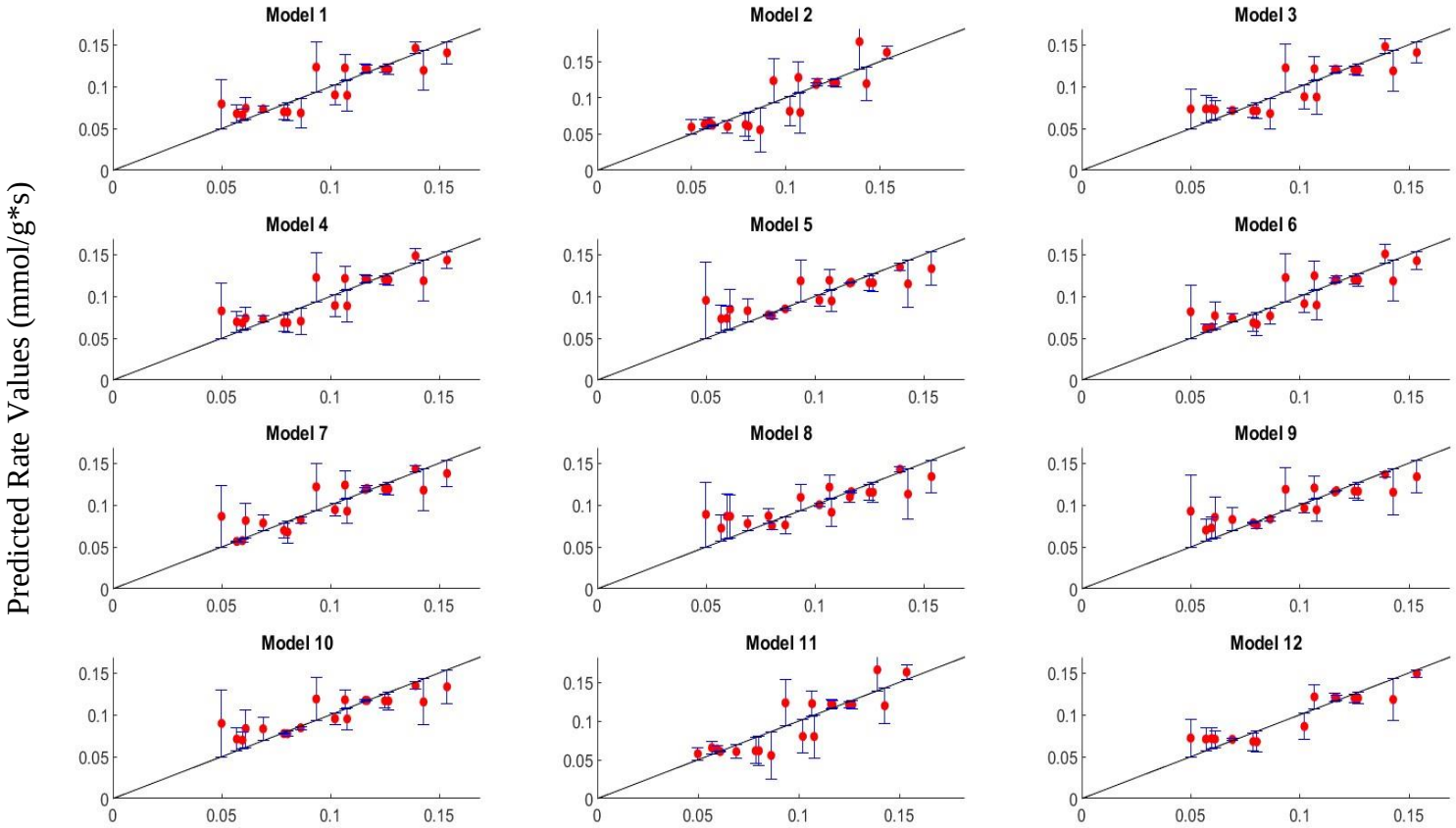

Figure 4.70. Comparison of LOO-predicted rate value for every step and actual rate values for all models with corresponding error bars.

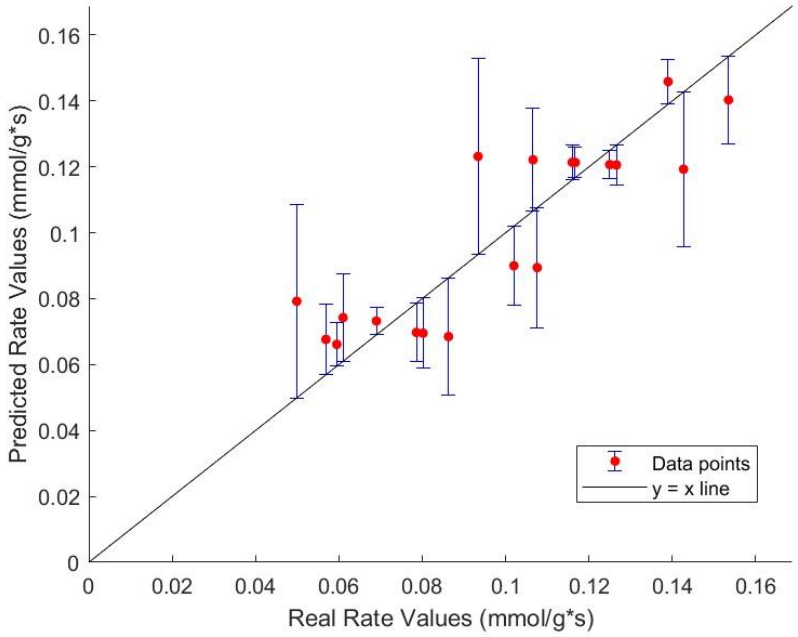

Figure 4.71. Comparison of LOO-predicted rate values and actual rate values for Model 1.

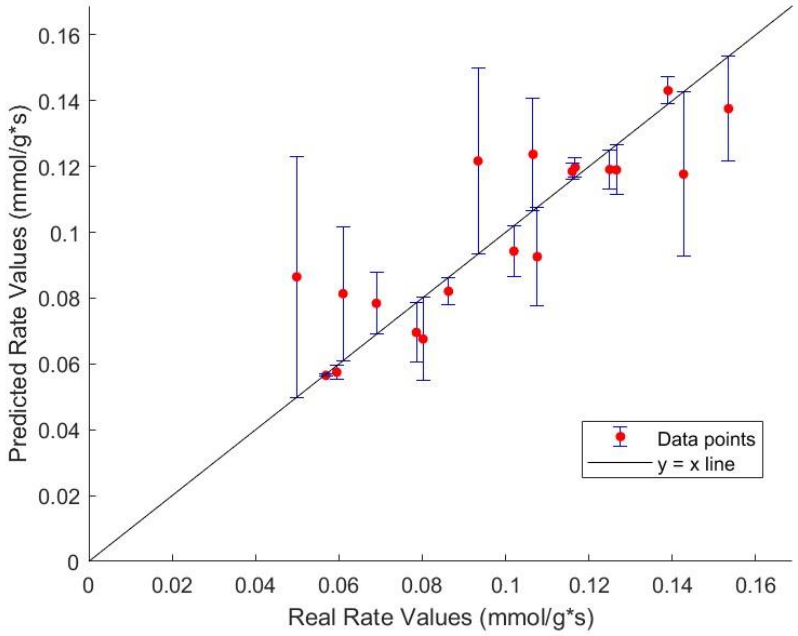

Figure 4.72. Comparison of LOO-predicted rate values and actual rate values for Model 7.

The power-law type rate expression was also subjected to LOO cross-validation method. The results showed that the average RMSE and MSE values were 1.10×10^{-2} and 1.78×10^{-4}, respectively. These values were lower than the average RMSE (1.16×10^{-2}) and

MSE ($2.26x10^{-4}$) values calculated for model 7, indicating that the power-law type rate expression performed better than model 7 based on these metrics (Figure 4.73).

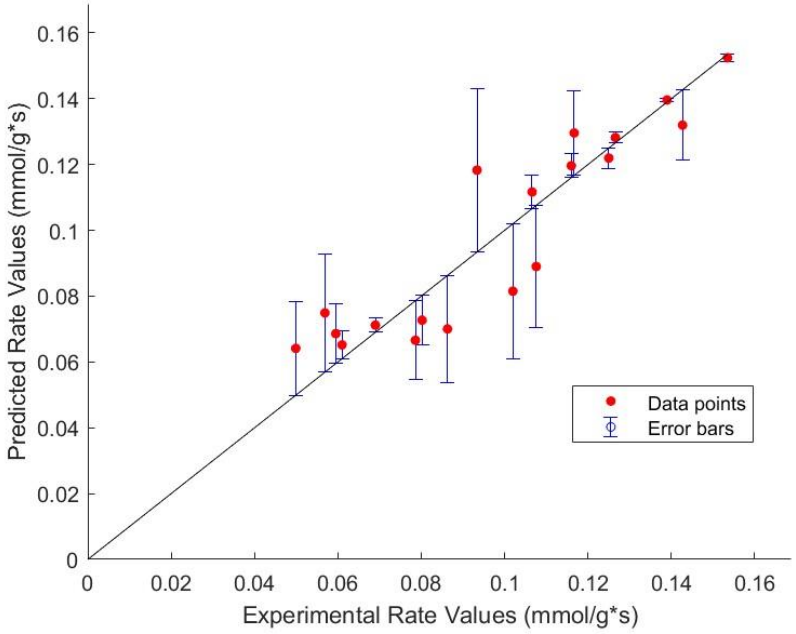

Figure 4.73. Comparison of LOO-predicted rate values and actual rate values for power-law type model

All performance metrics and model parameters from LOO cross-validation calculations and LOO-prediction graphs can be found in Appendix B.

After completing the cross-validation, all models were trained on the entire dataset to determine the final model parameters (Table 4.15). Model 1 provided the minimum MSE value and the best fit, whereas the trend of the graphs indicated that Model 7 demonstrated a similar performance (Figure 4.74).

Table 4.15. Model parameters for all models.

#	RDS	Rate	MSE
1	*Surface reaction*	$r_{CH_4} = \frac{28.4 \frac{mmol}{g\ s\ bar^2}\ P_{H_2} P_{CO}}{\left(1 + 1.6\ bar^{-1} P_{H_2} + 11.8\ bar^{-1} P_{CO}\right)^2}$	1.56E-04
2	*Surface reaction*	$r_{CH_4} = \frac{\frac{25.8 mmol}{g\ s\ bar^2} P_{H_2} P_{CO}}{\left(1 + 0.8\ bar^{-1} P_{H_2O} + 15\ bar^{-1} P_{CO}\right)^2}$	2.36E-04
3	*H_2 Adsorption*	$r_{CH_4} = \frac{4 \frac{mmol}{g\ s} 0.7\ bar^{-1} P_{H_2}}{1 + 0.7 bar^{-1} P_{H_2} + 0.1\ bar^{-1} P_{CO}}$	1.71E-04
4	$C* + 2H*$	$r_{CH_4} = \frac{11.4 \frac{mmol}{g\ s} 1.4\ bar^{-0.5} (0.7\ bar^{-0.5})^2 P_{CO}^{0.5} P_{H_2}}{\left(1 + 1.4\ bar^{-0.5} P_{CO}^{0.5} + 0.7\ bar^{-0.5} P_{H_2}^{0.5}\right)^3}$	1.62E-04
5	$C* + H*$	$r_{CH_4} = \frac{0.6 \frac{mmol}{g\ s} 1.9\ bar^{-1} P_{CO}^{0.5} P_{H_2}^{0.5}}{\left(1 + 1.9\ bar^{-1} \mathrm{P_{CO}} + 0.1\ bar^{-0.5} \mathrm{P_{H_2O}} \mathrm{P_{H_2}^{-0.5}}\right)^2}$	2.13E-04
6	$CH* + H*$	$r_{CH_4} = \frac{1.0 \frac{mmol}{g\ s\ bar^{0.5}} 3.0\ bar^{-1} P_{CO}^{0.5} P_{H_2}}{\left(1 + 0.14\ bar^{-0.5} P_{H_2O} P_{H_2}^{-0.5} + 3.0\ bar^{-1} P_{CO}^{0.5} P_{H_2}^{0.5}\right)^2}$	1.65E-04
7	$COH* + H*$	$r_{CH_4} = \frac{0.9 \frac{mmol}{g\ s\ bar^{-0.5}} 13.7\ \mathrm{bar}^{-1.5} P_{CO} P_{H_2}}{\left(1 + 0.1\ \mathrm{bar}^{-0.5} P_{H_2O} P_{H_2}^{-0.5} + 13.7\ \mathrm{bar}^{-1.5} P_{CO} P_{H_2}^{0.5}\right)^2}$	1.78E-04
8	$CO* + H*$	$r_{CH_4} = \frac{253 \frac{mmol}{g\ s\ bar^{-0.5}} 10.9\ bar^{-1} 3x10^{-3} bar^{-1} P_{H_2}^{0.5} P_{CO}}{\left(1 + 10.9\ bar^{-1} P_{CO} + 3x10^{-3} bar^{-1} P_{H_2} + 0.5\ P_{H_2O} P_{H_2}^{-1}\right)^2}$	2.33E-04
9	$CO* + H*$	$r_{CH_4} = \frac{0.9 \frac{mmol}{g\ s\ bar^{-0.5}} 7.4\ bar^{-1} P_{H_2}^{0.5} P_{CO}}{\left(1 + 7.4\ bar^{-1} P_{CO} + 0.1\ P_{H_2O} P_{H_2}^{-1}\right)^2}$	2.04E-04
10	$CO* + H*$	$r_{CH_4} = \frac{0.9 \frac{mmol}{g\ s} 7.3\ bar^{-1} (0.8\ bar^{-0.25})^2 P_{H_2}^{0.5} P_{CO}}{(1 + 7.3\ bar^{-1} P_{CO})^2}$	2.05E-04
11	$HCO* + H*$	$\mathrm{r_{CH_4}} = \frac{25.4 \frac{mmol}{g\ s\ bar^2} P_{H_2} P_{CO}}{(1 + 15\ bar^{-1} P_{CO})^2}$	2.42E-04
12	$H_2 + 2*$ $C* + H*$	$r_{CH_4} = \frac{11 \frac{mmol}{g\ s\ bar} P_{H_2}}{16.1 \left(1 + (0.3\ bar^{-1})^{0.5} P_{H_2}^{0.5}\right)^2 + 0.7}$	1.74E-04

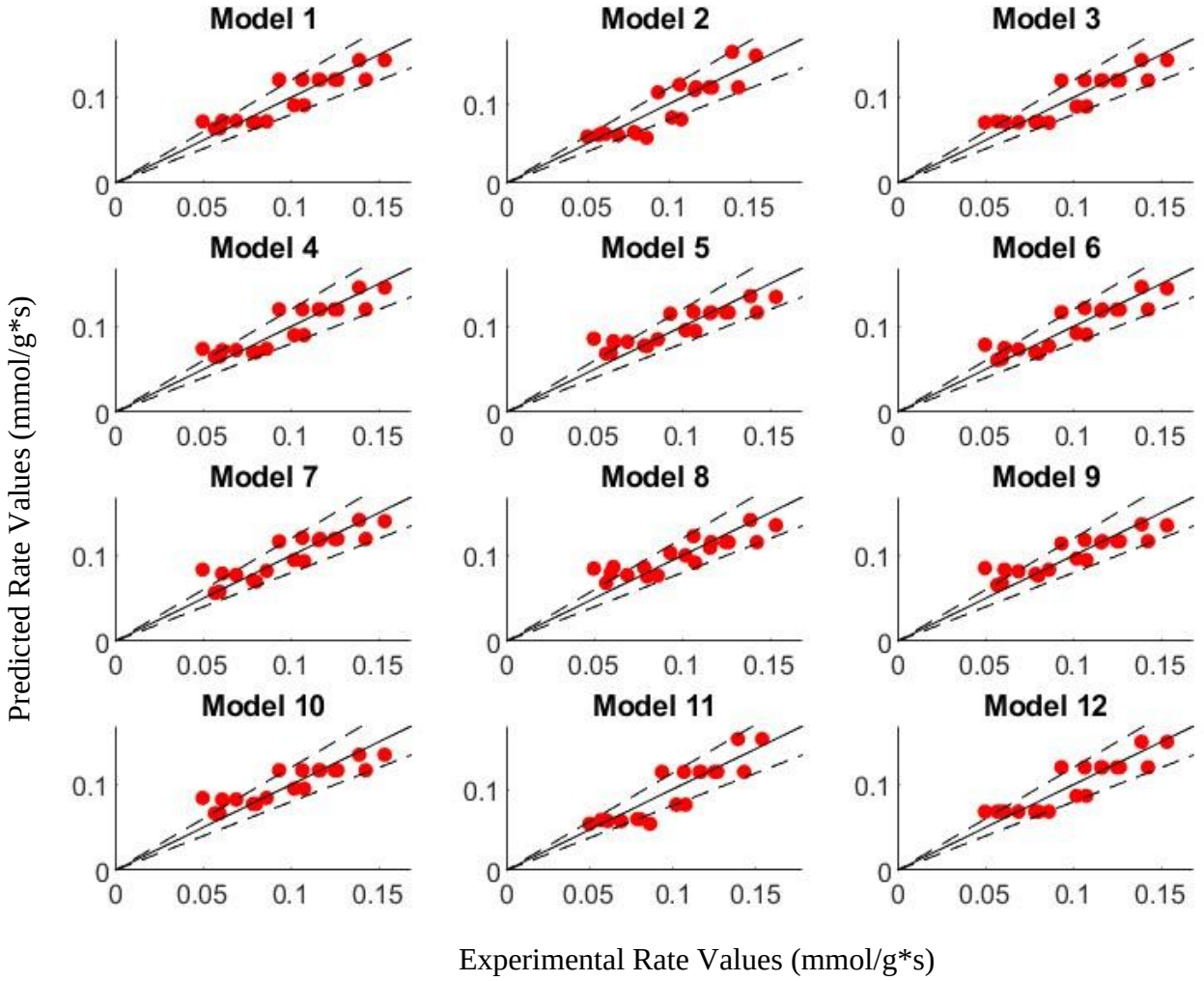

Figure 4.74. Experimental versus predicted CH_4 production rates within ±20% range.

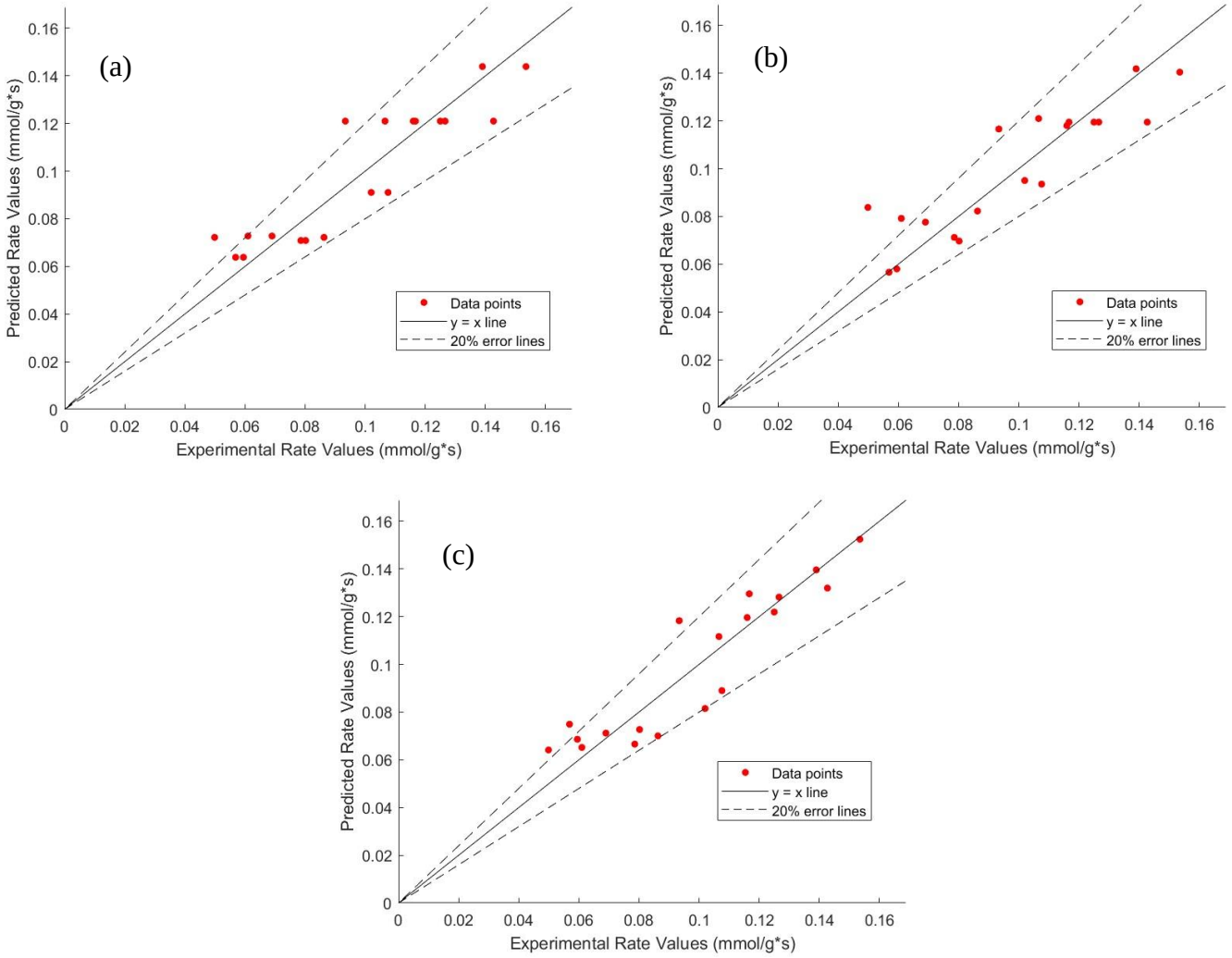

Figure 4.75. Predicted versus the experimental CH_4 production rates for Model 1(a), Model 7(b), and power-law type rate (c).

The results of Models 1 and 7 were compared with those of the power-law rate expression (Figure 4.75). However, this comparison alone does not allow for a definitive choice among the three models.

5. CONCLUSION

5.1. Conclusions

The purpose of this study was to design and develop Ni-based methanation catalysts with high and efficient methane production activity, selectivity, and stability under H2/CO<3 conditions by integrating CO methanation and WGS reactions.

In this context, a comprehensive study comprising five cohesive sections has been conducted. In the first section, preliminary tests were carried out to evaluate the impact of experimental parameters on methanation performance using a conventional catalyst. Secondly, various catalyst bed configurations, utilizing classical methanation and WGS catalysts, were investigated to assess their effect on methanation performance. In the third section, in order to explore bifunctionality through the integration of WGS and methanation reactions within a single catalyst, new catalyst formulations with different metals, metal precursors, metal loading combinations, preparation methods, and pretreatment conditions were synthesized and evaluated. Ce-Ni catalysts, which yielded the relatively highest and lowest performance results, were comprehensively characterized using XPS, XRD, HR-TEM, SEM, and RAMAN techniques in the fourth section. Finally, kinetic studies of the CO methanation reaction were conducted on the 5%Ce-10%Ni/γ-Al_2O_3 catalyst, which demonstrated the highest performance results.

The major conclusion obtained from the preliminary tests conducted as the first part of the study is as follows:

- Adding promoters significantly altered the observed H_2-TPR profiles of Ni/γ-Al_2O_3 catalysts. The peaks in the 350-550 °C range, previously observed in catalysts without promoters and associated with the reduction of NiO species having a low interaction with the alumina support, shifted to higher temperatures. This shift indicated an enhanced interaction between the metal and the support due to the addition of promoters.

The following conclusions can be drawn from the second part of the study, which

explores various catalyst bed configurations utilizing classical methanation and WGS catalysts, aiming for maximum CH_4 yield while minimizing undesirable byproducts:

- To assess the effect of a physical mixture of WGS and methanation catalysts on CO conversion and CH_4 yield, WGS and methanation catalysts were mixed in varying weight ratios and examined under different feed conditions to evaluate their performance. However, using a catalyst mixture, as opposed to a pure methanation catalyst, did not result in a positive effect on CO conversion and CH_4 yield values.
- To enhance methane production, beds of methanation reaction catalysts, prepared for CO and CO_2 methanation reactions, were utilized sequentially within the same reactor. However, using two- and three-bed configurations with different CO and CO_2 methanation catalysts did not demonstrate superior performance in terms of CO conversion and CH_4 yield.

In the third part, bi-metallic Ni-based methanation catalysts with different promoters (such as Ce, La, Mg, and Mn), supports (such as γ-Al_2O_3, ZrO_2, and SBA-15), and metal loading compositions were prepared to explore bifunctionality through the integration of WGS and methanation reactions within a single catalyst. These catalysts were investigated for their performance under different feed compositions and temperatures. The findings of this section can be summarized as follows:

- At 400 °C, with an H_2/CO ratio of 3, most catalysts exhibited high CO conversion performances, ranging from ca. 93% to 99%, with the highest conversion observed for 5%Ce-10%Ni/SBA-15-550. The lowest CO methanation value was recorded for 5%Ce-10%Ni/ZrO_2 at 86.5%.
- Reducing the H_2/CO ratio to 2 caused a drop in CO conversion for 1%Mg-10%Ni/γ-Al_2O_3 (from 92.9% to 84.2%) and 15% Ni/SBA-15-750 (from 92.7% to 72.6%). However, other catalysts maintained stable CO conversion values.
- At an H_2/CO ratio of 1, 1.7%Mn-15%Ni/γ-Al_2O_3 exhibited the highest CO conversion (84.6%), while 5%Ce-10%Ni/ZrO_2 had the lowest (39.9%). The highest CH_4 yield was obtained with 15% Ni/SBA-15-550 (43.8%).
- Temperature had a considerable impact on catalyst performance. Reducing the temperature to 350 °C caused a significant decrease in the performance of the 15%

Ni/SBA-15-750 catalyst. At 300 °C, 10% Ni/SBA-15 and 15% Ni/SBA-15-750 showed the worst performance, while at 250 °C, only six out of fourteen catalysts exhibited CO conversion.

- Among the six active catalysts at 250 °C (3%La-10%Ni/γ-Al_2O_3, 5%La-10%Ni/γ-Al_2O_3, 5%Ce-10%Ni/γ-Al_2O_3, 5%Ce-10%Ni/ZrO_2, 5%Ce-10%Ni/SBA-15-550, and 1.7%Mn-15%Ni/γ-Al_2O_3), 5%Ce-10%Ni/γ-Al_2O_3 demonstrated the best performance. Further tests with reduced catalyst amount at 250 °C and an H_2/CO feed ratio of 2 confirmed the superiority of 5%Ce-10%Ni/γ-Al_2O_3 catalyst.
- Two stability tests conducted over 72 hours with different H2/CO ratios established the stability of the 5%Ce-10%Ni/γ-Al_2O_3 catalyst at 400 °C. However, the stability test conducted at 250 °C with an H_2/CO ratio of 2 showed a 17% activity loss over 72 hours, with CO conversion dropping from ca. 95% to ca. 79%.

In the fourth part, the freshly reduced and spent samples of 5%Ce-10%Ni/γ-Al_2O_3, 5%Ce-10%Ni/ZrO_2, 5%Ce-10%Ni/SBA-15-550, and 10% Ni/γ-Al_2O_3 catalysts were characterized. The significant findings derived from this section are outlined as follows:

- XPS analysis revealed that all catalysts exhibited distinct peaks for metallic Ni, NiO, and Ni^{2+} in octahedral coordination. For Al_2O_3 supported catalysts, the introduction of Ce shifted the binding energies to slightly higher levels, indicating enhanced electronic interactions. Comparison of freshly reduced and spent samples showed a reduction in both metallic Ni and NiO during the reaction, while the Ni^{2+} content uniquely decreased for the 5%Ce-10%Ni/γ-Al_2O_3 catalyst.
- Metallic nickel (Ni^0) was evident in both freshly reduced Al_2O_3-supported catalysts, with a noted decrease in NiO diffraction peaks upon Ce addition, suggesting improved Ni dispersion, enhanced NiO reduction, or transformation to another phase like $NiAl_2O_4$. Ce addition also resulted in sharper Ni^0 peaks, indicating better crystallization or larger crystallite sizes. XRD spectra of spent 5%Ce-10%Ni/γ-Al2O3 samples under various conditions showed no significant differences, except for slightly more pronounced $NiAl_2O_4$ peaks in the 72-hour tests, indicating gradual formation of $NiAl_2O_4$ over time.
- Raman spectra analysis of spent 5%Ce-10%Ni/γ-Al_2O_3 catalysts revealed significant insights into the effects of reaction temperature on catalyst performance and carbon

deposition. The presence of the fluorite-like phase of CeO_2 was confirmed only in samples tested at 400 °C, suggesting better stability at higher temperatures. The spectra also identified amorphous and graphitic carbon deposition, with significantly more carbon accumulation observed at 250 °C compared to 400 °C. This indicates that lower temperatures favor carbon deposition, leading to catalyst deactivation, whereas higher temperatures mitigate this effect.

- Both SEM and TEM analyses revealed that Ce addition to Ni catalysts results in distinct Ce and Ni cluster formations, with Ce clusters appearing brighter and forming discrete structures on top of Ni aggregates. This specific arrangement was prominent in 5%Ce-10%Ni/γ-Al_2O_3 but not observed in 5%Ce-10%Ni/ZrO_2 and 5%Ce-10%Ni/SBA-15, indicating that the support material significantly influences the distribution and interaction of Ce and Ni particles.

The last part of this research was dedicated to kinetic studies of the CO methanation reaction conducted on the 5%Ce-10%Ni/γ-Al_2O_3 catalyst. Major conclusion of this section are as follows:

- A simple power-law type rate equation did not adequately explain the reaction data, with R^2 and MSE values of 0.85 and $1x10^{-4}$, respectively. Incorporating product terms into the rate expression did not significantly improve the model's prediction efficiency.
- The reaction orders were found to be 0.78 for H_2, -0.07 for CO. These results are consistent with literature, indicating that H_2 has a positive reaction order, CO has a slightly negative order.
- Experiments conducted at various temperatures revealed two distinct kinetic regimes between 300-350 °C and 350-400 °C, suggesting different reaction mechanisms or rate-determining steps. The activation energy decreased with increasing temperature, consistent with literature findings.
- Among the twelve Langmuir Hinshelwood type kinetic models evaluated using multivariable nonlinear regression and the Leave-One-Out (LOO) cross-validation method, Model 7, based on an associative mechanism with COH* hydrogenation as the rate-determining step (RDS) and including an H_2O inhibition term, showed the

best performance in terms of RMSE. Model 1, a Langmuir-Hinshelwood model based on surface C* hydrogenation as the RDS, yielded the best MSE.

- Models including H_2O inhibition terms, such as Models 2 and 11, demonstrated better performance at low reaction rates.
- The power-law type rate expression, subjected to LOO cross-validation, showed lower average RMSE and MSE values compared to Model 7, suggesting it performed better in terms of these metrics. However, final model parameter training indicated Model 1 provided the minimum MSE value and the best fit. The comparison among Models 1, 7, and the power-law rate expression did not definitively determine the best model.

5.2. Recommendations

Based on the findings of this study, the following recommendations are proposed for future research:

- Al_2O_3-supported catalysts with different Ce and Ni loadings/ loading ratios prepared through different methods and conditions can be characterized, tested for their methanation performance, and comparatively evaluated.
- Trimetallic catalysts can be designed and tested to increase CH_4 yield values.
- Kinetic experiments can be conducted over a wider range of temperatures and a more extensive set of reactant and product compositions.
- In order to determine the reaction mechanism and kinetic rate expression, *operando* transient kinetics tests utilizing FTIR-DRIFTS-MS can be conducted on the 5%Ce-10%Ni/γ-Al_2O_3 catalyst as an independent PhD thesis.

REFERENCES

Abdel-Mageed, A.M., S. Eckle and R.J. Behm, 2015, "High Selectivity of Supported Ru Catalysts in the Selective CO Methanation - Water Makes the Difference", *Journal of the American Chemical Society*, Vol. 137, pp. 8672-8675.

Alzamora, L.E., J.R.H. Ross, E.C. Kruissink and L.L. Vanreijen, 1981, "Coprecipitated Nickel–Alumina Catalysts for Methanation at High Temperature. Part 2. Variation of Total and Metallic Areas as a Function of Sample Composition and Method of Pretreatment", *Journal of the Chemical Society*, Vol. 1, pp. 665-681.

Anderson, R.B., *The Fischer-Tropsch Synthesis*, Academic Press, Orlando, 1984.

Audier, M., M. Coulon and L. Bonnetain, 1979, "Hydrogenation of Catalytic Carbons Obtained by CO Disproportionation or CH_4 Decomposition on Nickel", *Carbon*, Vol. 17, pp. 391-394.

Aziz, M.A.A., A.A. Jalil, S. Triwahyono and A. Ahmad, 2015, "CO_2 Methanation over Heterogeneous Catalysts: Recent Progress and Future Prospects", *Green Chemistry*, Vol. 17, pp. 2647–2663.

Başar, M.S, 2017, *A Study on CO-free Hydrogen Production and Adsorbent Design for Selective Carbon Dioxide Removal*, Ph.D. Thesis, Boğaziçi University.

Bell, D.A., B.F. Towler and M. Fan, *Coal Gasification and its Applications*, Elsevier, Oxford, 2011.

Berrar, D., 2019, "Cross-Validation", *Encyclopedia of Bioinformatics and Computational Biology*, Vol. 1, pp. 542-545.

Chen, A., T. Miyao, K. Higashiyama and M. Watanabe, 2014, "High Catalytic Performance of Mesoporous Zirconia Supported Nickel Catalysts for Selective CO Methanation", *Catalysis Science & Technology*, Vol. 4, pp. 26-29.

Choi, C., A. Khuenpetch, W. Zhang, S. Yasuda, Y. Lin, H. Machida, H. Takano, K. Izumiya, Y. Kawajiri and K. Norinaga, 2021, "Determination of Kinetic Parameters for CO_2 Methanation (Sabatier Reaction) Over Ni/ZrO_2 at a Stoichiometric Feed-Gas Composition under Elevated Pressure", *Energy Fuels*, Vol. 35, 20216-20223.

De, S., J. Zhang, R. Luque and N. Yan, 2016, "Ni-Based Bimetallic Heterogeneous Catalysts for Energy and Environmental Applications", *Energy & Environmental Science*, Vol. 9, pp. 3314-47.

Ding, M.Y., J.Y. Tu, T.J. Wang, L.L. Ma, C.G. Wang and L.G. Chen, 2015, "Bio-Syngas Methanation Towards Synthetic Natural Gas (SNG) over Highly Active Al_2O_3–CeO_2 Supported Ni Catalyst", *Fuel Processing Technology*, Vol. 134, pp. 480–486.

Dong, W.S., H.S. Roh, K.W. Jun, S.E. Park and Y.S. Oh, 2002, "Methane Reforming over Ni/Ce-ZrO_2 Catalysts: Effect of Nickel Content", *Applied Catalysis A: General*, Vol. 226, pp. 63–72.

Gao, J., Y. Wang, Y. Ping, D. Hu, G. Xu, F. Gu and F. Su, 2012, "A Thermodynamic Analysis of Methanation Reactions of Carbon Oxides for the Production of Synthetic Natural Gas", *RSC Advances*, Vol. 2, pp. 2358–2368.

Gao, J., C. Jia, M. Zhang, F. Gu, G. Xu and F. Su, 2013, "Effect of Nickel Nanoparticle Size in Ni/a-Al_2O_3 on CO Methanation Reaction for the Production of Synthetic Natural Gas", *Catalysis Science and Technology*, Vol. 3, pp. 2009-2015.

Gao, J., Q. Liu, F. Gu, B. Liu, Z. Zhong and F. Su, 2015, "Recent Advances in Methanation Catalysts for the Production of Synthetic Natural Gas", *RSC Advances*, Vol. 5, pp. 22759–22776.

Garbis, P., C. Kern and A. Jess, 2019, “Kinetics and Reactor Design Aspects of Selective Methanation of CO Over a Ru/Al_2O_3 Catalyst in CO_2/H_2 Rich Gases”, *Energies*, Vol. 12, pp. 469-84.

Hess, C., 2021, “New Advances in Using Raman Spectroscopy for the Characterization of Catalysts and Catalytic Reactions”, *Chemical Society Reviews*, Vol. 50, pp. 3519-3564.

Hwang, S., J. Lee, U. G. Hong, J. G. Seo, J. C. Jung, D. J. Koh, H. Lim, C. Byun and I.K. Song, 2011, “Methane Production from Carbon Monoxide and Hydrogen over Nickel–Alumina Xerogel Catalyst: Effect of Nickel Content”, *Journal of Industrial and Engineering Chemistry*, Vol. 17, pp. 154-157.

Hu, D., J. Gao, Y. Ping, L. Jia, P. Gunawan, Z. Zhong, G. Xu, F. Gu and F. Su, 2012, “Enhanced Investigation of CO Methanation over Ni/Al_2O_3 Catalysts for Synthetic Natural Gas Production”, *Industrial & Engineering Chemistry Research*, Vol. 51, pp. 4875-86.

Jimenez, R., K. Fuentes, M. Paz Medina, S. Godoy, F. Gracia and A. Karelovic, 2019, “The Kinetic Effect of H_2O Pressure on CO Hydrogenation over Different Rh Cluster Sizes”, *International Journal of Hydrogen Energy*, Vol. 44, pp. 768-777.

Jurascı´k, M., A. Sues and K.J. Ptasinski, 2009, “Exergetic Evaluation and Improvement of Biomass-to-Synthetic Natural Gas Conversion”, *Energy & Environmental Science*, Vol. 2, pp. 791–801.

Kesim, B., 2017, *An Experimental Study on Optimization of Pt-Based Trimetallic WGS Catalysts*, M.Sc. Thesis, Boğaziçi University**.**

Kim, M.J., J.R. Youn, H.J. Kim, M.W. Seo, D. Lee, K.S. Go, K.B. Lee and S.G. Jeon, 2020, “Effect of Surface Properties Controlled by Ce Addition on CO_2 Methanation over $Ni/Ce/Al_2O_3$ Catalyst”, *International Journal of Hydrogen Energy*, Vol. 45, pp. 24595-24603.

Klose, J. and M. Baerns, 1984, "Kinetics of the Methanation of Carbon Monoxide on an Alumina-Supported Nickel Catalyst", *Journal of Catalysis*, Vol. 85, pp. 105-116.

Kopyscinski, J., T.J. Schildhauer and S.M.A. Biollaz, 2010, "Production of Synthetic Natural Gas (SNG) From Coal and Dry Biomass – A Technology Review from 1950 to 2009", *Fuel*, Vol. 89, pp. 1763-1783.

Kopyscinski, J., T.J. Schildhauer, F. Vogel, S.M.A. Biollaz, and A. Wokaun, 2010, "Applying Spatially Resolved Concentration and Temperature Measurements in a Catalytic Plate Reactor for the Kinetic Study of CO Methanation", *Journal of Catalysis*, Vol 271, pp. 262-279.

Kruissink, E.C., L.L. Vanreijen and J.R.H. Ross, 1981, "Coprecipitated Nickel–Alumina Catalysts for Methanation at High Temperature. Part 1. Chemical Composition and Structure of the Precipitates", *Journal of the Chemical Society*, Vol. 1, pp. 649-663.

Kumabe, K., T. Hanaoka, S. Fujimoto, T. Minowa and K. Sakanishi, 2007, "Co-Gasification of Woody Biomass and Coal with Air and Steam", *Fuel*, Vol. 86, pp. 684-689.

Kustov, A.L., A.M. Frey, K.E. Larsen, T. Johannessen, J.K. Nørskov and C.H. Christensen, 2007, "CO Methanation over Supported Bimetallic Ni–Fe Catalysts: From Computational Studies Towards Catalyst Optimization", *Applied Catalysis A: General*, Vol. 320, pp. 98-104.

Li, J., L. Zhou, Q. Zhu and H. Li, 2015, "CO Methanation over a Macro–Mesoporous Al_2O_3 Supported Ni Catalyst in a Fluidized Bed Reactor", *RSC Advances*, Vol. 5, pp. 64486-64494.

Liu, Q., J. Gao, F. Gu, X. Lu, Y. Liu, H. Li, Z. Zhong, B. Liu, G. Xu and F. Su, 2015, "One-Pot Synthesis of Ordered Mesoporous Ni–V–Al Catalysts for CO Methanation", *Journal of Catalysis*, Vol. 326, pp. 127-138.

Liu, Y., Y. Wu, Z. Akhtamberdinova, X. Chen, G. Jiang and D. Liu, 2018, "Dry Reforming of Shale Gas and Carbon Dioxide with Ni-Ce-Al_2O_3 Catalyst: Syngas Production Enhanced over Ni-CeO_x Formation", *ChemCatChem*, Vol. 10, pp. 4689-4698.

Masnadi-Shirazi, M.S., 2014, *Biomass/Fossil Fuel Co-Gasification with and without Integrated CO_2 Capture*, Ph.D. Thesis, The University of British Columbia.

Maziviero, F.V., D.M.A. Melo, R.L.B.A. Medeiros, J.C.A. Silva, T.R. Araújo, A.A.S. Oliveira, Y.K.R.O. Silva and M.A.F. Melo, 2024, "Influence of Mn, Mg, Ce and P Promoters on Ni-X/Al_2O_3 Catalysts for Dry Reforming of Methane", *Journal of the Energy Institute*, Vol. 113, pp. 101523-101534.

Mebrahtu, C., S. Perathoner, G. Giorgianni, S. Chen, G. Centi, F. Krebs, R. Palkovits and S. Abate, 2019, "Deactivation Mechanism of Hydrotalcite-Derived Ni–Alox Catalysts During Low-Temperature CO_2 Methanation via Ni-Hydroxide Formation and the Role of Fe in Limiting This Effect", *Catalysis Science & Technology*, Vol. 9, pp. 4023-4035.

Miguel, C.V., M.A. Soria, A. Mendes and L.M. Madeira, 2015, "Direct CO_2 Hydrogenation to Methane or Methanol from Postcombustion Exhaust Streams: A Thermodynamic Study", *Journal of Natural Gas Science and Engineering*, Vol. 22, pp. 1-8.

Razzaq, R., C. Li and S. Zhang, 2013, "Coke Oven Gas: Availability, Properties, Purification, and Utilization in China", *Fuel*, Vol. 113, pp. 287–299.

Romano, L. and F. Ruggeri, 2015, "Methane from Syngas – Status of Amec Foster Wheeler VESTA Technology Development", *Energy Procedia*, Vol. 81, pp. 249–254.

Sanchez-Escribano, V., M.L Vargas, E. Finocchio and G. Busca, 2007, "On the Mechanisms and the Selectivity Determining Steps in Syngas Conversion over Supported Metal Catalysts: An IR Study" *Applied Catalysis A: General*, Vol. 316, pp. 68-74.

Sarkari, M., F. Fazlollahi, H. Atashi, A.A. Mirzaei and V. Hosseinpour, 2012, "Fischer–Tropsch Synthesis: Development of Kinetic Expression for a Sol–Gel Fe–Ni/Al_2O_3 Catalyst", *Fuel Processing Technology*, Vol. 97, pp. 130–139.

Si, J., G. Liu, J. Liu, L. Zhao, S. Li, Y. Guan and Y. Liu, 2016, "Ni Nanoparticles Highly Dispersed on ZrO_2 and Modified with La_2O_3 for CO Methanation", *RSC Advances*, Vol. 6, pp. 12699-12707.

Sughrue, E.L. and C.H. Bartholomew, 1982, "Kinetics of Carbon Monoxide Methanation on Nickel Monolithic Catalysts", *Applied Catalysis*, Vol. 2, pp. 239-256.

Tada, S. and R. Kikuchi, 2014, "Preparation of Ru Nanoparticles on TiO_2 Using Selective Deposition Method and Their Application to Selective CO_2 Methanation", *Catalysis Science & Technology*, Vol. 4, pp. 26-29.

Tampa Electric Integrated Gasification Combined-Cycle Project - Project Performance Summary, Tampa, 2004.

Teh, L.P., S. Triwahyono, A.A. Jalil, C.R. Mamat, S.M. Sidik, N. A.A. Fatah, R.R. Mukti and T. Shishido, 2015, "Nickel-Promoted Mesoporous ZSM5 for Carbon Monoxide Methanation", *RSC Advances*, Vol. 5, pp. 64651-64660.

Tian, D., Z. Liu, D. Li, H. Shi, W. Pan and Y. Cheng, 2013, "Bimetallic Ni–Fe Total-Methanation Catalyst for the Production of Substitute Natural Gas Under High Pressure", *Fuel*, Vol. 104, pp. 224-229.

Vlasenko, V.M. and G.E. Yuzefovich, 1969, "Mechanism of the Catalytic Hydrogenation of Oxides of Carbon to Methane", *Russian Chemical Reviews*, Vol. 38, pp. 728-739.

Wang, B., Z. Hu, S. Liu, M. Jiang, Y. Yao, Z. Li and X. Ma, 2014, "Effect of Sulphidation Temperature on the Performance of NiO–MoO_3/G-Al_2O_3 Catalysts for Sulphur-Resistant Methanation", *RSC Advances*, Vol. 4, pp. 56174-56182.

Wang, B., Y. Yao , M. Jiang , Z. Li , X. Ma , S. Qin and Q. Sun, 2014, "Effect of Cobalt and Its Adding Sequence on the Catalytic Performance of MoO_3/Al_2O_3 Toward Sulfur-Resistant Methanation", *Journal of Energy Chemistry*, Vol. 23, pp. 35-42.

Wang, H., Y. Fang, Y. Liu and X. Bai, 2012, "Perovskite $LaFeO_3$ Supported Bi-Metal Catalyst for Syngas Methanation", *Journal of Natural Gas Chemistry*, Vol. 21, pp. 745-752.

Wang, H., Y. Pei, M. Qiao and B. Zong, 2017, "Advances in Methanation Catalysis", *Catalysis*, Vol. 29, pp. 1-28.

Wang, R., Y. Li, R. Shi and M. Yang, 2011, "Effect of Metal–Support Interaction on the Catalytic Performance of Ni/Al_2O_3 for Selective Hydrogenation of Isoprene", *Journal of Molecular Catalysis A: Chemical*, Vol. 344, pp. 122‑127.

Wang, S., H. Wang, Q. Yin, L. Zhu and S. Yin, 2014, "Methanation of Bio-Syngas over a Biochar Supported Catalyst", *New Journal of Chemistry*, Vol. 38, pp. 4471-4477.

Xu, J. and G.F. Froment, 1989, "Methane Steam Reforming, Methanation and Water-Gas Shift: 1. Intrinsic Kinetics", *AIChE Journal*, Vol. 35, pp. 88-96.

Yan, X.L., Y. Liu, B.R. Zhao, Z. Wang, Y. Wang and C.J. Liu, 2013, "Methanation over Ni/SiO_2: Effect of the Catalyst Preparation Methodologies", *International Journal of Hydrogen Energy*, Vol. 38, pp. 2283-2291.

Yi, Q., W. Li, J. Feng and K. Xie, 2015, "Carbon Cycle in Advanced Coal Chemical Engineering", *Chemical Society Reviews*, Vol. 44, pp. 5409-5445.

Zhang, J., H. Xu, X. Jin, Q. Ge and W. Li, 2005, "Characterizations and Activities of The Nano-Sized Ni/Al_2O_3 and $Ni/La–Al_2O_3$ Catalysts for NH_3 Decomposition", *Applied Catalysis A: General*, Vol. 290, pp. 87–96.

Zhang, Q., X. Liao, S. Liu, H. Wang, Y. Zhang and Y. Zhao, 2022, "Tuning Particle Sizes and Active Sites of Ni/CeO_2 Catalysts and Their Influence on Maleic Anhydride Hydrogenation", *Nanomaterials*, Vol. 12, pp. 2156-2173.

Zhang, X., W.J. Sun and W. Chu, 2013, "Effect of Glow Discharge Plasma Treatment On The Performance of Ni/SiO_2 Catalyst in CO_2 Methanation", *Journal of Fuel Chemistry and Technology*, Vol. 41, pp. 96-101.

Zhao, A., W. Ying, H. Zhang, H. Ma and D. Fang, 2012, "Ni–Al_2O_3 Catalysts Prepared by Solution Combustion Method for Syngas Methanation", *Catalysis Communications*, Vol. 17, pp. 34-38.

Zhao, D., J. Feng, Q. Huo, N. Melosh,G. H. Fredrickson, B. F. Chmelka and G. D. Stucky, 1998, "Triblock Copolymer Syntheses of Mesoporous Science", *Science*, Vol. 279, pp. 548–552.

Zhou, X. and Y. Shen, 2014, "A Comparative Study of Pure Nickel and the Ni–CeO_2 Nanocrystalline Coatings: Microstructural Evolution, Oxidation Behavior, and Thermodynamic Stability" *Journal of Material Science,* Vol. 49, pp. 3755–3774.

Zhu, H., R. Razzaq, L. Jiang and C. Li, 2012, "Low-Temperature Methanation of CO in Coke Oven Gas Using Single Nanosized Co_3O_4 Catalysts", *Catalysis Communications*, Vol. 23, pp. 43-47.

APPENDIX A: CONVERSION VERSUS RESIDENCE TIME GRAPHS

CO conversion versus residance time graphs for methanation reaction are given below for experiments detailed in Table 3.7.

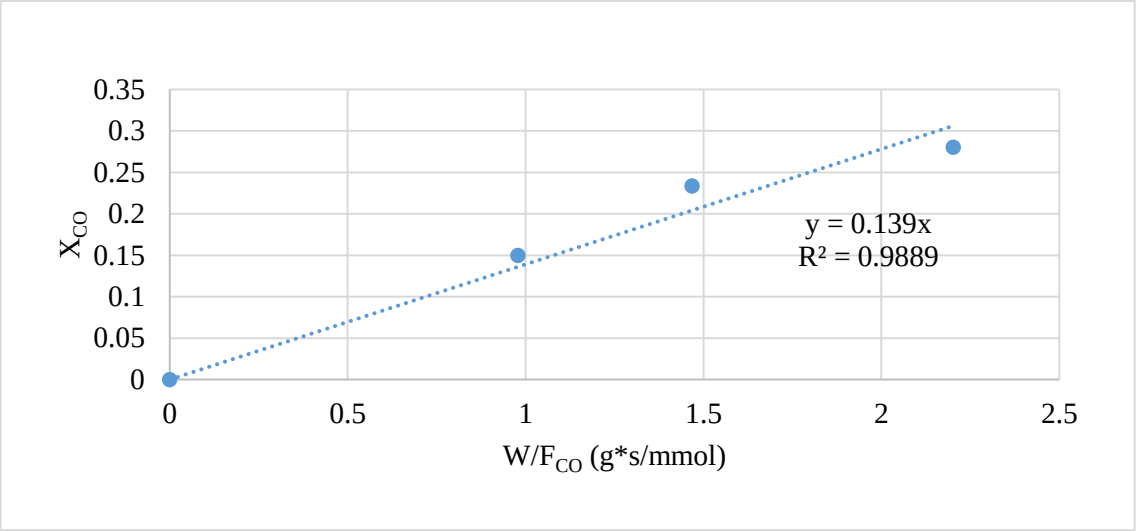

Figure A.1. Fractional CO conversion versus residence time graph for Experiment 1.

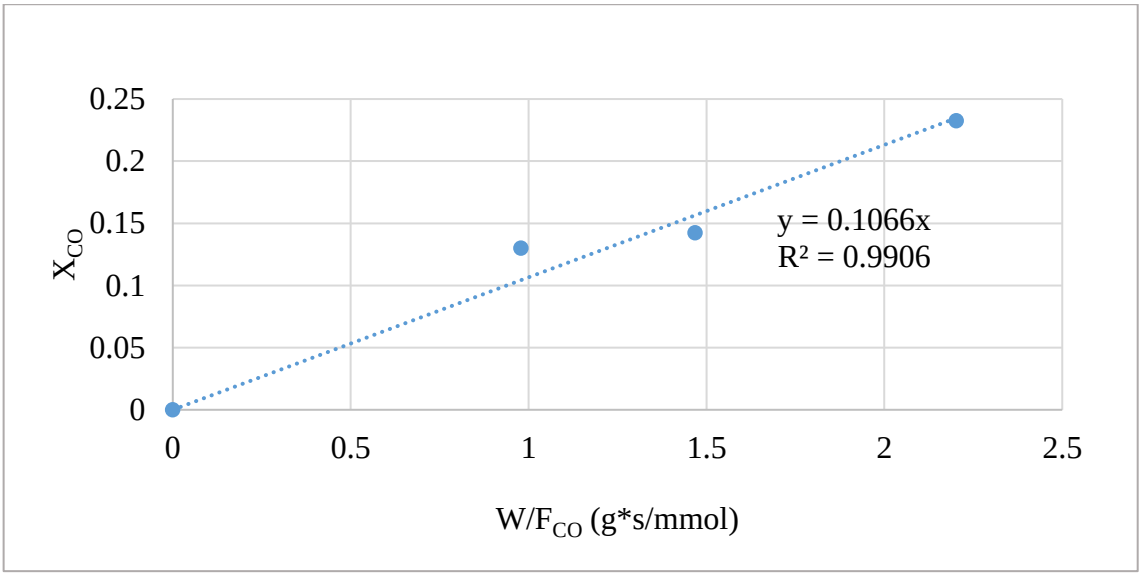

Figure A.2. Fractional CO conversion versus residence time graph for Experiment 2.

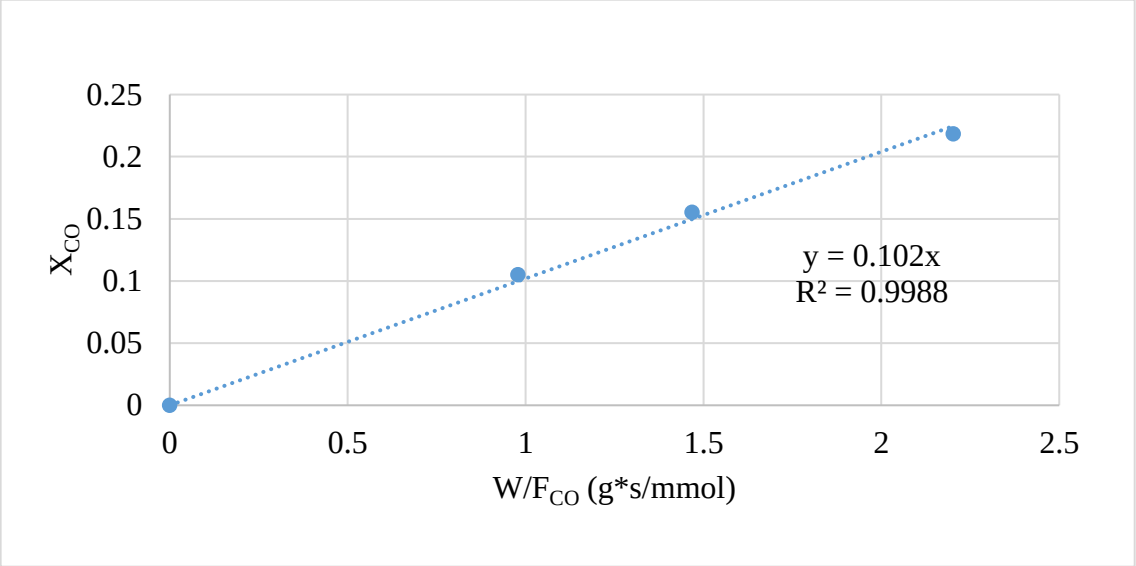

Figure A.3. Fractional CO conversion versus residence time graph for Experiment 3.

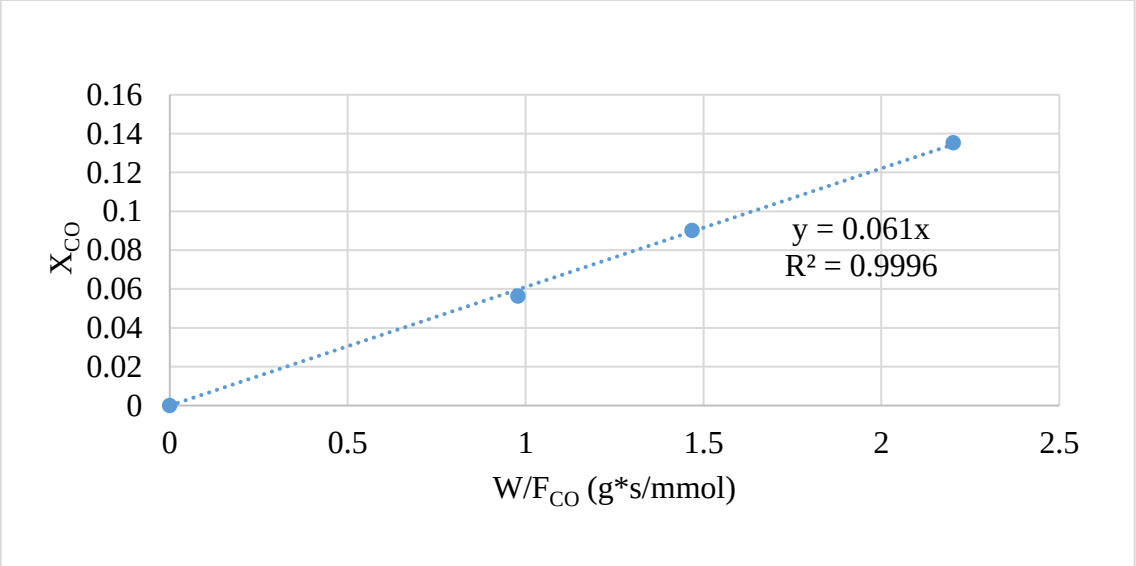

Figure A.4. Fractional CO conversion versus residence time graph for Experiment 4.

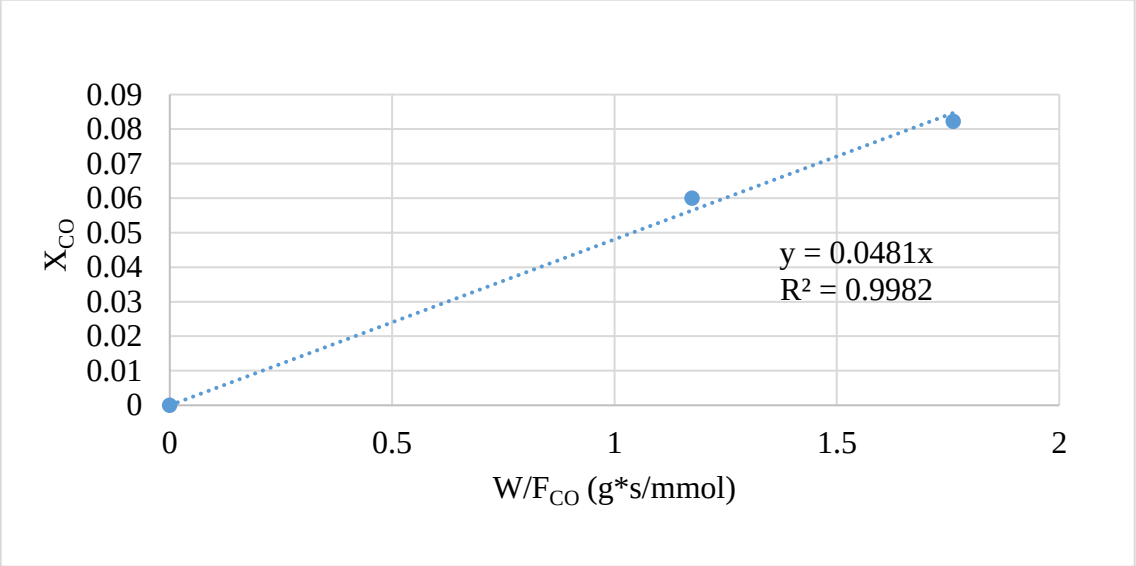

Figure A.5. Fractional CO conversion versus residence time graph for Experiment 5.

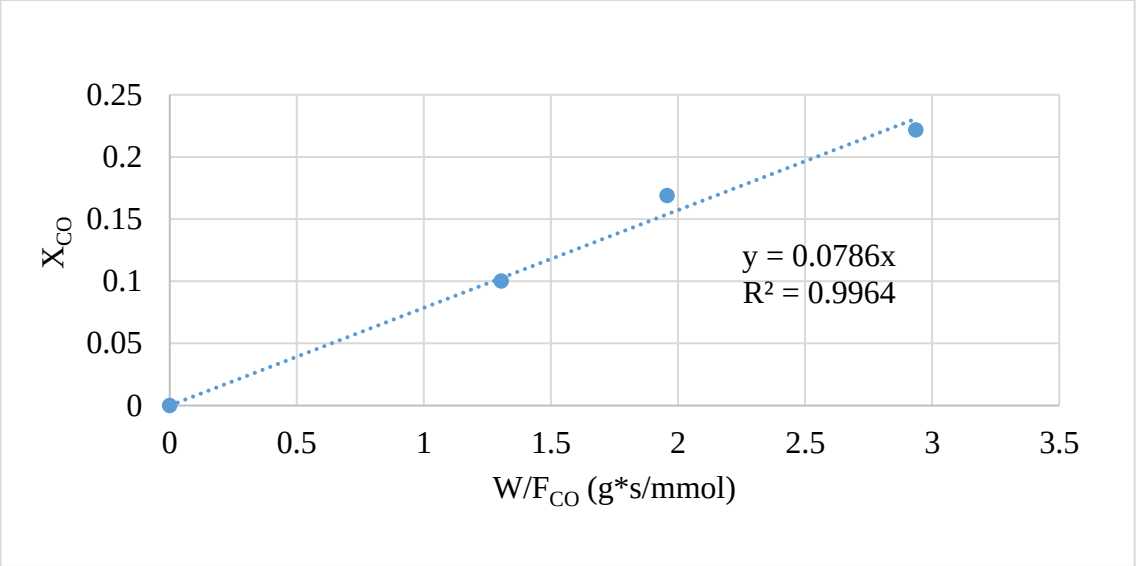

Figure A.6. Fractional CO conversion versus residence time graph for Experiment 6.

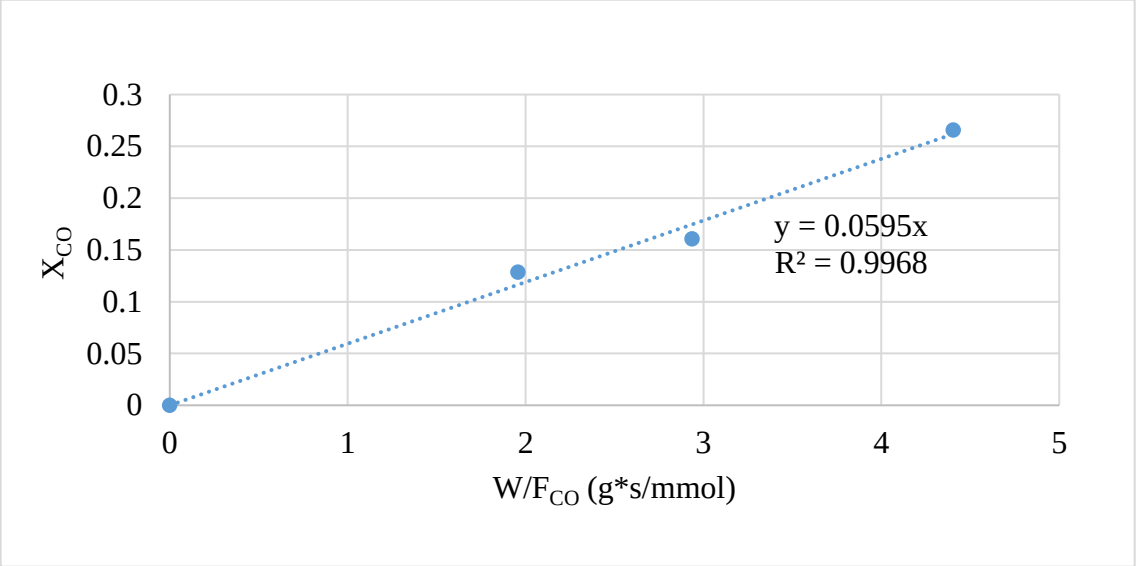

Figure A.7. Fractional CO conversion versus residence time graph for Experiment 7.

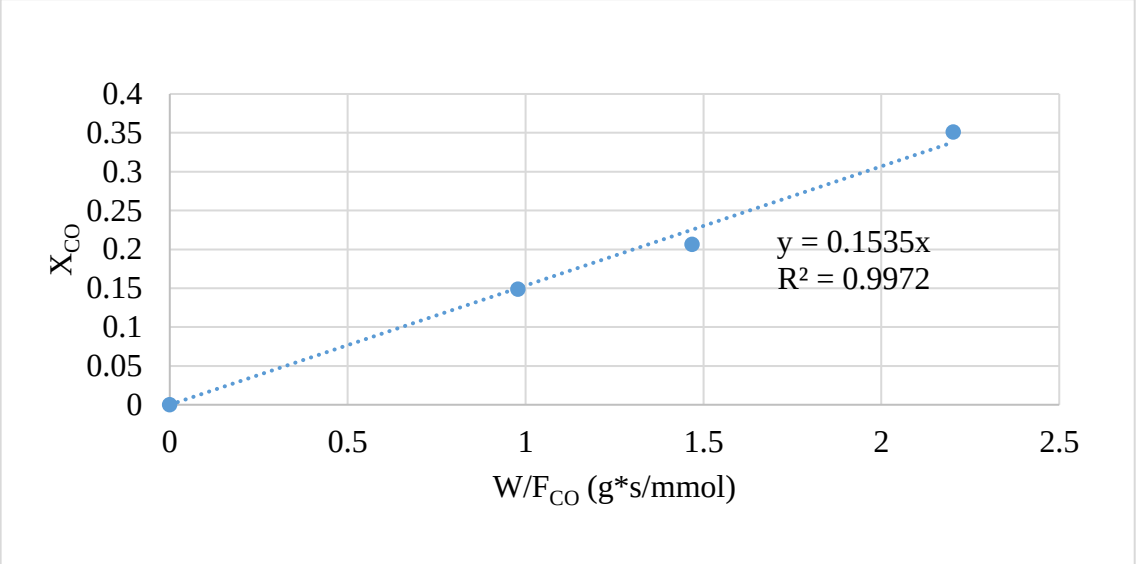

Figure A.8. Fractional CO conversion versus residence time graph for Experiment 8.

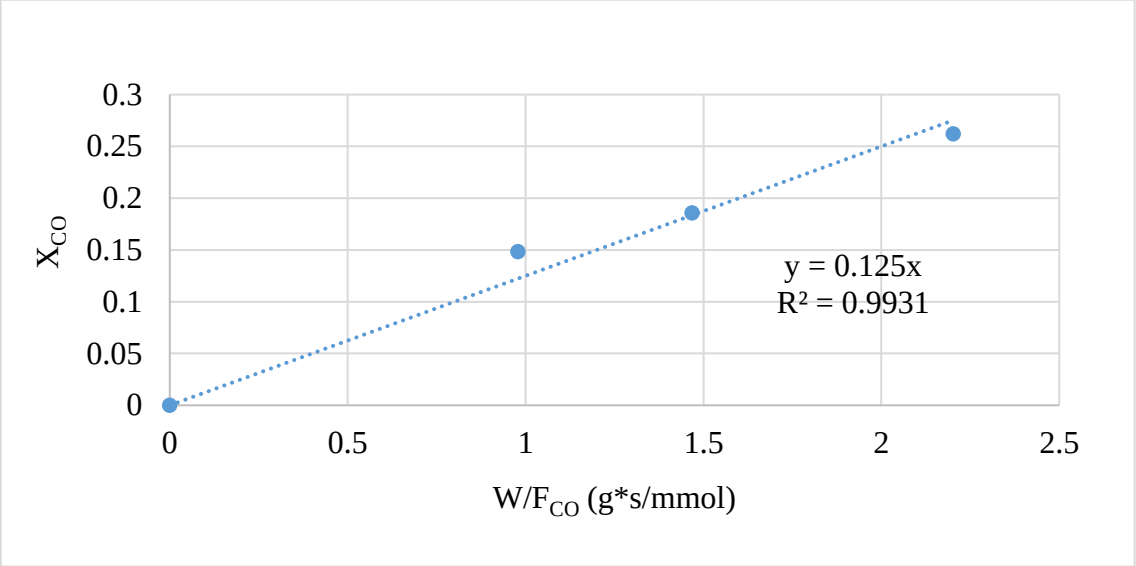

Figure A.9. Fractional CO conversion versus residence time graph for Experiment 9.

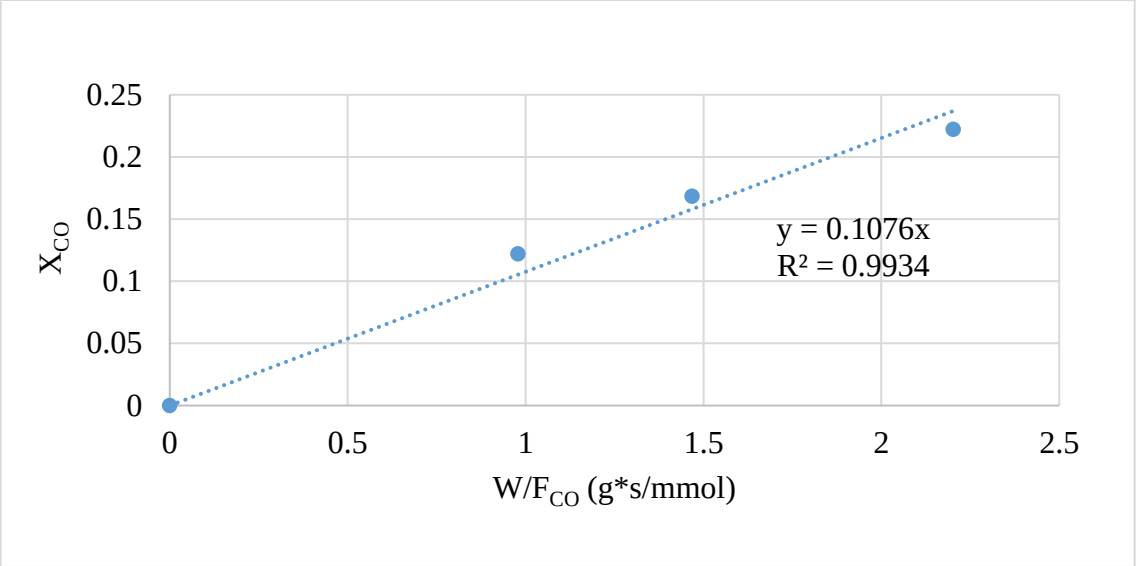

Figure A.10. Fractional CO conversion versus residence time graph for Experiment 10.

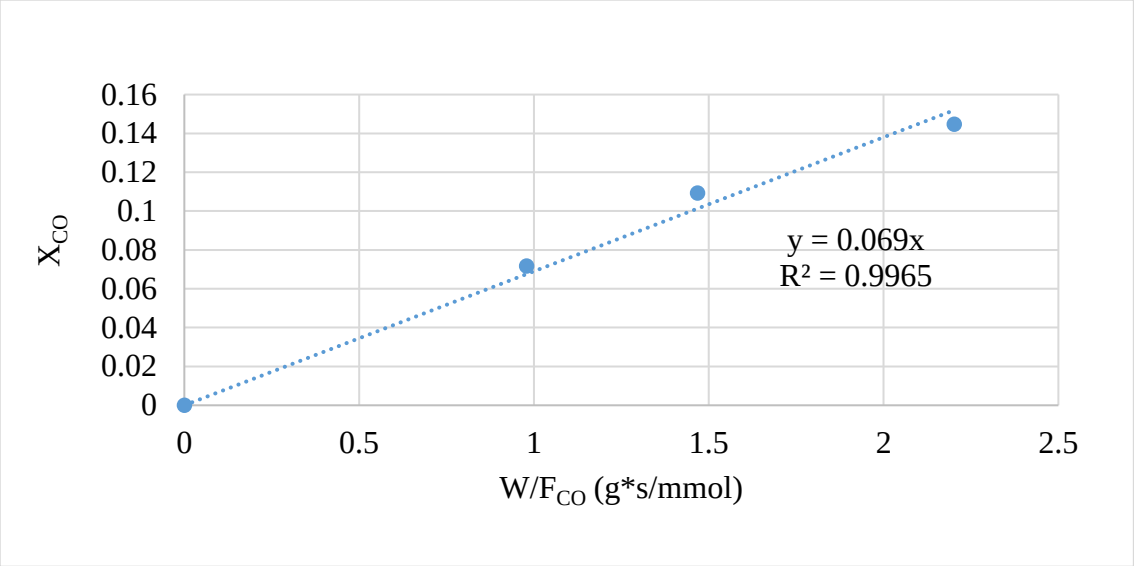

Figure A.11. Fractional CO conversion versus residence time graph for Experiment 11.

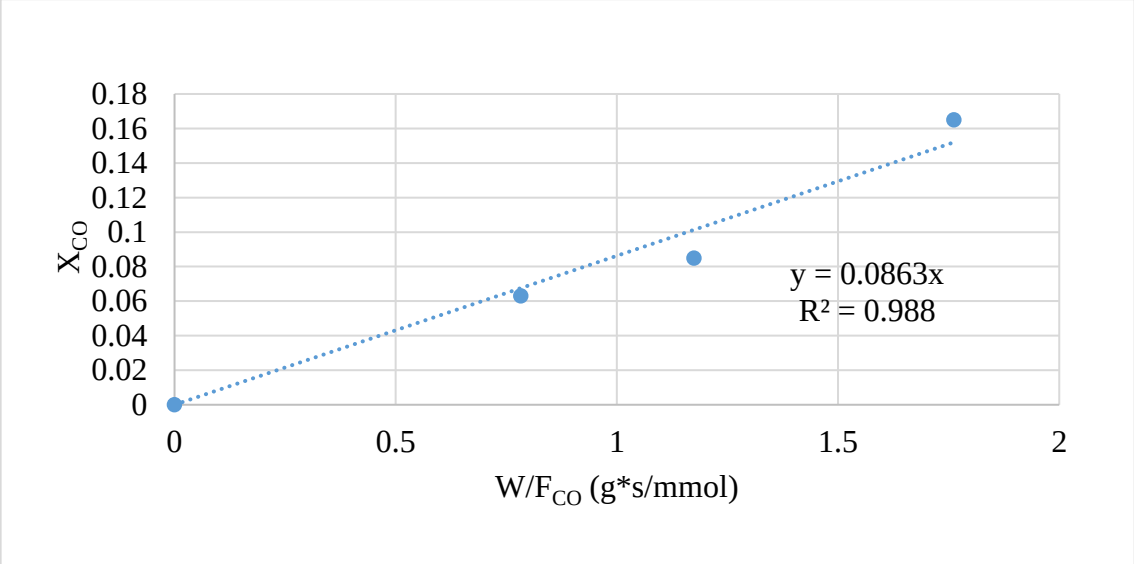

Figure A.12. Fractional CO conversion versus residence time graph for Experiment 12.

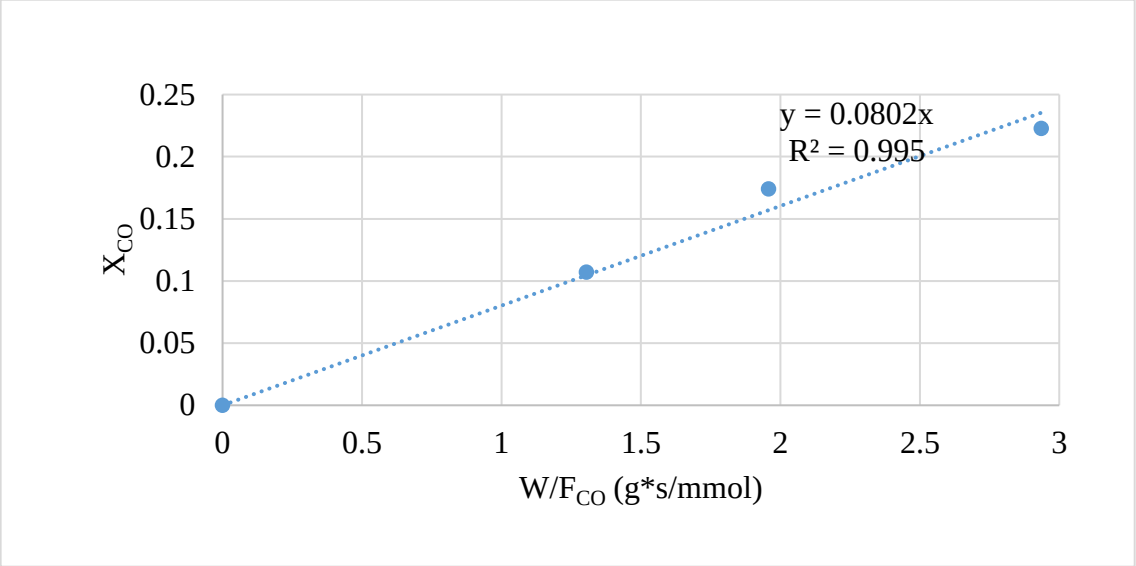

Figure A.13. Fractional CO conversion versus residence time graph for Experiment 13.

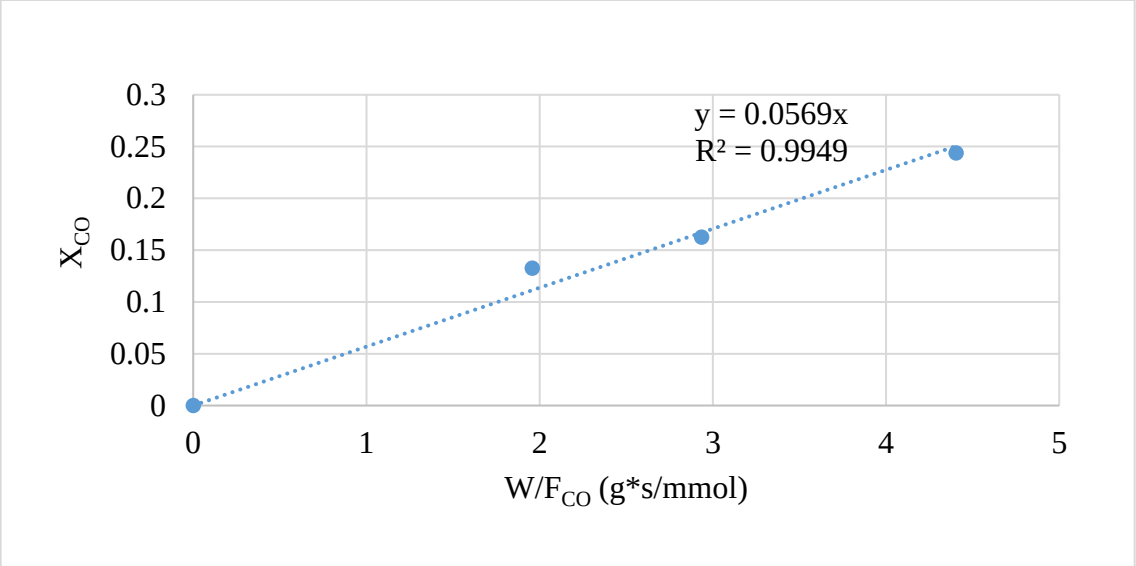

Figure A.14. Fractional CO conversion versus residence time graph for Experiment 14.

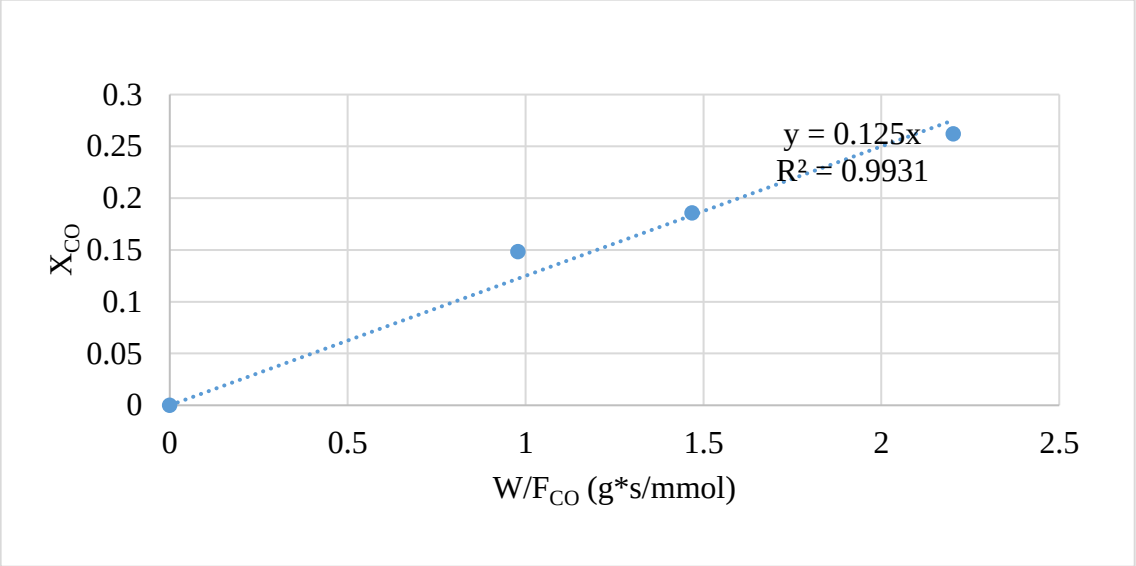

Figure A.15. Fractional CO conversion versus residence time graph for Experiment 15.

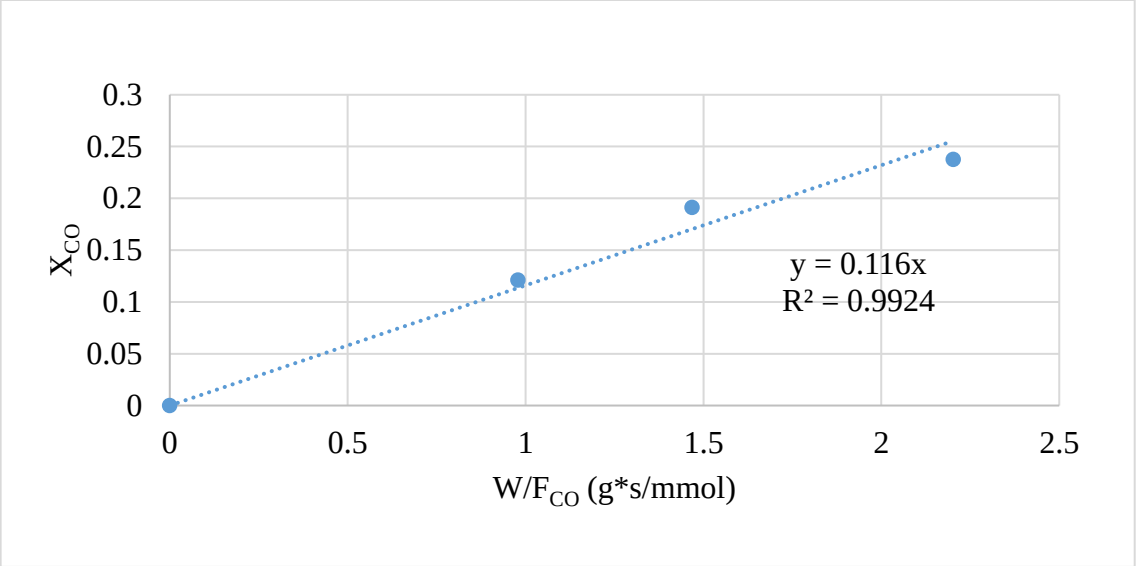

Figure A.16. Fractional CO conversion versus residence time graph for Experiment 16.

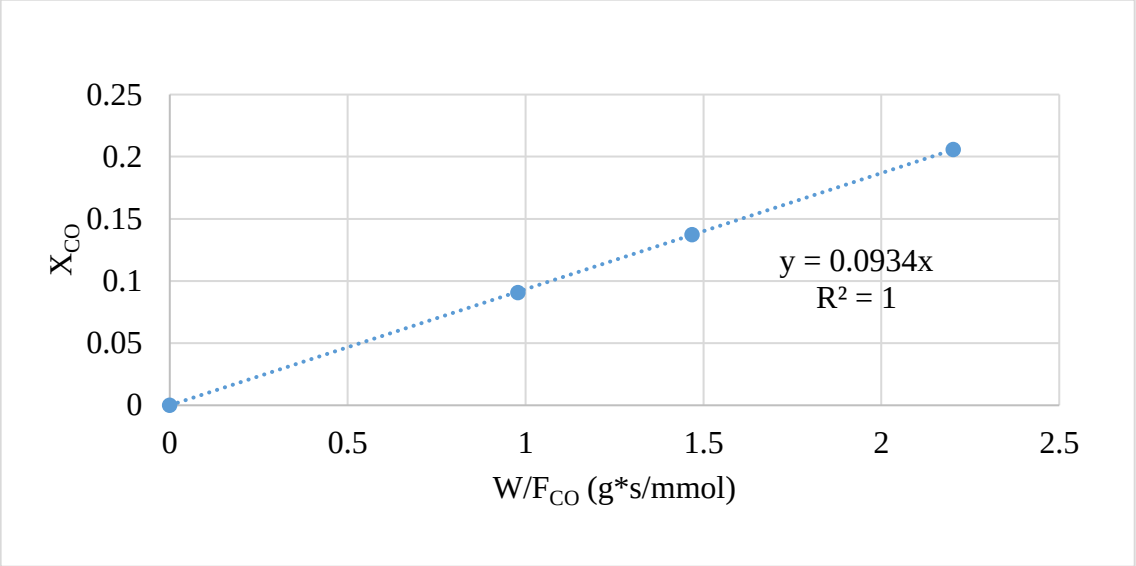

Figure A.17. Fractional CO conversion versus residence time graph for Experiment 17.

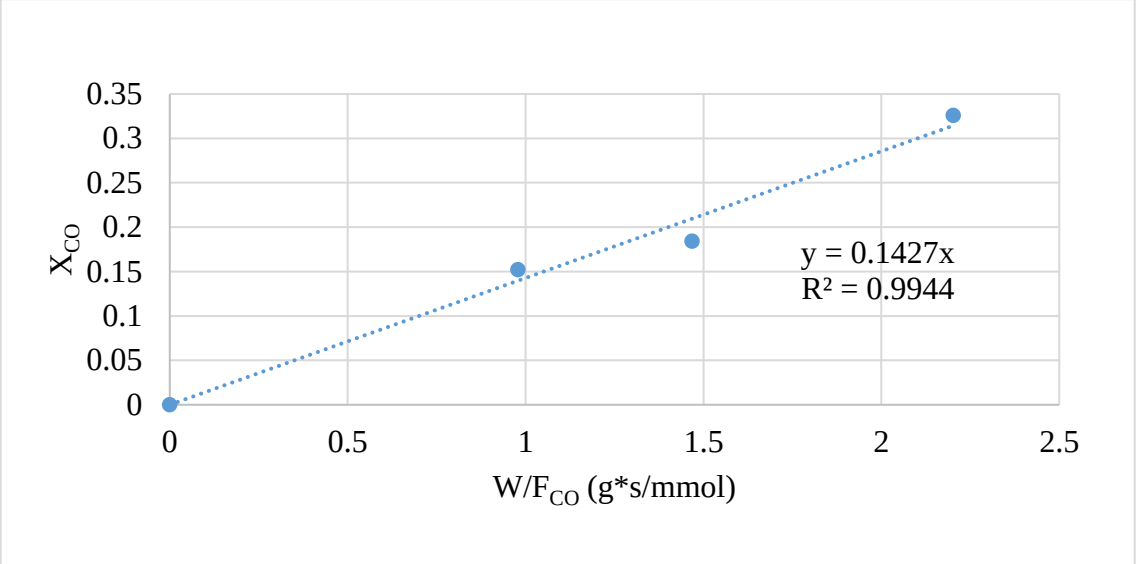

Figure A.18. Fractional CO conversion versus residence time graph for Experiment 18.

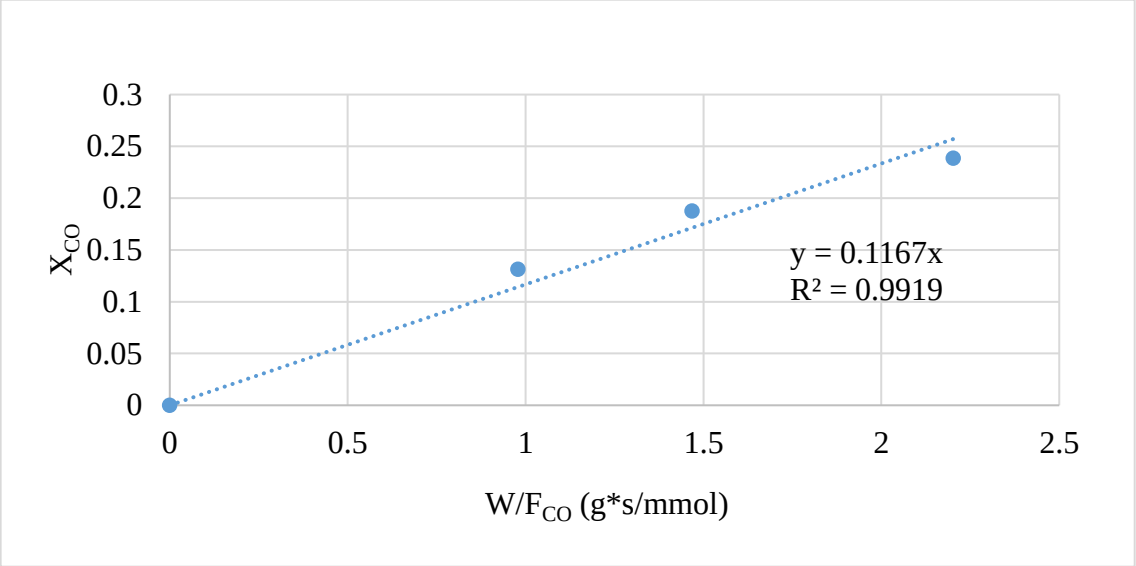

Figure A.19. Fractional CO conversion versus residence time graph for Experiment 19.

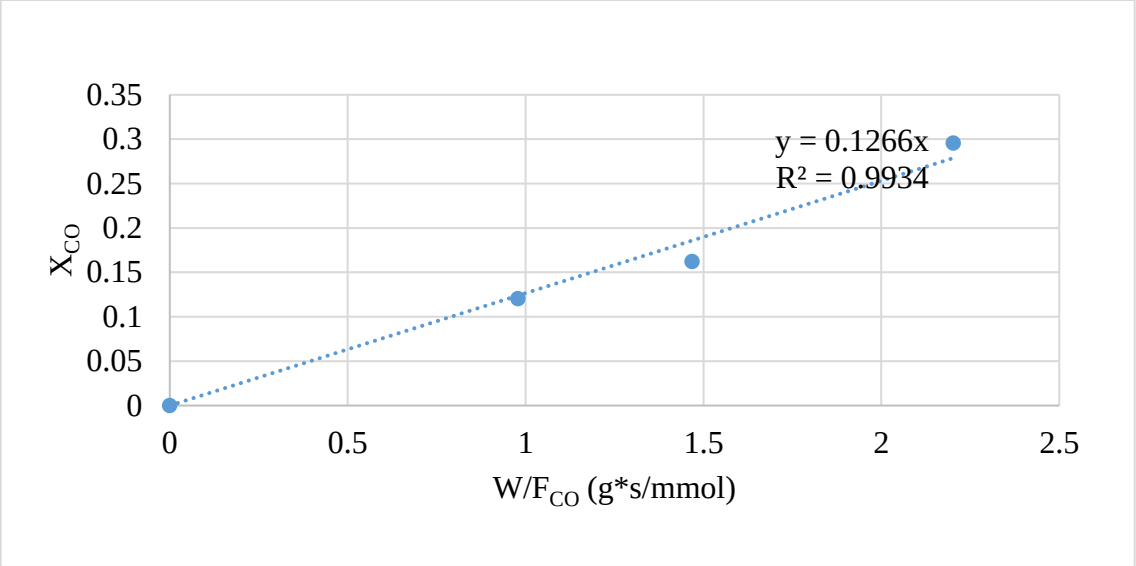

Figure A.20. Fractional CO conversion versus residence time graph for Experiment 20.

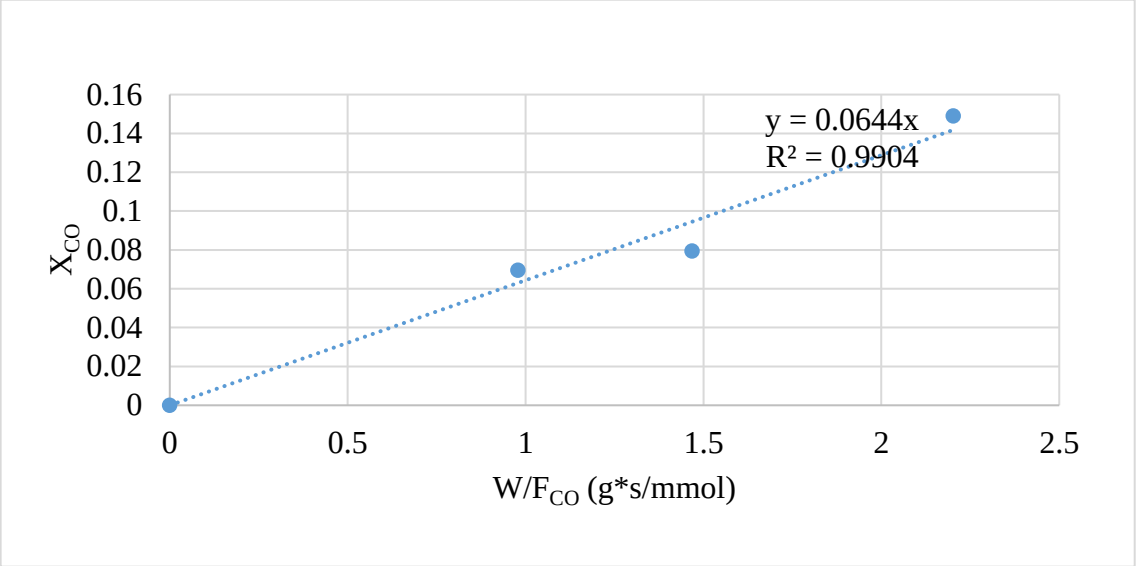

Figure A.21. Fractional CO conversion versus residence time graph for Experiment 21.

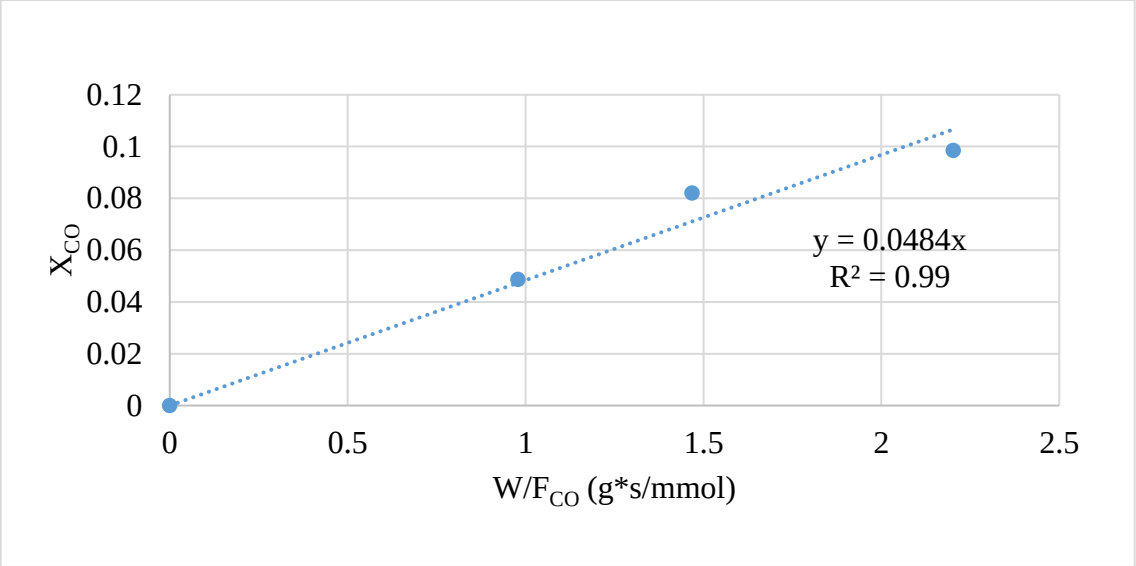

Figure A.22. Fractional CO conversion versus residence time graph for Experiment 22.

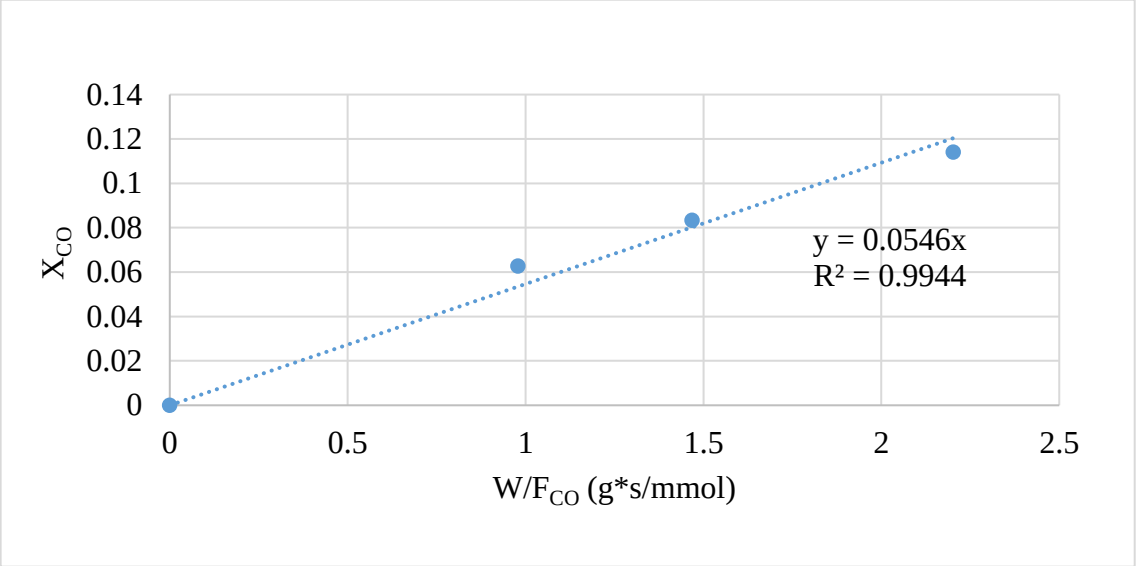

Figure A.23. Fractional CO conversion versus residence time graph for Experiment 23.

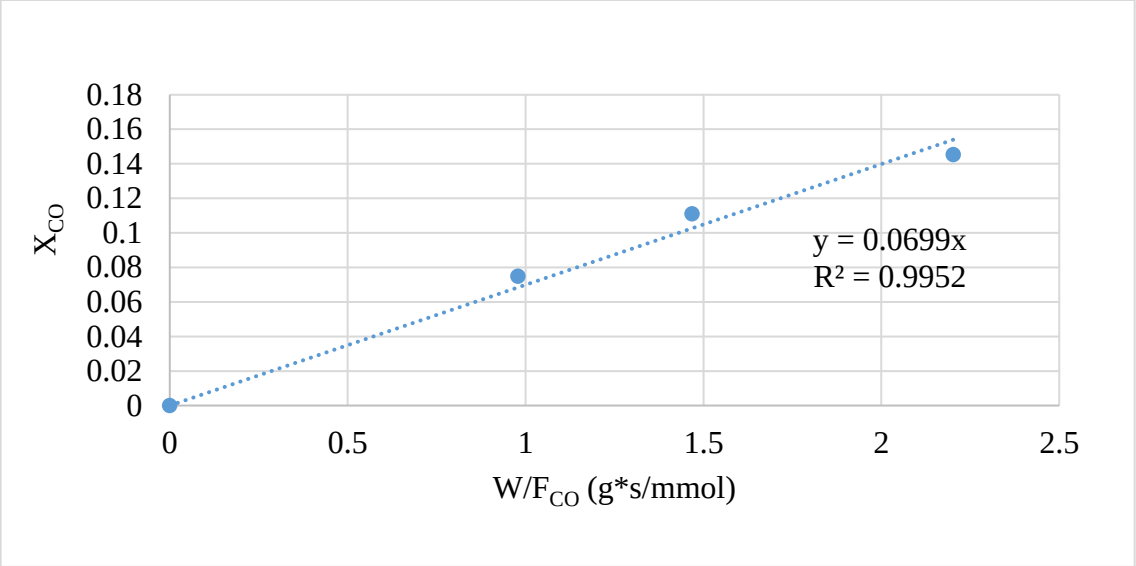

Figure A.24. Fractional CO conversion versus residence time graph for Experiment 24.

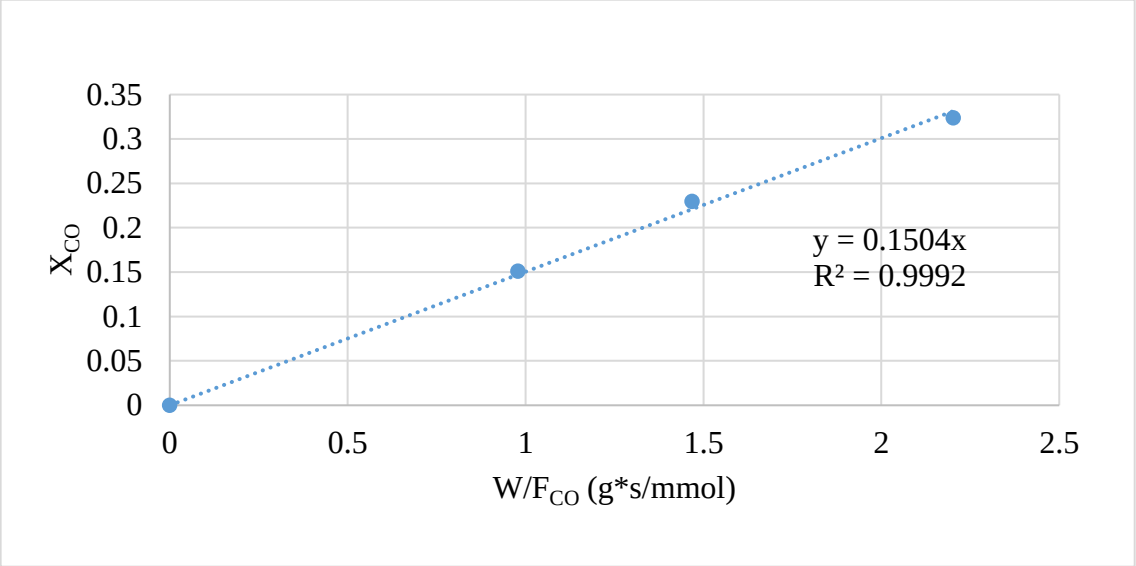

Figure A.25. Fractional CO conversion versus residence time graph for Experiment 25.

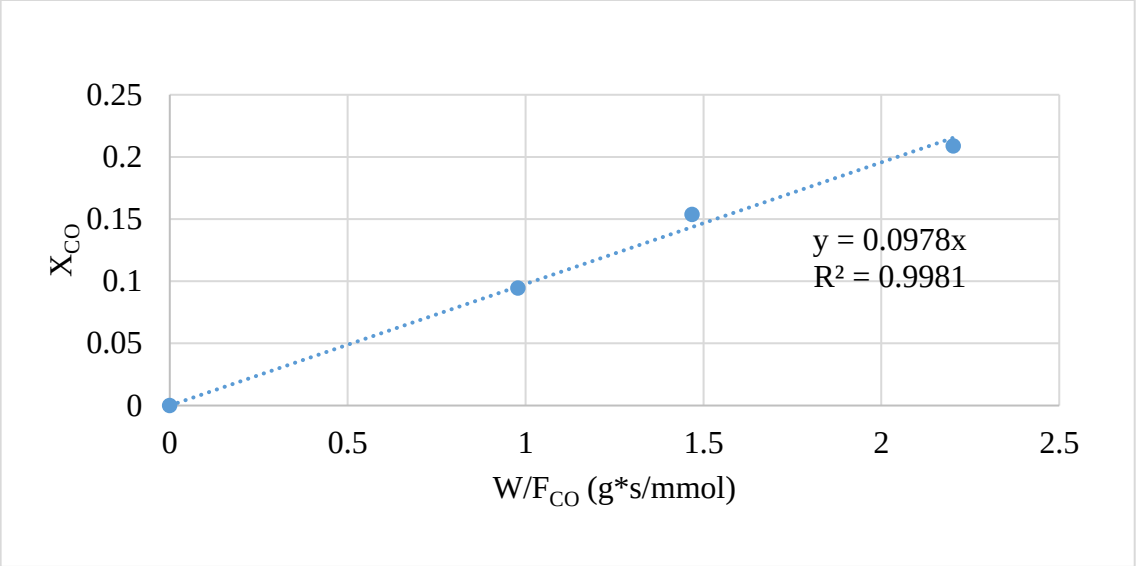

Figure A.26. Fractional CO conversion versus residence time graph for Experiment 26.

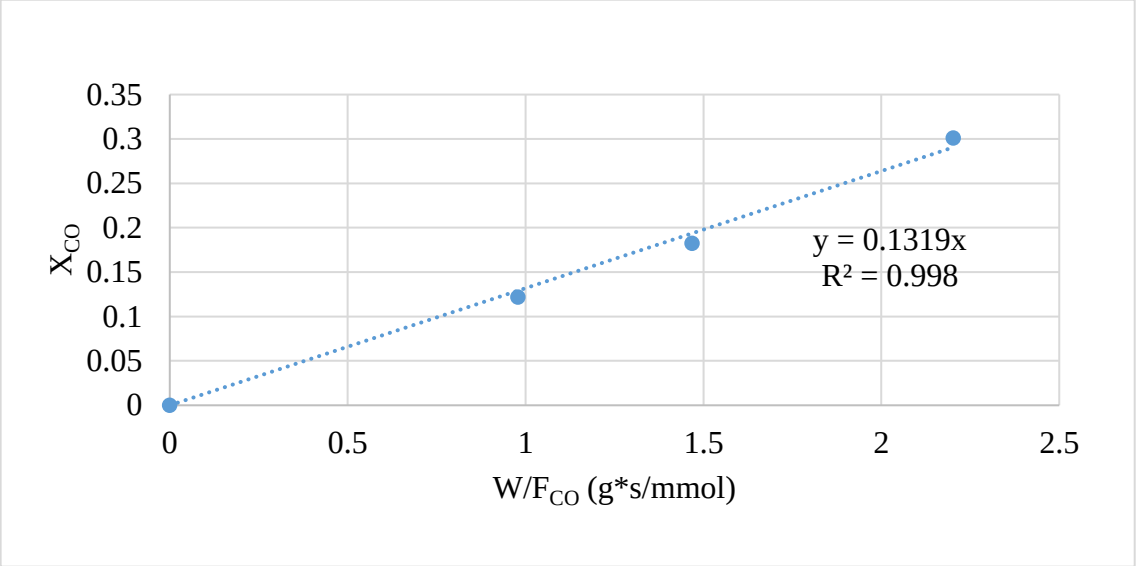

Figure A.27. Fractional CO conversion versus residence time graph for Experiment 27.

APPENDIX B: PERFORMANCE METRICS AND MODEL PARAMETERS FOR THE LEAVE-ONE-OUT CROSS-VALIDATION

Performance metrics and model parameters calculated using the LOO cross-validation method are given below.

Table B.1. Performance metrics and model parameters of Model 1 calculated using the LOO cross-validation method.

DATA #	RMSE	MSE	R^2	k	K_{CO}	K_{H2}
1	6.85E-03	4.69E-05	0.97	27.81	11.87	1.44
2	1.55E-02	2.41E-04	-3.68	27.87	11.63	1.51
3	1.20E-02	1.44E-04	-25.32	28.31	12.16	1.46
4	1.32E-02	1.75E-04	0.89	28.73	11.54	1.70
5	2.93E-02	8.60E-04	0.69	23.26	8.67	1.75
6	8.83E-03	7.80E-05	0.84	26.05	11.12	1.44
7	6.64E-03	4.41E-05	0.98	32.42	13.30	1.68
8	1.32E-02	1.74E-04	0.95	29.66	11.86	1.80
9	4.31E-03	1.86E-05	0.97	28.55	11.92	1.57
10	1.82E-02	3.30E-04	-3.87	28.28	12.32	1.41
11	4.24E-03	1.80E-05	0.98	28.50	11.75	1.61
12	1.78E-02	3.17E-04	-0.58	31.67	13.86	1.41
13	1.07E-02	1.14E-04	0.73	25.58	10.97	1.41
14	1.07E-02	1.15E-04	0.94	35.35	14.30	1.76
15	4.31E-03	1.86E-05	0.97	28.55	11.92	1.57
16	5.40E-03	2.91E-05	0.90	28.21	11.78	1.54
17	2.98E-02	8.87E-04	-18.69	27.40	11.43	1.47
18	2.34E-02	5.48E-04	0.73	29.26	12.21	1.64
19	4.64E-03	2.16E-05	0.93	28.24	11.79	1.55
20	6.04E-03	3.64E-05	0.95	28.62	11.95	1.58

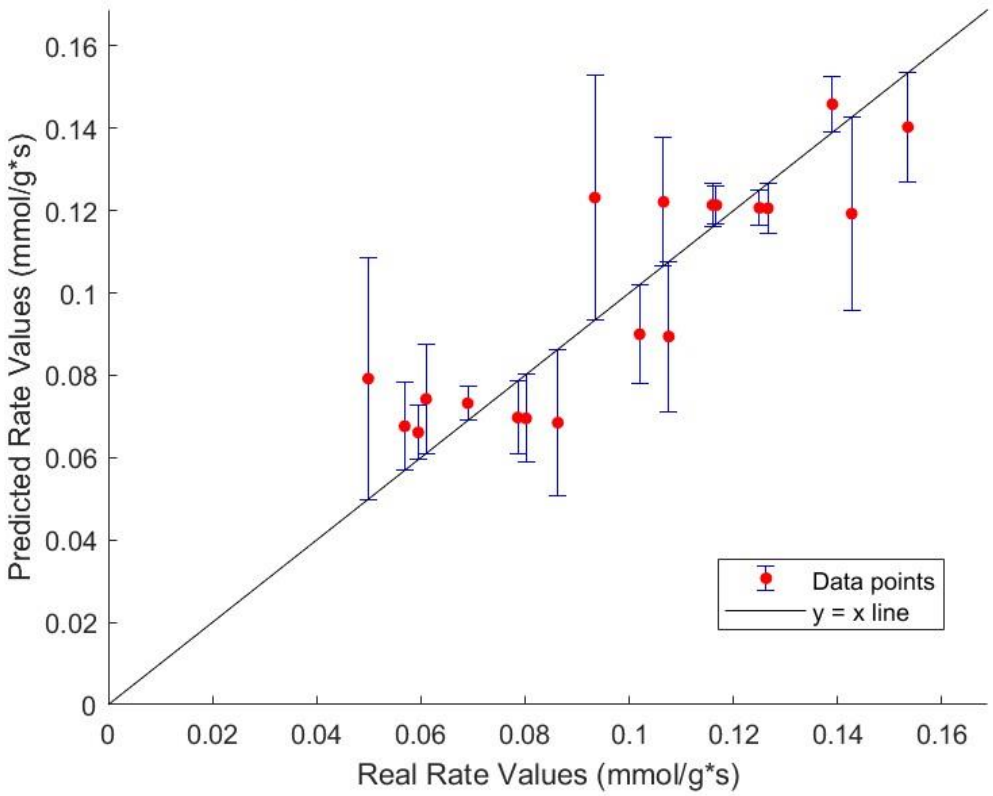

Figure B.1. LOO-predicted rate values for Model 1.

Table B.2. Performance metrics and model parameters of Model 2 calculated using the LOO cross-validation method.

DATA #	RMSE	MSE	R^2	k	K_{CO}	K_{H2O}
1	3.82E-02	1.46E-03	0.14	24.44	13.49	1.98
2	2.12E-02	4.51E-04	-7.74	25.24	14.34	1.32
3	2.05E-02	4.21E-04	-75.74	26.14	15.33	0.53
4	1.24E-03	1.53E-06	1.00	25.73	14.90	0.85
5	9.74E-03	9.48E-05	0.97	23.98	13.97	0.92
6	1.57E-02	2.46E-04	0.50	22.19	13.23	0.62
7	6.89E-03	4.75E-05	0.97	30.31	17.01	0.99
8	9.04E-03	8.16E-05	0.97	25.34	14.65	0.80
9	4.30E-03	1.85E-05	0.97	25.90	15.02	0.86
10	2.78E-02	7.74E-04	-10.41	26.42	15.36	0.91
11	8.65E-03	7.48E-05	0.93	25.90	15.02	0.86
12	3.05E-02	9.30E-04	-3.62	31.55	17.75	0.91
13	1.93E-02	3.72E-04	0.12	21.70	12.89	0.85
14	6.60E-03	4.35E-05	0.98	29.77	16.82	0.84
15	4.30E-03	1.85E-05	0.97	25.90	15.02	0.86
16	2.18E-03	4.73E-06	0.98	25.66	14.88	0.78
17	3.01E-02	9.03E-04	-19.06	24.49	14.39	0.00
18	2.34E-02	5.47E-04	0.73	26.60	15.48	0.93
19	4.65E-03	2.17E-05	0.93	25.59	14.81	0.82
20	6.02E-03	3.63E-05	0.95	25.96	15.06	0.86
Average	1.45E-02	3.27E-04	-5.22	25.94	14.97	0.87

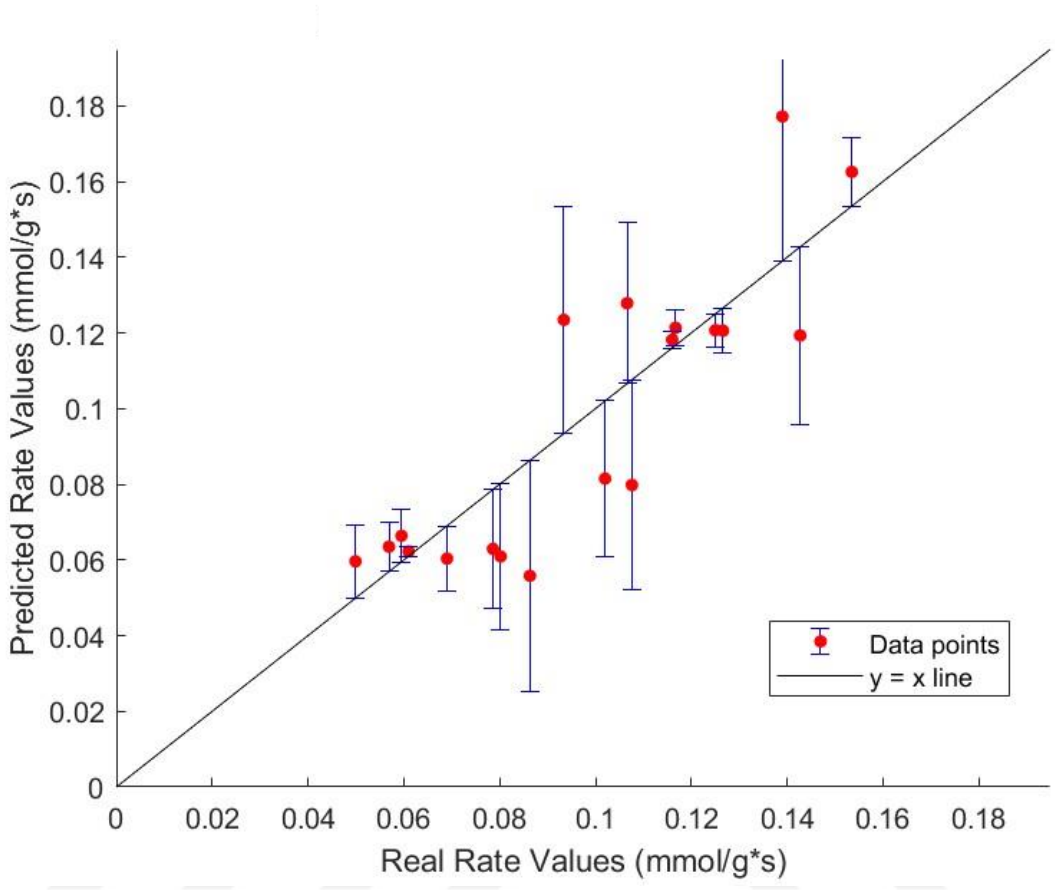

Figure B.2. LOO-predicted rate values for Model 2.

Table B.3. Performance metrics and model parameters of Model 3 calculated using the LOO cross-validation method.

DATA #	RMSE	MSE	R^2	k	K_{CO}	K_{H2}
1	8.73E-03	7.62E-05	0.96	4.07	0.14	0.54
2	1.46E-02	2.13E-04	-3.13	3.63	0.16	0.64
3	1.41E-02	2.00E-04	-35.44	3.96	0.14	0.55
4	1.13E-02	1.27E-04	0.92	4.48	0.14	0.72
5	2.32E-02	5.40E-04	0.80	6.46	0.10	0.78
6	7.41E-03	5.50E-05	0.89	4.37	0.13	0.64
7	1.39E-02	1.94E-04	0.89	2.04	0.30	0.67
8	1.29E-02	1.66E-04	0.95	4.41	0.14	0.76
9	5.24E-03	2.74E-05	0.96	3.83	0.15	0.67
10	2.02E-02	4.09E-04	-5.03	2.54	0.22	0.54
11	2.52E-03	6.37E-06	0.99	4.04	0.15	0.68
12	1.85E-02	3.42E-04	-0.70	2.06	0.27	0.52
13	9.14E-03	8.35E-05	0.80	4.24	0.14	0.63
14	1.64E-02	2.70E-04	0.87	2.50	0.24	0.68
15	5.24E-03	2.74E-05	0.96	3.83	0.15	0.67
16	4.47E-03	1.99E-05	0.93	3.69	0.16	0.65
17	2.88E-02	8.32E-04	-17.48	3.67	0.16	0.62
18	2.41E-02	5.80E-04	0.72	3.86	0.15	0.63
19	3.72E-03	1.38E-05	0.96	3.82	0.15	0.65
20	6.96E-03	4.85E-05	0.94	3.84	0.15	0.67
Average	1.26E-02	2.12E-04	-2.41	3.77	0.17	0.64

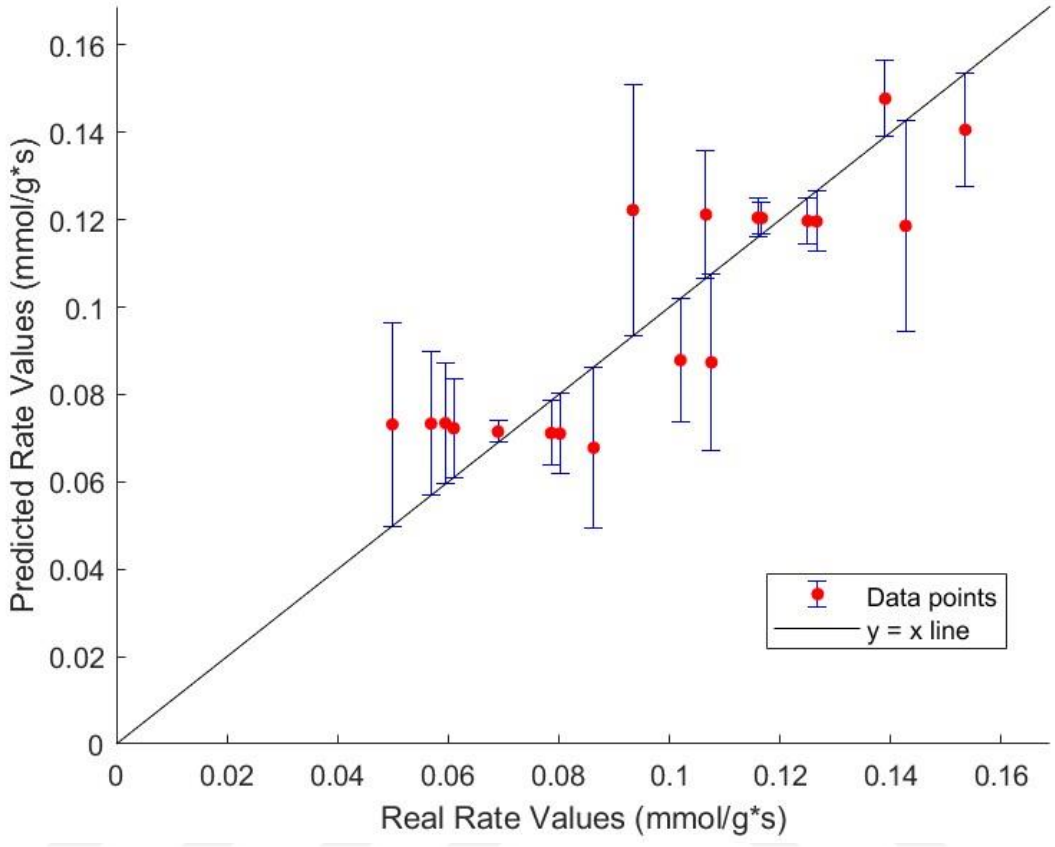

Figure B.3. LOO-predicted rate values for Model 3.

Table B.4. Performance metrics and model parameters of Model 4 calculated using the LOO cross-validation method.

DATA #	RMSE	MSE	R^2	k	K_{CO}	K_{H2}
1	9.25E-03	8.56E-05	0.95	13.40	1.43	0.62
2	1.47E-02	2.17E-04	-3.21	12.15	1.38	0.67
3	1.30E-02	1.69E-04	-29.74	12.33	1.48	0.65
4	1.31E-02	1.70E-04	0.90	10.24	1.34	0.76
5	3.26E-02	1.07E-03	0.61	13.53	0.65	0.81
6	9.91E-03	9.83E-05	0.80	13.42	1.26	0.63
7	8.60E-03	7.39E-05	0.96	9.50	1.79	0.76
8	1.03E-02	1.06E-04	0.97	9.73	1.40	0.77
9	5.12E-03	2.62E-05	0.96	11.16	1.43	0.70
10	1.91E-02	3.64E-04	-4.37	12.86	1.52	0.63
11	4.03E-03	1.63E-05	0.98	11.01	1.39	0.71
12	1.59E-02	2.53E-04	-0.26	12.55	1.81	0.62
13	1.17E-02	1.38E-04	0.68	13.85	1.23	0.62
14	1.26E-02	1.60E-04	0.92	8.80	1.98	0.80
15	5.12E-03	2.62E-05	0.96	11.16	1.43	0.70
16	4.59E-03	2.11E-05	0.93	11.63	1.40	0.68
17	2.90E-02	8.40E-04	-17.64	12.92	1.34	0.65
18	2.43E-02	5.89E-04	0.71	10.27	1.47	0.73
19	3.84E-03	1.47E-05	0.95	11.60	1.40	0.69
20	6.85E-03	4.69E-05	0.94	11.07	1.43	0.70
Average	1.27E-02	2.24E-04	-2.10	11.66	1.43	0.70

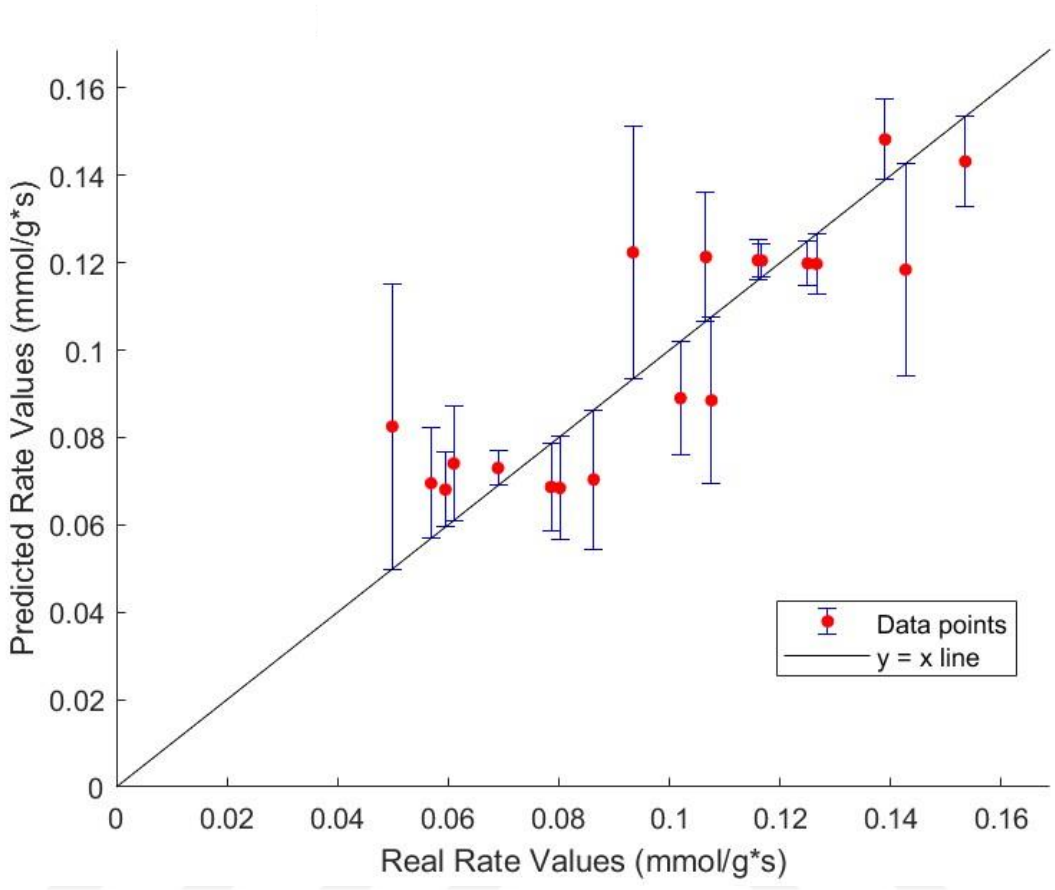

Figure B.4. LOO-predicted rate values for Model 4.

Table B.5. Performance metrics and model parameters of Model 5 calculated using the LOO cross-validation method.

DATA #	RMSE	MSE	R^2	k	K_C	K_{OH}
1	4.17E-03	1.74E-05	0.99	0.50	1.89	0.03
2	1.25E-02	1.56E-04	-2.03	0.52	1.84	0.12
3	6.71E-03	4.50E-05	-7.21	0.50	1.90	0.03
4	2.37E-02	5.60E-04	0.66	0.53	1.83	0.14
5	4.53E-02	2.05E-03	0.26	1.90	0.40	0.21
6	7.50E-04	5.62E-07	1.00	0.51	1.86	0.05
7	1.42E-02	2.02E-04	0.89	0.42	2.62	0.11
8	2.05E-02	4.19E-04	0.87	0.49	1.96	0.04
9	8.94E-03	7.99E-05	0.89	0.50	1.91	0.06
10	1.31E-02	1.72E-04	-1.54	0.50	1.92	0.07
11	1.39E-02	1.93E-04	0.82	0.52	1.84	0.02
12	1.35E-03	1.84E-06	0.99	0.50	1.92	0.05
13	3.36E-03	1.13E-05	0.97	0.53	1.79	0.06
14	1.64E-02	2.67E-04	0.87	0.40	2.72	0.02
15	8.94E-03	7.99E-05	0.89	0.50	1.91	0.06
16	8.11E-05	6.58E-09	1.00	0.51	1.88	0.05
17	2.50E-02	6.23E-04	-12.84	0.53	1.79	0.00
18	2.79E-02	7.77E-04	0.62	0.48	1.98	0.06
19	2.56E-05	6.55E-10	1.00	0.51	1.88	0.05
20	1.06E-02	1.13E-04	0.86	0.50	1.91	0.06
Average	1.29E-02	2.88E-04	-0.50	0.57	1.89	0.06

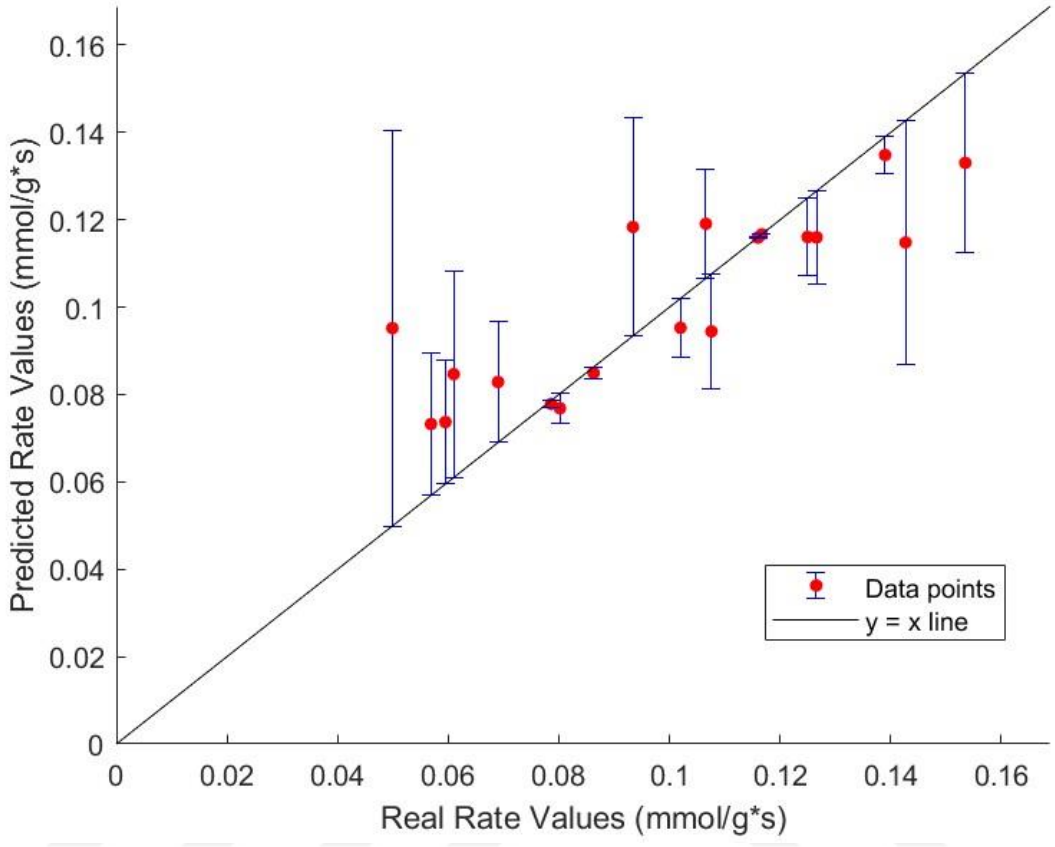

Figure B.5. LOO-predicted rate values for Model 5.

Table B.6. Performance metrics and model parameters of Model 6 calculated using the LOO cross-validation method.

DATA #	RMSE	MSE	R^2	k	K_{CH}	K_{OH}
1	1.15E-02	1.31E-04	0.92	1.05	2.66	0.23
2	1.79E-02	3.21E-04	-5.23	1.03	2.86	0.26
3	1.09E-02	1.18E-04	-20.49	0.99	2.86	0.08
4	1.58E-02	2.50E-04	0.85	0.97	3.27	0.21
5	3.17E-02	1.01E-03	0.64	0.98	3.36	0.30
6	1.02E-02	1.03E-04	0.79	1.01	2.74	0.09
7	3.73E-03	1.39E-05	0.99	0.98	3.10	0.15
8	1.11E-02	1.23E-04	0.96	0.95	3.28	0.13
9	5.33E-03	2.84E-05	0.96	0.98	3.01	0.14
10	1.81E-02	3.29E-04	-3.84	1.01	2.77	0.17
11	4.97E-03	2.47E-05	0.98	0.98	3.07	0.12
12	9.63E-03	9.28E-05	0.54	1.00	2.87	0.16
13	1.35E-02	1.83E-04	0.57	1.03	2.66	0.17
14	5.14E-03	2.64E-05	0.99	0.97	3.14	0.12
15	5.33E-03	2.84E-05	0.96	0.98	3.01	0.14
16	2.98E-03	8.88E-06	0.97	0.99	2.96	0.11
17	2.89E-02	8.33E-04	-17.50	1.01	2.82	0.00
18	2.44E-02	5.98E-04	0.71	0.96	3.14	0.15
19	3.63E-03	1.32E-05	0.96	0.99	2.96	0.13
20	7.06E-03	4.98E-05	0.94	0.98	3.03	0.14
Average	1.21E-02	2.14E-04	-1.67	0.99	2.98	0.15

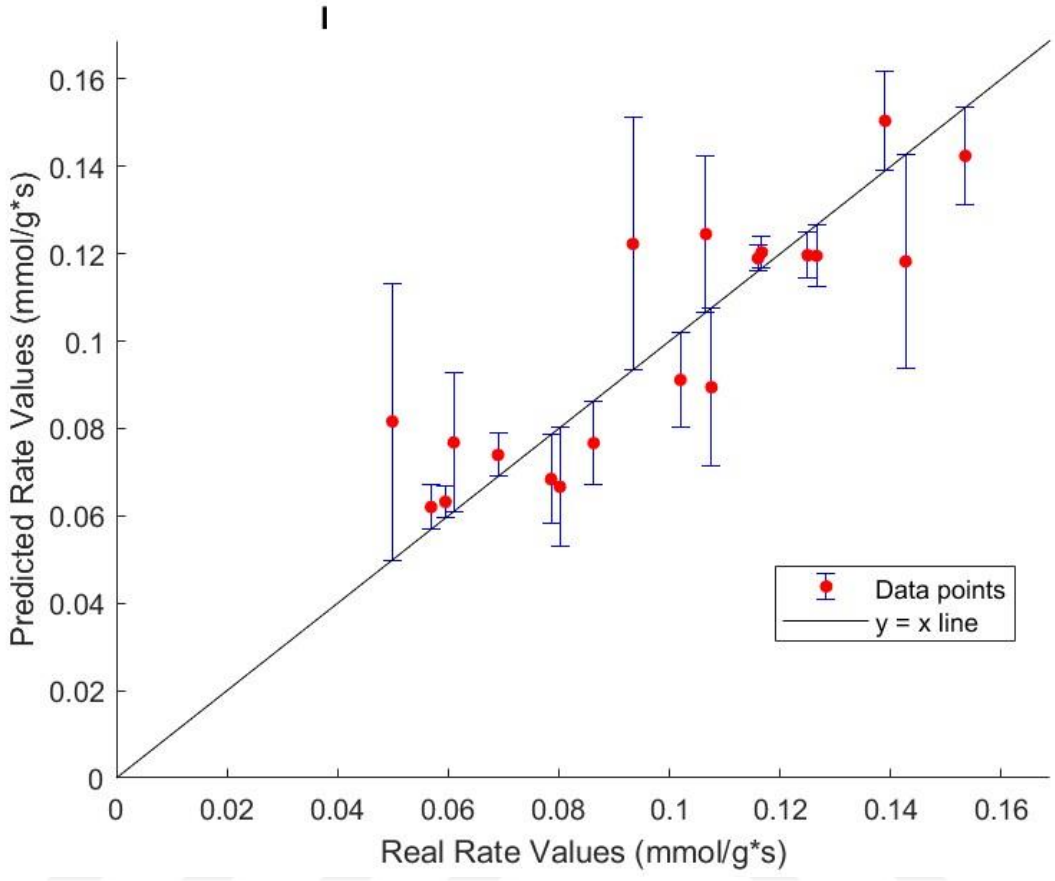

Figure B.6. LOO-predicted rate values for Model 6.

Table B.7. Performance metrics and model parameters of Model 7 calculated using the LOO cross-validation method.

DATA #	RMSE	MSE	R^2	k	K_{COH}	K_{OH}
1	4.10E-03	1.68E-05	0.99	0.91	13.40	0.18
2	1.71E-02	2.93E-04	-4.68	0.93	13.34	0.28
3	7.72E-03	5.96E-05	-9.87	0.90	13.50	0.10
4	2.04E-02	4.15E-04	0.75	0.90	14.93	0.27
5	3.66E-02	1.34E-03	0.51	0.93	14.16	0.36
6	9.01E-03	8.11E-05	0.84	0.91	12.85	0.10
7	2.00E-03	4.01E-06	1.00	0.90	13.49	0.14
8	1.59E-02	2.53E-04	0.92	0.88	15.09	0.13
9	5.89E-03	3.47E-05	0.95	0.90	13.89	0.15
10	1.50E-02	2.25E-04	-2.32	0.90	13.25	0.18
11	9.44E-03	8.90E-05	0.92	0.90	14.28	0.11
12	4.22E-03	1.78E-05	0.91	0.90	13.70	0.16
13	1.26E-02	1.59E-04	0.63	0.92	12.53	0.19
14	3.62E-04	1.31E-07	1.00	0.90	13.71	0.15
15	5.89E-03	3.47E-05	0.95	0.90	13.89	0.15
16	2.50E-03	6.27E-06	0.98	0.90	13.70	0.12
17	2.83E-02	8.01E-04	-16.79	0.91	13.11	0.00
18	2.50E-02	6.26E-04	0.69	0.88	14.36	0.16
19	3.07E-03	9.45E-06	0.97	0.90	13.68	0.14
20	7.62E-03	5.80E-05	0.93	0.90	13.93	0.15
Average	1.16E-02	2.26E-04	-0.99	0.90	13.74	0.16

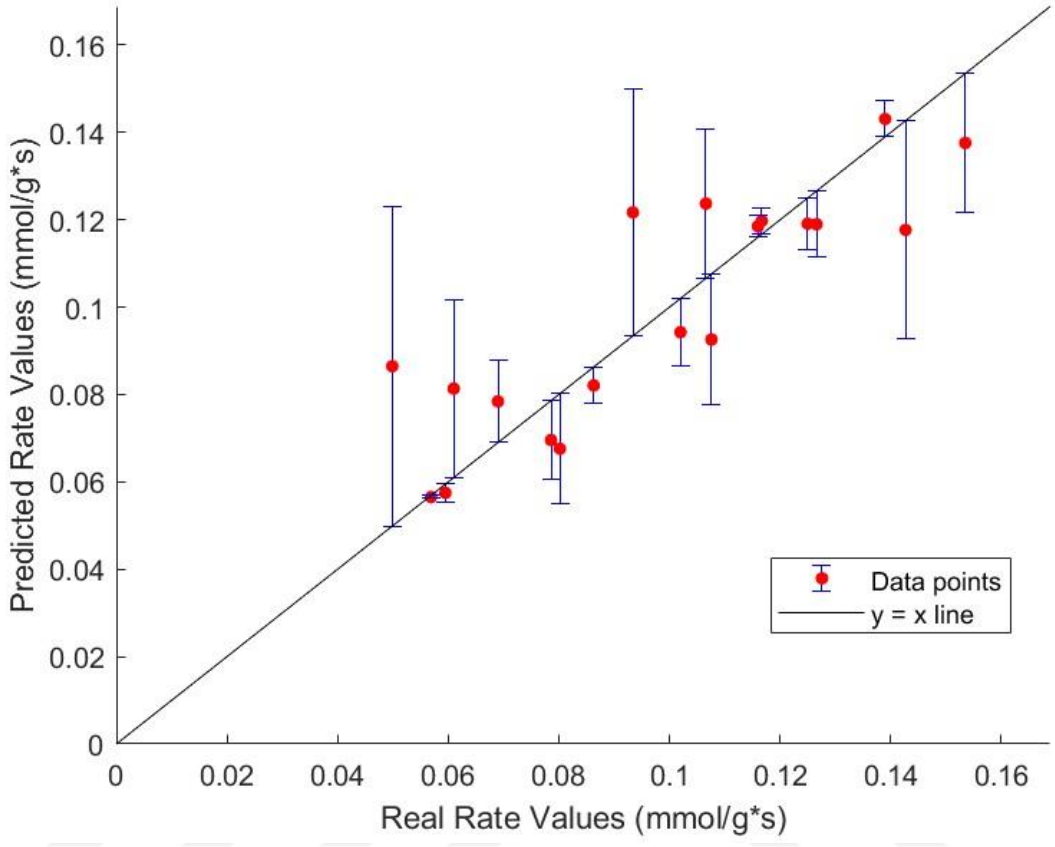

Figure B.7. LOO-predicted rate values for Model 7.

Table B.8. Performance metrics and model parameters of Model 8 calculated using the LOO cross-validation method.

DATA #	RMSE	MSE	R^2	k	K_{CO}	K_{H2}	K_{CH4}	K_{H2O}
1	3.61E-03	1.31E-05	0.99	498.45	10.64	0.00	0.00	0.47
2	1.46E-02	2.14E-04	-3.15	208.85	8.29	0.00	0.54	0.13
3	1.68E-03	2.81E-06	0.49	253.33	10.91	0.00	0.00	0.46
4	2.55E-02	6.52E-04	0.61	254.65	7.86	0.00	0.00	0.24
5	3.88E-02	1.51E-03	0.45	208.36	7.23	0.00	0.48	0.13
6	8.37E-03	7.00E-05	0.86	253.50	11.24	0.00	0.00	0.48
7	2.70E-02	7.31E-04	0.59	250.45	12.48	0.00	0.00	0.81
8	1.96E-02	3.84E-04	0.88	253.21	11.22	0.00	0.00	0.47
9	9.80E-03	9.60E-05	0.86	253.52	10.99	0.00	0.00	0.46
10	1.63E-02	2.66E-04	-2.92	498.69	10.80	0.00	0.00	0.45
11	8.95E-03	8.01E-05	0.92	253.29	11.05	0.00	0.00	0.43
12	1.02E-02	1.03E-04	0.49	253.49	11.24	0.00	0.00	0.47
13	4.87E-03	2.38E-05	0.94	508.65	10.52	0.00	0.00	0.43
14	1.55E-02	2.39E-04	0.88	252.29	12.73	0.00	0.00	0.44
15	9.80E-03	9.60E-05	0.86	253.52	10.99	0.00	0.00	0.46
16	6.50E-03	4.23E-05	0.86	253.59	10.75	0.00	0.00	0.42
17	1.58E-02	2.49E-04	-4.52	501.39	9.89	0.00	0.00	0.27
18	2.97E-02	8.81E-04	0.57	204.62	8.33	0.00	0.46	0.02
19	9.15E-04	8.38E-07	1.00	253.48	10.96	0.00	0.00	0.45
20	1.15E-02	1.32E-04	0.83	253.54	11.00	0.00	0.00	0.46
Average	1.40E-02	2.89E-04	0.13	296.04	10.46	0.00	0.07	0.40

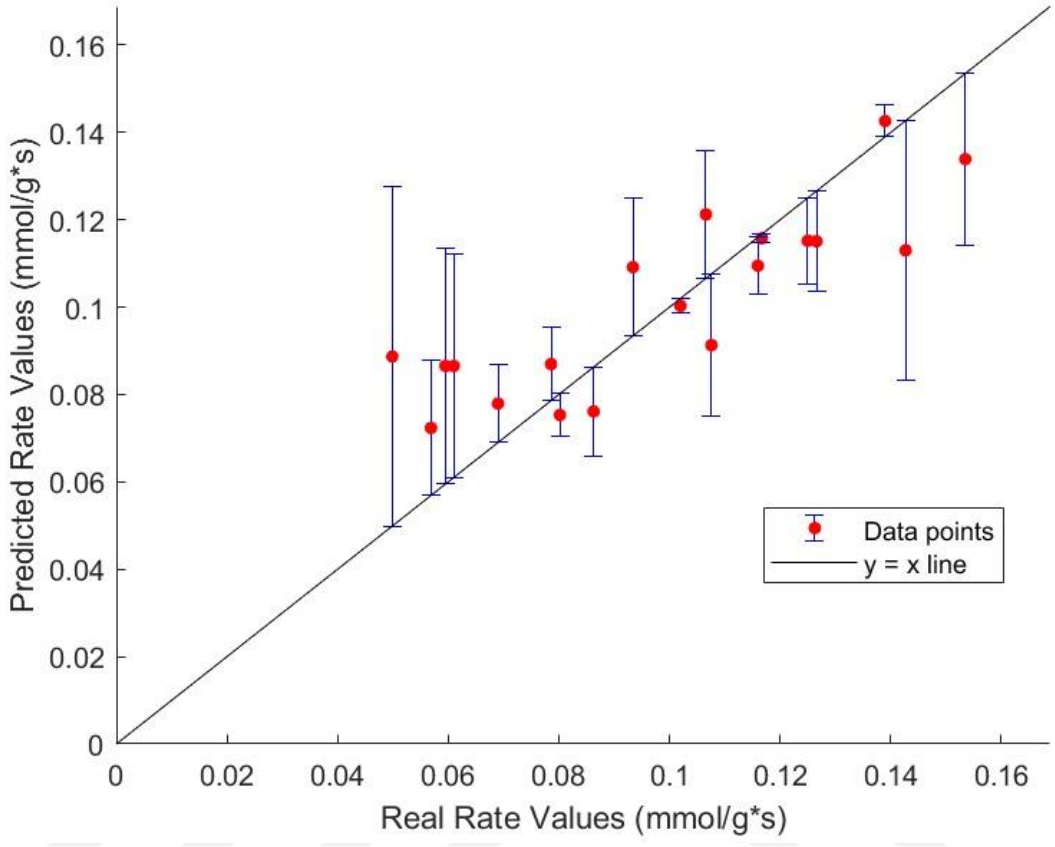

Figure B.8. LOO-predicted rate values for Model 8.

Table B.9. Performance metrics and model parameters of Model 9 calculated using the LOO cross-validation method.

DATA #	RMSE	MSE	R^2	k	K_{CO}	K_{H2O}
1	2.75E-03	7.56E-06	1.00	0.88	7.44	0.06
2	1.38E-02	1.89E-04	-2.66	0.90	7.38	0.13
3	5.83E-03	3.40E-05	-5.21	0.88	7.45	0.06
4	2.45E-02	5.98E-04	0.64	0.90	7.37	0.14
5	4.28E-02	1.83E-03	0.34	1.01	5.05	0.17
6	1.05E-04	1.10E-08	1.00	0.88	7.44	0.08
7	1.30E-02	1.70E-04	0.91	0.87	9.03	0.13
8	1.98E-02	3.92E-04	0.88	0.87	7.60	0.05
9	8.52E-03	7.26E-05	0.90	0.88	7.51	0.08
10	1.33E-02	1.78E-04	-1.63	0.88	7.56	0.10
11	1.37E-02	1.89E-04	0.82	0.89	7.31	0.04
12	3.03E-03	9.20E-06	0.95	0.88	7.61	0.08
13	4.05E-03	1.64E-05	0.96	0.89	7.26	0.09
14	1.32E-02	1.73E-04	0.91	0.86	8.83	0.04
15	8.52E-03	7.26E-05	0.90	0.88	7.51	0.08
16	3.75E-04	1.41E-07	1.00	0.88	7.44	0.08
17	2.53E-02	6.41E-04	-13.24	0.89	7.13	0.00
18	2.75E-02	7.55E-04	0.63	0.87	7.68	0.08
19	3.66E-04	1.34E-07	1.00	0.88	7.43	0.08
20	1.02E-02	1.05E-04	0.87	0.88	7.53	0.08
Average	1.25E-02	2.72E-04	-0.45	0.89	7.48	0.08

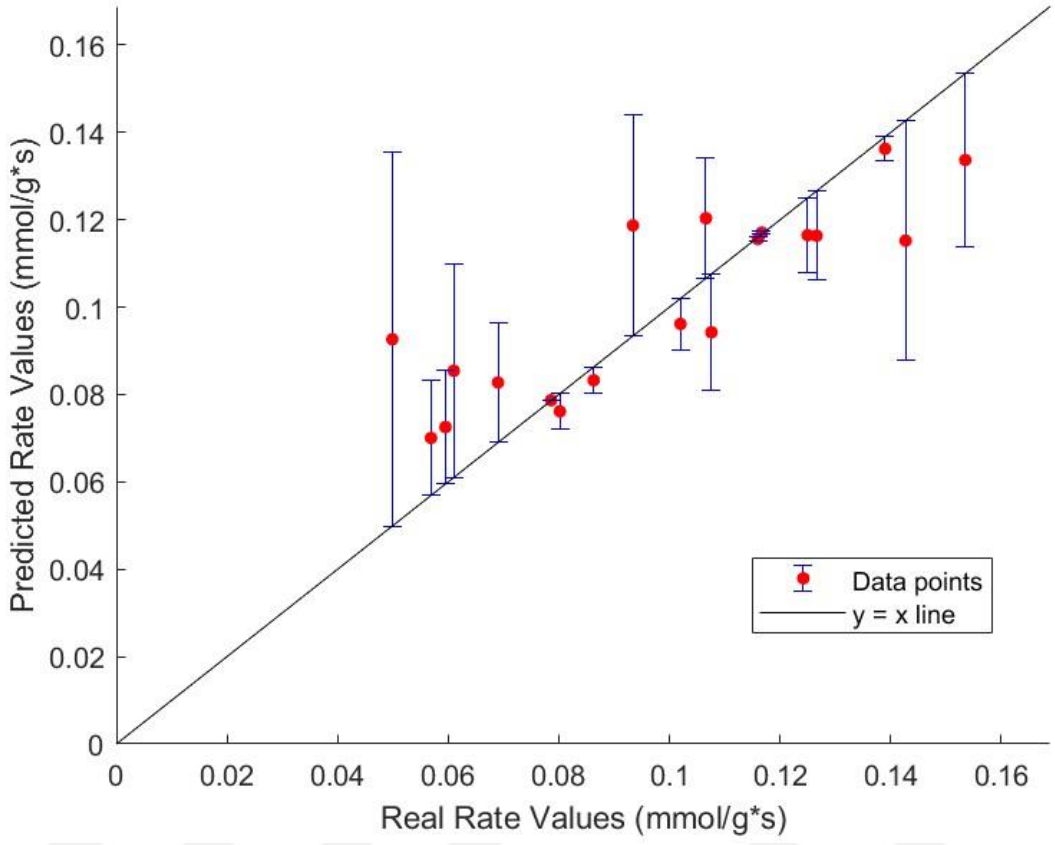

Figure B.9. LOO-predicted rate values for Model 9.

Table B.10. Performance metrics and model parameters of Model 10 calculated using the LOO cross-validation method.

DATA #	RMSE	MSE	R^2	k	K_{CO}	k'
1	2.69E-02	7.23E-04	0.58	24.60	14.35	0.02
2	1.58E-02	2.51E-04	-3.86	24.93	14.72	0.00
3	2.18E-02	4.77E-04	-85.93	25.95	15.44	0.00
4	3.60E-04	1.30E-07	1.00	25.46	15.10	0.00
5	7.85E-03	6.17E-05	0.98	24.03	14.35	0.00
6	1.70E-02	2.88E-04	0.42	21.70	13.20	0.00
7	4.17E-03	1.74E-05	0.99	27.96	16.29	0.00
8	9.43E-03	8.90E-05	0.97	25.04	14.79	0.00
9	4.00E-03	1.60E-05	0.98	25.59	15.19	0.00
10	2.76E-02	7.63E-04	-10.25	26.09	15.54	0.00
11	8.51E-03	7.24E-05	0.93	25.60	15.20	0.00
12	3.07E-02	9.40E-04	-3.67	31.29	17.97	0.00
13	1.87E-02	3.49E-04	0.18	21.42	13.06	0.00
14	8.56E-03	7.33E-05	0.96	30.98	17.68	0.00
15	4.00E-03	1.60E-05	0.98	25.59	15.19	0.00
16	5.68E-03	3.23E-05	0.89	25.24	14.94	0.00
17	3.00E-02	9.03E-04	-19.05	24.48	14.39	0.00
18	2.31E-02	5.32E-04	0.74	26.27	15.67	0.00
19	4.95E-03	2.45E-05	0.92	25.22	14.94	0.00
20	5.72E-03	3.27E-05	0.96	25.65	15.23	0.00
Average	1.37E-02	2.83E-04	-5.51	25.65	15.16	0.00

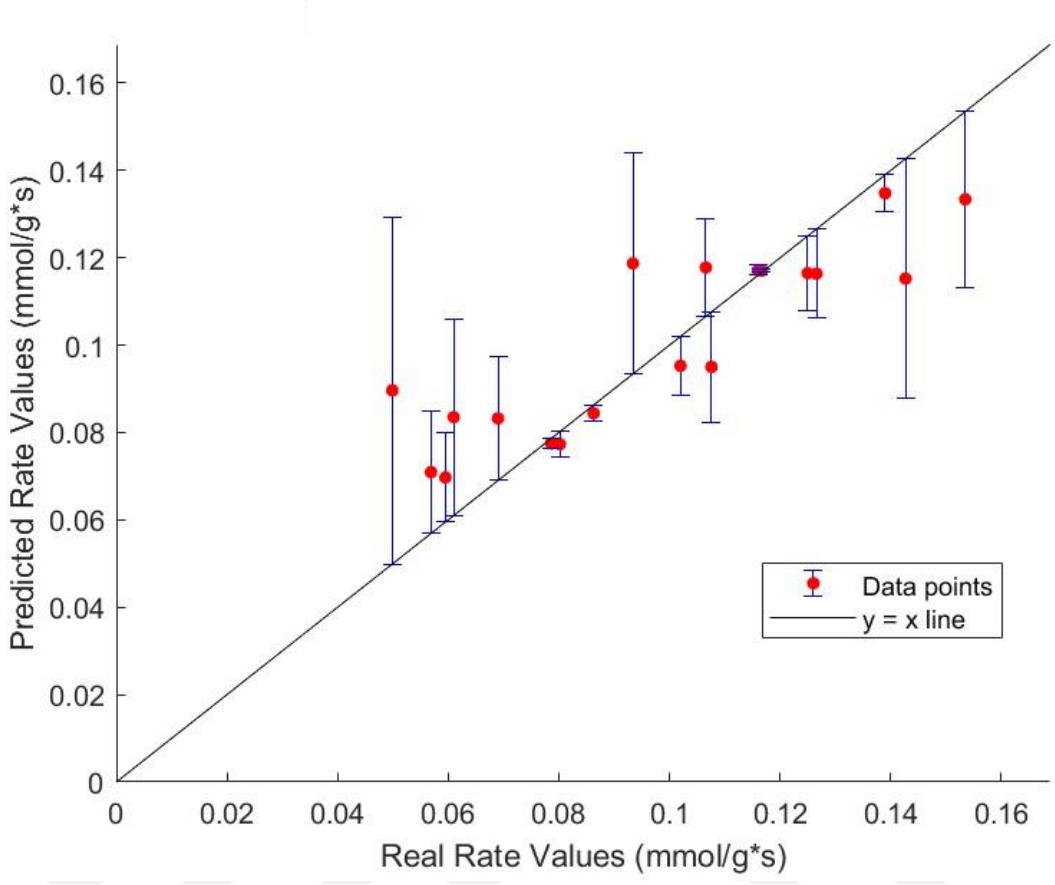

Figure B.10. LOO-predicted rate values for Model 10.

Table B.11. Performance metrics and model parameters of Model 11 calculated using the LOO cross-validation method.

DATA #	RMSE	MSE	R^2	k	K_{CO}	k'
1	2.69E-02	7.23E-04	0.58	24.60	14.35	0.02
2	1.58E-02	2.51E-04	-3.86	24.93	14.72	0.00
3	2.18E-02	4.77E-04	-85.93	25.95	15.44	0.00
4	3.60E-04	1.30E-07	1.00	25.46	15.10	0.00
5	7.85E-03	6.17E-05	0.98	24.03	14.35	0.00
6	1.70E-02	2.88E-04	0.42	21.70	13.20	0.00
7	4.17E-03	1.74E-05	0.99	27.96	16.29	0.00
8	9.43E-03	8.90E-05	0.97	25.04	14.79	0.00
9	4.00E-03	1.60E-05	0.98	25.59	15.19	0.00
10	2.76E-02	7.63E-04	-10.25	26.09	15.54	0.00
11	8.51E-03	7.24E-05	0.93	25.60	15.20	0.00
12	3.07E-02	9.40E-04	-3.67	31.29	17.97	0.00
13	1.87E-02	3.49E-04	0.18	21.42	13.06	0.00
14	8.56E-03	7.33E-05	0.96	30.98	17.68	0.00
15	4.00E-03	1.60E-05	0.98	25.59	15.19	0.00
16	5.68E-03	3.23E-05	0.89	25.24	14.94	0.00
17	3.00E-02	9.03E-04	-19.05	24.48	14.39	0.00
18	2.31E-02	5.32E-04	0.74	26.27	15.67	0.00
19	4.95E-03	2.45E-05	0.92	25.22	14.94	0.00
20	5.72E-03	3.27E-05	0.96	25.65	15.23	0.00
Average	1.37E-02	2.83E-04	-5.51	25.65	15.16	0.00

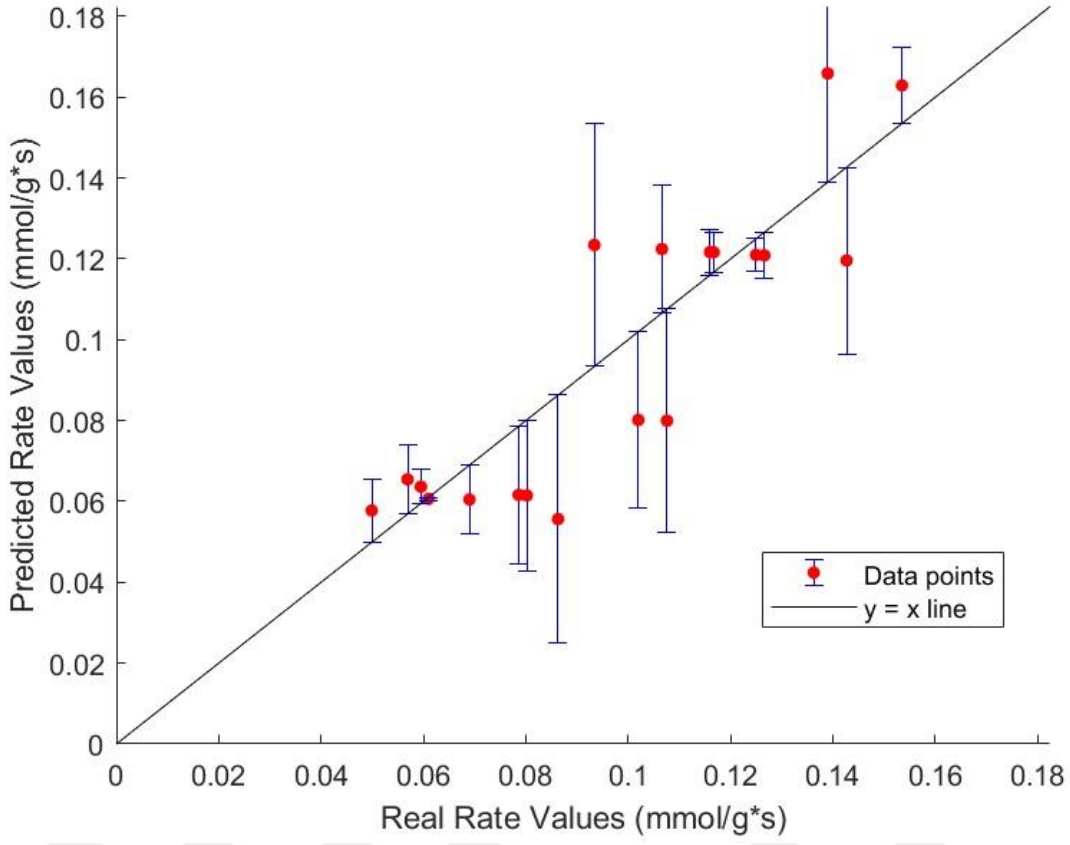

Figure B.11. LOO-predicted rate values for Model 11.

Table B.12. Performance metrics and model parameters of Model 12 calculated using the LOO cross-validation method.

DATA #	RMSE	MSE	R^2	k_1	k_2	K_{CO}	K_{H2}
1	-	-	-	-	-	-	-
2	1.48E-02	2.18E-04	-3.23	9.20	0.72	0.00	0.31
3	1.59E-02	2.54E-04	-45.29	94.49	0.65	0.06	0.24
4	9.80E-03	9.61E-05	0.94	39.60	0.78	0.09	0.47
5	2.23E-02	4.96E-04	0.82	70.47	0.82	0.01	0.60
6	1.06E-02	1.11E-04	0.78	29.60	0.65	0.12	0.22
7	1.22E-02	1.49E-04	0.92	15.89	0.83	0.00	0.59
8	4.57E-03	2.09E-05	0.99	28.35	0.71	0.12	0.32
9	5.34E-03	2.85E-05	0.96	28.55	0.76	0.00	0.46
10	-	-	-	-	-	-	-
11	1.66E-03	2.75E-06	1.00	42.80	0.76	0.00	0.46
12	-	-	-	-	-	-	-
13	1.24E-02	1.54E-04	0.64	29.60	0.64	0.12	0.20
14	1.40E-02	1.96E-04	0.90	12.28	0.79	0.00	0.49
15	5.32E-03	2.83E-05	0.96	28.55	0.76	0.00	0.46
16	4.65E-03	2.17E-05	0.93	69.60	0.68	0.11	0.27
17	-	-	-	-	-	-	-
18	2.46E-02	6.03E-04	0.70	64.95	0.78	0.00	0.55
19	3.38E-03	1.14E-05	0.96	83.50	0.77	0.00	0.48
20	6.70E-03	4.49E-05	0.94	10.11	0.73	0.00	0.35
Average	1.05E-02	1.52E-04	-2.25	41.10	0.74	0.04	0.40

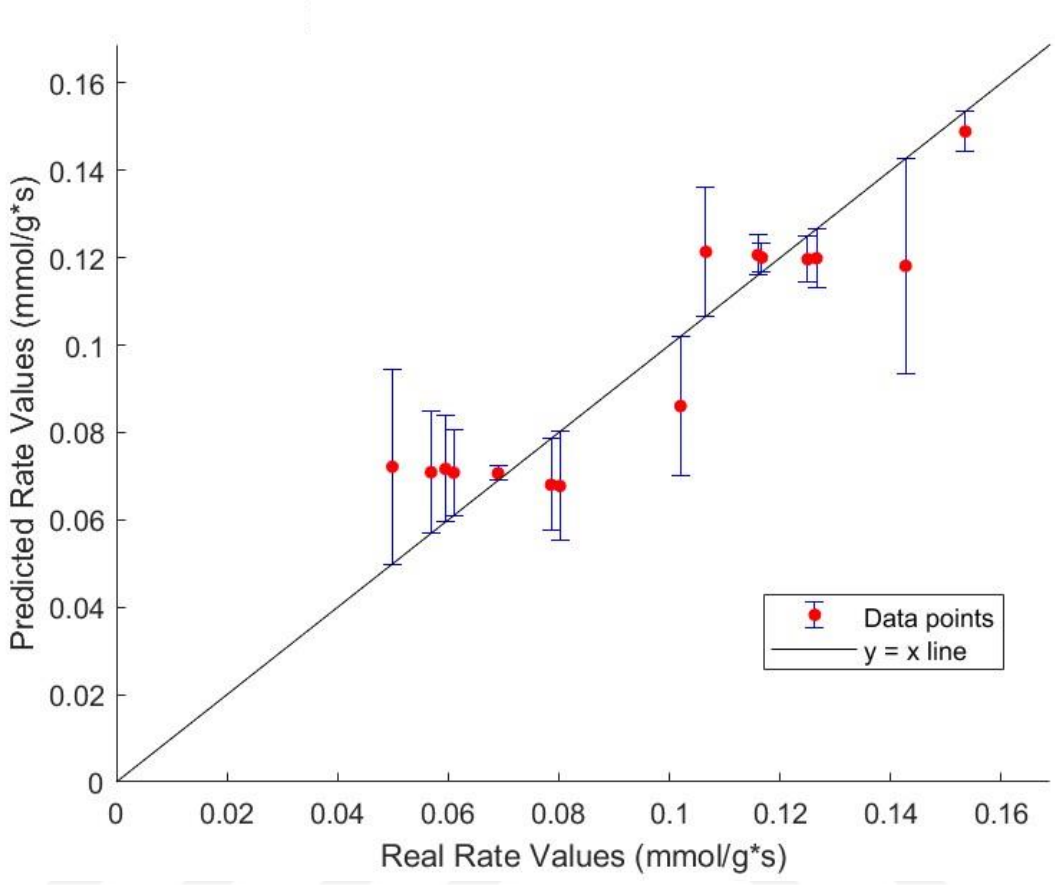

Figure B.12. LOO-predicted rate values for Model 12.